UNIVERSITÉ DE SHERBROOKE
Faculté de génie
Département de génie mécanique

MICROTURBOPOMPE AVEC ISOLATION THERMIQUE POUR CYCLE RANKINE SUR PUCE

Thèse de doctorat

Spécialité : génie mécanique

Amrid AMNACHE

Sherbrooke (Québec) Canada Mai, 2020

Jury :

Luc Fréchette (directeur)
Mohamed Omri (encadreur)
Dominique Drouin (évaluateur)
Martin Brouillette (évaluateur)
Jean-Philippe Colonna (évaluateur)

Résumé

Les micromoteurs thermiques (*Power-MEMS*) pourraient offrir une alternative aux batteries pour répondre aux besoins d'énergie compacte et distribuée pour des applications telles que l'électronique portable, les robots, les drones et les systèmes embarqués, les capteurs et les actionneurs. La microturbine à vapeur de cycle thermodynamique de Rankine fait partie de ce domaine de micromoteurs. Ce dispositif est destiné à la génération d'électricité à petite échelle à partir de la récupération de la chaleur perdue. Dans ce contexte, l'objectif de ce travail est la fabrication et la démonstration expérimentale d'une microturbopompe à haute température pour implémenter le cycle de Rankine. Une configuration originale qui intègre l'isolation thermique est, tout d'abord, proposée. Cette configuration est constituée d'un empilement de cinq tranches (silicium et verre) pour enfermer un rotor hybride (silicium et verre) supporté par des paliers hydrostatiques. Le rotor est un disque de 4 mm de diamètre et de 400 µm d'épaisseur avec des pales de turbine sur le dessus et une pompe visqueuse à rainures en spirale sur le dessous. Une technique de micromoulage de verre a été développée dans ce travail pour intégrer du verre dans le rotor comme un matériau isolant thermiquement. La microturbopompe est fabriquée avec succès en utilisant les méthodes de microfabrication des MEMS. Tout d'abord, les paliers hydrostatiques, la turbine et le fonctionnement de la pompe sont caractérisés, jusqu'à une vitesse de rotation de 100 kRPM. La turbine a fourni 0,16 W de puissance mécanique et le débit de la pompe était supérieur à 2.55 mg/s. Ensuite, la première démonstration d'une turbopompe MEMS fonctionnant à des températures élevées a été réalisée. Une comparaison a été faite avec un rotor non isolé pour prouver l'efficacité des stratégies d'isolation thermique. La turbopompe MEMS isolée a été démontrée à 160°C du côté de la turbine. Par extrapolation, la microturbopompe devrait fonctionner jusqu'à une température de 400°C avant que la température dans la pompe n'atteigne 100°C. Pour la première fois, une microturbopompe pour un fonctionnement à haute température est fabriquée et caractérisée.

Mots clés : *Power-MEMS*, conversion d'énergie, Rankine, micropompe, microturbine, microturbopompe, isolation thermique, micromoulage.

Remerciements

Je tiens, tout d'abord, à remercier mon directeur de thèse, le Prof. Luc Fréchette pour son encadrement durant toute la durée de mon doctorat. Il m'a offert la chance de mener un de ses plus gros projets de recherche. Ceci témoigne qu'il croyait en mes compétences à bien mener ce projet jusqu'à la fin. Je suis très honoré de travailler sous sa supervision. Il était pour moi une source d'inspiration. Je tiens également à le remercier très sincèrement pour la confiance qu'il m'avait accordée à travailler sur d'autres projets de recherche stimulants en parallèle de mon doctorat (STREAMS, Thales, SOFHE). Sa pédagogie dans le travail et ses connaissances irréprochables m'ont permis de développer des compétences non seulement dans le domaine des MEMS, mais aussi des compétences complémentaires, à savoir, la capacité de développer et mener des projets de recherche. Je lui exprime aussi ma gratitude pour sa disponibilité et sa patience, pour son soutien moral dans les moments difficiles et son aide pour surmonter les obstacles que j'ai rencontrés durant ces années d'études doctorales, son écoute et sa compréhension tout le long de cette thèse. Je tiens également à remercier le Prof. Mohamed Omri pour son encadrement. Ses connaissances de la mécanique des fluides et de la turbomachine ont été très utiles dans cette thèse.

Je tiens à remercier les membres de jury, Prof. Martin Brouillette, Prof. Dominique Drouin, Prof. Mohamed Omri et Jean-Philippe Colonna, de l'honneur qu'ils m'ont fait en acceptant d'évaluer ma thèse.

Je remercie tout le staff des salles blanches du 3IT pour l'aide et le soutien technique. Un merci spécial à René Labrecque qui répondait toujours présent tout en gardant le sourire, et à Daniel Blackburn, Caroline Roy et à Pierre Langlois pour la qualité de leur service. Je remercie également le Pr. Paul Charrette et Guillaume Beaudin pour m'avoir prêté leur caméra infrarouge que j'ai utilisée dans ce projet.

Je veux également remercier toutes les personnes qui m'ont aidé pendant l'élaboration de ma thèse. Je pense à Paul Gond-Charton pour ses précieuses informations sur le collage des gaufres, Gholamreza Mirshekari, c'est sous sa supervision que j'ai fait mes premiers pas en salles blanches, Étienne Léveillé pour ses solutions ingénieuses pour relever les défis que j'ai rencontrés en laboratoire, Marie-Josée Gour pour ses conseils concernant la gravure de silicium, Abdelatif Jaouad et Artur Turala pour avoir répondu à mes questions concernant les matériaux et le dépôt de couches minces, Pr. Dominique Drouin et Serge Ecoffey pour leurs conseils sur le polissage, Rajesh Pandiyan pour sa disponibilité et ses offres de service et Émilie Fréchette pour le traitement des images.

Je remercie tous les stagiaires qui ont participé au développement de ce projet, José Francisco Ambía Campos, Marie-Ève Paré, Deepanshi Sisodiya et Charles Sévigny.

Je remercie Thomas Monin et Andrée Dompierre de m'avoir donné la chance de travailler ensemble pour surmonter les défis en microfabrication rencontrés dans leurs projets respectifs.

Je remercie tous mes collègues et mes anciens collègues du groupe MICROS pour les discussions amicales et scientifiques. En particulier : Louis-Michel, Mokhtar, Mahmoodreza, Marc-André, Pascal et Doriane.

Je remercie Abdelkrim Mazouzi de m'avoir donné la chance d'être l'auxiliaire d'enseignement de son cours.

Je remercie mes amis Allaeddine Benchikh Le Hocine pour les discussions sur la CFD et la turbomachine et surtout pour son soutien moral et Youcef Bioud pour son service en salles blanches.

Je remercie finalement et très chaleureusement mes parents Samia et Rabah, et mon frère Nazim pour leur soutien inconditionnel.

« *Today's scientists have substituted mathematics for experiments, and they wander off through equation after equation, and eventually build a structure which has no relation to reality* »
—Nikola Tesla

TABLE DES MATIÈRES

LISTE DES FIGURES

LISTE DES TABLEAUX

1 INTRODUCTION

1.1 Introduction générale

Des MEMS aux *Power MEMS*

Depuis leur création dans les années 60 et l'explosion de leur commercialisation dans les années 80 [1], le développement des microsystèmes électromécaniques, MEMS, ne cesse de croître. Dans les années 90, les MEMS se sont vus multipliés en plusieurs sous-domaines, tels que les Bio-MEMS, les RF-MEMS, les MEMS-optiques et la microfluidique [1]. Ces MEMS se sont trouvé dans diverses applications telles que l'industrie automobile (accéléromètres et capteurs de pression), la médecine (les puces *Lab-on-chip* et les systèmes d'injection de médicaments), les équipements électroniques (gyroscope pour les téléphones portables et cavités d'injection pour les imprimantes jet d'encre). La croissance du marché des MEMS est évalué à environ 1 milliard de dollars américains par an sur la dernière décennie [2]. Cette croissance démontre l'utilité des MEMS dans notre vie. Les avantages potentiels des MEMS qui ont créé cet attrait se résument à leur faible coût de fabrication (fabrication en volume), à leur facilité d'intégration aux circuits électroniques et à leur petite dimension [3]. Ce développement des MEMS est associé principalement au développement des techniques de microfabrication (gravures profondes, photolithographie, déposition de couches minces et collage de gaufres). À la fin des années 90, Alain Epstein, professeur au Massachussetts Institute of Technology (MIT), a proposé un nouveau concept de MEMS, les *Power-MEMS* ou les micromoteurs pour la conversion d'énergie de l'ordre de 1-100 W [4]. L'énergie produite peut être, par exemple, sous forme d'électricité, propulsion ou thermique. La source d'énergie de ces micromoteurs peut être mécanique, chimique, radiative ou thermique. Les micromoteurs thermiques pourraient offrir une alternative aux batteries pour répondre aux besoin d'énergie compacte et distribuée pour des applications telles que l'électronique portable, les robots, les drones et les systèmes embarqués, les capteurs et les actionneurs. Un premier projet de *Power-MEMS* a été immédiatement lancé au MIT. Il s'agit du développement d'une microturbine à gaz de cycle thermodynamique de Brayton pour la génération d'électricité [5]. Cette technologie a été opérée à des vitesses supérieures à 1 MRPM produisant 5 W de puissance mécanique [6]. La densité de puissance (puissance mécanique/volume du dispositif) est

de l'ordre de 4000 MW/m^3 (1.7 MW/kg, silicium comme matériau du dispositif), très supérieure la densité de puissance des batteries de lithium actuelles (~10^2 W/kg) [7].

Micromoteurs thermiques (*Power-MEMS*)

Par la suite, de nombreux groupes de recherche ont tenté de développer des micromoteurs thermiques avec une variété d'approches incluant les micromoteurs Wankel [8,9] et les micromoteurs à combustion interne de cycle Otto [10]. À ce jour, ces dispositifs n'ont pas atteint des rendements comparables à ceux de leurs homologues à grande échelle en raison de certains effets négatifs inhérents à la miniaturisation. Par exemple, les faibles nombres de Reynolds proportionnels à la taille entraînent des pertes visqueuses relativement élevées, ce qui réduit l'efficacité. À leur avantage, ils ont montré une densité de puissance élevée. Tous les dispositifs décrits ci-dessus sont entraînés par une source de chaleur provenant de la combustion interne, qui nécessite une conversion propre et efficace du combustible en énergie électrique. Des micromoteurs thermiques résonants entraînés par des sources de chaleur externes ont également été étudiés. Le micromoteur thermique P^3 a été développé à Washington University [11]. La puissance thermique produite à partir d'une source de chaleur externe est convertie en puissance mécanique (oscillation) grâce au changement de phase liquide-gaz d'un fluide de travail. Un convertisseur piézoélectrique est utilisé pour convertir la puissance mécanique en puissance électrique. En utilisant un principe de fonctionnement similaire, d'autres micromoteurs thermiques ont été rapportés [12,13]. Un micromoteur thermique original basé sur les oscillations d'un piston liquide chauffé a été fabriqué et testé à l'Université de Sherbrooke [14,15,16]. Le principe de ce micromoteur fluidique auto-oscillant (SOFHE) consiste en un mouvement cyclique d'un piston liquide (par changement de phase) à l'intérieur d'un tube qui est exposé à une source de chaleur constante d'un côté et à une source de froid de l'autre. Basé sur le cycle de Stirling, un micromoteur Stirling (MISTIC) pour la production d'électricité par récupération de chaleur a été étudié à l'Université de Sherbrooke [17]. Comme avantage, ces micromoteurs thermiques résonnants fonctionnent avec des composants flexibles et une source de chaleur relativement à basse température. Cependant, ils ont montré une faible densité de puissance par rapport aux micromoteurs à combustion interne.

Microturbine à vapeur de cycle Rankine

Cette thèse s'inscrit dans le cadre du projet de développement d'une microturbine utilisant le cycle Rankine à vapeur destinée pour la récupération de chaleur perdue. Inspiré du projet de microturbine à gaz du MIT, ce concept a été proposé en premier par le Pr. Luc Fréchette à Columbia University [18]. Comparé aux micromoteurs cités ci-dessus, le concept de microturbine à vapeur Rankine a l'avantage de combiner un fonctionnement à des températures modérées (isolation thermique moins complexe) avec la possibilité de fonctionner avec n'importe quelle source de chaleur, tout en produisant une densité de puissance relativement élevée [19].

Une microturbopompe de première génération nécessaire pour le développement de la microturbine de cycle Rankine a été fabriquée en silicium et testée à l'air comprimé à température ambiante [20,21]. Cette microturbopompe de première génération n'a intégré aucune isolation thermique étant donné que l'objectif était la démonstration du fonctionnement à température ambiante. Cependant, dans les applications réelles, le dispositif doit être conçu pour fonctionner à la vapeur surchauffée dans la turbine et à l'eau liquide dans la pompe. Pour assurer un bon fonctionnement, une isolation thermique au sein de ce dispositif est requise pour éviter l'évaporation de l'eau dans la pompe ou la condensation de la vapeur dans la turbine et les paliers d'équilibre.

L'objectif de ce travail est la fabrication et la démonstration d'une microturbopompe de deuxième génération opérationnelle à haute température. Cette microturbopompe présente un design optimisé et des fonctionnalités nouvelles basées sur des modèles améliorés et des connaissances acquises lors de l'expérimentation de la première génération.

1.2 Plan de la thèse

Le manuscrit prend le format de thèse par articles. Il est constitué de trois articles de journal lesquels sont précédés par un chapitre de mise en contexte pour situer le projet de recherche et décrire les objectifs.

Le chapitre 2 présente une mise en contexte du projet microturbine suivie d'une revue des travaux antérieurs effectués dans ce cadre. Par la suite, l'ensemble des défis de fabrication sont parcourus en focalisant sur l'isolation thermique. Le choix des stratégies d'isolation thermique au sein de la

microturbopompe fabriquée et caractérisée dans ce travail est présenté et expliqué. Finalement, les objectifs du projet seront décrits.

Le chapitre 3, sous le format d'un article de journal (publié), est consacré au développement d'un procédé de micromoulage de verre destiné à la fabrication des microstructures à hauts rapports de forme. Cette technique sera utilisée pour intégrer le verre dans le rotor. Le verre ici aura pour but l'isolation thermique dans la microturbopompe.

Le chapitre 4, sous un format d'un article de journal (soumis), couvre le design et la fabrication d'une microturbopompe de deuxième génération pour un fonctionnement à haute température. Une configuration originale qui intègre l'isolation thermique est présentée. Les défis de fabrication sont présentés. Subséquemment, les méthodes et les techniques de fabrication pour surmonter ces défis sont proposées. Le processus complet de microfabrication est ensuite décrit en détail. Finalement, les résultats obtenus sont présentés et discutés.

Le chapitre 5, sous format d'un article de journal (soumis), est consacré à la démonstration et la caractérisation expérimentale de la microturbopompe. La turbine, les paliers axial et radial et la pompe sont caractérisés à haute vitesse de rotation. Les stratégies d'isolation thermique utilisées sont évaluées démontrant ainsi le fonctionnement à haute température.

1.3 Contribution de la thèse

La contribution originale de la thèse réside dans la démonstration, pour la première fois, le fonctionnement d'une microturbopompe à haute température. Plusieurs contributions scientifiques sont apportées, à la fois utiles pour la suite du développement de projet et surtout pour la communauté scientifique des MEMS [42,43,57]. Nous résumons ci-dessous ces contributions spécifiques :

Micromoulage de verre

- Étude détaillée des capacités et des limites de la technique de micromoulage de verre pour la fabrication des structures en verre à haut rapport de forme.
- Développement d'une technique d'intégration du verre dans les substrats de silicium.

Microfabrication de la microturbopompe

- Développement des stratégies d'intégration de l'isolation thermique dans la microturbopompe.
- Développement d'un procédé complet de microfabrication de la microturbopompe de deuxième génération.
- Fabrication de la première microturbopompe opérationnelle intégrant des stratégies d'isolation thermique pour un fonctionnement à haute température.

Démonstration expérimentale

- Caractérisation expérimentale des composantes de la microturbopompe (turbine, pompe, et paliers hydrostatiques) à température ambiante et à haute vitesse de rotation.
- Démonstration et test de fonctionnement de la microturbopompe à haute température.
- Évaluation de l'efficacité de l'isolation thermique.

2 MISE EN CONTEXTE

2.1 Microturbine à vapeur de cycle Rankine

2.1.1 Concept du cycle Rankine

Les turbines à vapeur traditionnelles pour la génération d'électricité fonctionnent selon le cycle thermodynamique de Rankine. C'est un cycle thermodynamique de conversion d'énergie sous forme de chaleur en énergie mécanique. Cette dernière est convertie en énergie électrique via d'une génératrice. Le cycle est assuré par quatre éléments essentiels : la turbine, la pompe, l'évaporateur et le condenseur (Figure 2-1). En général, l'eau est utilisée comme fluide moteur qui subit quatre transformations thermodynamiques en cycle fermé :

1 à 2 compression adiabatique : l'eau liquide est pressurisée à une haute pression dans la pompe. Le travail de la pompe (W_P) est fourni par le travail de la turbine (W_T).

2 à 3 évaporation isobare : l'eau liquide est évaporée à pression constante dans l'évaporateur par un apport de chaleur de l'extérieur (Q_{in})

3 à 4 détente adiabatique : la vapeur à haute pression est détendue dans la turbine pour engendrer un travail mécanique rotatif (W_T)

4 à 1 condensation isobare : la vapeur saturée à basse pression sortante de la turbine est liquéfiée dans le condenseur. L'évacuation de la chaleur (Q_{out}) se fait par une source externe.

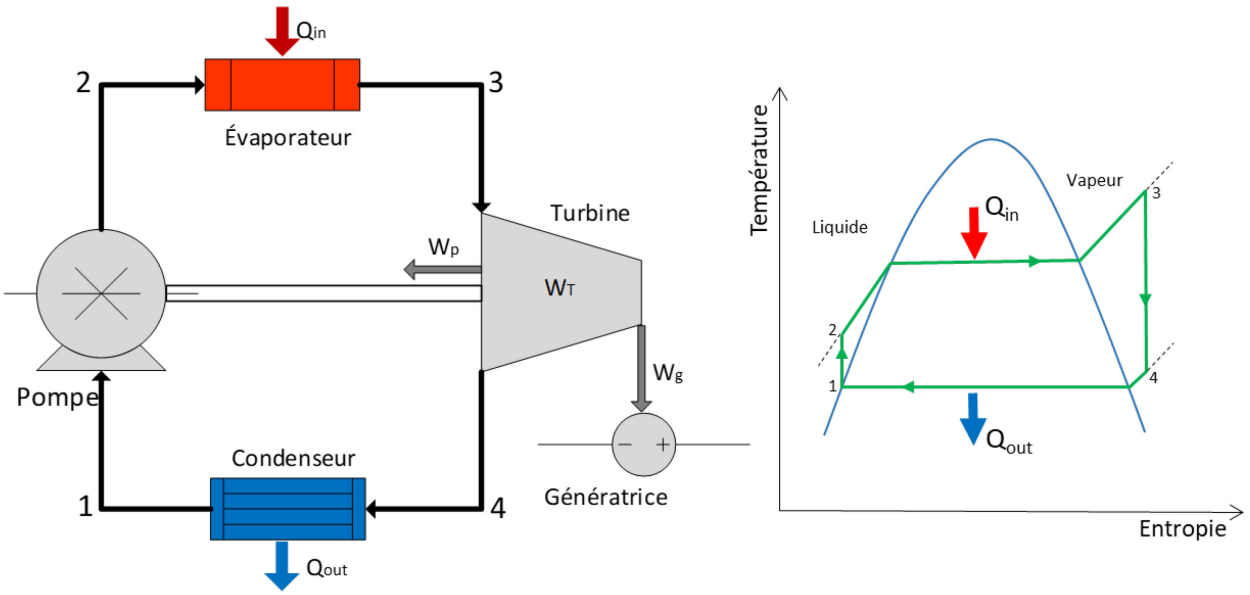

Figure 2-1 Cycle thermodynamique de Rankine. a) Éléments du cycle b) Diagramme T-s idéalisé.

2.1.2 Miniaturisation

La microturbine à vapeur est une miniaturisation de la turbine à vapeur traditionnelle. Elle fonctionne selon le même cycle thermodynamique, Rankine. La source d'énergie pour le fonctionnement provient de la récupération de la chaleur perdue. La miniaturisation, à part l'adaptation dimensionnelle pour l'intégrer dans des petits systèmes, a pour but d'exploiter les avantages du cycle de Rankine à petite échelle. Le principal avantage de la miniaturisation est de permettre l'obtention d'une densité d'énergie (puissance développée/volume du dispositif) élevée par rapport aux échelles macroscopiques. Dans la microturbine à vapeur, la densité d'énergie peut être exprimée par :

$$\frac{Puissance}{Volume} = \frac{Q\ \Delta P}{Volume} \tag{2.1}$$

La puissance développée est proportionnelle au débit du fluide, Q, qui est lui aussi proportionnel à la section (L_c^2), où L_c est la longueur caractéristique. Avec une écriture dimensionnelle, la densité d'énergie peut s'exprimée en la manière suivante :

$$\frac{Puissance}{Masse} \propto \frac{L_c^2}{L_c^3} = \frac{1}{L_c} \tag{2.2}$$

Ce qui démontre une densité d'énergie inversement proportionnelle à la dimension caractéristique du dispositif.

2.1.3 Avantages et applications du concept de microturbine à vapeur

Par comparaison avec la microturbine à gaz de Brayton développée au MIT, la microturbine à vapeur présente plusieurs avantages. Contrairement à la microturbine à gaz, la compression se fait en phase liquide qui requiert beaucoup moins d'énergie [19]. L'efficacité de la microturbine à gaz est considérable seulement à très hautes températures (1200-1600K) [22]. Cependant, à des échelles micrométriques, les températures élevées rendent les techniques d'isolation thermique nécessaire pour assurer un bon gradient de température plus complexe. Aussi, les effets thermomécaniques sont plus importants à des températures plus élevées rendant la conception plus complexe. D'un point de vue écologique, l'application de la microturbine à vapeur de cycle Rankine a un avantage majeur puisqu'elle pourrait fonctionner avec de la récupération de chaleur perdue, chose impossible pour une microturbine à gaz dépendante de la combustion d'un carburant.

Des quantités d'énergie considérables dans les procédés industriels, dans les secteurs de transport et pétrolier sont perdues dans l'atmosphère sous forme de chaleur. Le concept de microturbine à vapeur de cycle Rankine pourrait être une opportunité pour la récupération d'une partie de cette chaleur perdue. La récupération de chaleur a pour impact la diminution de la consommation d'énergie et aussi les émissions des gaz à effet de serre. L'électricité convertie par cette technologie pourrait être, par exemple, utilisée pour alimenter des équipements électriques et différents capteurs et actionneurs dans ces systèmes. Une microturbine à vapeur de cycle Rankine est prédite pour développer entre 3 et 10 W d'énergie électrique selon la température de la source de chaleur. Un dispositif constitué de 140 microturbines (volume total d'environ 1120 cm^3) peut être utilisé dans la récupération de chaleur des gaz d'échappement des voitures pour ainsi diminuer la consommation de carburant de plus de 10% [23].

2.2 Revue des travaux antérieurs et défis de fabrication

L'objectif général du projet de recherche auquel s'inscrit cette thèse est le développement d'une microturbine à vapeur de cycle Rankine destinée à la récupération de la chaleur perdue dans différentes applications. Pour arriver à terme de cette technologie, plusieurs recherches couvrant différents aspects technologiques à petite échelle ont été entrepris, notamment, les travaux effectués dans le cadre du projet *Micro-Engine* au MIT et ses institutions collaboratrice qui ont été d'une grande utilité dans le développement du concept de microturbine à vapeur de cycle Rankine. Des technologies clés ont été étudiées et démontrées expérimentalement, qui forment la base du développement du projet de microturbine à vapeur. Cela inclut les paliers hydrostatiques qui assurent la stabilité axiale et radiale du rotor [24], les microgénératices [25] et leur intégration [26]. Une première génération de microturbopompe pour un fonctionnement à température ambiante est aussi fabriquée et testée à *Columbia University* [27] comme détaillé dans la section suivante. D'autres volets restent encore à développer, dont fait partie l'objectif de la présente thèse qui a pour but la démonstration du fonctionnement à haute température, mais aussi l'intégration et la démonstration du fonctionnement de la génératrice à haute température, la démonstration du fonctionnement avec un cycle fermé, pour arriver enfin à la démonstration de la technologie pour la récupération de chaleur. La figure 2-2 présente un schéma du plan de développement de cette technologie. Les deux sections suivantes présentent les travaux déjà effectués pour atteindre l'objectif final de ce projet.

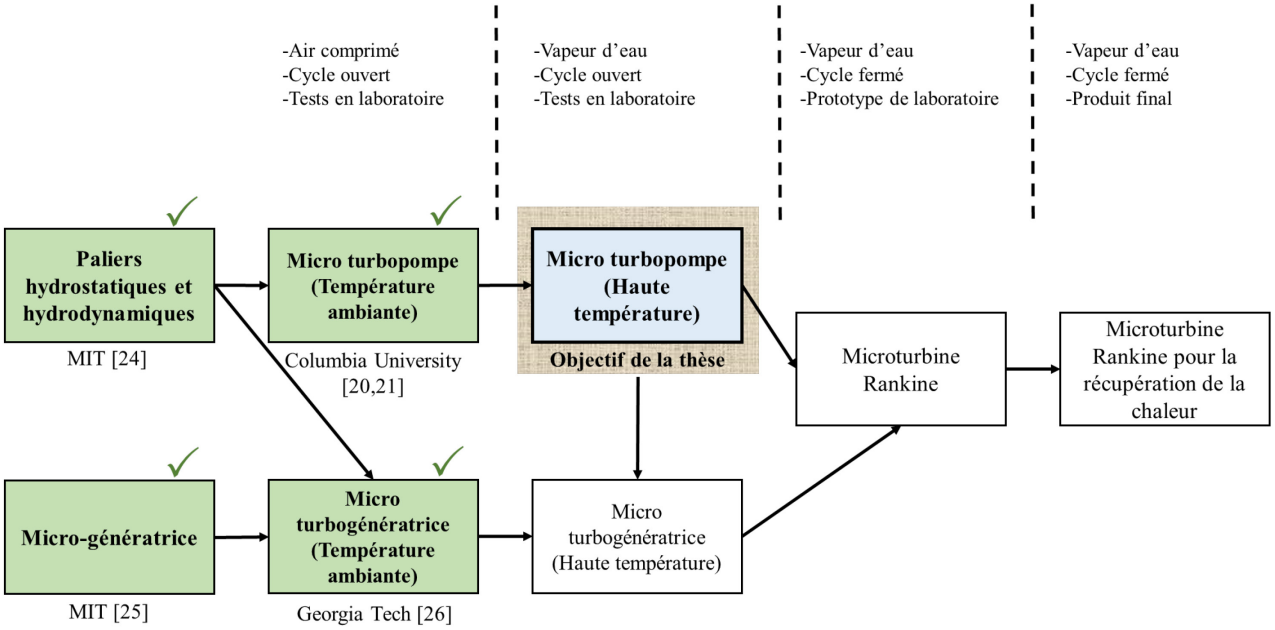

Figure 2-2 Plan de développement du projet microturbine à vapeur de cycle Rankine pour la récupération de la chaleur. Les cases en vert représentent les volets technologiques déjà développées, tandis que les cases sans couleur représentent les technologies qui restent encore à développer.

2.2.1 Microturbopompe pour un fonctionnement à température ambiante

Dans le but d'explorer le potentiel du cycle thermodynamique de Rankine à petite échelle, une microturbopompe de première génération a été fabriquée et testée [20,21]. Le dispositif comprend seulement une turbine et une pompe. Les échangeurs de chaleur (évaporateur et condenseur) et la génératrice sont exclus de cette première génération à raison de faciliter la fabrication et l'expérimentation. Elle est constituée d'un empilement de 4 tranches de silicium (B, C, D, E) et une tranche de verre (A) comme montré à la Figure 2-3.

La turbine dans laquelle le fluide fait une détente est composée de quatre étages de pales formées par une gravure DRIE (*Deep Reactive Ion Etching*) sur le dessus du rotor. La longueur de corde des pales est de 100 µm et une hauteur de 50 à 70 µm. La pressurisation de l'eau se fait dans une pompe visqueuse à rainures en spirale située au-dessous du rotor. La rotation du rotor (produite par la détente du fluide dans la turbine) engendre un écoulement d'eau dans le sens des rainures en spirale avec une augmentation de sa pression par le biais des forces visqueuses. La stabilité axiale et radiale du rotor sont assurées respectivement par le palier axial (*Thrust bearing*) et un palier radial (*Journal bearing*). Le palier radial est l'espace circonférentiel entre le rotor et sa cavité. En

introduisant un écoulement de gaz dans cet espace, un champ de pression sur la périphérie du rotor permettra de le garder centré radialement. Le palier axial est une série d'orifices situés dans le compartiment inférieur de la microturbopompe qui injectent un débit de gaz pour créer une force opposée à la force créée par la pression dans la turbine (au-dessus du rotor) et ainsi créer un équilibre de forces pour stabiliser le rotor axialement. Pour assurer l'étanchéité fluidique dans la microturbopompe, Lee a conçu des joints d'étanchéité (*seal*) à rainures en spirale fonctionnant avec le même concept que la pompe. Dans cette version, comme illustré dans la Fig. 2-3, deux joints d'étanchéité sont intégrés : 1) au niveau du compartiment inférieur pour empêcher les fuites entre l'entrée de la pompe vers le palier axial, et 2) au niveau du compartiment supérieur pour empêcher les fuites entre la sortie de la pompe et la turbine.

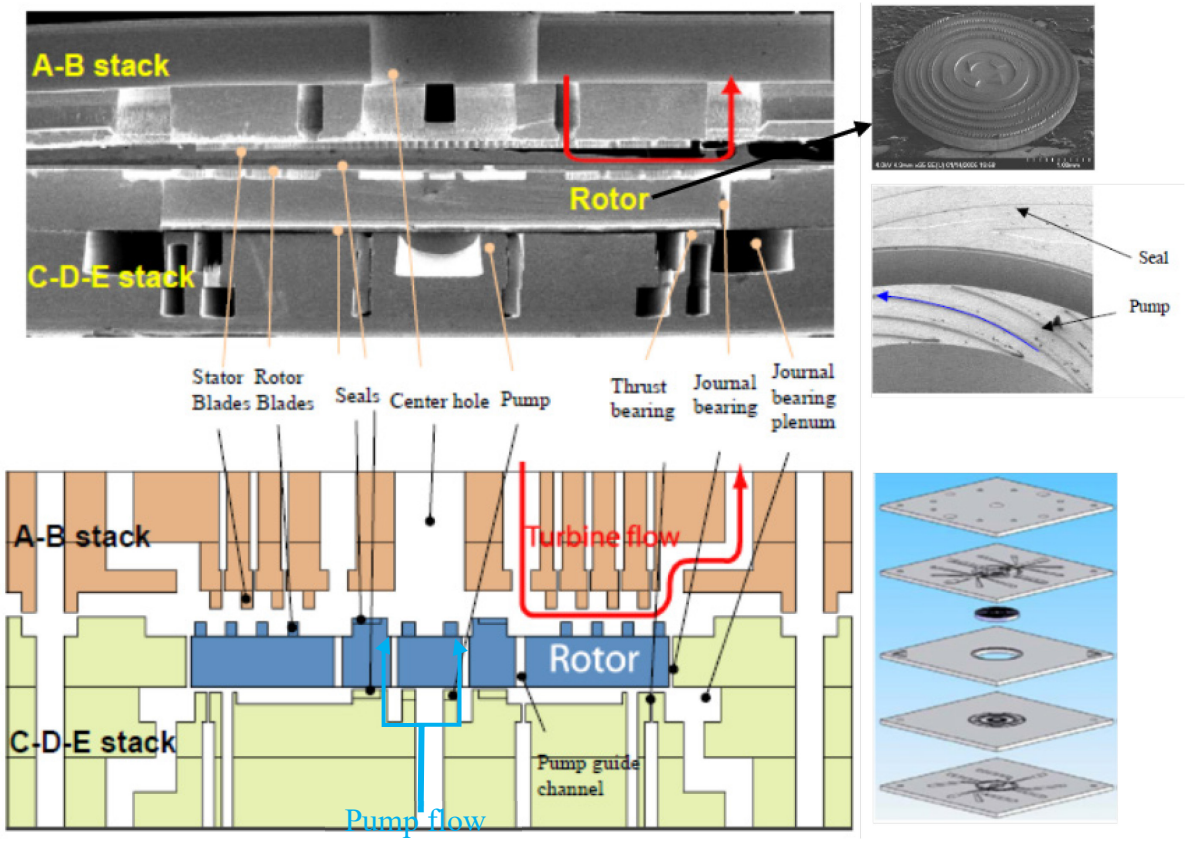

Figure 2-3 Première génération de microturbopompe [27]

Cette première génération de microturbopompe, n'ayant aucune isolation thermique, a été testée seulement à l'air comprimé à température ambiante. Les performances de ces premiers tests étaient très encourageantes. Le rotor a tourné à des vitesses de 330 kRPM sans pompage (sans eau dans la pompe) et à 116 kRPM avec pompage d'eau (débit de 4 mg/s et pressurisation de 88 kPa) [21].

L'application réelle de la microturbine à vapeur de cycle Rankine est à haute température. Le dispositif doit être conçu pour fonctionner à la vapeur surchauffée dans la turbine et à l'eau liquide dans la pompe. Pour assurer un bon fonctionnement, une isolation thermique au sein de ce dispositif est requise pour éviter l'évaporation de l'eau dans la pompe ou la condensation de la vapeur dans la turbine et les paliers d'équilibre.

2.2.2 Microturbopompe pour un fonctionnement à haute température

Depuis la démonstration de la microturbopompe à l'air comprimé [21], plusieurs recherches ont été effectuées dans le but de développer une microturbopompe de deuxième génération qui fonctionne à la vapeur surchauffée. Ces recherches ont mis en place des éléments essentiels et utiles pour la continuation de ce projet de recherche.

La caractérisation expérimentale de la miroturbopompe de première génération a montré quelques limitations dans le fonctionnement qui étaient peu analysées dans l'étude de Lee [27]. La plus importante limitation était au niveau de l'équilibre radial et axial du rotor. Il fallait donc approfondir la compréhension des écoulements internes pour bien cibler les sources qui limitaient les performances de la microturbopompe. C'était l'objectif du projet de maîtrise de Félix Gauthier [28]. L'auteur a effectué une modélisation des différents écoulements dans la microturbopompe. Le même auteur a effectué une caractérisation expérimentale de la microturbopompe (la même fabriquée par Lee [21]) à l'air comprimé et à température ambiante, en focalisant essentiellement sur les écoulements au niveau des paliers axial et radial, des joints d'étanchéité et de la pompe. Ce travail expérimental a permis de valider les modèles développés dans son étude.

L'étude de Gauthier a fait ressortir plusieurs recommandations, tant pour la conception de la microturbopompe de deuxième génération que pour son fonctionnement. L'auteur a étudié en utilisant des modèles analytiques l'effet de la température de l'eau dans la pompe sur sa puissance délivrée. Il s'est avéré que la variation de la température présente un impact considérable sur le pompage [28]. Par exemple, pour une vitesse de rotation de 600 kRPM, si la température de l'eau dans la pompe passe de 20 à 90°C, le débit délivré par la pompe chute de trois ordres grandeur. Comme la pompe utilisée est une pompe visqueuse, la diminution du pompage est due à la diminution de la viscosité et de la densité de l'eau avec l'augmentation de la température. Ce résultat démontre le besoin en termes d'isolation thermique entre les écoulements chauds de la vapeur et les écoulements froids de l'eau liquide au niveau de la pompe. Cette sensibilité suggère

aussi que la performance de la pompe est un indicateur de la température de l'eau dans la pompe, un principe qui nous servira dans ces travaux.

Le sens de pompage a été aussi étudié et modélisé, c'est-à-dire, le pompage vers l'extérieur et le pompage vers l'intérieur. L'auteur a trouvé que le pompage vers l'extérieur est plus efficace dû aux forces centrifuges. Cependant, un pompage vers l'extérieur demande une étanchéité plus efficace entre la pompe et le palier axial (pression plus élevée). Après l'étude de l'efficacité des joints d'étanchéité, l'auteur recommande un pompage vers l'intérieur.

La caractérisation effectuée par Lee [21] a démontré des lacunes au niveau de la stabilité du rotor qui ont empêché le fonctionnement à des vitesses supérieures à 330 kRPM. Une des causes est que le palier axial auxiliaire crée des forces insuffisantes pour contrer les forces appliquées sur le dessus du rotor par l'écoulement dans la turbine. La distribution des forces sur le rotor a été revue et étudiée par Gauthier dans le but de trouver les conditions d'opération adéquates pour assurer l'équilibre axial du rotor. Un autre modèle des écoulements dans le palier axial a été développé afin de bien prédire son comportement. L'auteur a recommandé de concevoir un autre palier axial sur le dessus du rotor afin d'améliorer le contrôle de la stabilité du rotor, tel qui sera implémenté dans les travaux de cette thèse.

Dans l'objectif de concevoir la turbine, Beauchesne-Martel a analysé numériquement les écoulements à travers les pales de turbine [29]. Le but était de comprendre la structure de l'écoulement et de déterminer les conditions opératoires et géométriques pour un fonctionnement optimal. Un design des pales de la turbine et du stator de la microturbopompe de deuxième génération a été défini. L'auteur a aussi proposé le concept *Multi-spool* comme schématisé sur la figure 2-4. L'idée est d'utiliser une combinaison en série d'une microturbopompe (turbine avec pompe) avec trois micro turbogénératrices (turbine avec micro génératrice seulement). Le pompage du liquide se fait dans la pompe de la microturbopompe alors que les 3 micro turbogénératrices (1, 2 et 3 sur le schéma) ont pour but de convertir le travail mécanique en électricité. La vapeur peut détendre dans les trois turbogénératrices pour ensuite entrainer la turbopompe. Cette configuration permet de réduire le gradient de température dans la microturbopompe puisque la température de la vapeur entrante est moins élevée, et ainsi réduire la complexité de l'isolation thermique et les effets thermomécaniques.

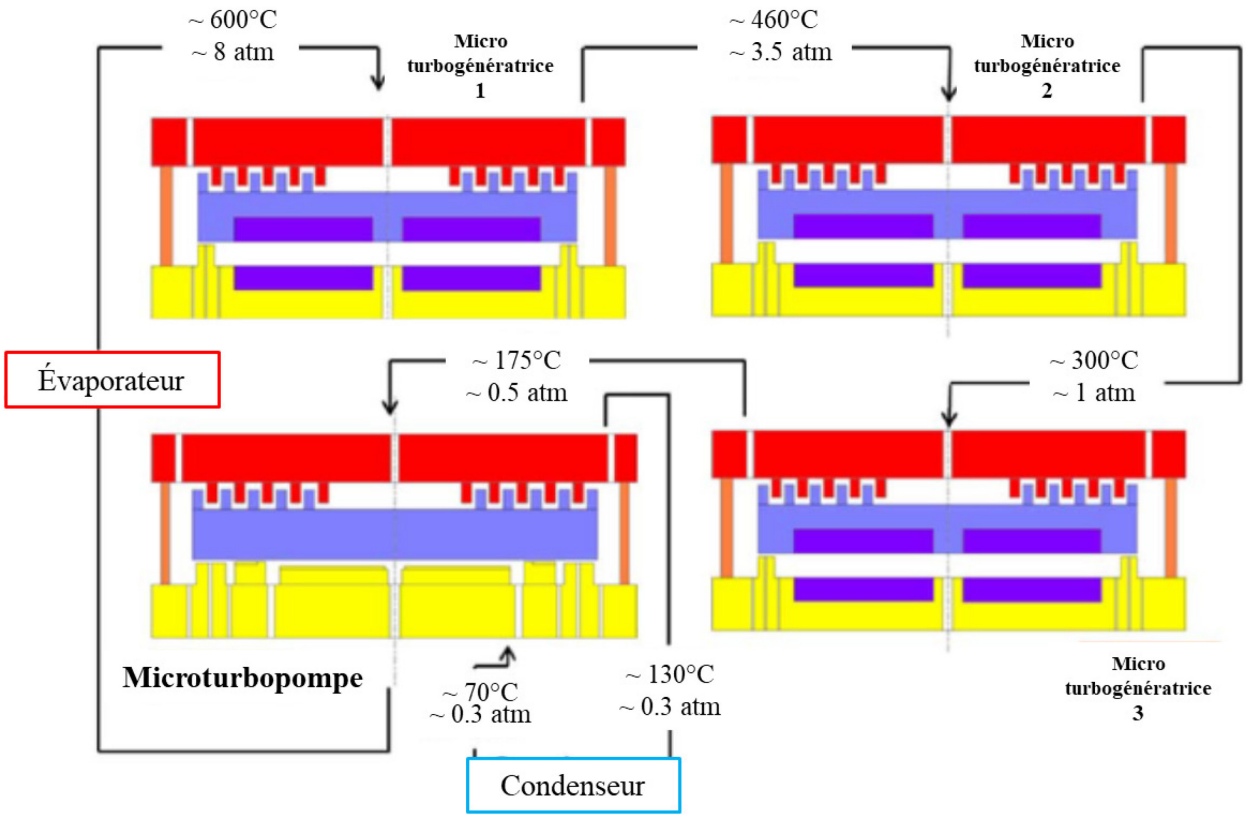

Figure 2-4 Configuration multipool de quatre microturbines : les turbines 1 à 3 intègrent une microgénératrice alors que la turbine 4 entraine une micropompe. [29]

Omri a continué les travaux de Beauchesne-Martel sur l'analyse numérique de l'écoulement (CFD 3D) à travers les pales de la turbine [30]. L'auteur a étudié essentiellement l'effet du jeu de pale i.e. distance entre la pale et la partie statique (*tip clearance*), l'effet de l'angle d'incidence de la pale et l'effet du nombre de Reynolds sur les pertes à travers un étage de pales de la turbine. Des corrélations du coefficient de perte à travers les pales de turbine ont été établies. Plusieurs points importants sont tirés de cette étude et sont très utiles pour le design de la microturbopompe de deuxième génération. L'auteur recommande notamment, afin d'avoir des pertes modérées, d'opérer la microturbopompe à des nombres de Reynolds supérieurs à 1000 et de concevoir un *tip clearance* ne dépassant pas 5 % de la hauteur de la pale. La conception de de la microturbopome dans ce travail suit ces recommandations.

Liamini a concentré ses travaux sur l'effet des transferts de chaleur à travers le rotor sur les performances de la microturbopompe pour un fonctionnement à la vapeur surchauffée [23]. L'auteur a, dans un premier lieu, étudié l'effet de la conductivité thermique du rotor sur l'efficacité

de la microturbopompe et la température dans la pompe. Des modèles analytiques couplés au calcul par éléments finis sont développés dans cette étude. Pour limiter l'élévation de température dans la pompe à 40°C (température acceptable qui n'affecte pas les performances de la pompe), ses résultats recommandent que le rotor ait un résistance thermique minimum de 3 K/W. En effet, ce résultat permet de déterminer le type de matériau et l'épaisseur optimale de l'isolation au niveau du rotor.

L'auteur a étudié aussi le comportement thermomécanique dans la microturbopompe en effectuant une simulation 2D d'un couplage thermique et mécanique [23]. Il a analysé les déformations au niveau de la cavité du rotor en imposant une différence de température de 200 K entre la zone chaude et la zone froide de la microturbopompe. Il a constaté des déformations considérables qui sont comparables aux gaps de fonctionnement de la pompe, des joints d'étanchéité et du palier axial (gap nominal de fonctionnement = 1µm). En effet, il a recommandé de créer des coins chanfreinés (rayon de 30 µm) au niveau de la cavité du rotor. Comme la fabrication de ce type de chanfreins s'avérait complexe, l'auteur a suggéré une autre approche. C'est de faire un système en trois sous assemblages au lieu d'une structure monolithique. C'est-à-dire que la tranche D qui crée la cavité du rotor (voir Figure 2-5) ne doit pas être collée sur les tranche E et B. L'étanchéité entre ces deux couches est assurée par des forces de serrage dans un *packaging*.

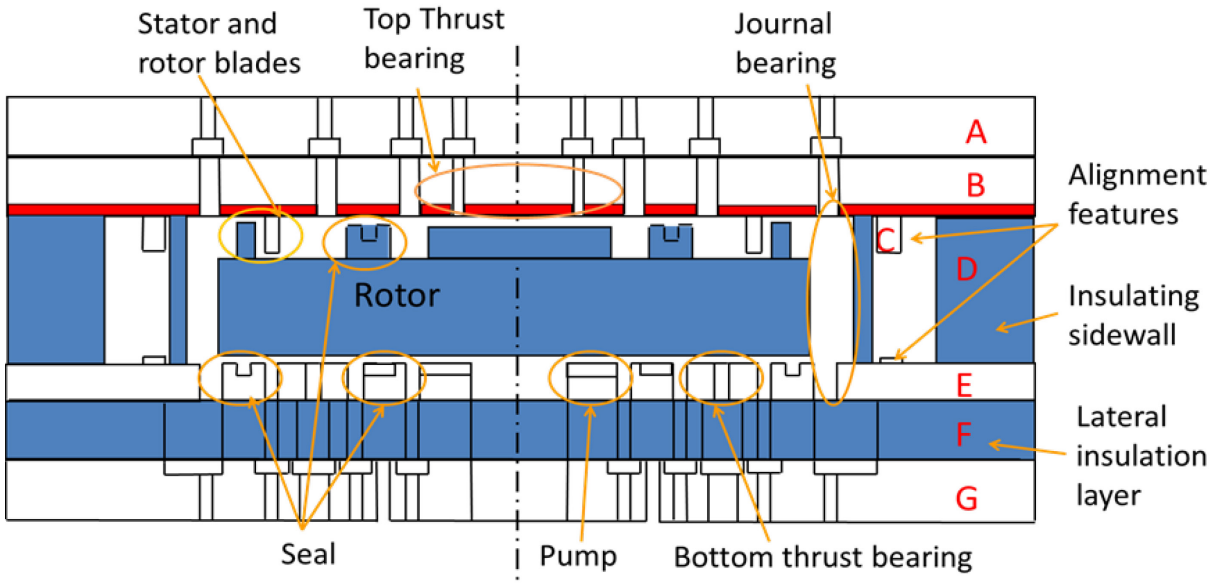

Figure 2-5 Vue de coupe du concept de microturbopompe avec isolation thermique proposé par Liamini [23].

La figure 2-5 schématise une vue de coupe du concept proposé par Liamini [23] pour une microturbopompe de deuxième génération. Cette configuration exclut l'évaporateur et le condenseur, donc l'alimentation en fluide (vapeur et eau liquide) se fait par une source extérieure. La turbine comprend seulement un étage de pales tel que conçu par Beauchesne-Martel [29], suffisant pour alimenter une microturbopompe. Le concept est constituée d'un empilement de 4 tranches de silicium et deux tranches de verre. Ce premier concept présente surtout un compromis entre le fonctionnement et les performances de la microturbopompe, mais il présente des complexités dans la microfabrication. Ces complexités sont détaillées dans la section ci-dessous.

2.3 Défis d'isolation pour le fonctionnement à haute température

L'isolation thermique dans la microturbopompe est un point très important pour garantir un bon fonctionnement à haute température. Deux points critiques sont à considérer. Le premier est l'isolation entre le côté supérieur (turbine et palier axial supérieur) et le côté inférieur de la microturbopompe (pompe). Cette isolation doit être assurée au niveau du rotor. Il faut alors que le rotor supporte un gradient de température suffisant pour éviter la condensation de vapeur du côté supérieur et/ou l'évaporation de l'eau dans la pompe. La fabrication d'un rotor totalement en silicium ne serait pas une bonne approche (matériau très conducteur thermiquement), surtout si on sait que l'épaisseur du rotor est très petite, de l'ordre de 400 µm. L'objectifs donc est de trouver des solutions alternatives pour offrir une résistance thermique suffisante.

L'isolation thermique radiale entre l'écoulement de vapeur dans le palier axial inférieur et l'écoulement d'eau dans la pompe n'a pas été traité dans l'analyse thermique de Liamini [23]. Cette isolation thermique doit être assurée au niveau du joint d'étanchéité entre le palier axial inférieur et la pompe. La fabrication d'un joint d'étanchéité en silicium comme proposé dans le concept de Liamini ne permettrait pas une isolation adéquate (voir Figure 2-5). En utilisant le silicium comme matériau du joint d'étanchéité, la résistance thermique, R_{th}, est estimée par l'équation suivante :

$$R_{th} = \frac{\ln\left(\frac{r_2}{r_1}\right)}{2\,\pi\,k\,L} = \frac{\ln\left(\frac{1.15\times10^{-3}}{10^{-3}}\right)}{2\times\pi\times160\times450\times10^{-6}} \approx 0.3\,\frac{\mathrm{K}}{\mathrm{W}} \tag{2.3}$$

où r_1, r_2 sont respectivement le rayon interne et le rayon externe du joint d'étanchéité. k est la conductivité thermique du silicium.

En supposant que la température sur la surface du côté chaud du joint d'étanchéité est à 120°C et la température sur la surface de la pompe est à 100°C (température maximale pour éviter l'évaporation de l'eau dans la pompe), le taux de transfert de chaleur, P, est estimé par :

$$P = \frac{\Delta T_s}{R_{th}} = \frac{20}{0.3} \approx 66\ W \tag{2.4}$$

où ΔT_s est la différence de température de surface entre le côté chaud et le côté froid du joint d'étanchéité.

D'un autre côté, par conservation d'énergie, le flux chaleur nécessaire, P_{min}, pour atteindre la température d'évaporation dans la pompe est calculé par :

$$P_{min} = \dot{m} c_p \Delta T_p = 80\ \times 10^{-6} \times 4200 \times 80 \approx 27\ W \tag{2.5}$$

Où $\dot{m}$ est le débit nominal de la pompe, c_p est la capacité calorifique de l'eau et ΔT_p est la différence de température de l'eau entre l'entrée et la sortie.

L'écoulement dans la pompe a besoin de seulement 27 W pour enclencher une évaporation, ce qui est très probable puisque ce flux de chaleur minimal est inférieur au flux de chaleur que la partie chaude pourrait transférer à la zone de la pompe.

Avec ce simple calcul estimatif, on en déduit que l'évaporation de l'eau dans la pompe est très probable si on utilise un joint d'étanchéité en silicium sans aucune stratégie d'isolation thermique. Dans le sens inverse, la condensation de la vapeur dans le palier axial est aussi probable. Il est nécessaire alors de trouver une autre alternative ou une autre configuration qui respecte simultanément le besoin en isolation thermique et le besoin en termes d'étanchéité fluidique.

Éventuellement, dans ce projet de doctorat, la question de recherche se pose ainsi:

Quelle serait la configuration, le procédé de fabrication et les matériaux requis pour avoir une bonne gestion thermique dans la microturbopompe pour l'opération à haute température?

2.4 Approches d'isolation thermique dans les MEMS

On peut distinguer deux catégories d'isolation thermique dans les MEMS : l'utilisation de substrats à faible conductivité thermique et l'isolation thermique localisée.

2.4.1 Les substrats à faible conductivité thermique

L'utilisation de substrats de verre ou de céramique pour remplacer les substrats de silicium pour fabriquer les micromoteurs thermiques offrirait un grand avantage en terme d'isolation thermique. La conductivité thermique du verre (~1.2 W/m/K), par exemple, est plus que cent fois moins de celle du silicium cristallin (148 W/m/K).

À des fins d'isolation thermique, les substrats en verre ou en céramique sont, en général, utilisés dans les MEMS nécessitant la microfabrication de surface comme les microéléments chauffants [31] et les capteurs de vitesse d'écoulement d'air [32] où le MEMS est formé de couches minces déposées sur ces substrats pour l'isoler thermiquement. Ils sont aussi utilisés en fabrication de volume où la gravure humide isotrope du verre est utilisée pour former le MEMS comme dans la fabrication des résonateurs fluidiques [14].

La fabrication des *Power-MEMS* tels que les microturbines nécessite une microfabrication de volume avec des gravures profondes pour former les structures à haut rapport de forme. La fabrication de microstructures en verre profond à l'aide de méthodes de gravure plasma à base de fluor a donné des résultats prometteurs, par exemple, des microstructures en verre borosilicaté d'une profondeur de 80 µm, d'une verticalité de paroi de 85 ° et de rapports de forme jusqu'à 40:1 ont été fabriquées par RIE (*reactive ion etching*) en utilisant un masque en nickel [33]. En utilisant la technique de gravure au plasma NLD (*magnetic neutral loop discharge*), des tranchées en quartz et en verre borosilicaté ont été gravées à une profondeur de 100 µm, avec des rapports de forme allant jusqu'à 8:1 [34]. La gravure au laser est une autre approche de gravure de verre. Cependant, elle permet de réaliser des structures simples telles que les trous. Jusqu'à date d'aujourd'hui, les techniques de gravure de verre nécessitent plus de développement pour obtenir les mêmes performances de la gravure DRIE du silicium. En utilisant les techniques citées ci-dessus, il serait, par exemple, très difficile de fabriquer de la tranchée du palier radial (*journal bearing*) de la microturbopompe, soit 300 µm de profondeur et 15 µm de largeur (rapport de forme de 20 :1).

2.4.2 L'isolation thermique localisée

Les membranes suspendues

La méthode d'isolation thermique la plus répandue dans le domaine des MEMS est l'utilisation des membranes suspendues. En général, le MEMS est fabriqué sur un substrat de silicium lequel est

gravé de la face arrière jusqu'à atteindre le MEMS pour le suspendre. Une autre façon est de fabriquer le MEMS sur une couche sacrificielle qui est gravée à la fin du procédé pour le relâcher. Cette technique d'isolation thermique est largement utilisée dans fabrication des micro débitmètres [25], des capteurs infrarouges [36] et des capteurs thermiques [37]. Cette technique offre une très grande résistance thermique due à la réduction de l'épaisseur de la membrane. Par contre, les membranes suspendues ont la particularité d'être mécaniquement fragiles.

Les couches d'oxyde de silicium

L'oxyde de silicium est un matériau très utilisé en microfabrication et dans les MEMS pour ses propriétés électriques et optiques. Il est aussi caractérisé par une faible conductivité thermique de l'ordre de 1.4 W/m/K. Ce qui fait de lui un excellent candidat pour l'isolation thermique localisée. Cependant, il est utilisé dans des applications où seulement une couche de 10 à 20 µm d'épaisseur est suffisante. L'épaisseur de l'oxyde de silicium est limitée par le temps de déposition (oxyde thermique) ou par les contraintes mécaniques résiduelles après le dépôt (oxyde PECVD, *plasma enhanced chemical vapor deposition*) [38].

De l'oxyde de silicium plus épais pourrait être obtenu en utilisant la technique de l'oxydation thermique d'un réseau de tranchées de Si formé par DRIE comme illustré à la figure 2-6 [39]. En utilisant cette technique, des épaisseurs allant jusqu'à 100 µm peuvent être atteintes. Les performances d'isolation thermique d'un microélément chauffant avec une différence de température de 190°C ont été démontrées en utilisant cette technique [39]. La non-planarité de la surface après l'oxydation thermique au niveau des tranchées et les contraintes mécaniques résiduelles représentent les inconvénients majeurs de cette technique.

Le silicium poreux

Le silicium poreux a une conductivité thermique encore plus faible que les oxydes et des couches plus épaisses peuvent être formées (plus de 100 µm). Il est utilisé, par exemple, comme isolant thermique dans les microdébitmètres thermiques [40]. L'inconvénient du Si poreux est sa faible tenue mécanique. De plus, il n'est pas compatible à plusieurs chimies utilisées en microfabrication, ce qui rend son intégration difficile. Sa faible résistance à la température (400°C) [41] limite son utilisation dans les *power-MEMS* qui fonctionnement à hautes températures.

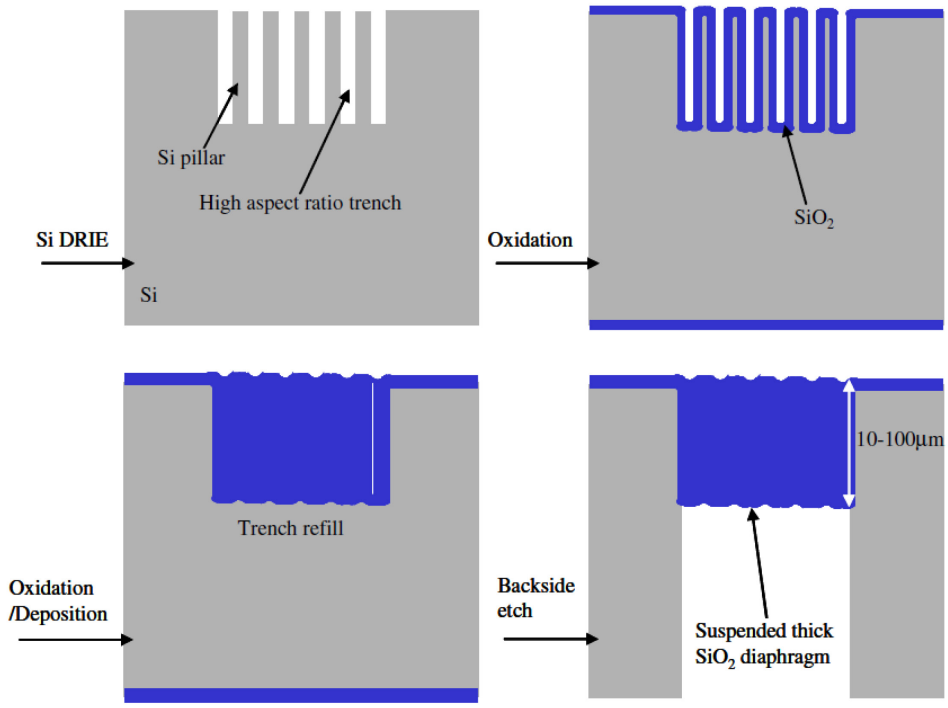

Figure 2-6 Isolation thermique par oxydation d'un réseau de tranchées de Silicium [39].

Le carbure de silicium poreux

Un carbure de silicium poreux plus robuste a également été proposé comme candidat à l'isolation dans le MEMS [41] en raison de sa bonne résistance chimique, de sa résistance mécanique et de sa stabilité à haute température (jusqu'à 1000°C), mais la gravure profonde du SiC reste un défi.

Le micromoulage de verre

La technique de micromoulage du verre est une approche alternative pour l'isolation thermique dans les MEMS et les *Power-MEMS* [42]. Cette technique est basée sur un traitement thermique du verre à haute température pour devenir un matériau viscoélastique ou liquide visqueux, lui permettant de couler sous son propre poids ou un gradient de pression. La figure 2-7a illustre les étapes de fabrication de la technique de micromoulage [50]. Les principales étapes consistent à : 1) photolithographie, 2) créer des cavités dans le silicium par DRIE, 3) collage anodique avec un verre borosilicaté (collage sous vide), 4) traitement thermique pour faire mouler le verre dans les cavités de silicium, 5) polissage du verre superflu et 6) amincissement et polissage du silicium. La Fig. 2-7b montre le résultat de la fabrication après l'étape 6 où des structures de verre (transparent) sont intégrées dans le silicium (gris). Cette méthode présente l'avantage d'être compatible avec les outils et équipements de salles blanches généralement utilisés en microfabrication.

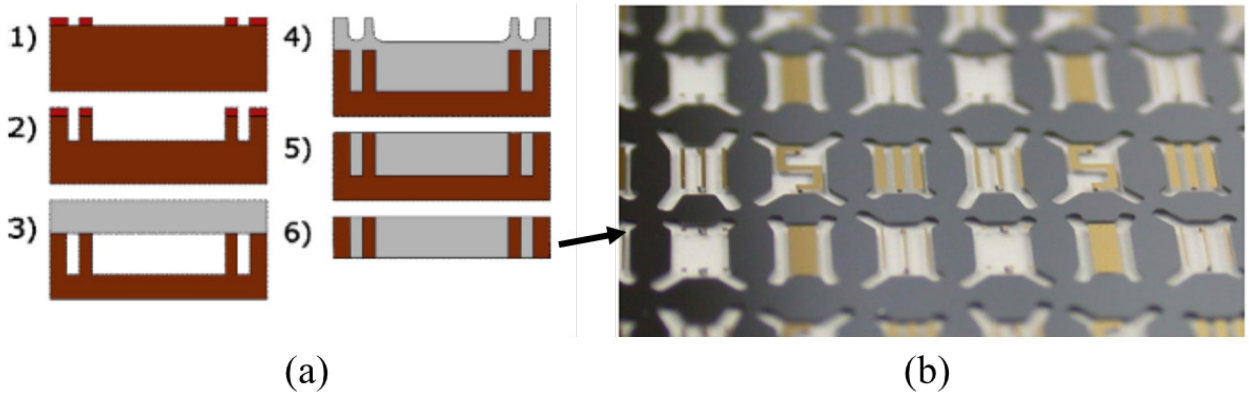

Figure 2-7 Micromoulage du verre borosilicaté dans les tranchées de Si gravées par DRIE : (a) processus de fabrication (Si : marron, verre : gris), (b) image montrant le verre intégré dans une tranche de silicium (verre : transparent, Si : gris, la couleur dorée est un métal déposé qui aura le rôle de masquage du silicium lors des étapes de gravure subséquentes) [50].

2.5 Approche proposée

Liamini [23], dans son concept, a proposé de fabriquer un rotor en quartz. Cependant, le rotor comprend des structures critiques notamment les pales de turbine (de l'ordre de 100 µm de hauteur). La réussite de la fabrication de celles-ci dépend directement de la qualité de gravure. Au regard des techniques de gravure des verres qui existent, il serait très complexe de fabriquer un rotor en verre. Une autre complexité dans la fabrication d'un rotor en verre est le relâchement du rotor et au même temps que la formation du palier radial. Pour le réaliser, on doit effectuer une gravure profonde de 300 µm avec une largeur de 15 µm et une verticalité souhaitée avoisinant les 90°. Jusqu'à présent, les techniques de gravure existantes ne permettent pas de réaliser cette gravure profonde dans le verre.

La couche D dans le concept de Liamini (voir Figure 2-5) est composée de structures en nid d'abeilles en verre. L'auteur l'a conçue ainsi pour assurer une isolation thermique entre le compartiment supérieur et le compartiment inférieur de la microturbopompe. L'objectif de l'auteur est de minimiser le transfert de chaleur entre ces deux compartiments. Une même problématique comme dans la fabrication du rotor se pose ici, qui est la difficulté de fabriquer de telles structures sur une tranche de verre. D'autant plus, les structures en nid-d'abeilles fragilisent la tenue mécanique de la microturbopompe. Surtout si on sait que la manipulation de cette dernière sera manuelle.

Le concept de la microturbopompe proposé par Liamini [23] a été modifié et optimisé dans cette

thèse dans l'objectif d'intégrer des stratégies d'isolation thermique localisée. La configuration proposée dans ce travail est représentée sur la figure 2-8. Cette configuration est conçue en gardant les mêmes objectifs en terme de performances mécaniques à atteindre telles que conçues par Liamini (vitesse de rotation, stabilité axial et radial, pompage de l'eau) mais aussi, conçue pour être réalisable en utilisant les méthodes de microfabrication en intégrant l'isolation thermique.

La zone de la pompe a été conçue pour être complètement isolée thermiquement pour empêcher l'ébullition indésirable de l'eau dans la pompe ou la condensation de la vapeur dans le palier axial inférieur ou la turbine pendant le fonctionnement à haute température. Comme illustré sur la figure 2-8, deux stratégies d'isolation thermique ont été développées pour ce travail afin d'isoler thermiquement la pompe : *i)* une épaisse couche de verre intégrée dans le rotor afin d'empêcher la conduction thermique de la turbine vers la pompe à travers le rotor créée par la technique de micromoulage, *ii)* un oxyde de silicium épais dans le plan pour l'isolation radiale afin d'empêcher la conduction thermique entre le palier axial inférieur et la pompe, créé par l'oxydation des tranchées de silicium comme expliqué à la section précédente.

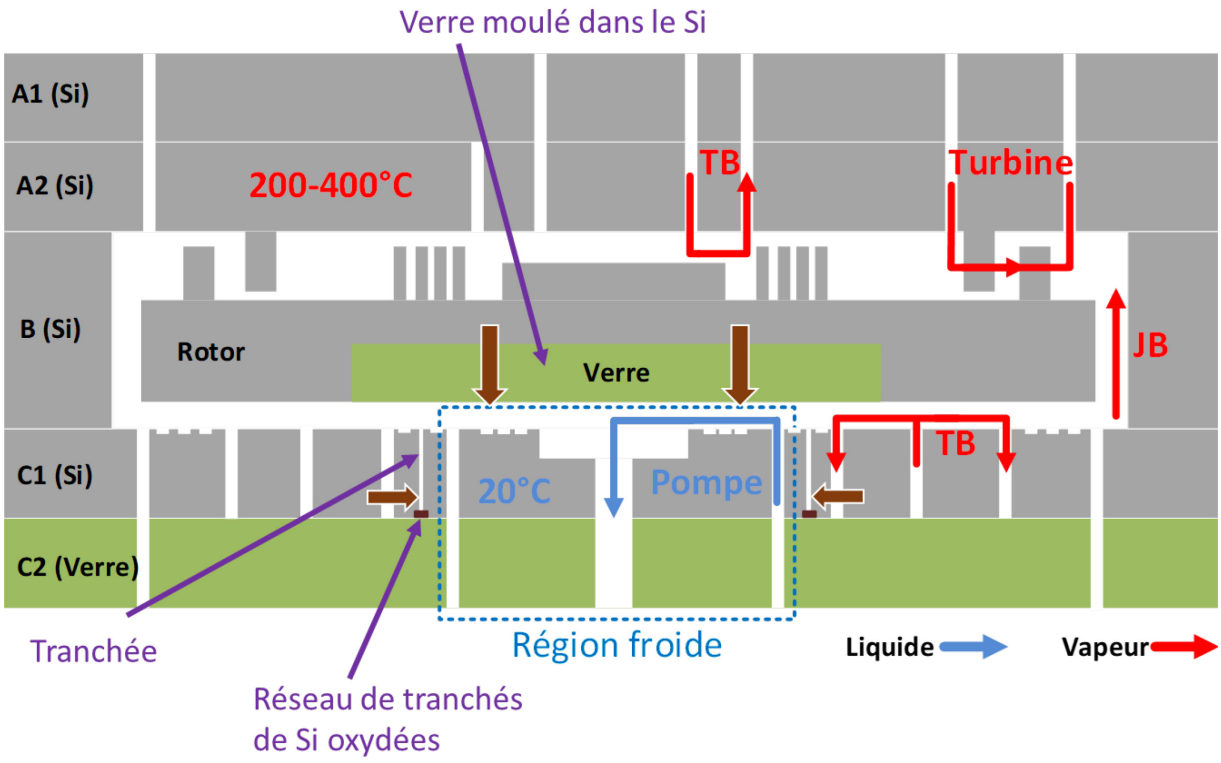

Figure 2-8 Schéma de la vue de coupe de la microturbopompe intégrant les stratégies d'isolation thermique. Les flèches de couleur marron montrent les chemins thermiques vers la région de la pompe.

L'intégration de la technique de micromoulage de verre dans le procédé de fabrication de la microturbopompe nous permet de fabriquer un rotor hybride silicium/verre. L'utilisation du silicium pour pouvoir fabriquer les structures complexes du rotor avec les méthodes de microfabrication tandis que le verre sert à l'isolation thermique.

2.6 Objectifs du projet de recherche

L'objectif principal du présent projet de recherche est de démontrer le fonctionnement d'une microturbopompe à haute température. Les objectifs spécifiques sont :

- Modifier et optimiser le design proposé par Liamini [23] en focalisant sur la microfabrication, c'est-à-dire, un design qui respecte les conditions de fonctionnement mais qui présente des méthodes de microfabrication plus simples et réalisables en intégrant l'isolation thermique.
- Développer la technique de micromoulage de verre pour pouvoir l'intégrer comme un matériau isolant thermiquement dans le rotor de la microturbopompe.
- Développer un procédé complet de microfabrication permettant la fabrication de la microturbopompe de deuxième génération qui intègre les stratégies d'isolation thermiques.
- Concevoir et mettre en place un banc d'essais spécifique pour la caractérisation de la microturbopompe à haute température.
- Démontrer le fonctionnement de la microturbopompe à haute température et évaluer les stratégies d'isolation thermique utilisées. Dans cette thèse, pour raison de complexité du banc d'essais, nous nous limitons à utiliser l'air chaud à la place de vapeur surchauffée.

3 CAPABILITIES AND LIMITS TO FORM HIGH ASPECT-RATIO MICROSTRUCTURES BY MOLDING BOROSILICATE GLASS

3.1 Avant-propos

Auteurs et affiliation :

A. Amnache : étudiant au doctorat, Université de Sherbrooke, Faculté de génie, Département de génie mécanique.
J. Neumann : PhD, SPTS Technologies Ltd, Allentown.
L. Fréchette : professeur, Université de Sherbrooke, Faculté de génie, Département de génie mécanique.

Date d'acception : 9 février 2019

État de l'acceptation : version finale publiée

Revue : IEEE *Journal of MicroElectroMechanical Systems* (JMEMS)

Référence : [Amnache, A. Neumann, J. and Fréchette, L.G. (2019). Capabilities and limits to form high aspect-ratio microstructures by molding of borosilicate glass. Journal of Micromechanical Systems, vol. 28, no. 3, p. 432–440.]

Titre français : Les capacités et les limites pour la fabrication de microstructures en verre borosilicaté en utilisant une technique de micro-moulage

Contribution de l'auteur :

La contribution scientifique et technique de l'auteur dans cet article, en excluant l'encadrement du directeur de recherche, est estimée à 95%.

Tout le travail dans cet article est effectué par l'auteur sauf le développement de la gravure du silicium au XeF_2 qui a été faite au SPTS Technologies Ltd (USA) par John Neumann.

L'auteur a rédigé 100% du contenu de l'article.

Contribution au document :

Dans cette article, nous avons étudié et développé une approche de micro-moulage pour intégrer du verre dans des microcavités de silicium gravées par DRIE. C'est en utilisant cette technique que le verre est intégré dans le rotor de la microturbopompe pour l'isolation thermique entre la turbine (chaud) et la pompe (froid). C'est une contribution très originale qui permet à la microturbopompe de fonctionner à haute température. Sans cette contribution, il aurait été très difficile de développer

des techniques de gravure de matériaux isolants thermiquement pour fabriquer le rotor de la microturbopompe.

Pour la communauté scientifique, cet article défini un procédé de micro-moulage permettent la fabrication de microstructures à haut rapport de forme en verre borosilicaté avec un meilleur contrôle et une meilleure précision que précédemment. L'article définit notamment les conditions optimales de conception pour éviter les défauts dans le verre après le micro-moulage. Ces avancées dans le procédé de micro-moulage du verre permettent son utilisation dans le domaine des MEMS, l'encapsulation et la microfluidique où les propriétés du verre sont recherchées à savoir la transparence optique, la stabilité chimique, et l'isolation thermique et électrique.

Résumé français :

Cet article présente une étude expérimentale des capacités de fabrication de microstructures à rapport de forme élevé en verre. La fabrication a été réalisée en moulant du verre borosilicaté dans des tranchées profondes en silicium créées par gravure ionique réactive profonde (DRIE) dans le silicium, et en libérant les structures par gravure à l'hydroxyde de potassium (KOH) et au difluorure de xénon (XeF_2) du moule de silicium. Une sur-gravure du verre peut également être utilisée pour augmenter le rapport de forme des structures en verre. En utilisant cette méthode de moulage, les structures en verre ont été fabriquées avec succès en atteignant un rapport de forme de 42:1, une hauteur de 212 µm et un angle de paroi latérale verticale de 89,7°. Nous avons également étudié l'effet des paramètres de moulage (temps de traitement thermique, température et pression) sur les capacités et les limites du procédé pour fabriquer des structures sans défaut. Ce travail démontre les capacités de fabrication de structures de verre à rapport de forme élevé qui ne peuvent pas être atteintes à ce jour par les techniques de gravure conventionnelles, ouvrant de nouvelles perspectives pour l'utilisation du verre dans les MEMS et la microfluidique.

3.2 Abstract

This paper presents an experimental study of capabilities to fabricate high aspect-ratio microstructures in glass. The fabrication was done by molding borosilicate glass in deep silicon trenches created by deep reactive ion etching (DRIE) in silicon, and releasing the structures by Potassium hydroxide (KOH) and Xenon difluoride (XeF_2) etching of the Si mold. Subsequent over-etching of the glass can also be used to increase the aspect ratio of the glass structures. By using this molding method, glass structures have been successfully fabricated achieving an aspect-ratio of 42:1, a height of 212 µm and vertical sidewall angle up to 89.7°. We also investigated the effect of molding parameters (heat treatment time, temperature and pressure) on the process capabilities and limitations for defect free structures. This work demonstrates the capabilities to fabricate high aspect-ratio glass structures that cannot be achieved by conventional etching techniques to date, opening new perspectives for the use of glass in MEMS and microfluidics.

Index Terms— Aspect-ratio, Borosilicate glass, DRIE, Etching, Glass flow.

3.3 Introduction

Glass is an interesting complement to silicon as a material for MEMS, microfluidics and packaging due to its useful properties, such as optical transparency, chemical stability, thermal insulation and electrical isolation. An additional property of borosilicate glass is its thermal expansion coefficient similar to silicon, offering the possibility of bonding glass and silicon wafers. Wet etching of borosilicate glass using hydrofluoric acid solution (HF) is a cost-effective process and provides a high etch rate and smooth surfaces [44], but the isotropic etch profile prevents the use of this technique to create vertical and high aspect ratio structures commonly done in silicon. Fabrication of deep glass microstructures using fluorine based plasma etching methods has shown promising results, by using inductively coupled plasma reactive ion etching (ICP-RIE) [45,33,46,47] or magnetic neutral loop discharge (NLD) [34]. For example, microstructures of borosilicate glass with 80 µm depth, wall verticality of 85° and aspect-ratios up to 40:1 were fabricated by ICP-RIE using a hard mask of Nickel [33]. Through-fused silica glass vias of 50 µm depth, an aspect-ratio of 2:1 and a wall profile angle of nearly 90° were obtained by ICP etching using aluminum as a hard mask [47]. Using NLD plasma etching technique, trenches in fused and borosilicate glass were etched to a depth of 100 µm, with aspect-ratios of up to 8:1 [34]. However, combining vertical sidewall profiles, high aspect-ratios and smooth surfaces remains a challenge and will require more

development to achieve similar etching performances achieved in silicon by using plasma etching techniques, such as deep reactive ion etching (DRIE) based on the Bosch process [48]. Furthermore, relatively thick metal masks are typically required for deep glass plasma etching. Glass molding is an alternative approach to form glass microstructures. This method has enabled the fabrication of several devices including glass micro lenses [49], capacitive pressure sensors [50] and glass resonators [51]. This technique is based on a heat treatment of glass at high temperature to become a viscoelastic material or viscous liquid, allowing it to flow under its own weight or a pressure gradient. Using a mold, we can create different geometries such as trenches, walls or membranes. Compared to molten glass printing for example [52], this method has an advantage to be compatible with cleanroom tools and equipment typically used in microfabrication. In addition, anodic bonding used in this technique has a benefit to create vacuum inside the narrow silicon cavities in order to improve the flow into them. To use the molten glass, it would be necessary to make a mold in a vacuum chamber to prevent gas taken in the trenches to prevent their filling. Glass features of 50 µm width and aspect-ratios of 8:1 have been fabricated by molding borosilicate (Pyrex®7740) glass into a silicon mold, containing cavities formed by DRIE [53]. The microstructures have been released by etching the silicon with KOH or ICP-RIE. This study pushes this approach further by exploring its potential to fabricate deep vertical structures. The effect of heating time and temperature on the molding of borosilicate glass was characterized previously [49,54,55], but the aspect-ratios were lower than 1. Hence, the glass bends rather than flows into cavities. Therefore, in order to precisely control the glass molding and to achieve high aspect-ratios, it is essential to characterize the flow behavior into such cavities. Although challenges to ensure the full filling of the cavities have been reported, namely for small patterns [50,56], there is a lack of understanding of the glass flow into narrow trenches. Indeed, the impact of process conditions on the molding capabilities and the limits of the process for high aspect-ratios are not well understood. In addition, there is no quantitative study of the aspect-ratio dependent molding (ARDM), defined here as the non-uniform velocity of the glass as it flows down trenches of different widths to fill them. So, what are the capabilities and limits to create high aspect-ratio microstructures in borosilicate glass, and what controls them?

In this work, we aimed to conduct glass molding into Si DRIE high aspect-ratio trenches. We report here a development of the glass molding and releasing processes which enable the fabrication of high aspect-ratio microstructures in borosilicate glass. We aimed to quantitatively characterize the

glass flow behavior as a function of the trench width, and the heating treatment temperature, pressure and time. We then defined the capabilities and limits of this technique. Initial results of this work were presented at the 16th Hilton Head Workshop [57].

3.4 Experimental

3.4.1 Microfabrication Method

The fabrication of borosilicate glass microstructures was performed using a 100 mm diameter, p type, <100> orientation, 1-10 Ω-cm resistivity, 500 µm thick silicon wafer (mold) and a Borofloat®33 glass wafer of 500 µm thick from Schott. The microfabrication process flow is schematically illustrated in Fig. 3-1. Deep trenches with different widths (12, 23, 54, 104, 254, 506, 760 and 1020 µm) were fabricated by photolithography and DRIE in the silicon wafer (Fig. 3-1b). The DRIE was done using a photoresist mask (AZ®9245 from MicroChemicals GmbH). The trenches were etched to a depth up to 230 µm for wide trenches using Advanced Silicon Etch STS ICP. The etching conditions were: 130 sccm of SF_6 and 13 sccm of O_2, 600 W RF coil power, 18 W RF platen power for a 13 sec etching cycle and 85 sccm of C_4F_8, 600 W RF coil power and 0 W RF platen power for 7 sec passivation cycle (0 s overlap with etching cycle). The automatic pressure control valve (APC) was fixed at 82 % leading to a pressure of 30 mTorr and 16 mTorr for etching and passivation cycle, respectively. It was possible to achieve an etch rate of up to 4.3 µm/min for large trenches. Due to the aspect-ratio dependent etching effect (ARDE), the etch depth is smaller for narrow trenches compared to wider ones. The DRIE gave reentrant walls with profile angle, α, about 88° for large trenches. The profile angle tends to 90° for the narrow ones.

Before bonding, the etched Si wafer and the glass wafer were cleaned in a Piranha solution (1:2 mixture of H_2O_2:H_2SO_4) for 15 min, followed by SC1 solution (1:1:5 mixture of NH_4OH:H_2O_2:H_2O) at 75°C for 15 min. The etched Si wafer was also immersed in a hydrofluoric acid solution (1:50 mixture of HF:H_2O) for 30 s to remove the native oxide. Both wafers were rinsed with deionized water and dried by nitrogen gaz. The two wafers were then anodically bonded in a wafer bonder (AML) to create low-pressure hermitic micro-cavities (Fig. 3-1c). The bonding is carried out under vacuum (150 µTorr, air). The wafers were heated simultaneously to 370°C to increase the mobility of positive ions in the glass wafer before bringing them in contact. Once the temperature is reached and the pressure is stabilized, the wafers were put in contact and a mechanical force of 200 N was applied uniformly over the surface of 100 mm diameter wafers. A

voltage of 500 V was then applied with a current limit fixed to 4 mA. The bond is completed when the current decays to a residual value of 0.1 mA. The elapsed time was 20 min. Subsequent cooling was done with a rate of 3°C/min, down to room temperature. The bonding strength was examined by the crack-opening characterization method [58]. When a wedge of a thickness of 0.3 mm was inserted into the bond interface, the silicon side cracked. This suggests that the bonding energy is greater than the fracture surface energy of the silicon [59].

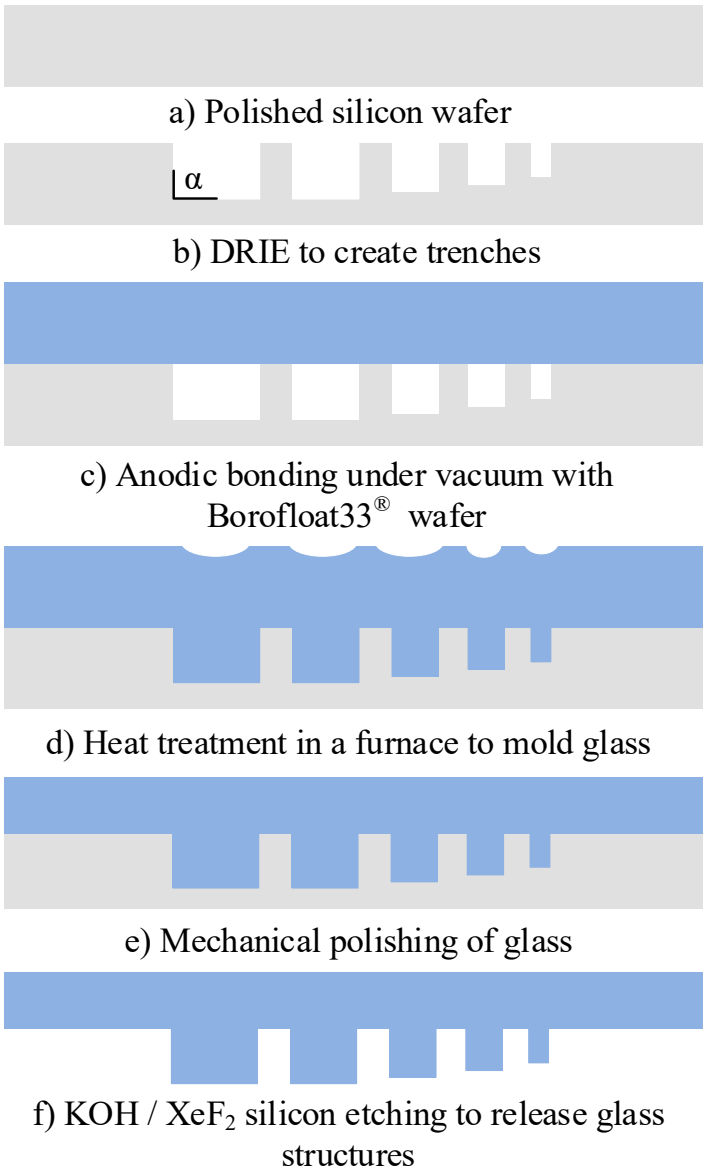

Figure 3-1 Microfabrication process flow to create vertical structures in borosilicate glass by molding into silicon trenches and releasing.

Afterwards, the bonded wafers were diced into square pieces of 15 mm per side. Each piece contains a series of micro-cavities with different widths. In order to reflow the glass and fill the

micro-cavities, the sample is heated in a furnace lowering the glass viscosity. Therefore, the softened glass flows into the micro-cavities (Fig. 3-1d) due to the pressure difference between the vacuum micro-cavities and furnace ambient. Nitrogen or argon gases were used as an environment gas. Since the top glass surface will deform, lapping and polishing of the surface is done to planarize and smooth the glass surface (Fig. 3-1e). To create glass structures, the silicon mold is removed by two different etching methods: by KOH and XeF_2 (Fig. 3-1f), as will be discussed later.

3.4.2 Heating Treatment Procedure

The range of interest for the heat treatment steps and the process conditions were defined based on the temperature dependence of viscosity, $\lg \eta = f(T)$. Fig. 3-2 shows the viscosity variation with temperature of the Borofloat®33 glass. The curve was obtained by using data from Schott [60]. As shown, the viscosity decreases exponentially with temperature in the range 518-1270°C. The strain point where the internal stresses are released in a matter of hours is 518°C corresponding to a viscosity of 1014.5 dPa.s. The annealing point, where the internal stresses are released in a matter of minutes but the glass holds, its shape is 560°C corresponding to a viscosity of 1013 dPa.s. To ensure the dissipation of internal stresses, it is important to cool down the Borofloat®33 glass at a small rate at the temperature comprises between 518°C and 560°C.

In this experiment, the studied range of temperature is chosen in relation of the softening point of the Borofloat®33 glass i.e. 820°C corresponding to a viscosity of 107.6 dPa.s. The American Society for Testing and Material (ASTM) defines it as the temperature at which a thin fiber of the glass (0.65 mm in diameter and 235 mm long) elongates under its own weight at a rate of 1 mm/min [61].

To characterize the glass molding into deep trenches, a matrix of experiments was conducted. Different heating treatment experiments have been carried out by varying temperature in the range of 750-950°C, furnace pressure in the range of 1-20 bars and heating time from 10 min to 32 hours. The heating treatment was conducted in an atmospheric quartz tube furnace. In the first step, the bonded sample is heated rapidly from ambient temperature to 400 °C by an uniform heating rate of 12.6 °C/min. Afterwards, the heating is continued to up the desired treatment temperature at a rate of 3°C/min. After the isothermal heat treatment, the sample is cooled to a temperature of 400 °C (below the strain point of Borofloat®33 glass) with a very small cooling rate of 0.7 °C/min.

Finally, the cooling is continued without controlling the rate by free convection inside the oven down to room temperature.

Given that the furnace pressure is the driving force to flow the glass, a specific set-up was used for pressurized molding. It comprises of a stainless steel tube within which the sample was placed. The tube is blocked at one end while the other is connected to a high pressure argon gas bottle. The closed tube end enclosing the sample is introduced inside the furnace chamber for the heat treatment described above.

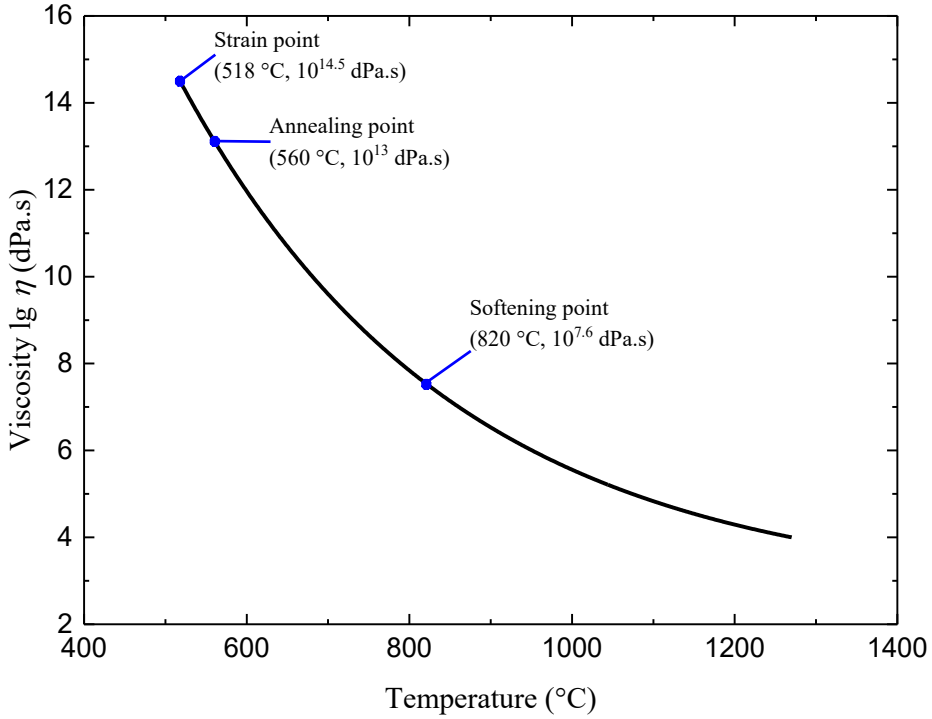

Figure 3-2 Viscosity variation with temperature of the Borofloat®33 glass. Data from Schott [60].

3.5 Results and Dicussion

3.5.1 Atmospheric molding

The scanning electron microscope (SEM) images in Fig. 3-3 illustrate an example of atmospheric (pressure difference = 100.9 kPa) glass flow evolution in the trenches at 800°C with different heat treatment times (1, 2, 4 and 6h) and various trench widths (12, 23, 54 and104 µm). It is clear from the images that molding glass in trenches presents an ARDM. In fact, the glass flows faster in the wide trenches than in the narrower ones. This flow behavior is due to the strong viscous forces at smaller dimensions. Note that there is no ARDM observed for trenches of 254, 506, 760 and 1020

µm since the width is greater than the depth of the trenches. Indeed, the trenches were completely filled in 4 h at 750°C, less than 1 h at 800°C and 850°C, and less than 10 min at 900°C and 950°C.

The effect of the heating time on the flow length is presented in Fig. 3-4 for different heating temperatures (750, 800, 850, 900 and 950°C) and trench widths (12, 23, 54 and 104 µm). The flow length was measured on the cross section by SEM after dicing the molded sample. The uncertainty of the measurements is estimated by measuring the flow length variation between different trenches having same widths and at the same heat treatment conditions. It can be seen that for fixed trench width and temperature, the flow length increases with a linear relationship with the heating time. This means that the flow velocity of glass is a constant quantity at given temperature and trench width.

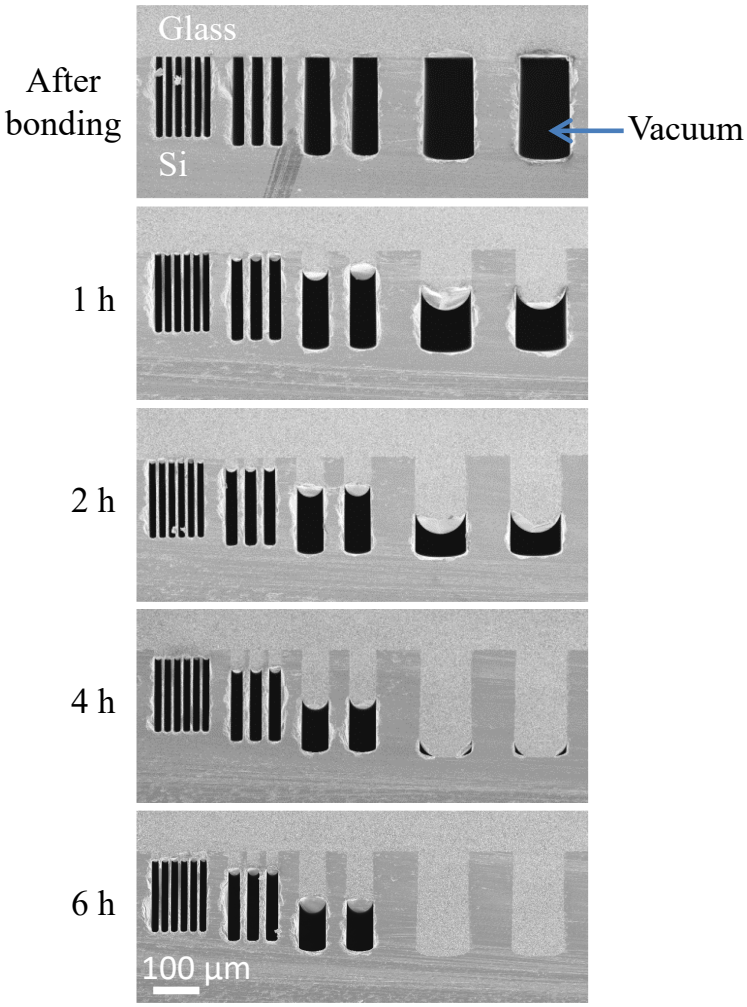

Figure 3-3 SEM images showing the effect of heating time (1, 2, 4 and 6h) on the glass flow length through silicon trenches for a molding temperature of 800°C and atmospheric pressure. Trenches width from left to right: 12, 23, 54 and 104 µm.

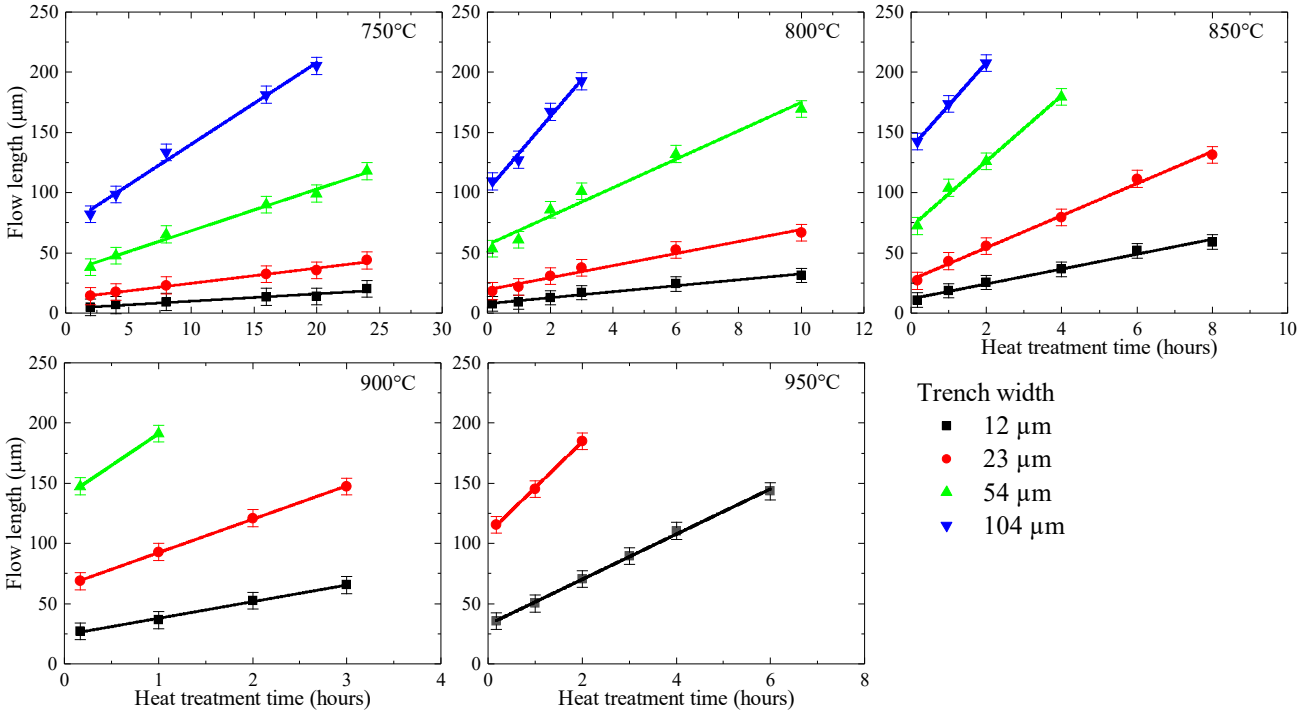

Figure 3-4 Measured glass flow length as a function of heating time, temperature and width. The glass molding was performed at atmospheric pressure. Lines are linear fit.

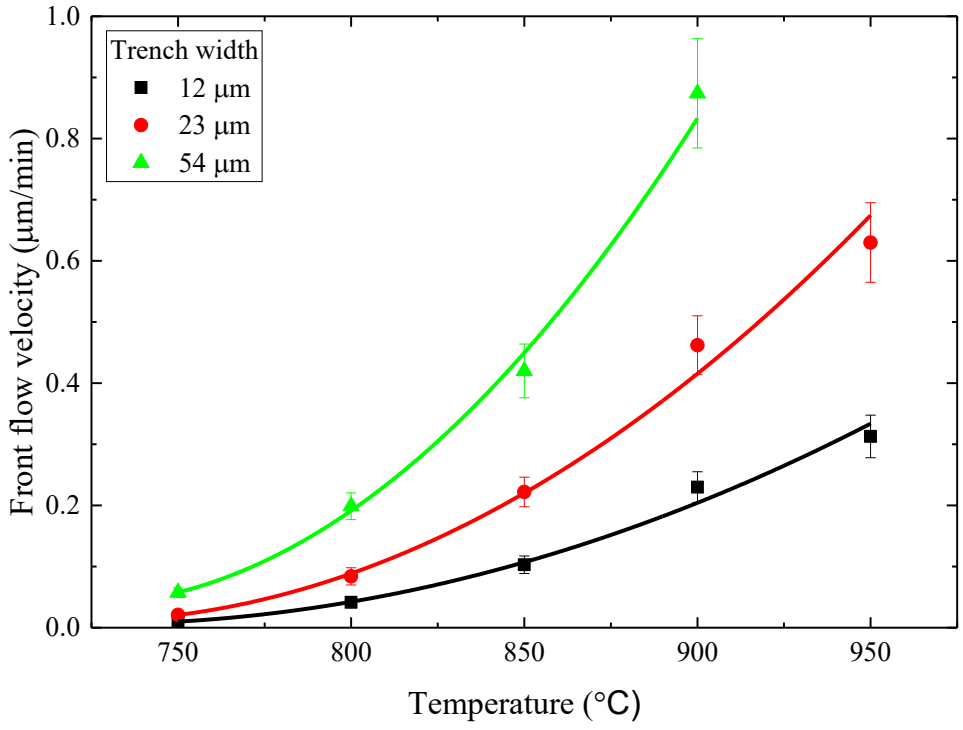

Figure 3-5 Extracted front flow velocity plotted against molding temperature and trench width for atmospheric molding. The velocity is calculated by linear fitting the data in Fig. 3-4. Lines are parabola curve fitting.

In addition, increasing temperature results in a significant increase of the flow length due to the decreasing glass viscosity. The slope of the fitted lines provides an estimate for the flow velocity. On the other hand, assuming a linear trend, the intercept of the linear fit represents the total flow during the periods of heating and cooling.

Figure 3-5 shows the extracted flow velocity from data of Fig. 3-4 as a function of heating temperature and the varied trench widths, 12, 23 and 54 µm. It can be observed that, with increasing heating temperature, the flow velocity increases following a nonlinear relationship due to the decreasing glass viscosity. Due to the viscous forces, at a fixed heating temperature, the velocity is favored by a higher trench width.

3.5.2 Pressurized molding

To achieve greater aspect-ratios as molded, AR_m, the same heat treatment method was done by increasing the environment pressure in the furnace. The AR_m is defined as the ratio of glass flow length and the width of trenches. It should be mentioned that, in this article, the AR_m is different from the aspect-ratio of released structures AR since isotropic etching will be shown to increase the AR. Figure 3-6 shows an example of glass flow evolution in the trenches at 800°C and for different pressures (0.1, 0.3, 1, 1.5 and 2 MPa). The heating treatment time is fixed to 2 hours. It is apparent that the glass flows faster in the trenches when forced with higher pressure. For a heating time of two hours, the required pressure for the glass front to reach the bottom of the trenches of 104 µm and 254 µm deep is ≤ 0.3 MPa and ≤ 2 MPa respectively, for trenches of 23 µm width. However, the trenches of 12 µm width still require higher pressure. The effect of the applied pressure and heating time on the flow length at a heating temperature of 800°C for two hours and for two different trench widths (12 and 23 µm) is shown in Fig. 3-7. Since the glass rapidly fills the trenches at high pressure, it was impossible to measure the flow length for trench widths greater than 23 µm. For a fixed trench width and heating time, a larger gradient pressure between the cavities and furnace results in increased flow length. In other words, it takes shorter time for the glass to move a given length as the pressure increases. We observed that the flow length increases following a linear relationship with the heating time, for pressures of 0.1 MPa (as detailed in the atmospheric molding section) and 0.3 MPa. However, for pressures ≥ 1 MPa the results show a non-linear behavior with high velocity at low heating time and then a slower velocity at high heating time. We noticed that the non-linear behavior becomes significant when the flow length is

equal to 5 times the trench width, suggesting a hydrodynamic behavior or shear-sensitive viscosity.

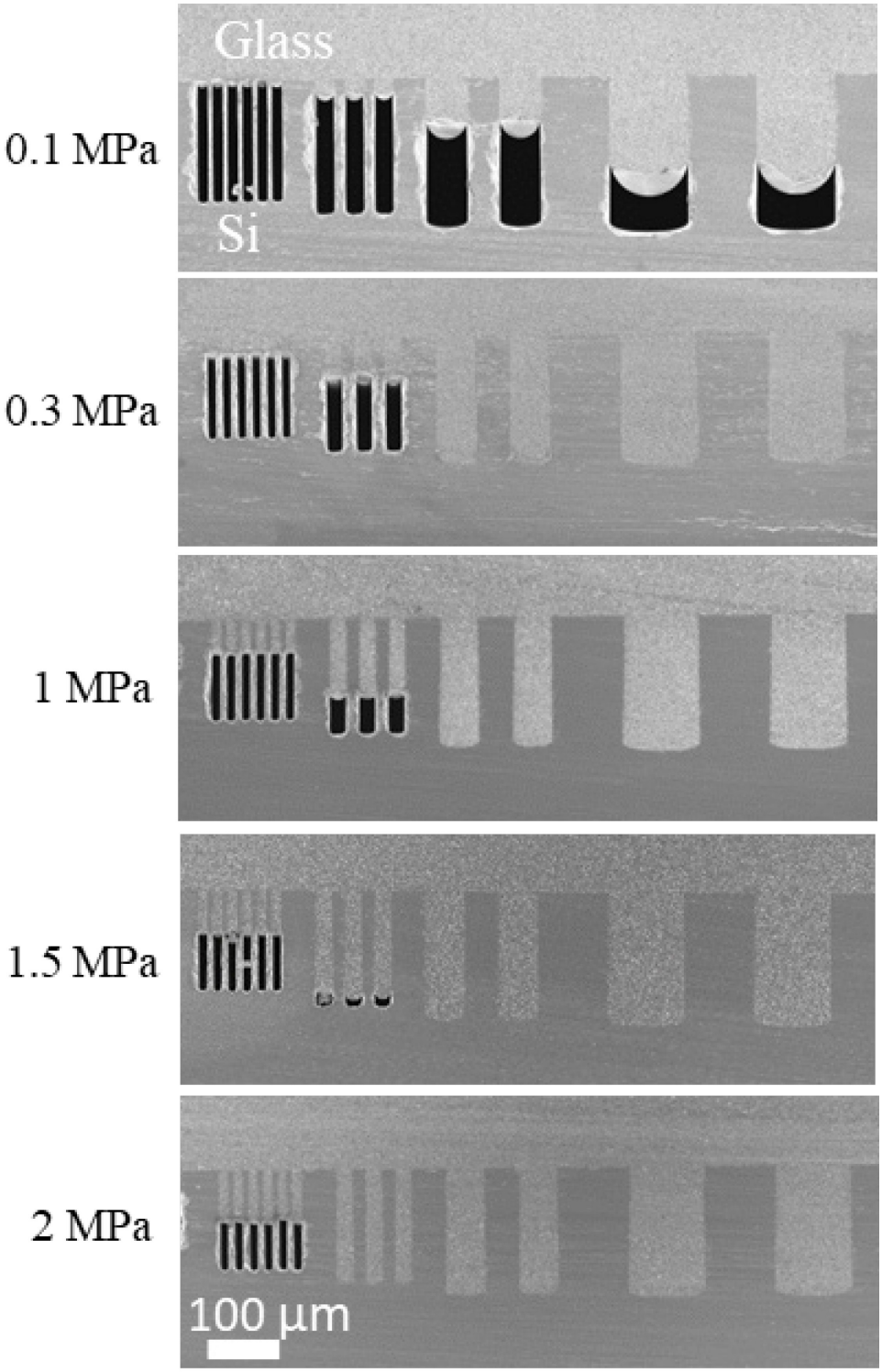

Figure 3-6 SEM images showing the pressure effect on the molding glass length through silicon trenches for a molding temperature of 800°C and heat treatment time of 2 hours. Trenches width from left to right: 12, 23, 54 and 104 µm

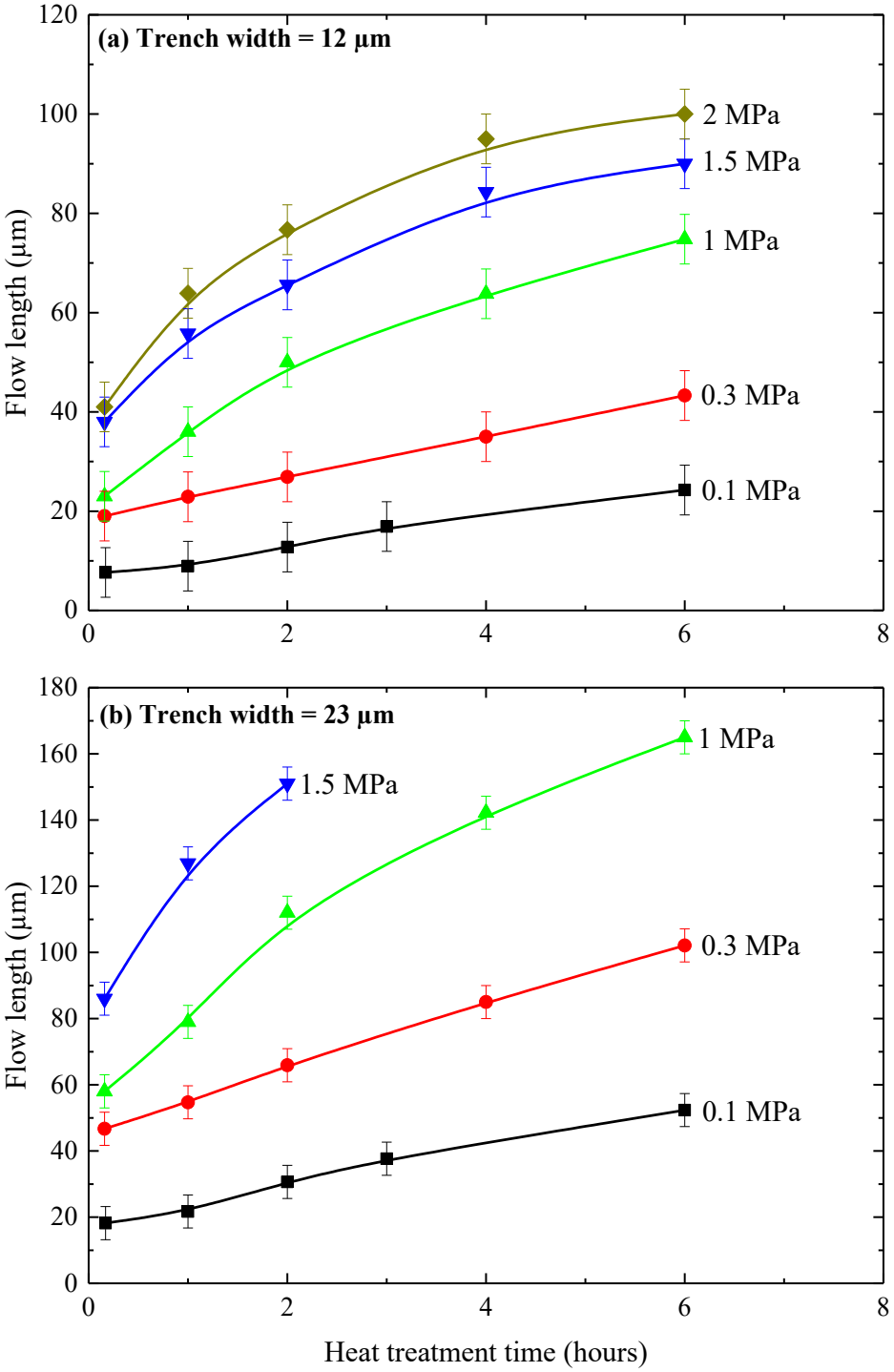

Figure 3-7 Measured glass flow length as a function of heat treatment time and pressure for trench width: (a) 12 µm and (b) 23 µm. The glass molding was performed at 800 °C.

3.6 Defects and impact on molding limits

Defects on the surface of glass and at the Si/glass interface were observed for extended heat treatments. The conditions of heating time and temperature when the defects were observed are

mapped in Fig. 3-8. Three molding zones were identified. In the first zone, the molding shows no defect and results in high quality filling as shown in Fig. 3-8a. Molding performed in the second zone results in the appearance of defects on the surface of the glass, as shown in Fig. 3-8b. The defects become deeper when the heating time is increased. However, these defects in the glass can be removed by a simple mechanical polishing. As the heating temperature was increased, the width of zones 1 and 2 was observed to get narrower. Finally, defects on the surface and voids at the Si/glass interface were observed on the molded glass when the heating conditions are within the third zone, as shown in Fig. 3-8c-d. At a given temperature, the number of voids increased with longer heating time. Diffusion of chemical elements contained in glass and the Teflon like coating on the etched mold after the DRIE may play a role in the defects after a long heat treatment. Because of these limitations, the heat treatment time should be limited in order to avoid defects. Therefore, the aspect-ratio as molded AR_m presents a maximum.

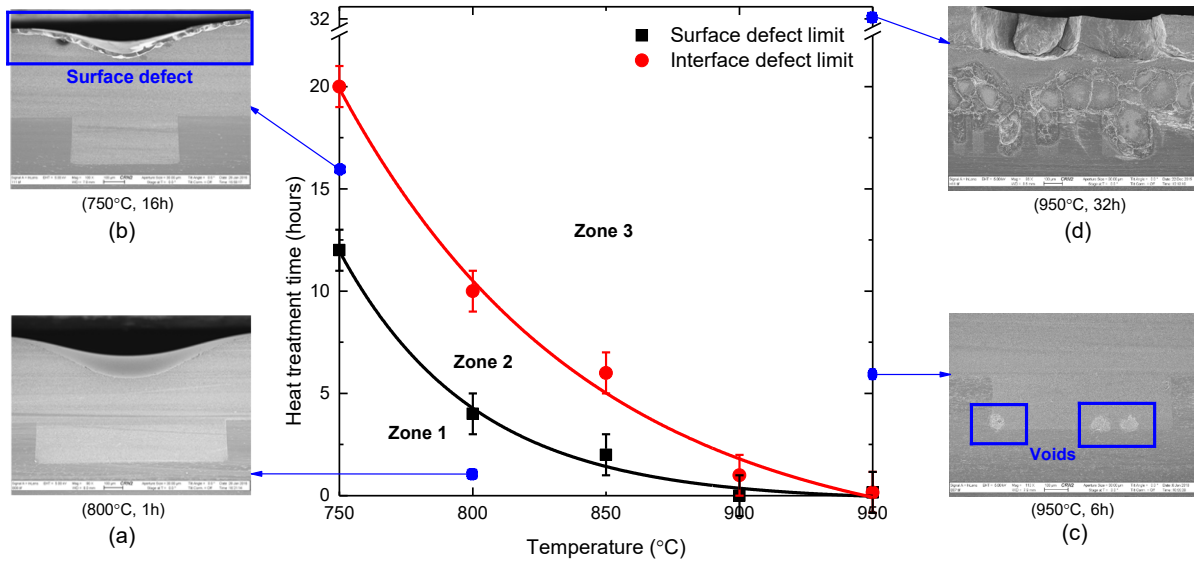

Figure 3-8 Atmospheric molding of borosilicate glass chart showing the heating time limits plotted against temperature. Zone 1: high quality molding. Zone 2: defects occur on the glass surface. Zone 3: void formation on the Si/glass interface and defects on the surface. Zone 3: void formation on the Si/glass interface and defects on the surface of glass.

The maximum achievable aspect-ratio as molded $AR_{m,max}$ by molding borosilicate glass at atmospheric pressure have been calculated by combining of the results concerning the flow velocity (Fig. 3-5) and the temperature and heating time limits (Fig. 3-8). These results of the maximum $AR_{m,max}$ versus heating temperature for two limits (i.e. surface and interface defect limits) are plotted in Fig. 3-9. The plots indicate that the choice of heating temperature influences the

achievable $AR_{m,max}$. When increasing the heating temperature, the $AR_{m,max}$ increases to a temperature of 850°C, but above, the $AR_{m,max}$ decreases. From the plots, the optimal heating temperatures for maximum $AR_{m,max}$ is located in the range of 800 to 900°C.

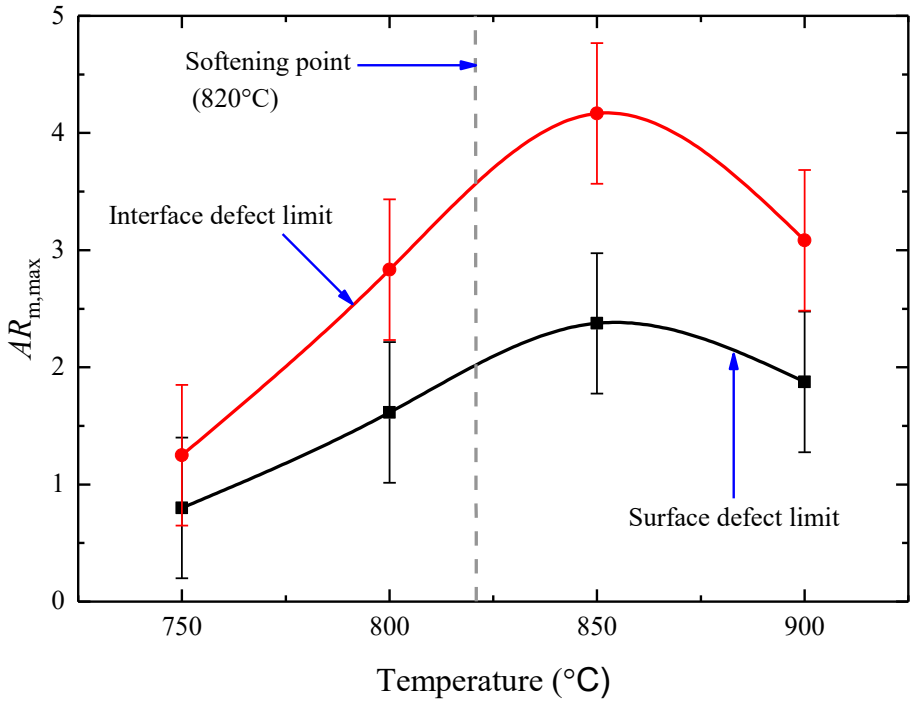

Figure 3-9 Maximum achievable aspect-ratio by molding borosilicate glass into silicon trenches at atmospheric pressure.

3.7 Fabrication of high aspect-ratio structures

3.7.1 Lapping and polishing

Lapping and polishing were performed on the molded sample (square piece of 1.5 cm) to planarize and smooth the deformed top surface of glass after molding and before releasing the structures. We used a traditional mechanical polishing machine with manual drip slurry. The lapping process was carried out using a cast iron plate, a silicon carbide (SiC) abrasive of 16 µm particle sizes, a wheel speed of 50 rpm and a load of 1 kg. By using a micrometer gauge tool, the removal rate was measured to 20.8 µm/min on the deformed surface. When the glass surface was flat, the removal rate diminished to 16.4 µm/min. This is due to the force being redistributed over the entire area once the surface is flat. The polishing step was done using aluminum oxide (Al_2O_3) slurry of 0.3 µm particle sizes, a nylon polishing plate, a wheel speed of 50 rpm and a load of 1 kg. The polishing rate was estimated to 0.23 µm/min. Fig. 3-10a and Fig. 3-10b show SEM images of a molded glass

sample before and after planarization, respectively. Lapping was done for 20 min removing 360 µm of glass followed by polishing step for 30 µm of glass followed by polishing step for 30 min removing 6.9 µm of glass. A mechanical profile measurement showed roughness of 165 nm rms after lapping while the rms value of 22 nm measured on the glass surface after polishing. To reach better rms values, the polishing still requires development and optimization. If needed, the extra glass can be completely removed until the level of silicon as shown in Fig. 3-10c. In this case, lapping was continued for 8 min leaving a layer of glass of almost 9 µm thick. The remaining glass was removed by polishing process for 38 min. It is important to stop the lapping process before arriving at the Si surface to avoid significant dishing of the glass.

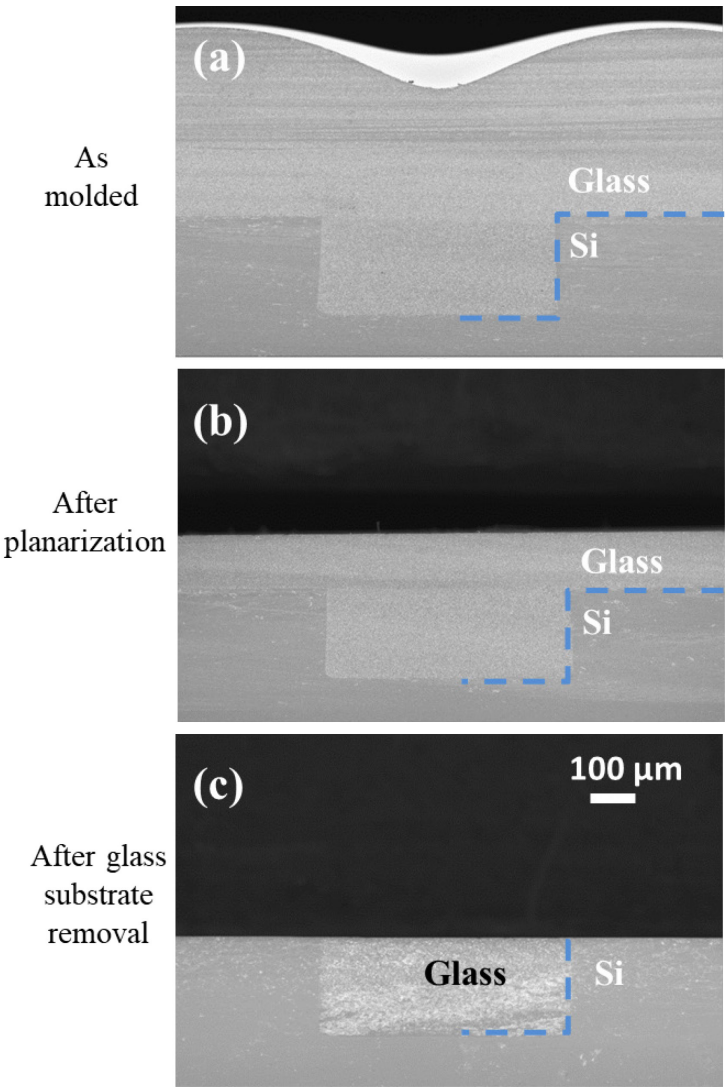

Figure 3-10 SEM cross-sectional views showing the stages of polishing process performed on the molded glass surface. (a) After molding. (b) After planarization. (c) After glass substrate removal.

Figure 3-11 shows the surface of the sample where the extra glass is completely removed following the lapping and polishing processes. This shows that, except the edge of the sample, the polished surface is free from mechanical damage. The mean variation between the level of Si and glass was measured to 200 nm. There are still some small pits observed on the surface. Further polishing optimization is required if higher surface quality is needed.

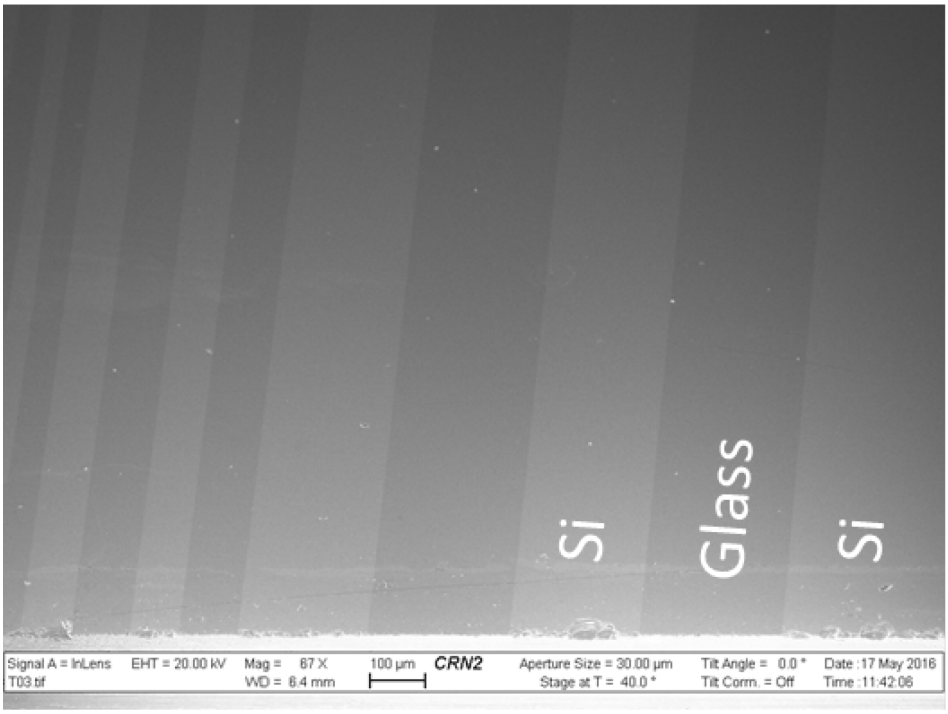

Figure 3-11 SEM image showing the TOP surface of a molded sample following lapping and polishing. The extra glass is completely removed, showing the glass (dark) and silicon (light) zones on the wafer surface.

3.7.2 Release using KOH etch

The first method to release the glass microstructures from the silicon mold is by KOH wet etching. The molded samples were etched in a KOH solution (45% by weight) heated at a temperature of 95 ±5°C. The etch rate of the silicon and the molded glass under these etching conditions was 2 µm/min and 50 nm/min respectively, for a selectivity of 40:1. SEM was used to measure the etch depth, and by varying the etching time, the etch rate was calculated for both silicon and glass.

Glass structures with high verticality were fabricated as shown in Fig. 3-12a. Initially, glass was molded in 104 µm width trenches for 3 hours at atmospheric pressure and temperature of 850°C to completely fill the trenches of 220 µm depth. The required KOH etching time to release the structures was 250 min. Aspect-ratio of 3:1, depth of 212 µm and trench angle θ=89.7° were

achieved. It is interesting to note that the depth of the glass structures has slightly decreased. That is because the glass was etched from the top of structures during the silicon etch. Similarly, the

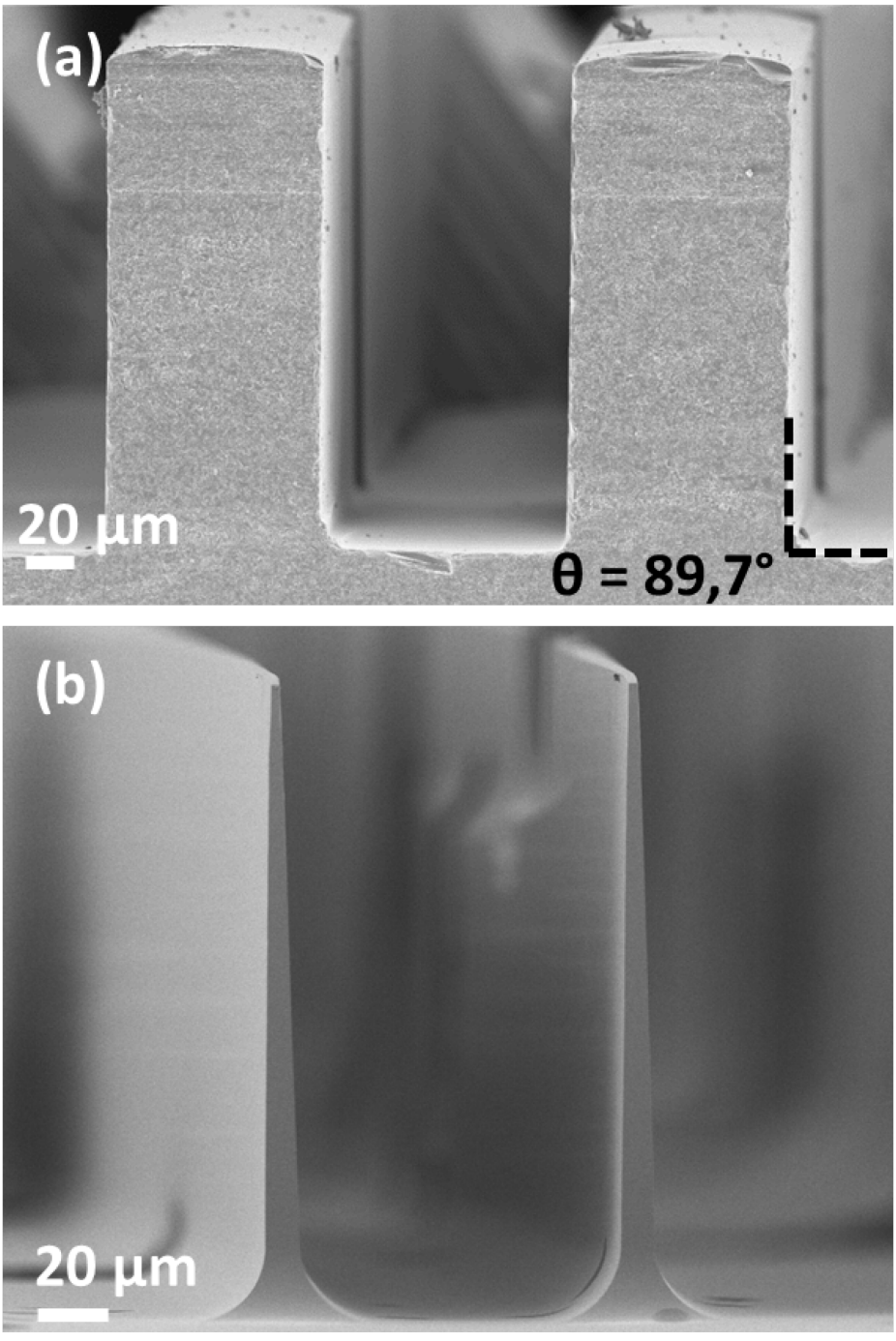

Figure 3-12 SEM of borosilicate glass structures fabricated by molding glass into silicon deep trenches at atmospheric pressure after silicon has been removed by KOH etching. (a) Molding for 330 min at 850°C and atmospheric pressure, $AR \approx 3{:}1$, height = 212 µm, wall angle = 89.7°. (b) Molding for 3 hours at 850°C and atmospheric pressure, AR ≈ 42:1, height = 207 µm, wall angle = 88.6° (KOH over-etching for 400 min).

sidewalls also get etched during the release process. Since the top of the structures are exposed to the etchant for a longer period than the bottom, the sidewall angle α given by DRIE was affected. The final sidewall angle θ of glass microstructures can be estimated as:

$$\theta(°) = 90° + \tan^{-1}\left(\frac{1}{S} - \frac{1}{\tan\alpha}\right) \quad (3.1)$$

where S is the selectivity of KOH etch of silicon with respect to glass (defined as the ratio of the silicon etch rate to glass etch rate).

To increase the aspect-ratio, the glass structures were over-etched after removing the silicon mold. The results obtained by KOH over-etching are shown in Fig. 3-12b. In this case, the glass was molded in trenches of 54 µm width and 220 µm depth at temperature of 850°C for 330 min. The KOH over-etching for 400 min was performed using the same conditions reported above. We achieved an aspect-ratio of 42:1 based on the average width (i.e. bottom width = 8 µm and top width = 1.9 µm) and a vertical depth of 207 µm.

3.7.3 Using Xenon Difluoride etching

The releasing step was also tested with XeF_2, since it is expected to have a good etching selectivity to glass while removing the silicon. Before the etching, an oxygen plasma was performed on the molded sample (60 s, 100 mTorr and 400 Watt) to remove organic contaminations followed by CF_4/O_2 RIE plasma (5s, 200 mTorr and 400 W) to remove the native oxide. The molded sample was then introduced in a pulsed XeF_2 etching system E1 of SPTS (150 mm platen, quartz showerhead) for silicon removal. Figure 13 shows vertical glass structures after this release step. Initially, the molding was done for 8 hours at 800°C and 2 MPa in 12 µm (Fig. 3-13a), 23 µm (Fig. 3-13b) and 54 µm (Fig. 3-13c) widths. The XeF_2 etching was performed for 318 cycles to completely remove the Si. The cycle includes a XeF_2 pulse of 10 s at 3 Torr and an overhead (pump time between pulses) of 18 s. Based on the measurements, the etching selectivity is estimated at 300:1. The height of the structures is 155, 165 and 175 µm, thus obtaining aspect-ratios of 15, 8 and 3.5 for the 12, and 23 and 54 µm structures respectively. Since the 12 µm width structures were not completely filled, the top of the released structures shows a curved form (glass front profile). We observed roughness on the top of larger structures. This is a consequence of the DRIE roughness on the bottom of deep trenches. By using optimal DRIE parameters, this roughness could be reduced.

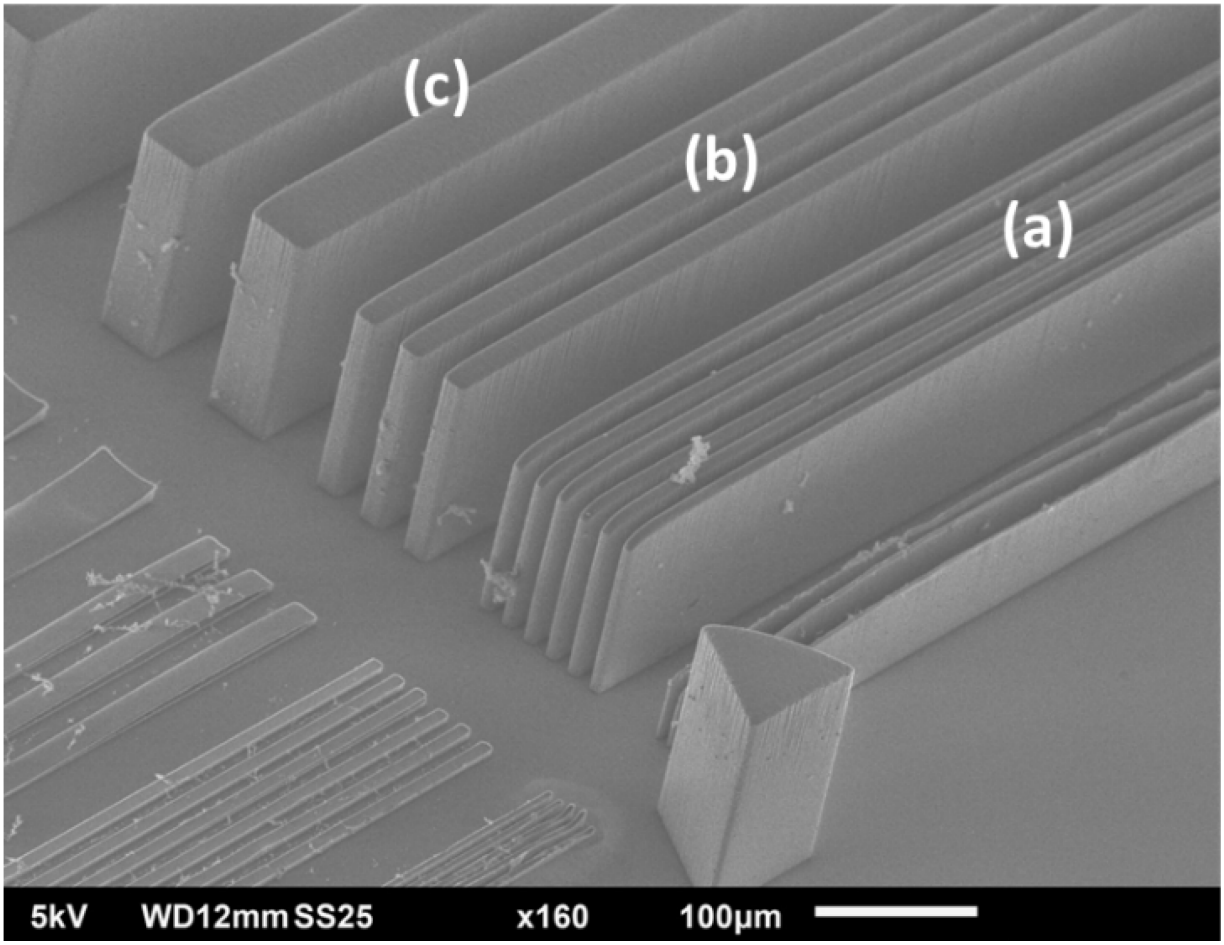

Figure 3-13 SEM of borosilicate glass structures fabricated by molding glass into silicon deep trenches after silicon has been removed by XeF_2 etching. Molding for 4 hours at 850°C and 2 MPa. (a) *AR*≈15:1, height=155 µm, (b) *AR*≈8:1, height=164 µm, (c) *AR*≈3.5:1, height=176 µm.

3.7.4 Discussion

Since the Si mold is fabricated by the Bosch process, the vertical surface of the molded glass is rough leaving a low transparency. This technique may be more beneficial for a variety of applications needing a non-conductive wall for thermal or electrical isolation. For optical applications, surface smoothing processes would be required.

Higher aspect ratios should be achievable if the released glass wall verticality is further improved after etching of the Si mold. Over etching of the released glass structure would then be possible down to thinner structures, leading to higher aspect-ratio. This would be simpler to achieve with highly selective XeF_2 mold removal, since compensation or glass etching during the release etch with a re-entrant Si mold trench would not be required.

As described by Eq. 3.1, the wall angle will therefore change compared to the wall angle of the original Si mold trench. To fabricate more fine uniform structure we should use first high selectivity etching such as XeF_2 as explained in section V-C following KOH over-etching of the glass. If KOH etching is used, then the trench in the Si mold needs to be etching in the Si with a re-entrant angle to allow compensation for the glass etching during the release.

3.8 Conclusion

We have developed a fabrication process to successfully create high aspect-ratio microstructures in borosilicate glass by molding into deep silicon trenches and etching the mold away, followed by an optional over-etch of the released glass structures. Aspect-ratios up to 42:1 with heights > 200 µm were demonstrated. Two releasing methods were studied: using KOH or XeF_2 etching. The XeF_2 has shown excellent etch selectivity of 300:1 and up to five times the selectivity observed for KOH etching. Increasing the ambient furnace pressure at the heat treatment step has shown a significant benefit to increase the glass flow velocity, and thus to achieve higher aspect-ratios.

The molding of borosilicate has shown a limitation in term of heating time and temperature. Indeed, defects have been observed on the glass when the heating time is too long. The range of process conditions for defect-free molding was mapped, defining the limits of the process. The defects could be due to the atomic diffusion of impurities contained in borosilicate glass which may require a dedicated study. The influence of diffusion could be better understood by studying the atomic composition of glass after the heat treatment. In addition, diffusion barrier layers could be a good solution to prevent the glass defects.

The paper defines the optimal design conditions to avoid defects on the glass after molding. These advances in the glass molding process enable the fabrication of microstructures in borosilicate glass with better control and precision than previously possible.

Aknowledgment

The authors would like to thank Dr. Dominic Drouin, Dr. Serge Ecoffey and Mr. Étienne Léveillé for their technical contribution and discussion. The fabrication work was performed at the Interdisciplinary Institute for Technological Innovation (3IT) and at SPTS Technologies Ltd.

4 A MEMS TURBOPUMP FOR HIGH TEMPERATURE RANKINE MICRO HEAT ENGINES – PART I: DESIGN AND FABRICATION

4.1 Avant-propos

Auteurs et affiliation :

Amrid Amnache : étudiant au doctorat, Université de Sherbrooke, Faculté de génie, Département de génie mécanique.
Mokhtar Liamini : PhD, École de Technologie Supérieure, Montréal.
Félix Gauthier : M. Sc. A., ing. jr., Pratt & Whitney Canada
Philippe Beauchesne-Martel : M. Sc. A., Pratt & Whitney Canada
Mohamed Omri : PhD, King Abdulaziz University
Luc Fréchette : professeur, Université de Sherbrooke, Faculté de génie, Département de génie mécanique.

Date d'acceptation : 28 avril 2020

Revue : IEEE *Journal of MicroElectroMechanical Systems* (JMEMS)

Titre français : Développement d'une turbopompe MEMS pour le micromoteur thermique de cycle Rankine – Partie I : conception et fabrication

Contribution de l'auteur :

La contribution de l'auteur dans cet article, en excluant l'encadrement du directeur de recherche, est estimée à 80 %.

L'auteur a contribué à :

- développer les techniques d'isolation thermique dans la microturbopompe (moulage de verre, collage anodique, oxyde thermique épais).
- proposer une configuration complète de la microturbopompe avec isolation thermique en intégrant les composantes préconçues par les co-auteurs (Turbine : Liamini, Beauchesne-Martel et Omri, Pompe : Liamini, Paliers hydrostatiques : Liamini et Gauthier.
- développer le procédé de fabrication au complet et dessiner les photomasques.
- développer les techniques utilisées dans la fabrication (gravure, collage de gaufres, *nested mask*, nettoyage d'échantillons).
- fabriquer au complet (à 100%) la microturbopompe au 3iT.Nano.
- caractériser la microturbopompe (microscopie, SEM, profilométrie, caméra infrarouge).
- rédiger 80% du contenu de l'article.

Contribution au document :

Cet article constitue le cœur de cette thèse. Il présente la fabrication de la microturbopompe. La configuration de la microturbopompe de deuxième génération incluant les stratégies d'isolation thermique est proposée. Le procédé complet de microfabrication de la microturbopompe est présenté dans cet article. Les défis en terme de microfabrication ont été énumérés en proposant des solutions originales pour surmonter ces défis. La microturbopompe est fabriquée avec succès et les résultats sont présentés dans cet article. C'est ce dispositif qui sera testé et caractérisée dans l'article suivant.

Résumé français :

Nous présentons la conception et la microfabrication d'une turbopompe MEMS avec isolation thermique, en tant que composant principal d'une centrale électrique à vapeur sur puce pour la récupération de chaleur basée sur le cycle thermodynamique de Rankine. Basé sur l'expérience précédente sur la microturbopompe de première génération pour un fonctionnement à température ambiante, ce dispositif de deuxième génération introduit des matériaux pour l'isolation thermique et des améliorations de conception des composants rotodynamiques pour un fonctionnement à des températures élevées. Une gestion thermique est nécessaire pour empêcher l'évaporation de l'eau dans la pompe et la condensation de la vapeur dans la turbine, les paliers hydrodynamiques et les joints d'étanchéité. Le dispositif est constitué d'un empilement de cinq gaufres qui renferme un rotor de 4 mm de diamètre avec des pales de turbine sur le dessus et une pompe visqueuse à rainures en spirale au-dessous. Cette turbopompe MEMS de deuxième génération met en œuvre des stratégies d'isolation thermique originales pour isoler la pompe des flux chaleur environnants. Un verre moulé épais est intégré dans le rotor pour empêcher la conduction de chaleur de la turbine à la pompe. De plus, un oxyde épais est utilisé pour empêcher la conduction thermique de la région du palier axiale vers la pompe.

4.2 Abstract

We report the design and microfabrication of a MEMS turbopump with thermal insulation, as the core component of a steam power plant-on-a-chip for waste heat recovery based on the Rankine thermodynamic cycle. Based on a first-generation microturbopump for ambient temperature operation, this second-generation device introduces materials for thermal insulation and design improvements to the rotordynamic components for operation at high temperatures. Thermal management is required to prevent water boiling in the pump and vapor from condensing in the turbine, bearings and seals. The device is a five-wafer stack that encloses a 4-mm diameter rotor disk with microturbine blades on one side and a viscous micropump on the other. This second-generation microturbopump implements unique thermal insulation strategies to isolate the pump from the surrounding hot flows. An out-off-plane thick molded glass embedded into the rotor prevents heat conduction from the turbine to the pump. In addition, an in-plane thick array of oxidized trenches prevents heat conduction from the thrust bearing region to the pump. The assembled microturbopump is fabricated and tested, resulting in the first MEMS turbopump demonstrated at high temperature. Design and fabrication are covered herein, whereas experimental demonstration and characterization are presented in Part II of this two-part paper.

Index Terms— Energy conversion, Rankine, thermal insulation, micromolding, Power MEMS, micropump, microturbine, waste heat, wafer bonding.

4.3 Introduction

Electric power generation is shifting focus to increasingly distributed energy nodes. Much smaller in scale than traditional power plant facilities, centimeter scale heat engines, such as miniature gas turbines [62,63] and Stirling engines [64] have emerged for distributed power generation in the 1-100 W scale. Currently, the most dominant portable power sources are Li-ion batteries [65]. However, they offer limited energy density (0.3 MJ/kg) compared to gasoline for example (47 MJ/kg), resulting in limited autonomy. The power density of the traditional combustion engines (~10^3 W/kg) is also significantly higher than batteries (~10^2 W/kg) [7]. Finally, heat engines also offer the opportunity to harvest waste heat from the ambient, allowing everlasting power sources. Micro heat engines could therefore offer high power and energy density alternatives to batteries for applications such as portable electronics, robots, drones, and distributed computing, sensing and actuation. Traditional manufacturing methods however exhibit constraints and limitations to

create micro engines at the centimeter scale or less. The concept of batch manufacturing micro heat engines using silicon microfabrication and other MEMS fabrication processes has therefore been proposed by Epstein [4,22]. Using photolithography and etching of silicon wafers, the semiconductor fabrication approach allows parallel fabrication of complex devices with micrometer scale resolutions, at low unit cost, and has stimulated the development of multiple chip-sized micro heat engines.

Based on the Brayton thermodynamic cycle, MEMS-based gas turbines of less than a cubic centimeter in volume capable of producing 10-20 W of electric power have been studied at MIT starting in the mid 1990's [5]. The predicted power conversion efficiency of this device is about 10 % [66]. For a decade, scientists and engineers at MIT and collaborating institutions developed the core technologies for micro gas turbines including micro-combustors [67], fluid film bearing [6,24] and micro generators [25,26]. These efforts have proven the feasibility of such a concept by demonstrating the first Silicon MEMS-based gas turbine producing 5 W of mechanical power [66].

Efficiency of micro heat engines depends strongly on the operating temperature difference between the hot source and the cold sink. The larger this temperature difference, higher is the efficiency to convert thermal to mechanical power. At microscale however, this can lead to significant heat losses, so thermal insulation is required. To date, manufacturing these devices using low thermal conductivity bulk materials such as oxides remains challenging. Unlike for high conductive silicon, the state-of-the-art microfabrication processes of glass or ceramics has limited capabilities to create high aspect-ratio microstructures that are required for the fabrication of microturbines. An interesting approach is to locally insulate the critical components. Thick PECVD (plasma enhanced chemical vapor deposition) oxide [38] could be implemented as localized insulation for application where 10-20 μm layer of oxide is sufficient. The thickness is limited by the residual stress after deposition causing fracture and wafer bow. Porous silicon has even lower conductivities than oxides and thicker layers can be formed (over 100 μm), but is fragile mechanically. More robust porous silicon carbide was also proposed as an insulation candidate in MEMS [41] due to it good chemical resistance, mechanical strength and high temperature stability, but deep etching of SiC remains a challenge. Integration of thick thermal insulation in micro heat engines therefore remain a key roadblock to their viability, motivating this work.

Directly inspired by the MIT micro gas turbine project, Fréchette pioneered since 2001 the development of a micro steam turbine based on the Rankine thermodynamic cycle [18]. The low temperature operation of the Rankine cycle makes the thermal insulation implementation in such small device less complex [19]. The Rankine steam microturbine presents similar power density (12 kW/kg) and efficiency (11%) [18] than the Brayton micro gas turbine cycle due to its low pumping power consumption using liquid instead of a gas. In addition, it makes waste heat scavenging possible in many applications given that it uses an external heat source, such as automotive exhaust or industrial process heat recovery. These characteristics motivated the development of the Rankine microturbine approach.

To achieve high efficiency and power density, the Rankine cycle is operated at high turbine inlet temperature and pressure, up to tens of atmospheres. To expand this high pressure, a configuration with multiple rotors (spools) is envisioned, as illustrated in Fig.1 [23,29]. It consists of three micro turbogenerators (turbine-driven generator), one microturbopump (turbine-driven pump) and an external evaporator and condenser. Steam expands first through the three micro turbogenerators for electric power generation and then through the microturbopump to pressurize the working fluid (water). Proposed inlet conditions to the first micro turbogenerator are 600°C, and 8 atm. Once the steam reaches the microturbopump, its temperature and pressure are expected to be 175°C and 0.5 atm. The predicted total turbines power of this system is 58 W (20, 21 and 12W for the micro turbogenerators 1, 2 and 3 respectively, and 5W for the microturbopump) [29]. Assuming mechanical-to-electrical conversion efficiency of 50%, the overall efficiency and the total electric power output of this system are estimated to be 10% and 25W (1.5W consumed by the pump and total drag is 6.5W).

Due to the low pumping power consumption, steam temperature entering the microturbopump only has a slight effect on the overall efficiency of the multi-spool system. However, it is important to maintain the steam at superheated temperatures to avoid condensation in the turbine and bearings. On the other hand, evaporation of water in the pump must be avoided, so thermal insulation in required to maintain the temperature gradient. One of the benefits of this multi-spool configuration is the lower temperature gradient in the microturbopump, making thermal insulation achievable.

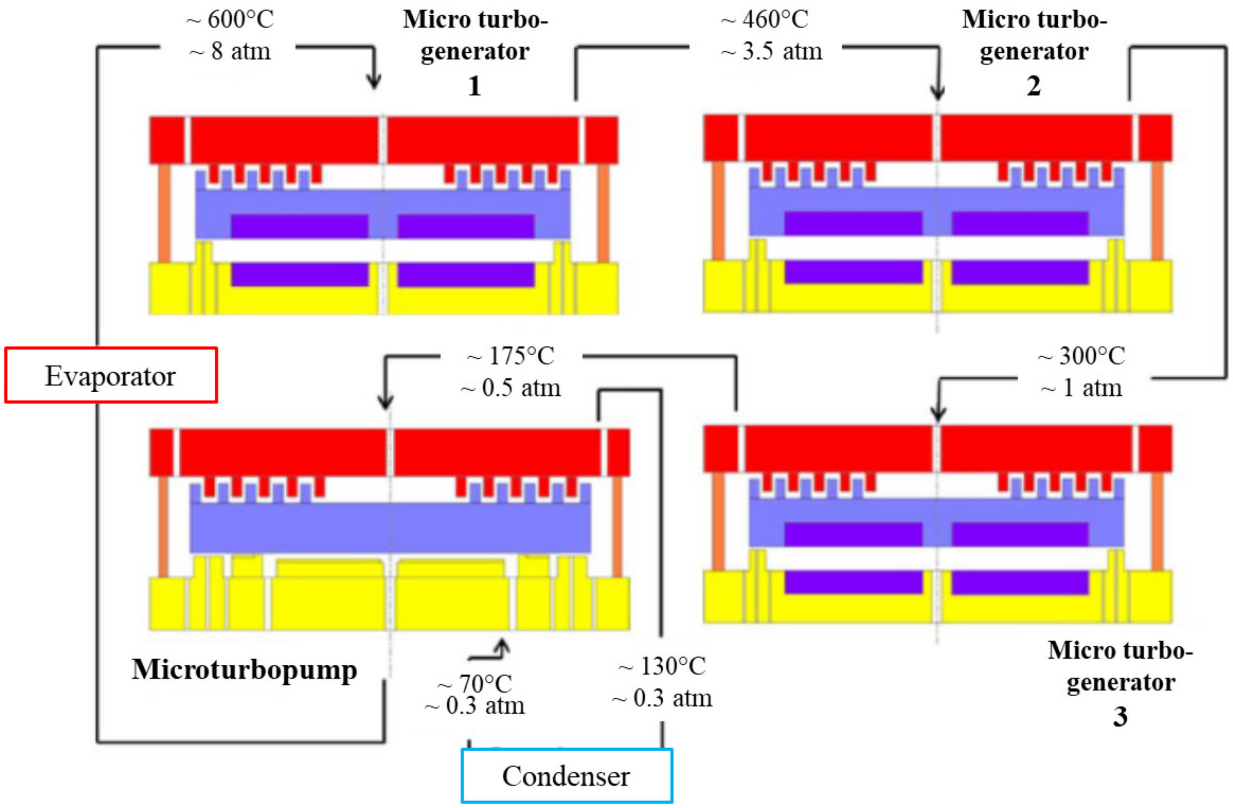

Figure 4-1 : Schematic illustration of a multi-spool configuration of a Rankine steam micoturbine system [23,29].

A first-generation silicon microturbopump required to implement the Rankine cycle was fabricated and tested in Columbia University [20,21]. The microturbopump, which corresponds to the rotating subsystem of a micro steam turbine power plant-on-a-chip, has a turbine, a micropump, bearings and seals. To simplify the experiments and fabrication, this microturbopump was designed to operate with ambient temperature air. Many key technologies could be demonstrated during this previous study including multistage microturbomachinery and rotating viscous micropumps with high power density and high efficiency. The current phase of this project aimed at developing a microturbopump with the required thermal insulation for high temperature operation. The point of operation is representative of real operating conditions in waste heat recovery applications as studied by Liamini [23]. Most of the core components of the micro steam turbine have been investigated earlier including 2D and 3D numerical analysis of the turbine flow [29,30], experimental investigation and modeling of the hydrostatic bearings for rotor stability [28], heat transfer management and material selection [67], and thermal insulating strategies [42].

The aim of this paper is to present the design and fabrication of the second generation of microturbopump that features an improved design and implements thermal insulation strategies to prevent undesirable boiling of water or vapor condensation during high temperature operation. In the following section, the device design will be presented, covering the turbine, pump, bearings and seals. Section 4.4 will introduce the proposed device configuration and its unique fabrication challenges, followed by the key fabrication processes to address these challenges (Sec. 4.5). The resulting process flow (Sec. 4.6) and fabrication results (Sec. 4.7) will then be presented. Part II of this two-part paper will present the experimental characterization methods and results for this device.

4.4 System and rotordynamic component design

In the following section, the design of the rotordynamic components and the prototype layout are presented. This follows critical choices that have been made regarding the materials and the configuration considering the challenge of managing elevated temperatures for such a device. In general, a decent part of the methodology exposed here inherits from the former design that was presented by Lee *et al*. [69]. However, the first generation (GEN 1) of prototypes was designed to be operated with air at ambient temperature. The second generation (GEN 2) components are designed considering hot steam flows. Additionally, many changes were made to improve the operation of the MEMS turbopump, which are summarized in Table 4-1. The considerations summarized in Table 4-1 allow to define the configuration proposed in Fig. 4-2.

Overall, four main principles govern the design process of such a device:

- The balance of power between the driving component (the turbine) and the power-consuming components, (the pump and the various aerodynamic losses in the bearings and seals) needs to be satisfied at the desired rotation speed.
- All the components need to be carefully designed in a way that guarantees the stability of the rotor both axially and radially, at all steps of operation.
- The obtained dimensions of the components must be manufacturable by known microfabrication techniques, considering the variations that can occur during microfabrication. A certain number of geometric features are shared between different components in order to reduce the number of microfabrication steps.

- Auxiliary components such as bearings and seals should consume a tiny portion of the mass flow passing through the turbine in order to minimize their impact on the overall system performance.

These main deign principles lead us to define the operating parameters listed in Table 4-2. These parameters in turn are used as inputs for the detailed design of each component of the device that is described in the coming sections.

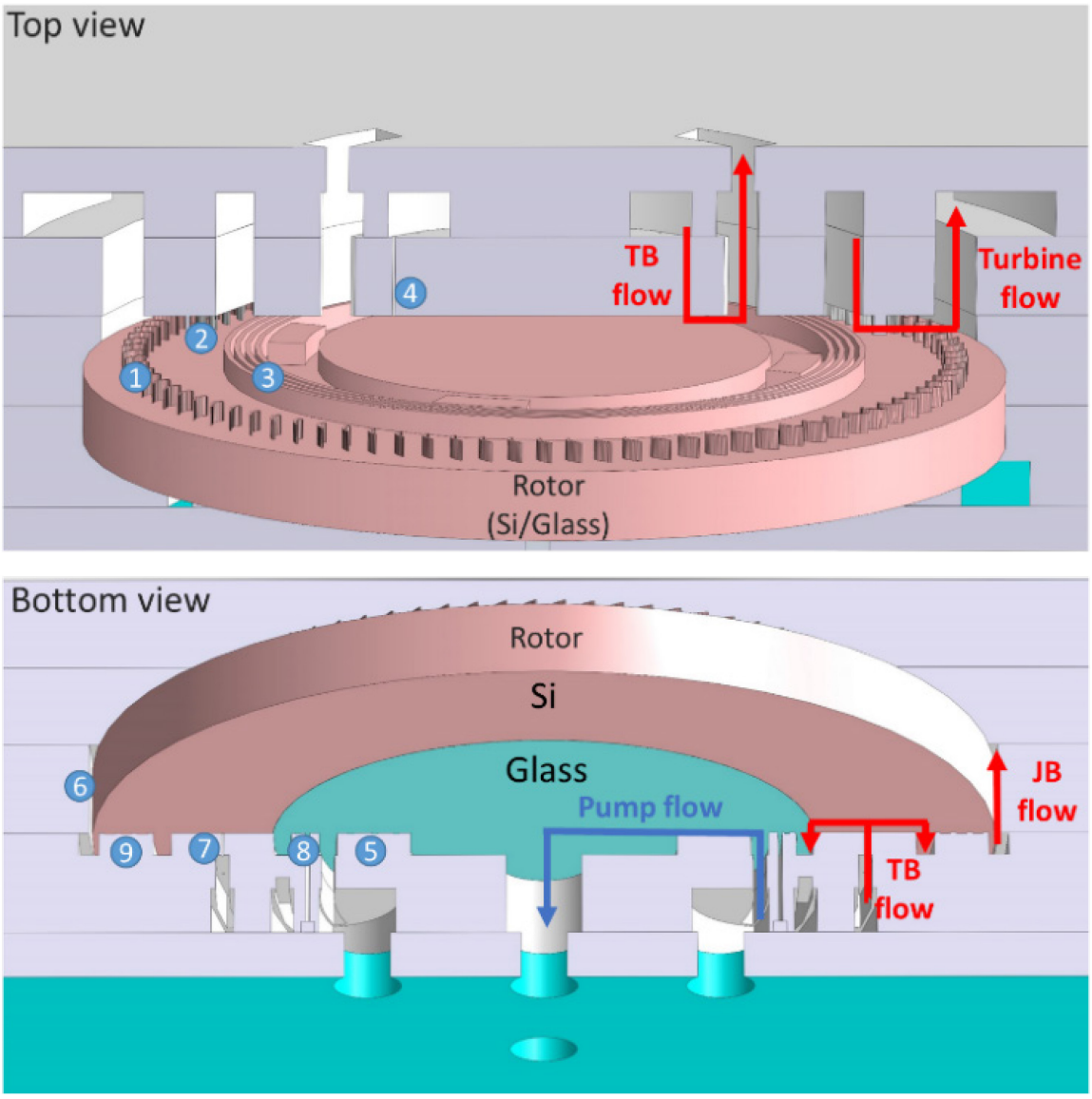

Figure 4-2 Cross-sectional views (top and bottom) of the proposed MEMS turbopump. Steam and water flows are illustrated with red and blue arrows respectively. Legend: JB: Journal bearing, TB: Thrust bearing, 1.Turbine blades, 2.Stator blades, 3.Top annular seal, 4.Top thrust bearing, 5.Pump, 6.Journal bearing, 7.Bottom thrust bearing, 8.Pump seal, 9.Bottom annular seal.

Table 4-1 Improvements made between GEN 1 and GEN 2 of the MEMS turbopump.

Component	GEN 1 [69]	GEN 2 This work	Rationale
Pump	Outward and Inward were tested	Inward	Inward was found easier to operate (no leakage at the output of the pump)
Turbine	Four stages	One stage	One stage is optimized to provide sufficient work to drive the pump, where GEN1 turbine was overdesigned in provision for adding a generator.
Thrust bearings (TB)	One bottom thrust bearing	Two thrust bearing (top and bottom)	Improved axial control of the rotor
Journal bearing (JB)	Two reservoirs	Four reservoirs, anisotropic pressures	Studies on journal bearings have shown an improved stability using anisotropic journal bearings [24]
Seals	One viscosity seal	One viscosity seal plus two annular seals	Allow for a better separation of the components

Table 4-2 Operating specifications of GEN2 MEMS turbopump [23].

Parameter	Nominal value	Justification
Rotational speed	600 kRPM	Reasonable target based on Generation 1 testing [69]
Mass flow	80 mg/s	Based on the mass flow the pump can provide for the pressure increase required [29]
Outlet pressure	200 kPa	Accounting for pressure losses in conducts at the turbine outlet
Rotor external diameter	4 mm	Based on a rotor geometry previously tested and validated [6,69]
Power produced by the turbine	1.84 W	Equal to the power consumed by the pump and the drag losses bearings and seals
Inlet turbine temperature	175°C	Based on the thermal modeling of the system [68]
Temperature of the stator wall	175°C	Assumed to be close to the temperature of the steam entering the turbine
Temperature of the rotor wall	175°C	Based on the thermal modeling of the system [68]
Pressure rise in the pump	7.5 bar	As defined by the calculation of the total thermodynamic cycle [23]

4.4.1 Turbine

An outward turbine is designed using a mean line analysis based on rothalpy conservation and velocity triangles that requires an estimation of various losses (profile losses, mixing losses, deviation and thermal transfer) [29]. The latter are predicted from the simulation of 24 geometries under a hundred flow regimes to accurately predict the effect of the geometric parameters on turbine performances. The geometric parameters investigated were: solidity, thickness distribution, camber and stagger. From these simulations, correlations are extracted to estimate the various sources of loss. The parameters used to determine the losses include the Reynolds number, compressibility, incidence and geometry. Tridimensional effects on losses have additionally been extracted from empirical formulas.

The in-depth design of the turbine is beyond the scope of this article. The complete details of the design can be found elsewhere [29], but ultimately the thorough analysis of the turbine stages along with the modeling of the losses are summarized in convenient design charts of flow coefficient ϕ and loading coefficient ψ (see Figure 4-3). These coefficients allow for the determination of the turbine geometry starting from the desired mass flow $\dot{m}$, power W_T, radius r, speed rotation ω and a chosen degree of reaction Ω. Starting from this, we can calculate $\psi = {W_T}/{\dot{m}(\omega r)^2}$ and determine on the chart the flow coefficient defined as $\phi = {W_{r2}}/{U_2}$. Here W_{r2} is the relative velocity at the outlet of the stage, where U_2 is the radial velocity at the outlet (see Figure 4-4). This allows then to calculate the desired geometry of the stage to obtain the above velocities. It is determined first that a single level stage outward turbine is enough to provide the required power from the pump and auxiliary components.

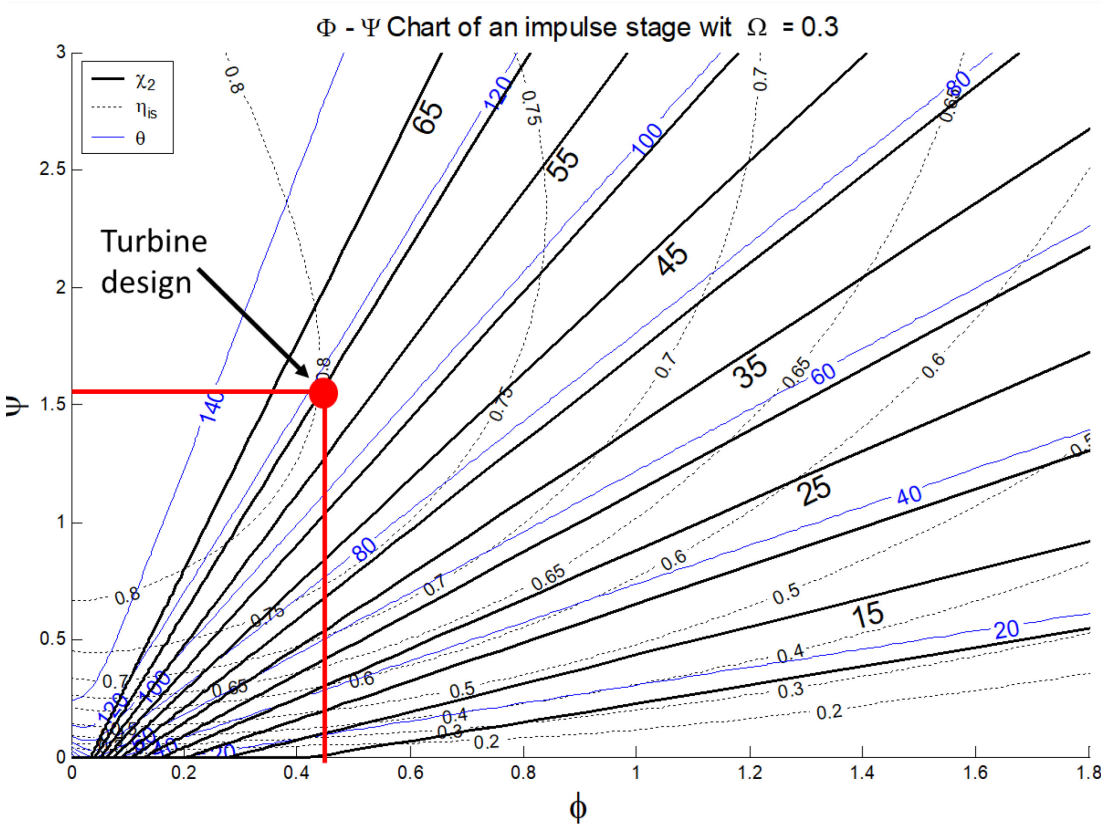

Figure 4-3 ϕ-ψ chart for an impulse stage with degree of reaction $\Omega = 0.3$ – Continuous black lines represent the outlet blade angle (χ_2), continuous blue lines represent the total flow deflection (θ) and dotted lines represent the stage efficiency (η_{is}) [29].

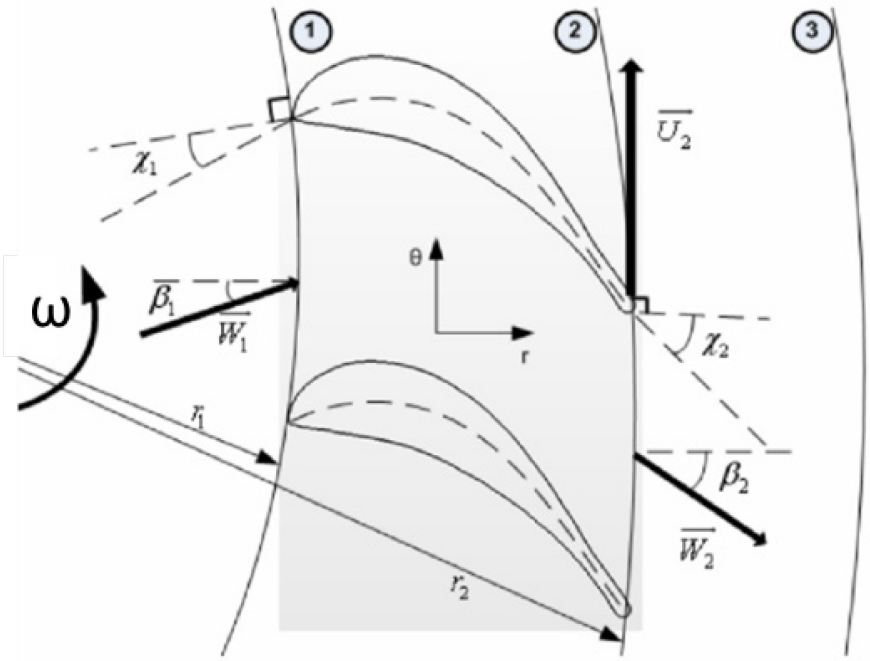

Figure 4-4 Nomenclature of a turbine blade row.

Based on the above approach, the main geometric features of the turbine are found and summarized in Table 4-3. The operating point of the turbine is chosen to have an efficiency≈80%.

Table 4-3 Designed turbine geometry (see Fig. 4-4 for nomenclature).

	χ_2	χ_2	r_1(μm)	r_2 (μm)	Chord (μm)	Solidity
Stator	0	72.8	1590	1690	185	1.5
Rotor	50	-54	1730	1830	109	1.5

The profile of the blade chosen is of type A3K7 with a maximum thickness reduced to 10%. The profile was slightly modified by thickening the trailing edge for fabrication consideration. With this design, the turbine is estimated to produce 1.83 W of power with an efficiency of 74.5%.

4.4.2 Viscous pump

Previous tests done on GEN 1 prototypes have shown the supremacy of the inward configuration over the outward one in terms of preserving the rotor stability. Principally, it is challenging to prevent flooding of the bottom thrust bearing with the high and varying output pressure of the pump during operation. Therefore, the inward configuration is preferred for the prototype presented in this article.

Modeling of the micropump is based on the Reynolds equation that describes the pressure distribution of thin viscous films in lubrication theory. The main assumptions are: a viscous, fully-developed flow of an incompressible fluid; a uniform pressure and density of the lubricating film; constant fluid properties. The delivered pressure rise and the torque required to drive the pump can be written in function of the characteristic dimensions of the pump (see Figure 4-5), the viscosity of the fluid μ_l, the mass flow in the pump $\dot{m}_l$, the density of the fluid ρ_l and the rotation speed of the rotor ω. They are expressed as follows [20]

$$\Delta P = \frac{3\mu_l\omega}{h_2^2}\left(r_{2eff}^2 - r_{1eff}^2\right)g_1(\alpha, H, \gamma) - \frac{6\mu_l\dot{m}_l(1+\gamma)}{\pi\rho_l h_1 h_2^2} A ln\left(\frac{r_{2eff}}{r_{1eff}}\right) \tag{4.1}$$

$$T_p = \frac{\pi\mu_l\omega r_2^4(1-\lambda^4)g_2(\alpha,H,\gamma)}{2h_2} - \frac{B\left(r_2^2-r_1^2\right)\mu_l\dot{m}_l}{\rho_l h_1 h_2} \tag{4.2}$$

where:

$$g_1(\alpha, H, \gamma) = \frac{\gamma H^2 \cot\alpha\,(1-H)(1-H^3)}{(1+\gamma H^3)(\gamma+H^3) + H^3\cot^2\alpha(1+\gamma)^2}$$

$$r_{1eff} = r_1 e^{\frac{\pi}{2n}\left(1-\frac{\alpha}{90}\right)tan\alpha\frac{2}{1+\gamma}\frac{1-H^3}{1+H^3}\frac{A_1 cot\alpha}{A_1 cot\alpha + C_1}}$$

$$r_{2eff} = r_2 e^{\frac{\pi}{2n}\left(1-\frac{\alpha}{90}\right)tan\alpha\frac{2}{1+\gamma}\frac{1-H^3}{1+H^3}\frac{A_2 cot\alpha}{A_2 cot\alpha + C_2}}$$

$$g_2 = \frac{(\gamma + H) + \dfrac{3\gamma H(1-H)^2(1+\gamma H^3)}{(1+\gamma H^3)(\gamma + H^3) + H^3 \cot^2\alpha\,(1+\gamma)^2}}{(1+\gamma)}$$

$$B = \frac{3\gamma H \cot\alpha\,(1-H)(1-H^3)}{(1+\gamma H^3)(\gamma + H^3) + H^3 \cot^2\alpha\,(1+\gamma)^2}$$

where H is defined as the ratio h_2/h_1, λ as r_1/r_2 and γ as a_2/a_1 (see Figure 4-5 for pump nomenclature) and n is the number of grooves. The force can be obtained by integrating the pressure over the surface while the torque and power consumed by the pump are derived from the above expression [20]. The model was validated in the first-generation MEMS turbopump [69] and is used for GEN 2 design.

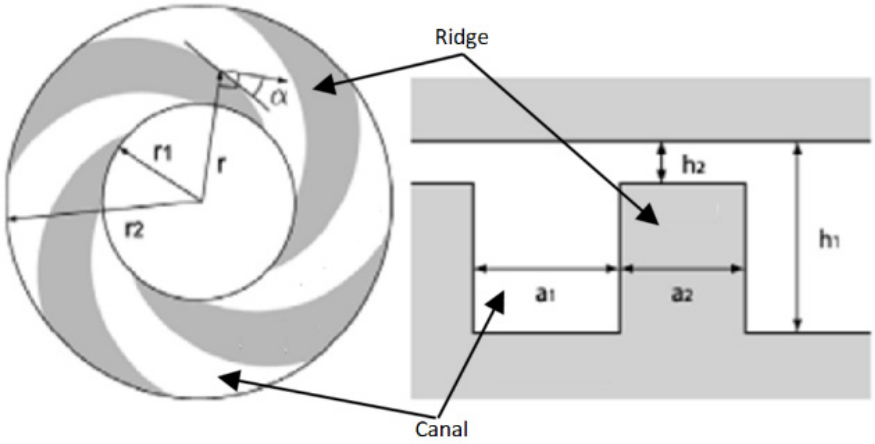

Figure 4-5 Geometry of the pump and nomenclature.

Optimizing over the above equations allows to define the geometry of the pump as shown in Table 4.4. The optimization process was to find a pump design that delivers a desired pressure rise while consuming least power.

Table 4-4 Geometry of the pump.

Parameter	Nominal value
r_1 (μm)	600
r_2 (μm)	920
h_1 (μm)	6.5
h_2 (μm)	0.5
γ	0.3
n	16

With this geometry, the pump is estimated to consume 1.4 W with an efficiency of 4.3% while delivering 80 mg/s of mass flow and 750 kPa of pressure rise.

4.4.3 Thrust bearings

The rotor is levitated on a pair of hydrostatic fluid film thrust bearings (TB). On the top side, the thrust bearing is a circular one that occupies the center of the rotor. On the bottom side, an annular thrust bearing is placed at the periphery of the pump. The use of two thrust bearings provides more controllability for the operation of the rotor and allows to place the rotor at the desired position by varying the pressure profiles in each thrust bearing independently.

The bearings are modeled as fluidic resistances in series between the entrance of the bearing and its exit (Figure 4-6). These resistances are based on either analytical or numerical models presented by Gauthier [28].

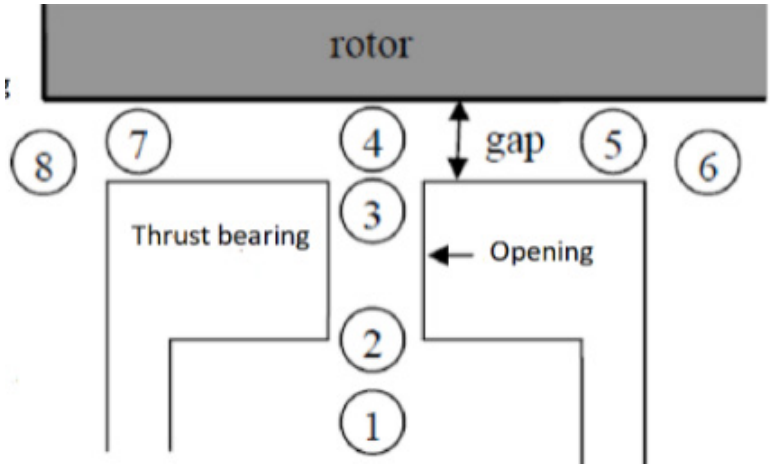

Figure 4-6 Thrust bearings geometry and nomenclature [28].

The thrust bearings should provide sufficient force to counteract those exerted on the rotor by the rotordynamic components during operation. Other criteria that are used for the bearing design are:

- Mass flow going through the bearings should be small compared to the total mass flow going through the turbine, to minimize their impact on cycle efficiency.
- The natural frequency of the bearings should be far above the design rotational speed to avoid instabilities during operation

Optimizing the geometry following the above principles allowed us to define the geometry of the thrust bearings as summarized in Table 4-5.

Table 4-5 Geometry of the thrust bearings.

Parameter	Bottom bearing	Top bearing
Number of capillaries	40	40
Depth of capillaries (µm)	200	200
Nominal gap (µm)	1.5	1.5
Capillaries diameter (µm)	13	13
Radial position of capillaries (µm)	1425	900
Internal radius (µm)	1200	0
External radius (µm)	1650	1000

4.4.4 Journal bearing

To support the rotor in the radial direction, a stabilizing pressure field is created on the periphery of the rotor disk, using the hydrostatic journal bearing principle [24]. Flow is fed from below the rotor through the journal bearing (JB) clearance formed between the rotor disk periphery and the surrounding wall. As opposed to the hydrostatic thrust bearings, the journal bearing natural frequency is very low. We therefore want to operate the rotor in super critical mode and cross the natural frequency at low speed and with a low-pressure differential. Teo [24] has developed a criterion for preventing hydrodynamic instabilities of the rotor:

$$C/R = 2\left(L/D\right)^2 \tag{4.3}$$

where C is the journal bearing gap, R is the radius (defined by the rotor radius) and L is the length of the journal bearing. Applying this criterion results in a journal bearing with the following geometry: C = 15µm and L = 300µm.

Another outcome of Teo's work was the benefit of using four reservoirs for the anisotropic operation of the rotor: two low-pressure reservoirs facing each other and two high-pressure reservoirs in the remaining quadrants. The goal is to rise the whirl instability limit by introducing anisotropy in journal bearing stiffness (different hydrostatic stiffness in the X and Y directions). This anisotropy was found to improve stability for high-speed operation and will be adopted here.

4.4.5 Seals

Seals are used in this device to help minimizing undesired mass flows between the rotordynamic components. Two types of seals are used for this MEMS turbopump as shown on Fig. 4-2.

Annular seal

Seals with annular grooves are used to separate the turbine from the top thrust bearing, and the journal bearing from the bottom thrust bearing. They rely on successive contractions and expansions of the flow (see Figure 4-7) to create losses and hence limit the leakage while maintaining the pressure difference.

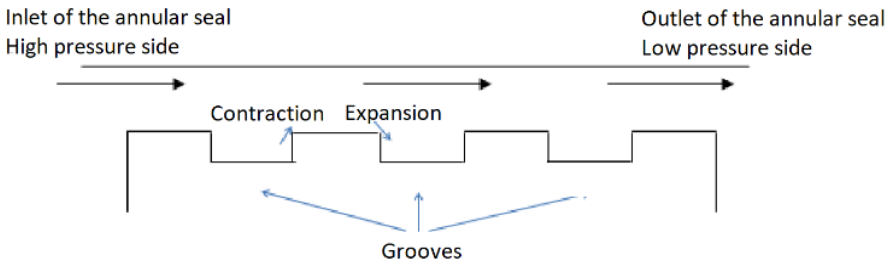

Figure 4-7: Annular type seal.

The pressure difference through the seal is expressed as $\Delta P = K\frac{1}{2}\rho V^2$. Here, V and ρ are the velocity and the density of the fluid.

Two-dimensional CFD simulations of the contraction and expansion losses have allowed to express K as a function of Reynolds number (Re) as [20]:

$$K = \frac{a_1}{Re} + \frac{a_2}{ln(Re)} + \frac{a_3}{ln(\mathrm{Re})^2} + \frac{a_4}{ln(\mathrm{Re})^3} + a_5 \times Re \tag{4.4}$$

with coefficients a_x depending on the flow regime and the loss type (contraction or expansion). Geometric parameters of the seals are varied within ranges imposed by the application and for each geometry the mass flow is calculated based on the imposed maximum pressure difference the seal would see during operation. The selected geometries correspond to the lowest mass flow obtained. Table 4-6 summarizes the geometries of the two optimal annular seals.

Table 4-6 Geometry of the annular seals.

Parameter	Bottom seal	Top seal
Ridge width (µm)	25	25
Groove width (µm)	50	20
Number of grooves	3	3
Gap variation (µm)	0 to 1	0 to 1
Nominal gap (µm)	0.5	0.5
Groove depth (µm)	4.5	80-100
Internal radius (µm)	1730	1230
External radius (µm)	1970	1390

Herringbone pump seal

A herringbone seal is used at the input of the pump to prevent the liquid from leaking out due to the pressure build-up from centrifugal forces. It also must prevent gas from the thrust bearings outlet to leak into the pump. The concept of this seal is similar to the pump concept as it builds a pressure rise from viscous shear of the fluid. Two opposing sets of grooves form a higher pressure in the center of the seal. In addition, it is only partially grooved in order to limit the mass flow of steam that passes through it (see figure 4-8 for geometry and nomenclature).

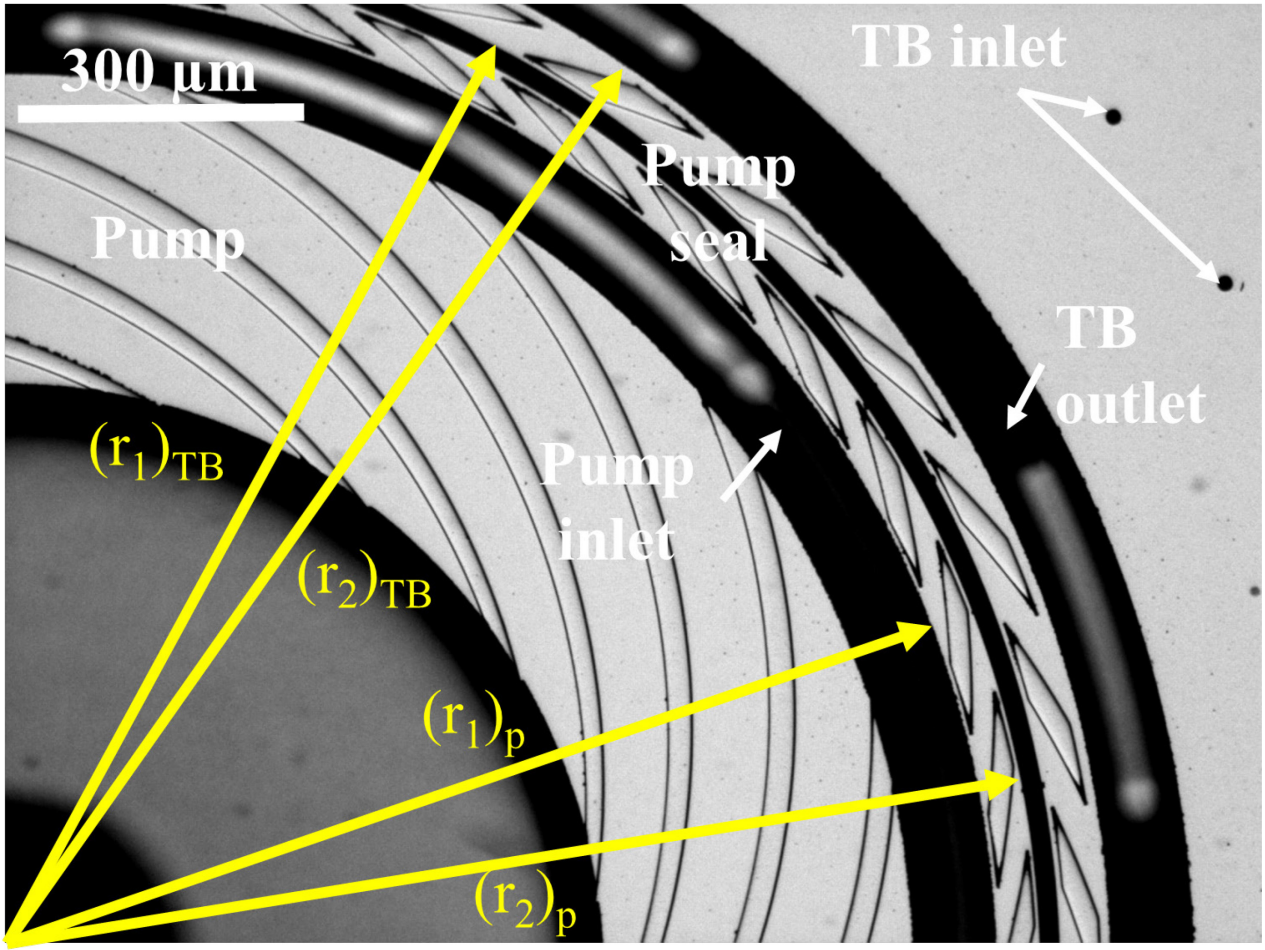

Figure 4-8 Pump seal geometry and nomenclature.

The optimization process aims at procuring the adequate pressure rise (given by Eq. 4.1, section II.B) while maintaining the mass flow small. The obtained geometry is summarized in Table 4-7.

Table 4-7 Geometry of the pump seal.

Parameter	Pump side	TB side
r_1 (μm)	1000	1070
r_2 (μm)	1060	1120
h_1 (μm)	5	0.5
h_2 (μm)	5	0.5
Number of grooves	40	35
α (°)	16	16
γ	1	1.26

4.5 MEMS Turbopump Device Configuration and Key Microfabrication Processes

Figure 4-9 shows a schematic cross-section view of the proposed design for the second-generation MEMS turbopump. It consists of a five-wafer stack made of silicon (A1, A2, B and C1) and glass (C2). Exploded views of the five-wafer stack viewed from the top and bottom side are illustrated on the right and left of Fig. 4-9, respectively. Overall, the center wafer (B) contains the rotor surrounded by the JB. The adjacent wafers (A2 and C1) comprise the stator blades, pump grooves, seals and TB orifices. Finally, the outer most wafers (A1 and C2) provide inlet/outlet flow canalizations and ports, as well as a through hole for optical probe speed measurement. In order to minimize thermomechanical deformation at high temperature operation only two wafer pairs are bonded together, these are A1/A2 and C1/C2. The multi-layers stack is formed by simply clamping the layers resulting three chips (A, B, C) in a packaging with polymeric O-rings contacting the outermost fluidic ports. There will be no problem of leakage at the interfaces A/B and B/C since the fluid here is at low pressure (turbine/JB outlet and JB inlet). In addition, the long interface (~5mm length) creates pressure loss and hence limits the leakage. Several technical challenges had to be overcome to succeed in the fabrication of the microturbopump and they are outlined below.

4.5.1 Thermal insulation

Performance of the microturbopump increases with the temperature difference between the hot (turbine) and the cold (pump) sides of the device, illustrated in Fig. 4-9. However, maintaining large temperature gradients in such small-scale devices is challenging, especially given the high thermal conductivity of Si. Thermal insulation of the pump is however important since the liquid

temperature must be kept below its evaporation point to avoid boiling that would halt its operation. Heat transfer in the microturbopump must therefore be carefully managed.

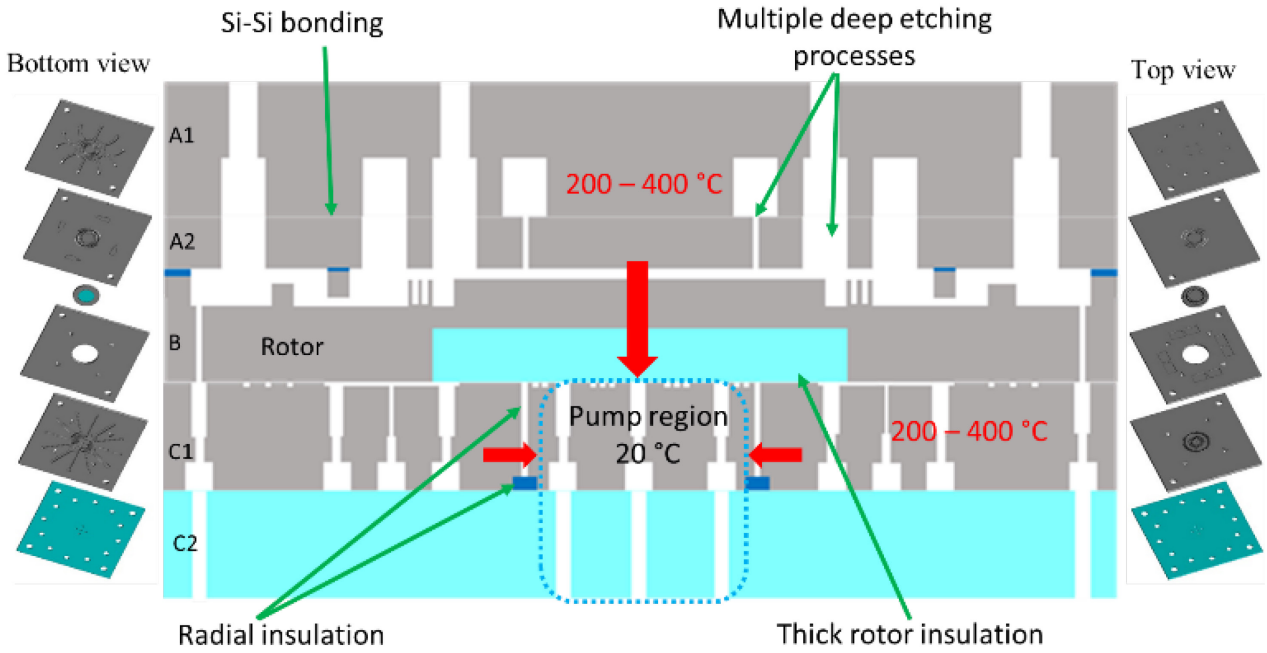

Figure 4-9 Schematic cross-section and exploded views of the microturbopump. Grey is silicon, light blue is glass and blue is SiO_2. Heat transfer paths are illustrated with red arrows.

Heat transfer occurring in the microturbine has been studied by Liamini *et al.* [68], suggesting a minimum thermal resistance of the rotor of about 3 K/W for adequate operation and acceptable cycle losses. This is equivalent to that insulation provided by a 100 µm thick oxide layer. To date, precision etching of thermally insulating materials such as glass do not meet the fabrication requirement of the microturbopump [42]. Unfortunately, highly thermally conductive silicon remains the dominant material that allows the patterning of complex 3D structures. In addition, depositing a 100 µm thick PECVD oxide layer [38] with good mechanical strength is not practical to obtain to this date.

As illustrated in Fig. 4-9, two innovative strategies of thermal insulation were developed for this work in order to thermally isolate the pump. An out-of-plane thick insulating glass layer in order to prevent the heat conduction from the turbine flow to the pump through the rotor created by micromolding [43], and an in-plane thick silicon oxide for radial insulation to prevent heat conduction from the surrounding bottom TB flows, created by oxidizing silicon trenches. These strategies are detailed in the following subsections.

Trenches filled by oxidation

To ensure the lateral thermal insulation, a thick oxide layer is formed in the silicon wafer that surrounds the pump region. It is created by etching an array of narrow silicon trenches by deep reactive ion etching (DRIE) and then thermally oxidize the trenches, resulting in refilling the space between the trenches. Figure 4-10 shows a SEM image of thick oxide formed by this technique. This technique of insulation was already reported and has shown good thermal insulation capability [39].

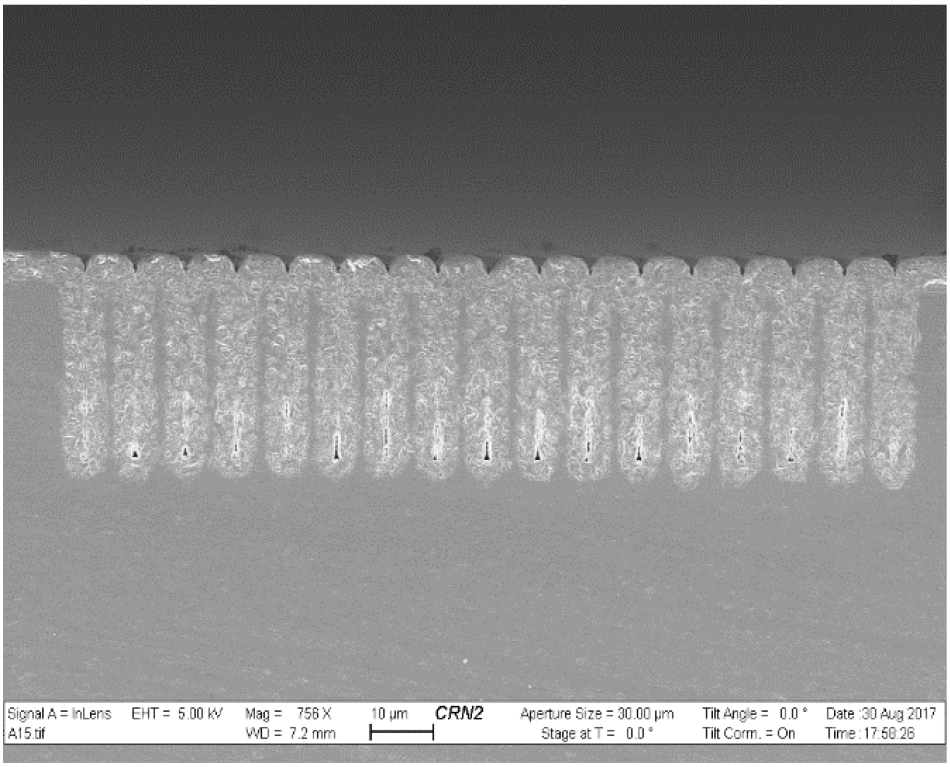

Figure 4-10 SEM image showing thick silicon oxide obtained by thermal oxidation silicon trenches.

Micromolding

Amnache *et al.* [43] have studied and developed an approach to fabricate an embedded glass into silicon cavity by molding borosilicate glass that is used in this work to fabricate the hybrid Si/glass rotor. Figure 4-11 shows SEM images that illustrate the fabrication steps of the micromolding technique. Main steps consist in: a) creating a cavity into silicon by DRIE and anodic bonding of silicon with borosilicate glass under vacuum, b) annealing to mold the glass into cavity, c) lapping and polishing the excess glass. Since the polishing is on two different materials with different mechanical properties i.e. silicon and glass, slight dishing is expected.

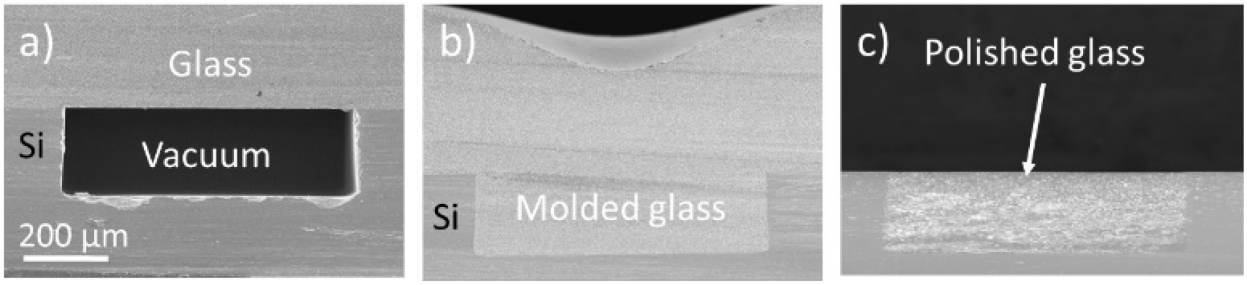

Figure 4-11 Polishing process performed on the molded glass surface. b) After molding. c) After completely removing the excess glass.

4.5.2 Nested Mask

As illustrated in Fig. 4-9, the microturbopump involves a combination of different aspect-ratio structures on the same wafer side (depth up to 250 µm). Realizing these structures in one DRIE step is challenging due to the aspect-ratio dependent etching (ARDE) effect in deep silicon etching [70]. Realizing these structures in two different DRIE steps is not practical because photolithography on such deep topography is incompatible. To overcome this challenge, we used the nested mask (or peeling mask) technique.

The nested mask technique is used in this work to realize two different aspect-ratio silicon structures on a same wafer side. The approach requires the deposition of two different mask materials patterned before the first silicon etching step. The materials must have a certain selectivity to each other and with silicon etchant in order to etch multilevel depths. In this work, a combination of photoresist (top) and silicon oxide (bottom) is used. In the case of a patterned surface, spin coating photoresist is not sufficient to cover the deep structures and masking them during the etching step. In addition, using very thick photoresist may lead to cracking in the plasma etching steps. Alumina mask (Al_2O_3) is used in this case instead of photoresist.

First DRIE step is done with the upper mask to start etching the highest aspect-ratio structures that need more time to achieve the desired total depth, h_{tot}. The first required etching time, t_1, can be estimated by:

$$t_1 = h_{tot}\left(\frac{1}{ER1} - \frac{1}{ER1}\right) \tag{4.5}$$

where *ER1* and *ER2* are the etching rates for the highest and lowest aspect-ratio structures respectively. The etch rates for the recipes used in this work are presented in the appendix. Once the intermediate depth is achieved, the photoresist (or Al_2O_3) is removed revealing the patterned

oxide mask. A second DRIE step is then done to continue etching until h_{tot} is reached. The second etching time required, t_2, can be estimated by:

$$t_2 = \frac{h_{tot}}{ER2} \tag{4.6}$$

4.5.3 Silicon deep etching

The well characterized DRIE recipe i.e. etch rate, etching profile, and etching selectivity was essential before starting the fabrication to control the etch depth. Two DRIE recipes (DRIE1 and DRIE2) were developed and characterized in this work and they are detailed in the appendix. DRIE1 has been developed for general etching and it is compatible for large exposed etching area. DRIE2 has been developed for notching free etching. In fact, in order to have a uniform operation gap, silicon-on-insulator (SOI) wafer is used to form the layer A2 taking advantage of the buried oxide layer as an etch stop for depth control. However, a notching effect may happen once the etching reaches the oxide layer (dielectric) due to charge accumulation. If the large trenches (greater than 100 µm) are slightly affected by this undercutting, narrower ones, such as the TB orifices can be more affected. The undercutting can reach several microns and this can completely change the functionality of the TB. It was hence necessary to prevent notching at the oxide interface. In this work, we developed and used a low frequency DRIE2 recipe to prevent notching.

4.5.4 Si-Si direct bonding with patterned features

The successful MEMS turbopump fabrication depends strongly on the quality of wafer bonding. Direct bonding is used in this work to bond layer A1 with layer A2. It is known that the quality of Si-Si direct bonding is enhanced using a SiO_2 thin layer on the bonding interface (greater than 50 nm) [71]. The SiO_2 layer dissolves hydrogen generated at the annealing step avoiding voids and bubbles at the bond interface. Direct bonding with thermal oxide layer (200 nm) was tried to bond layers A1 and A2 with no success. A thermal oxide layer was grown on wafer A1, characterized by dense patterned features. This thermal oxidation creates small protrusions (ears) on right-angled corner of the features that mechanically prevent bonding. Serrioglu *et al.* have reported this phenomenon [72]. Plasma enhanced chemical vapor deposition (PECVD) oxide can be an alternative approach. However, since the surface roughness of this oxide is not suitable for direct bonding, the wafers need to be polished. Hydrophilic Si-Si direct bonding without any intermediate layer is selected for this work. The remaining challenge to overcome is to protect the bonding

interface throughout the several fabrication steps and keep it free from contaminants and defects. The approach was the use of a thin thermal SiO_2 on the bonding interface as a protective layer during the fabrication steps and it will be removed before bonding. The thermal oxidation is done on a blank wafer without any features to prevent corner protrusions.

4.6 Microfabrication Process Flow

Silicon and borosilicate glass (Borofloat33) were selected as materials to fabricate the microturbopump. The use of silicon allows to fabricate of complex structures while borosilicate glass offers great potential for thermal insulation due to its low thermal conductivity and also for its micromolding capability [43]. Flatness and smoothness of the selected silicon wafers are essential parameters for direct bonding. In addition, the TB, seal and pump operate at micrometer-scale gaps. It is thus necessary to select wafers with low total thickness variation (TTV) and low wafer bow. In this work, ultra-flat double side polished silicon 4-inch diameter wafers were selected, with a TTV less than 1 µm and a maximum bow of 20 µm.

The fabrication process flow of the complete microturbopump is illustrated in Fig. 4-12. Note that the alignment marks (for lithography and bonding) were patterned before starting fabrication for each side of the wafers, while the alignment structures for the final chip assembly were included in the fabrication steps. To avoid repetition, SC1 cleaning is done before each lithography. AZ9245 photoresist (PR) from MicroChemicals is used in this work. PR striping is done with solvents and Piranha, and plasma O_2 when is mentioned. Prior to thermal oxidation, the wafers were cleaned with RCA. During etching through holes/trenches, the processed wafer is temporarily mounted to a quartz wafer using a low melting adhesive (Crystalbond 555HMP) avoiding He coolant leakage once the wafer is etched through. The carrier is removed by reheating the wafer. Remaining adhesive on the wafer can be dissolved simply by using hot water. For the reactive ion etching (RIE) and DRIE recipes, refer to the appendix.

Figure 4-12 Microfabrication process flow of the MEMS turbopump.

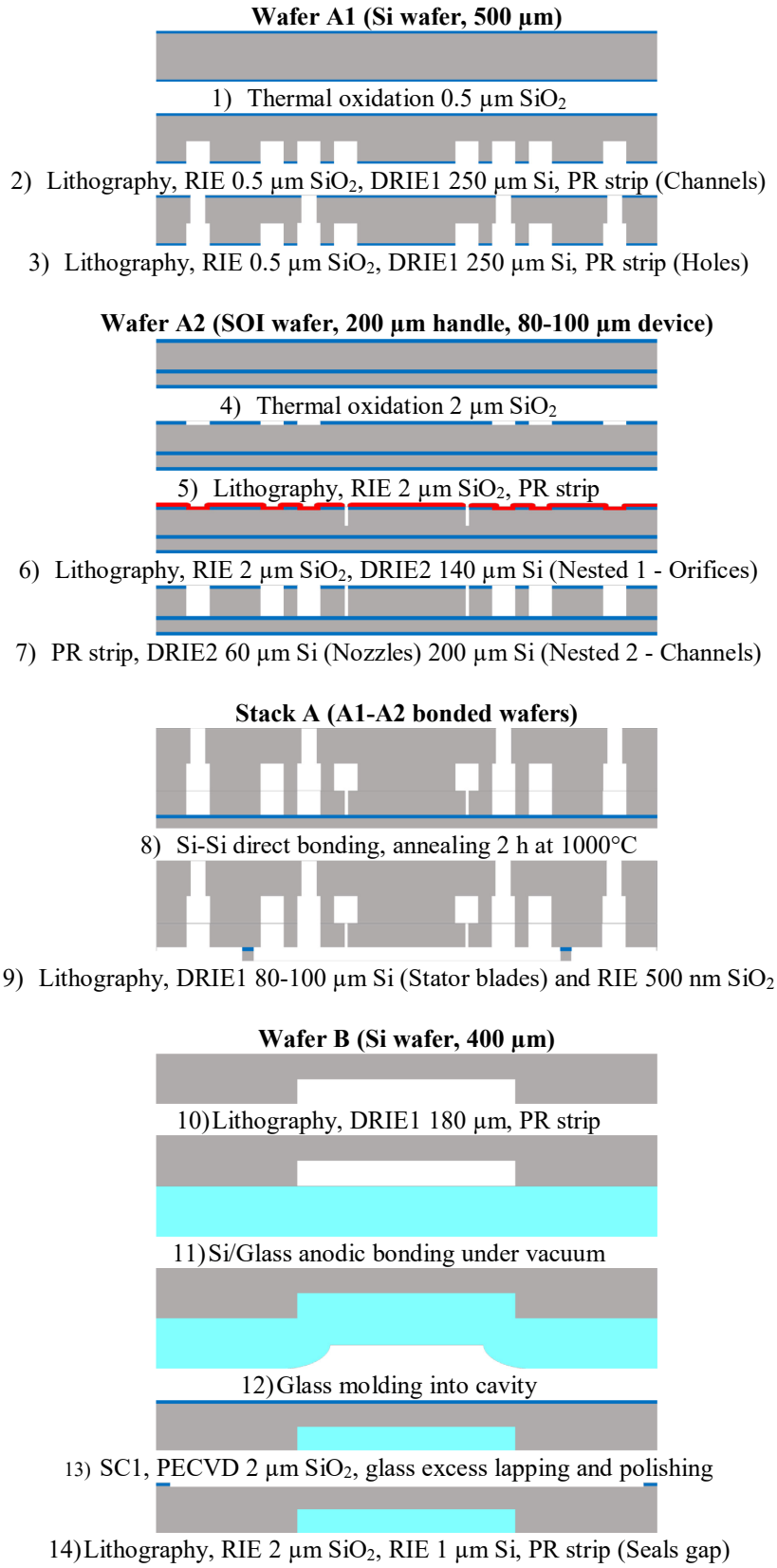

15) Lithography, RIE 1 µm Si, PR strip (TB gap)

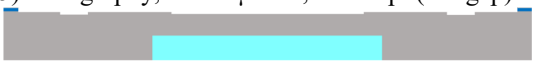

16) Lithography, DRIE1 4.5 µm Si, PR strip (Turbine tip clearance)

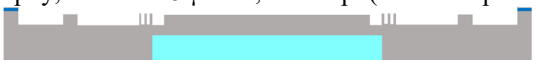

17) Lithography, DRIE1 80-120 µm Si, PR strip (Turbine blades, Seals)

18) Lithography (bottom), DRIE2 280-320 µm Si, PR strip (JB)

Wafer C1 (Si wafer, 450 µm)

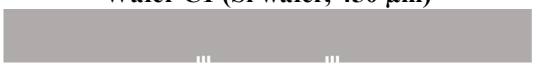

19) Lithography, DRIE1 50 µm Si, PR strip (Trenches)

20) Thermal oxidation 5 µm SiO_2

21) HF etch 3 µm SiO_2

22) Lithography, RIE 2 µm SiO_2, PR strip

23) Lithography, DRIE2 125 µm Si (Nested 1 - Channels)

24) PR strip, DRIE2 125 µm Si (Nested 2 - Channels)

25) Lithography, RIE 2 µm SiO_2, RIE 1 µm Si, PR strip (TB gap)

26) Lithography, RIE 2 µm SiO_2, DRIE1 4.5 µm Si, PR strip (Pump and Seals grooves)

27) SC1, PECVD 1 µm SiO_2

28) Lithography, RIE 3 µm SiO_2, PR strip

29) SC1, Sputtering 90 nm Al_2O_3

30) Lithography, RIE 90 nm Al_2O_3, RIE 3 µm SiO_2, DRIE2 Si 150 µm (TB orifices), (Nested 1 – TB orifices, insulation gap)

31) Piranha etch 90 nm Al_2O_3, DRIE2 50 µm Si (orifices) 200 µm Si (Nested 2 - Channels)

32) SC1, RIE 1 µm SiO_2 (top), HF etch 2 µm SiO_2 (top, bottom)

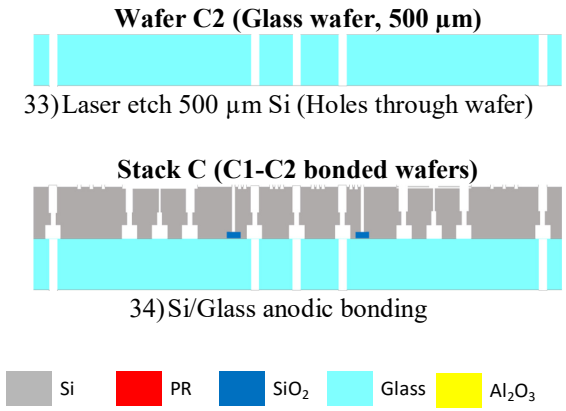

Wafer A1

The starting substrate is a silicon wafer 500 µm thick. Thermal oxide of 500 nm thick is formed on both sides of the wafer to protect the surface from degradation prior to bonding (Fig. 4-12-1). First, lithography, RIE followed by DRIE1 are used to etch 500 nm of SiO_2 and 250 µm of Si on the bottom side to form flow canalizations (Fig. 4-12-2). Same step is done on the top side to etch through wafer to form flow inlet/outlet and through holes for optical probe visualization (Fig. 4-12-3).

Wafer A2

Initially, an SOI wafer (200-µm handle layer, 80-100 µm device layer and 500 nm burrier layer) is thermally oxidized to form 2 µm of SiO_2 (Fig. 4-12-4). An SOI wafer is used in order to obtain a uniform top operation gap of the thrust bearing and also a uniform stator blade height. The top thermal oxide layer serves also as a masking layer, while the buried layer serves as a DRIE etch stop. A nested mask technique is used to manufacture different aspect-ratio trenches and holes on the topside of the wafer. First, lithography is followed by RIE to pattern the oxide layer (Fig. 4-12-5). Then, lithography and DRIE2 to start etching the thrust bearing orifices 140 µm deep (Fig. 4-12-6). DRIE2 is continued after PR striping with plasma O_2 revealing the oxide mask. The etching is stopped once reaching the buried layer resulting in same etch depth (Fig. 4-12-7).

Stack A

Following the individual processing of A1 and A2, the two wafers are aligned and fusion bonded to form stack A (Fig. 4-12-8). The thermal SiO_2 layer is removed using HF solution (49%). Compared to other solutions for removing SiO_2 such as Buffered Oxide Etch (BOE) or RIE, it was found that HF solution roughens less the silicon surface. After removing the SiO_2 layer, the root

mean square roughness is measured as 0.17 nm. It remains smaller than the standard roughness i.e. 0.2 nm [33] indicating the bondability of the silicon surface. Note that the exposure time of the Si surface with HF solution varies from 15 to 30 s. Prior to the direct bonding, the wafers were cleaned with SC1 (10 min) and SC2 (10 min). This cleaning process renders the surface hydrophilic by formation of a native oxide on the surface. Afterward, the wafers are rinsed and stored in water for 15 min. The storing step helps to hydrolyze the wafer surfaces (Si-OH groups). The wafers are then dried with nitrogen. The dwell time between cleaning and bonding does not exceed 15 min. The bonding is done in a wafer bonder from AML with in-situ alignment. The prebonded wafer pair was then annealed for 2 hours at 1000°C is an inert ambient. Next, lithography and DRIE1 of 80-100 µm of Si followed by RIE of SiO_2 are done on the backside of the stack to form the stator blades, reveal the thrust bearing holes, inlet/outlet flow ports and the throughout holes for optical probe measurement (Fig. 4-12-9).

Wafer B

Glass micromolding technique is used to form an embedded glass into a Si wafer. 400-µm thick Si substrate is used. First, lithography and DRIE1 are used on the backside of the wafer to etch a circular cavity of 200 µm deep and 2.4 mm diameter (Fig. 4-12-10). Anodic bonding is performed with a borosilicate glass (borofloat33) under vacuum (Fig. 4-12-11). RCA is used as a cleaning procedure prior to bonding, including an HF dip for the silicon wafer to remove its native oxide. Bonding is carried out under vacuum (150 µTorr) at a temperature of 370°C, applied voltage of 500 V with current limit of 4 mA and applied bonding force of 200 N. The bonded pair is then annealed at 800°C for 2 hours. Due to the pressure difference between the ambient and the cavity, the softened glass flows and entirely fills the cavity (Fig. 4-12-12). A second anodic bonding process is performed to increase the bonding strength in the cavity. Subsequent lapping and polishing sequences are done to remove the excess glass (Fig. 4-12-13). To protect the topside Si surface through these sequences, a 2-µm SiO_2 layer is deposited with PECVD. In the next step, a series of lithography/etching steps are accomplished as follows: RIE to etch 2 µm SiO_2 and 1 µm of Si to create the seal gap (Fig. 4-12-14), RIE to etch 1 µm of Si to create the TB gap (Fig. 4-12-15), DRIE1 to etch 4.5-5.5 µm of Si to create the turbine blade tip clearance (Fig. 4-12-16), and finally, DRIE1 to etch 80-120 µm of Si to create the turbine blades and top annular seal (Fig. 4-12-17). To complete the process, lithography and DRIE2 of 280-320 µm are done on the backside of

the wafer to create the 15 µm wide JB circumferential gap and consequently the rotor (Fig. 4-12-18). The hybrid rotor is released by submerging the wafer/quartz carrier in a hot water beaker, and simply collected with tweezers. Rotors without embedded glass (Si only) are also fabricated for the purpose of comparing them with the hybrid ones in Part II of this two-part paper.

Wafer C1

The starting substrate is a 450 µm thick Si wafer. First, circumferential narrow trenches for thermal insulation are etched (60 µm depth) by DRIE2 on the wafer backside (Fig. 4-12-19). Wet thermal oxidation is done to create 5 µm SiO_2. The trenches are then completely refilled forming a thick in-plane oxide (Fig. 4-12-20). In order to facilitate subsequent processing., the SiO_2 layer on both wafer sides is reduced to 2 µm by HF wet etching (Fig. 4-12-21).

A first nested mask technique is used to pattern the wafer backside as follows: lithography and RIE to pattern the SiO_2 layer (Fig. 4-12-22), after stripping PR, second lithography and DRIE2 to etch 125 µm of Si (Fig. 4-12-23), PR is afterwards stripped with plasma O_2 followed by DRIE2 to complete the etching of 125 µm Si resulting in multilevel channels (Fig. 4-12-24). Next, lithography and RIE are done on the topside of the wafer to etch 2 µm of SiO_2 and 1 µm of Si to create the bottom thrust bearing gap (Fig. 4-12-25). Another lithography is done followed by RIE to etch 2 µm of SiO_2 and DRIE1 to etch 4.5 µm of Si in order to create the pump and seal grooves (Fig. 4-12-26). Then, a 1 µm layer of SiO_2 is deposited by PECVD to protect the TB zone and the pump/seal grooves through the next etching steps (Fig. 4-12-27).

A second nested mask technique is used to pattern the topside of the wafer. First, lithography and RIE are done to pattern the SiO_2 layer (Fig. 4-12-28). After stripping PR and cleaning, 90 nm of Al_2O_3 is sputtered to form a masking layer for the second etching step of the nested mask (Fig. 4-12-29). The selectivity of Al_2O_3 to silicon in DRIE2 is too high and it was difficult to measure it. Afterwards, lithography, RIE and DRIE2 are done to etch 90 nm of Al_2O_3, 3 µm of SiO_2 and 150 µm of Si to start forming the TB orifices and the insulation gap (Fig. 4-12-30). After PR stripping and Al_2O_3 layer etching with Piranha, DRIE2 is continued to create the TB orifices (50 µm) and the inlet/outlet flow channels (200 µm) (Fig. 4-12-31). Finally, prior to anodic bonding, the SiO_2 layer is removed from both sides with RIE and HF wet etching (Fig. 4-12-32).

Wafer C2

Holes (or vias) of 200 µm and 400 µm diameters have been created through 500 µm thick borosilicate glass wafers using laser-induced deep etching (LPKF Laser & Electronics) (Fig. 4-12-33). The etching conditions are: power of 4 W, frequency of 40 Hz, tool speed of 50 mm/s, number of passes is 4 passes and a tool delay of 1s. The etched wafer is shown in Fig.4-13a. Chipping is observed on the hole edges (Fig. 4-13b) but it does not affect the quality of anodic bonding C1/C2 since it is not a convex topography.

Stack C

Anodic bonding is performed to bond wafers C1 and C2 (Fig. 4-12-34). The cleaning procedure and conditions are the same as detailed above for anodic bonding in wafer B fabrication.

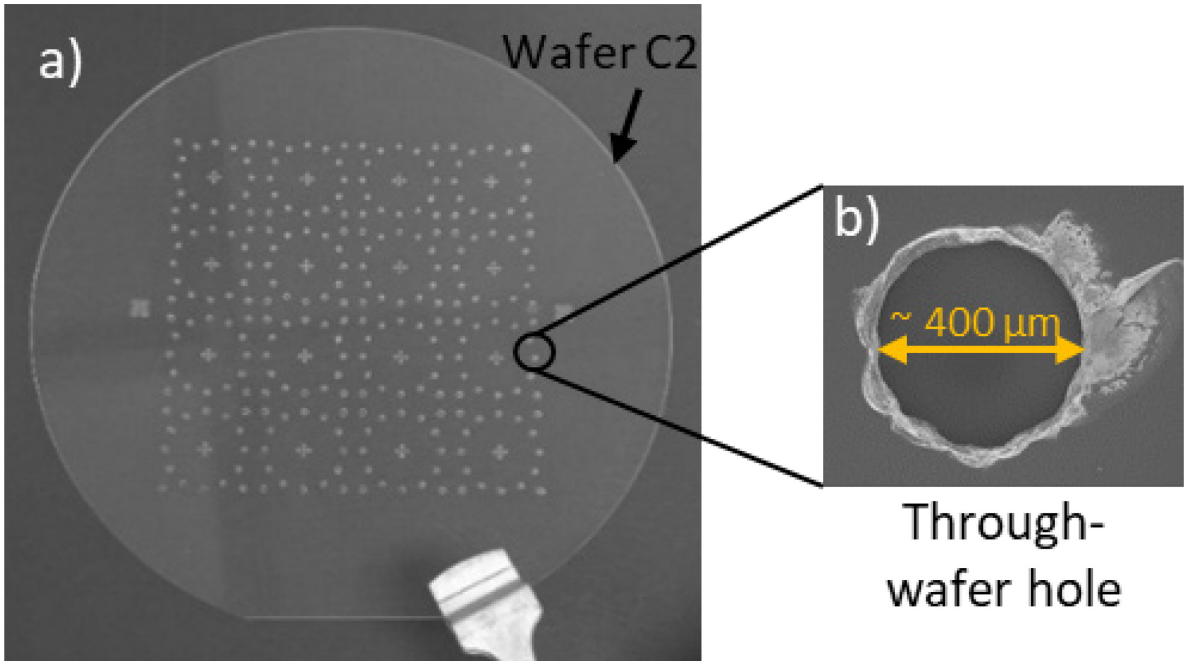

Figure 4-13 (a) Photograph image showing the wafer C2 after laser etching and (b) SEM image showing the etched through hole.

4.7 Microfabrication Results and Assembly

As a result, the above microfabrication process flow was realized with success allowing to produce good quality devices free of major defects (no broken turbine or stator blades, the bonding interface is free of defects, the fabricated dimensions are in respect with the design, the rotors have a smooth circumferential surface). The bonded wafer pairs A1/A2 and C1/C2 and the wafer B were diced into individual dies (1.5 × 1.5 cm) using a wafer dicer with a diamond-dicing blade of 270 µm thick. Photoresist was used to protect the stator blades throughout the dicing. Figure 4-14 shows

photographs of the complete fabricated A, B and C dies before assembly (top and bottom views). Infrared characterization of the bonded wafer A1/A2 was done before dicing as illustrated in Fig. 4-15. The image shows uniform bonding except random voids that can be caused by particles.

Accurate alignment of the dies is a primary step for operation of the microturbopump. For example, a misalignment between B and C dies results in decentering of the JB geometric center to the rotor's center of mass causing imbalance and failure [24]. In addition, a misalignment between A and B dies could result in interlocking of the stator and turbine blades (gap = 20 µm). The dies are designed to be self-aligned by simply applying a small manual clockwise rotation once superposed. Two mechanisms of alignment are used: interlocked concave and convex structures to align die A with die B and metallic microballs (300-µm diameter) that are introduced into triangular trenches to align die B with die C. The alignment features are designed to be created throughout the fabrication process flow of the microturbopump.

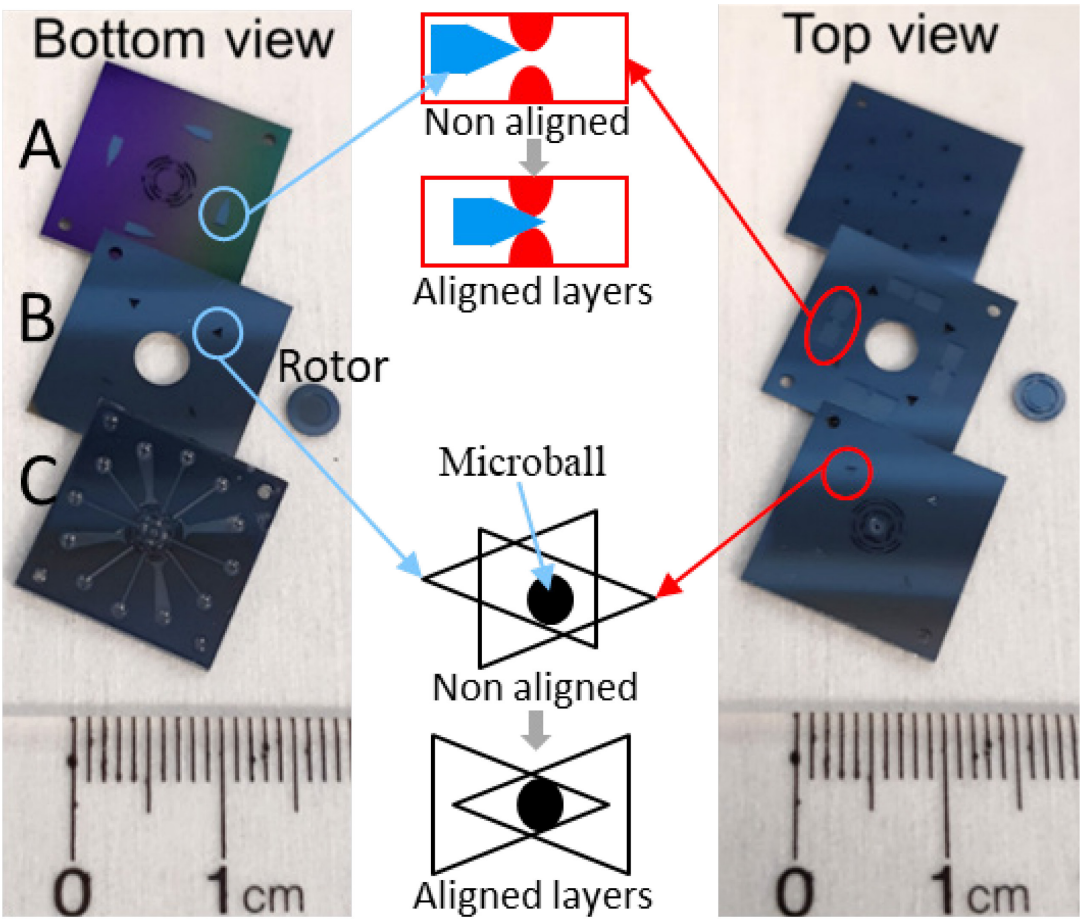

Figure 4-14 Die-level photograph showing top and bottom views of the three fabricated layers and the alignment methods.

Figure 4-15 Infrared photograph showing the quality of Si-Si direct bonding of layers A1-A2. After annealing of 2h at 1000°C.

Figure 4-16 shows (a) a SEM image of the cross section of the final assembled MEMS turbopump and (b) its equivalent schematic view. Main components of the micoturbopump are also shown in the figure (Fig. 4-16-c to h). The steam and water flow paths are illustrated with red and blue arrows respectively.

It is necessary to point out that there is no discernable bonding line between wafers A1 and A2. This proves once more the high bonding quality. This was required such that the dies can sustain the high-pressure flows within the device with good hermeticity. The rotor was successfully released as shown in Fig. 4-16c and Fig. 4-16f, without blade damage. Note that the turbine blades are the most fragile part of the microturbopump and can be easily damaged by an improper handling.

The thermal insulating strategies proposed here have been successfully implemented. Figure 4-16f shows the molded glass embedded into silicon, resulting in the hybrid Si/glass rotor. Due to the internal mechanical stresses, the thick oxide for the in-plane thermal insulation trenches was broken while cutting the stack for imaging. Hence, it is not viewed on the cross-section SEM image (Fig. 4-16d). However, a microscope image in Fig. 4-16e shows clearly the thick thermal oxide insulation.

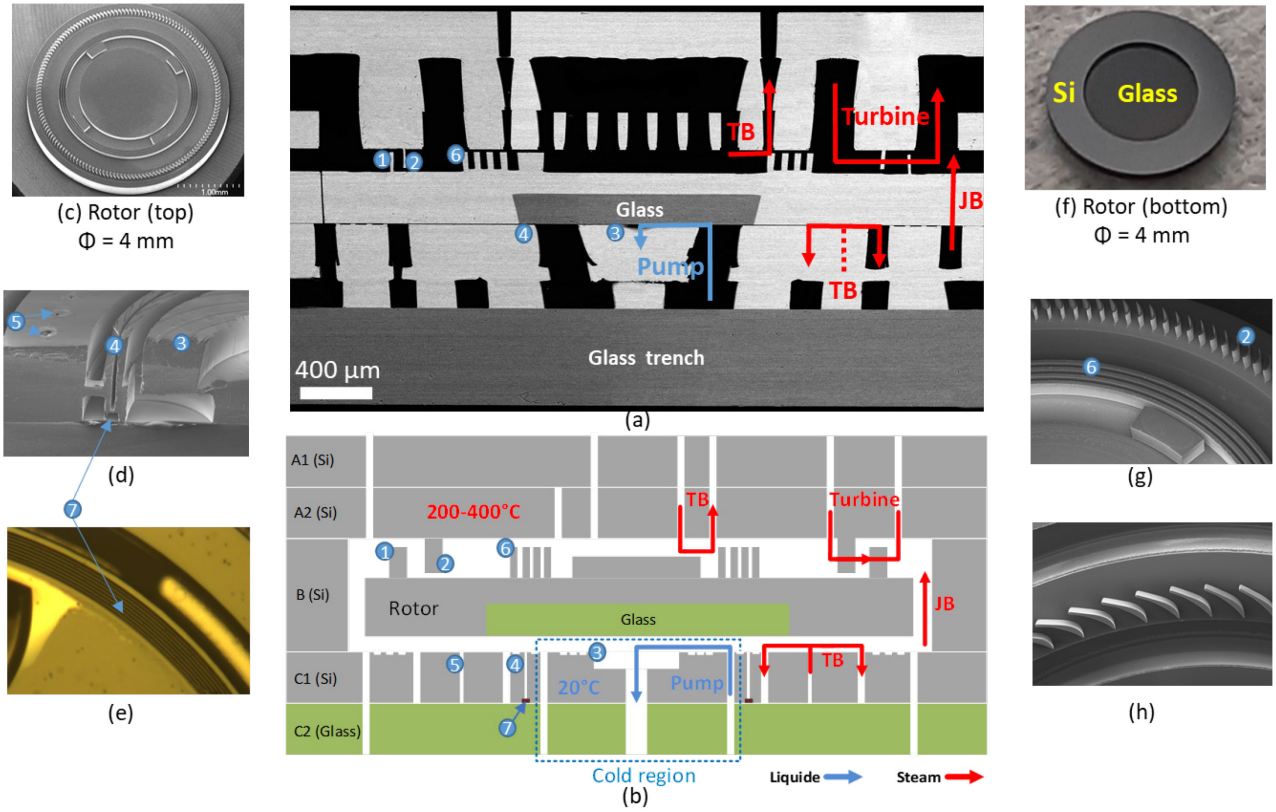

Figure 4-16 Complete fabricated microturbopump stack: a) SEM image of cross-section view (retouched by software to improve the clarity), b) Schematic cross-section view, c to h) Main device components. 1. Turbine blades 2. Stator blades 3. Pump 4. Pump seal 5. Thrust bearing orifices 6. Annular seal 7. Thick oxide insulating.

Planarity and profile of the bottom gap in the pump zone is defined by the glass polishing step. The resulting surface profile shows a slight depression of the glass surface on the bottom side of the rotor, reaching 1.2 µm in the center (Fig. 4-17). It was hard to achieve perfect planarity due to the dishing of the glass. It is useful to note that less than 200 nm dishing has however been achieved on a 15 mm square chip. Further optimization for polishing of 4-inch wafers is required if less dishing is needed. Consequently, the operation gaps of the pump and the pump seal will change. The nominal operation gaps of the pump and the pump seal change from 0.5 to ~ 1.5 µm and from 0.5 to ~ 1 µm (average values) respectively. Such change in the pump operation gap will be accounted for when comparing the experimental results to model predictions in Part II. In future works, the pump will be designed considering the dishing gap.

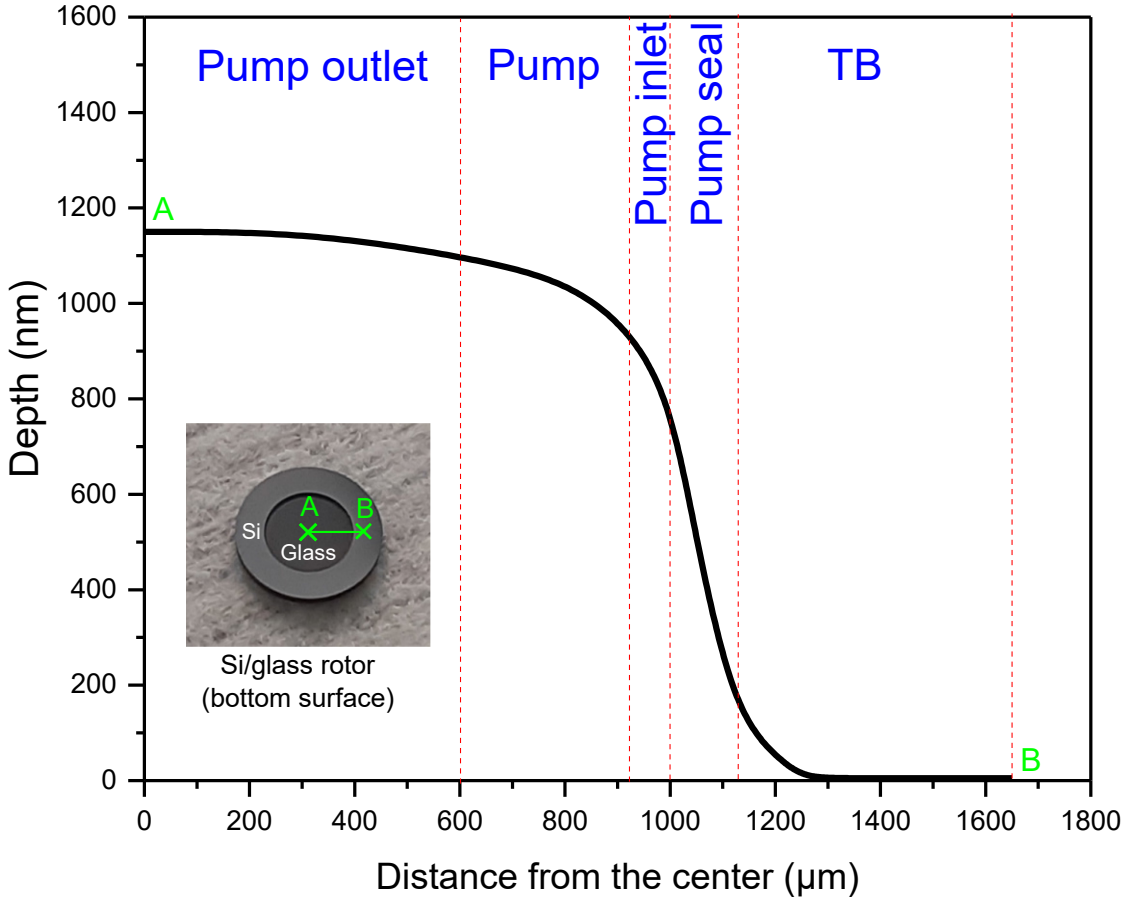

Figure 4-17 Rotor bottom surface scan profile of the molded glass region after CMP. The maximum dishing is about 1.2 μm.

4.8 Conclusion

A second generation MEMS turbopump with thermal insulation has been designed and successfully fabricated. The rotordynamic components have been designed considering power balance, stability of the rotor (force balance) and the ability to be microfabricated. Compared to the first generation designed to operate at ambient temperature, this second generation microturbopump has been designed for high temperature operation considering heat transfer management. The pump region has been designed to be completely thermally isolated to prevent undesirable boiling of water or vapor condensation during high temperature operation. Furthermore, design of the rotordynamic components has been improved in terms of axial and radial stability control (thrust and journal bearings).

The fabrication process flow has been developed and demonstrated. It consists of a five-wafer stack with the following processes:

- 19 lithographic masks
- 14 DRIE steps
- 11 RIE steps
- Si-Si fusion bonding
- Si-glass anodic bonding
- Glass micromolding and CMP

Two thermal insulating strategies have been developed and successfully implemented to insulate the pump. To prevent conduction from the hot turbine flow, a thick embedded glass was molded into the rotor. To prevent radial conduction from the thrust bearing, a thick oxide has been formed by oxidizing an array of silicon trenches. Complete MEMS turbopump devices have been fabricated, allowing experimental demonstration at high temperature, as will be reported in the Part II of this two-part paper.

Acknowledgment

The authors would like to thank Gholamreza Mirshekari for his development of fabrication methods, Srikar Vengallatore for guidance on the mechanical and materials aspects, Marie-Josée Gour and Paul Gond-Charton for microfabrication discussions, Étienne Léveillé and Marc-André Hachey for laser etch discussions, Guillaume Beaudin for his technical support on the infrared imaging camera and Émilie Fréchette for graphic art support. Funding support from the Canada Research Chair Program, NSERC, Canadian Foundation for Innovation (CFI), KACST and GM Canada is gracefully acknowledged.

4.9 Appendix

Plasma Etching recipes

DRIE is performed in a multiplexed ICP chamber using the Bosch process (STS-ASE tool). RIE is performed in a STS-AOE tool. Two DRIE and one RIE recipes have been developed and used in this work as described in Table 4-8. The etch rate of the RIE recipe is about 350 nm/min. Both DRIE recipes were characterized and presented in Fig. 4-18. Note that the aspect-ratio is calculated based on the mask opening width.

Table 4-8 Plasma etching recipes.

Recipe	DRIE1		DRIE2		RIE
	Pass	Etch	Pass	Etch	-
SF_6 (sccm)	0	130	0	130	-
C_4F_8 (sccm)	85	0	85	0	-
O_2 (sccm)	0	13	0	13	-
CF_4 (sccm)	-		-		20
Coil power (W)	600	600	600	800	600
Platen power (W)	0	18	2	13	300
Pressure (mTorr)	16	30	16	29	-
Cycle time (s)	7	13	7	12	-
Bias frequency (MHz)	13.56		0.38		13.56
Chiller temperature (°C)	20		20		0

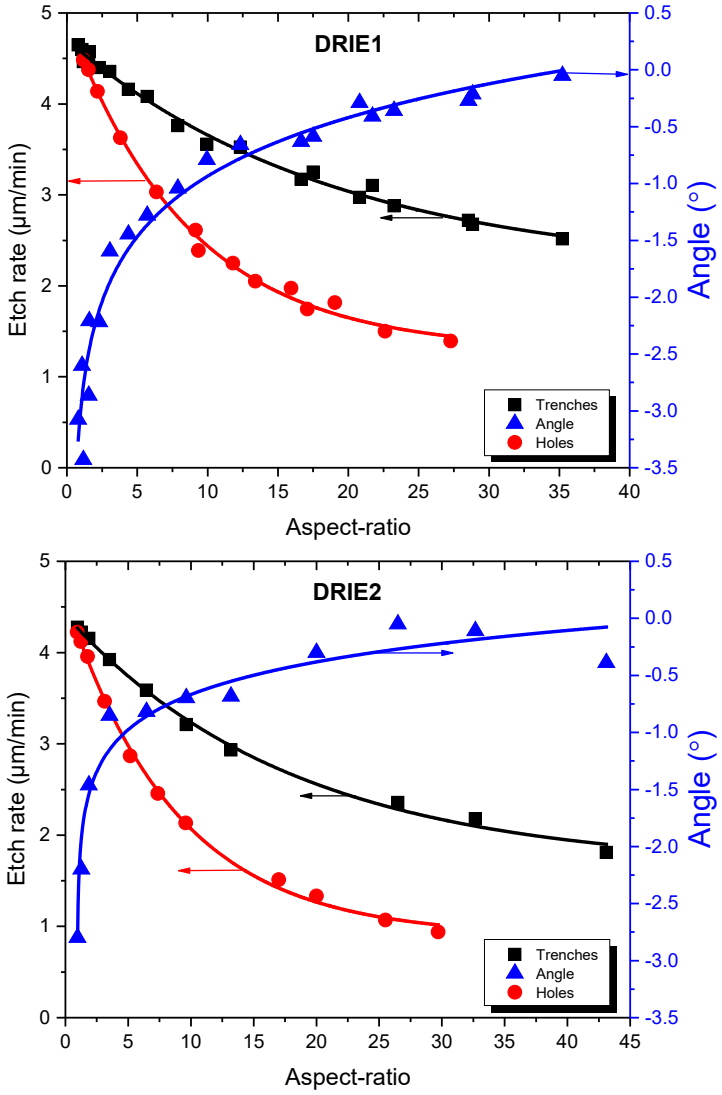

Figure 4-18 DRIE recipes characterization.

5 A MEMS TURBOPUMP FOR HIGH TEMPERATURE RANKINE MICRO HEAT ENGINES – PART II: EXPERIMENTAL DEMONSTRATION

5.1 Avant-propos

Auteurs et affiliation :

Amrid Amnache : étudiant au doctorat, Université de Sherbrooke, Faculté de génie, Département de génie mécanique.
Mokhtar Liamini : PhD, École de Technologie Supérieure, Montréal.
Félix Gauthier : M. Sc. A., ing. jr., Pratt & Whitney Canada
Philippe Beauchesne-Martel : M. Sc. A., Pratt & Whitney Canada
Mohamed Omri : PhD, King Abdulaziz University
Luc Fréchette : professeur, Université de Sherbrooke, Faculté de génie, Département de génie mécanique.

Date d'acceptation : 28 avril 2020

Revue : IEEE *Journal of MicroElectroMechanical Systems* (JMEMS)

Titre français : Développement d'une turbopompe MEMS pour le micromoteur thermique de cycle Rankine – Partie II : démonstration expérimentale

Contribution de l'auteur :

La contribution de l'auteur dans cet article, en excluant l'encadrement du directeur de recherche, est estimée à 95 %.

L'auteur a contribué à :

- développer un banc d'essais spécifique à la caractérisation de la microturbopompe.
- caractériser la microturbopompe (turbine, pompe, paliers hydrostatiques).
- démontrer expérimentalement le fonctionnement à haute température.
- rédiger 100 % du contenu de l'article.

Contribution au document :

La contribution majeure de cet article est la démonstration expérimentale du fonctionnement à haute température de la microturbopompe. C'est l'objectif principal de cette thèse qui est atteint. Le travail effectué dans cet article démontre le succès des stratégies d'isolation thermique intégrées dans la microturbopompe. Ces travaux ont permis de démontrer pour la première fois le fonctionnement d'une turbopompe MEMS à haute température. Les techniques d'isolation

thermique développées et démontrées dans ce travail pourraient être utilisées dans une large gamme d'applications MEMS.

Résumé français :

Cet article présente la démonstration expérimentale et la caractérisation d'une turbopompe MEMS avec isolation thermique intégrée pour un fonctionnement à haute température. Tout d'abord, les paliers hydrodynamiques, la turbine et le fonctionnement de la pompe sont caractérisés, jusqu'à une vitesse de rotation de 100 kRPM. La turbine a fourni 0.16 W de puissance mécanique et la pompe a pompé un débit d'eau de 2,55 mg/s. Ensuite, le fonctionnement de la microturbopompe à haute température est démontré. Une comparaison a été faite en utilisant un rotor non isolé thermiquement pour prouver l'efficacité des stratégies d'isolation thermique. La turbopompe MEMS isolée a été démontrée à une température de 160°C du côté turbine sans aucun signe d'instabilité ou d'évaporation de l'eau dans la pompe. Avec une analyse de prédiction, la microturbopompe pourrait fonctionner jusqu'à une température de 400°C dans la turbine.

5.2 Abstract

This paper presents the experimental demonstration and characterization of a MEMS turbopump with thermal insulation for high temperature operation. The fabrication and design were presented in the first part of this two-part paper. The device consists of a five-wafer stack enclosing a hybrid silicon-glass rotor supported by fluid film bearings, manufactured using MEMS fabrication methods. The rotor consists of a 4 mm diameter disk with microturbine blades on one side and a spiral groove viscous pump on the other side. First, the bearings, turbine and pump operation are characterised, up to a rotational speed of 100 kRPM. The turbine provided 0.16 W of mechanical power and the pump flow rate was above 2.55 mg/s. Then, the first demonstration of a MEMS turbopump operating at elevated temperatures was accomplished. Comparison was made with a non-insulated rotor to prove the effectiveness of the thermal insulation strategies. The insulated MEMS turbopump was demonstrated at 160°C on the turbine side without boiling water on the pump side. The maximum turbine flow temperature that prevents boiling in the pump is predicted to be 400°C. This work therefore enables the implementation of efficient and high-power density power plants-on-a-chip for a wide range of waste heat recovery applications.

Index Terms—Power generation, Turbine, MEMS, Rankine, waste heat, Thermal insulation, micropump.

NOMENCLATURE

g	Clearance gap
h_2	Clearance pump gap
k	Specific heat ratio
l	Journal bearing length
M	Mach number
P	Pressure
Q	Volumetric flow rate
Re	Reynolds number
r	Radius
T	Torque
W	Power
Y	Pressure loss coefficient
ΔP	Pressure difference
η_{is}	Isentropic efficiency
μ	Viscosity
ω	Rotational speed
Subscripts	
0	Stagnation
1	Turbine inlet
2	Turbine outlet
ext	External
int	Internal
is	Isentropic process

JB	Journal bearing
p	Pump
p-seal	Pump seal
seal	Annular seal
seal-top	Top annular seal
seal-bot	Bottom annular seal
T	Turbine
TB-top	Top thrust bearing
TB-bot	Bottom thrust bearing

5.3 Introduction

The concept of MEMS-based heat engines for power generation down to the 1-100W scale would offer an alternative to batteries in addressing the need for compact and distributed power. They are manufactured using silicon microfabrication technology (batch manufacturing), which makes this concept an economically viable solution. Since it was proposed by Epstein and Senturia [4], many research groups have attempted to develop micro heat engines with a variety of approaches. From the mid-1990 to the late 2000's, the MIT gas turbine group has focused into developing a micro gas turbine (Brayton cycle) [6,22]. It has been operated at rotational speed greater than 1 MRPM producing 5 W of mechanical power and achieves a power density greater than 4 MW/m3 [6]. However, the high operation temperature of this technology (1200-1600K) combined with scaling laws (surface to volume ratio) render the heat management within this device challenging. Performance levels at high temperature operation are limited to date by the compressor efficiency due to the high heat transfer from the turbine to the compressor [66]. This technology hence requires a performing thermal insulation solution using materials that can withstand high temperatures. Other high-power density micro heat engines have been advanced, including micro Wankel engines [8,9] and two-stroke Otto's cycle [10]. To date, these devices have not achieved the efficiencies of their large-scale counterparts due to some adverse effects inherent to miniaturization. For example, the low Reynolds numbers that is proportional to size results in high friction losses, reducing the efficiency. To their advantage, they have shown high power density. All the devices described above are driven by an internal combustion heat source, which requires a clean and efficient conversion of fuel into electrical power. Micro heat engines driven by external heat sources have been also investigated. The P^3 micro heat engine has been developed in Washington State University [11]. Thermal power produced from an external heat source is converted to mechanical power (oscillation) through liquid-gas phase change of a working fluid. A piezoelectric converter is used to convert the mechanical power to electrical power. Using a

similar working principle, other micro heat engines have been reported [12,13]. A unique micro heat engine based on self-induced oscillations of a heated liquid piston has been fabricated and tested at Université de Sherbrooke [14,15,16]. The self-oscillating fluidic heat engine (*SOFHE*) principle consists of a cyclic motion of liquid piston (by phase change) inside a tube that is exposed to a constant heat source on one side and a cold source on the other. Based on the Stirling cycle, a micro Stirling Cluster (*MISTIC*) for electrical power generation by waste heat harvesting has been validated at Université de Sherbrooke [17]. As an advantage, the above resonant micro heat engines operate with flexing components and low harvesting temperature. However, they have shown low power density compared to the internal combustion devices.

Compared to the Brayton micro gas turbine, the Rankine micro steam turbine concept combines low operation temperature (resulting in less complex thermal insulation) with the ability to operate with any heat source, while yielding similar power density and efficiency [19]. A MEMS turbopump required to implement the Rankine cycle has been fabricated and tested with air at room temperature [20,21]. This first generation MEMS turbopump made of silicon did not integrate thermal insulation as it was not meant to be operated at elevated temperatures. In real applications however, the device must be designed to operate with superheated steam in the turbine and bearings. Since boiling in the pump must be avoided, thermal insulation is required between the pump and the turbine/bearings.

Our work focused on the fabrication and demonstration of a second generation MEMS turbopump that implements the required thermal insulation for high temperature operation [43,42]. It incorporates also new and redesigned features based on enhanced models and knowledge acquired during experimentation with the first generation. Figure 5-1 shows photographs and SEM image of the complete second-generation MEMS turbopump with thermal insulation, fabricated successfully as detailed in Part I of this two-part paper. It consists of five-layer stack (four silicon wafers and one glass wafer) manufactured using silicon microfabrication technology to create three dies (static part, Fig. 5-1a) and a 4 mm diameter hybrid rotor (Si/glass, Fig 5-1b). Figure 5-1c shows the assembled stack of dies that form a complete microturbopump.

The aim of this work is to demonstrate the operation of the fabricated MEMS turbopump at elevated temperature. For this purpose, a test bench for experimental characterization is designed. It allows, first, the characterization of the thrust and journal bearings at room temperature. Secondly, we

report here the demonstration at high speed of the turbine and the viscous pump at room temperature. Finally, the operation of the prototype at high temperature while pumping water is presented, demonstrating the successful implementation of the insulation approaches and the first operation of a MEMS turbopump at elevated temperatures.

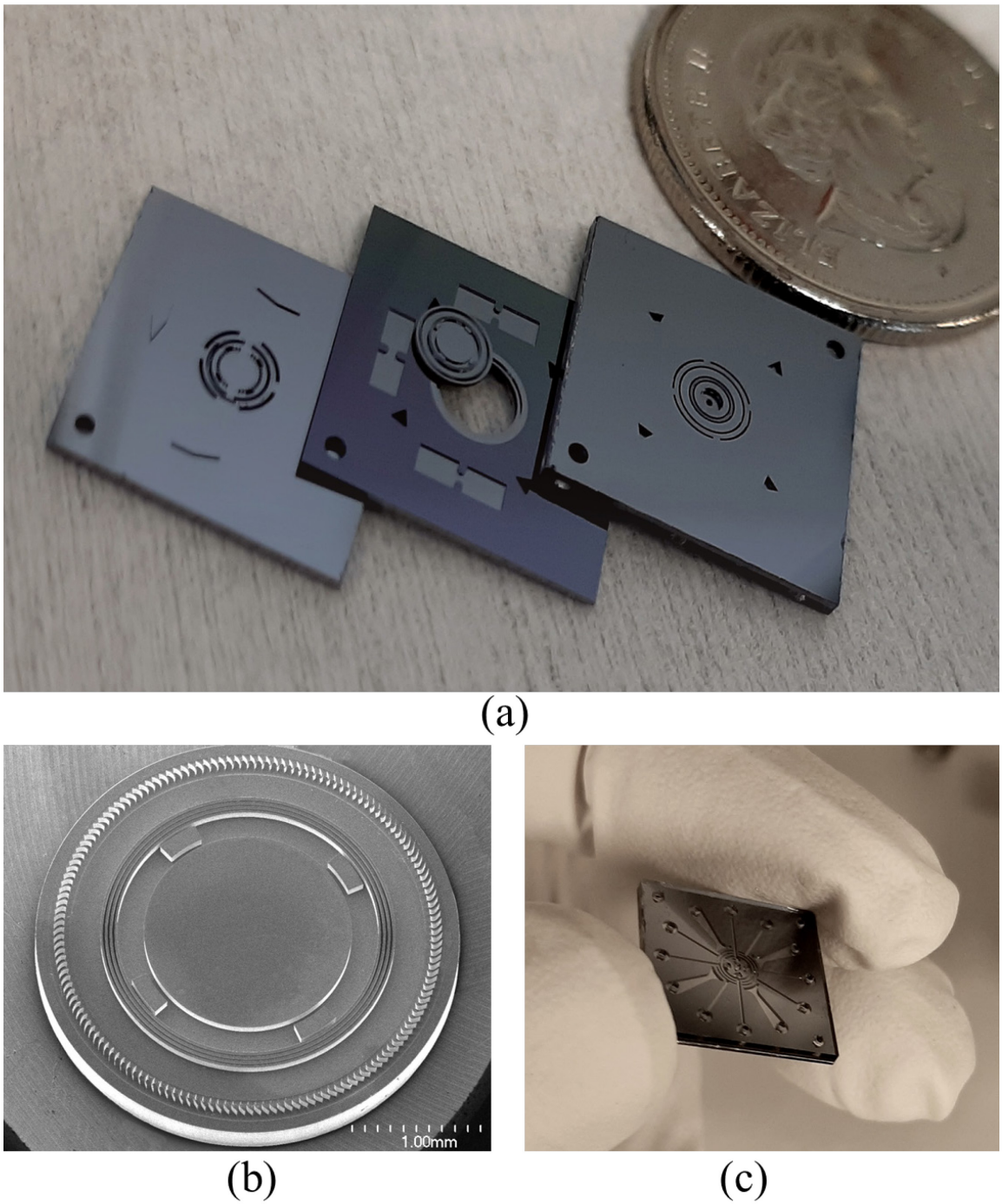

Figure 5-1 Photograph of the (a) three dies with rotor (from left to right: A, B and rotor, C), (b) SEM image, rotor top view, and (c) assembled MEMS turbopump device (bottom view).

5.4 Device Selection and Preparation

5.4.1 Thermal Insulation Evaluation

To evaluate the performance of the thermal insulation strategies, two versions of the microturbopump are tested in this work. Figure 5-2 shows SEM cross-section images of the two tested devices. Both of them include in-plane thermal insulation, radially around the pump. However, the first device has a Si-only rotor (conductive material, Fig. 5-2a), while the second device has a Si/glass hybrid rotor allowing for out-of-plane thermal insulation above the pump area (Fig. 5-2b). Table 5-1 summarizes the main geometric parameters of the two tested devices. Compared to the planned design geometry, there is a slight difference of the size of some features due to the tolerance in the microfabrication techniques used here.

5.4.2 Cleaning and Preparation

Before assembling, the dies and rotors are cleaned with solvents. Before assembling, the dies and rotors are cleaned with solvents (10 min immersion into acetone and isopropanol baths successively). Afterward, they are rinsed with water and dried with nitrogen. The rotors are carefully handled with plastic tweezers. In order to remove the infiltrated liquid into channels/trenches, the dies and rotors are placed into a vacuum chamber followed by a plasma O_2 cleaning to remove liquid traces. The plasma O_2 serves also to render the pump surface hydrophilic to prevent a prospective liquid blockage due to the high capillary forces.

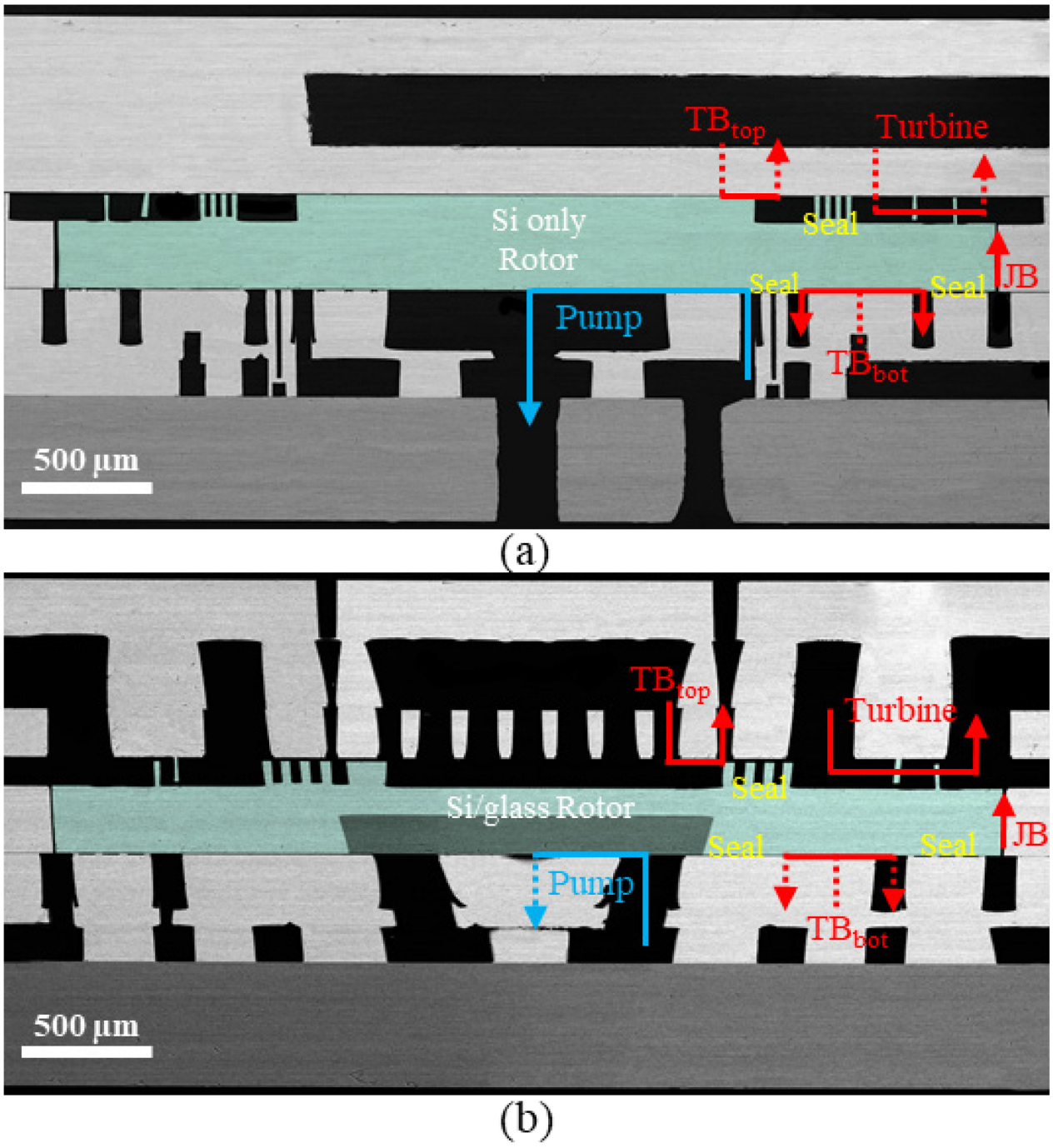

Figure 5-2 SEM cross-section view showing a) Microturbopump with Si rotor. b) Microturbopump with Si/glass rotor. Images are digitally retouched to improve clarity and colors. Legend: hot air and water flows are illustrated with red and blue arrows respectively. Dark grey is glass and light grey is silicon. The rotor is highlighted in green.

Table 5-1 Main dimensions of the fabricated microturbopumps.

	As initially designed	Fabricated Device 1 with Si only rotor	Fabricated Device 2 with Si/glass rotor
Top Thrust Bearing (TB_{top})			
Number of orifices	40	40	40
Length of orifices (μm)	200	200 +/- 1	200 +/- 1
Radial position of orifices (μm)	850	850	850
Outer radius (μm)	995	995	995
Operating gap range (μm)	1.0-2.0	1.0-3.8 +/- 0.2	1.0-2.0 +/- 0.2
Orifice diameter (μm)	13	13 +/- 1	13 +/- 1
Bottom Thrust Bearing (TB_{bot})			
Number of orifices	40	40	40
Length of orifices (μm)	200	200 +/- 2	200 +/- 2
Radial position of orifices (μm)	1425	1425	1425
Internal radius (μm)	1200	1200	1200
External radius (μm)	1650	1650	1650
Operating gap range (μm)	1.0-2.0	1.0-3.8 +/- 0.2	1.0-2.0 +/- 0.2
Orifice diameter (μm)	13	14 +/- 1	14 +/- 1
Journal Bearing (JB)			
Radius (μm)	2000	2000	2000
Gap (μm)	15	14.5 +/- 1	15 +/- 1
Length (μm)	300	287.5 +/-2	285.5 +/-2
Turbine			
Blade height (μm)	85	113 +/-2	115 +/-2
Chord length (μm)	109	108 +/-2	107 +/-2
Tip clearance (μm)	4.5	5.0-8.0 +/-0.2	5.0-5.5 +/-0.2
Stator			
Blade height (μm)	80	82 +/-2	82 +/-2
Chord length (μm)	185	185 +/-2	185 +/-2
Tip clearance (μm)	5	31 +/-2	33 +/-2
Pump			
Operating gap range (μm)	0-1.0	0-2.8 +/- 0.2	1.0-2.0 +/- 0.2
Grooves depth (μm)	4.5	4.5 +/- 0.2	4.5 +/- 0.2
Ratio (ridge/groove) width	0.3	3.08	3.08
Number of grooves	16	16	16
Ratio (inner/outer) diameter	0.65	0.65	0.65
Top annular seal			
Operating gap range (μm)	0-1.0	0-2.8 +/- 0.2	0-1.0 +/- 0.2
Grooves depth (μm)	85	90 +/-2	90 +/-2
Bottom annular seal			
Operating gap range (μm)	0-1.0	0-2.8 +/- 0.2	0-1.0 +/- 0.2
Grooves depth (μm)	4.5	4.5 +/- 0.2	4.5+/- 0.2
Pump seal			
Operating gap range (μm)	0-1.0	0-2.8 +/- 0.2	1.0-1.3 +/- 0.2
Grooves depth (μm)	4.5	4.5 +/- 0.2	4.5 +/- 0.2

5.5 Experimental Setup and Procedure

5.5.1 Assembly and Packaging

A packaging made of stainless steel was designed to connect the microturbopump to the tubing used for gas feeding and sensor measurements. It consists of two plates with piping (top and bottom) and a spacer having a square chamber in the center.

The spacer is aligned with the bottom plate using dowel pins and then the dies (A, B and C) and rotor are inserted into the chamber and aligned in-situ one by one using the microfabricated alignment structures on the dies, as explained in the first-part of this two-part paper (Fig. 5-3a). The top plate (Fig. 5-3b) is then aligned using the dowel pins and tightened on the top to completely encapsulate the microturbopump device. Fig. 5-3c shows a photograph of the package assembly.

Perfluoroelastomer O-rings for high temperature operation are used for sealing and to support the microturbopump device. The spacer is designed thicker than the microturbopump device to prevent contact between the package plates and the device after tightening the assembly. With that, the device is supported only with O-rings as illustrated in Fig. 5-3d. Thin Kapton shims are used to adjust the thickness when needed. The central portion of the bottom plate is used to feed and collect water from the pump. This region of the bottom plate is thermally isolated radially and cooled with an external water circuit as shown in Fig. 5-3c to control the pump water inlet temperature.

5.5.2 Experimental Setup

Figure 5-4 shows a schematic representation of the test setup used for the microturbopump characterization. Extra dry compressed air for turbine and bearings testing and water for pump testing were initially used as working fluids. The gas supplying subsystem provides compressed air to three subsystems: turbine, thrust bearings (top and bottom) and journal bearings (reservoirs 1 and 2). For each subsystem, three electrical heaters and three manual pressure regulators are used to control the flow temperatures and the pressures. The flows of the five microturbopump components (turbine, TB_{top}, TB_{bot}, and both sides of the journal bearing JB1 and JB2) are controlled by five mass flow controllers (MKS Instruments 1179A) and four solenoid valves (Hanbay MPA)

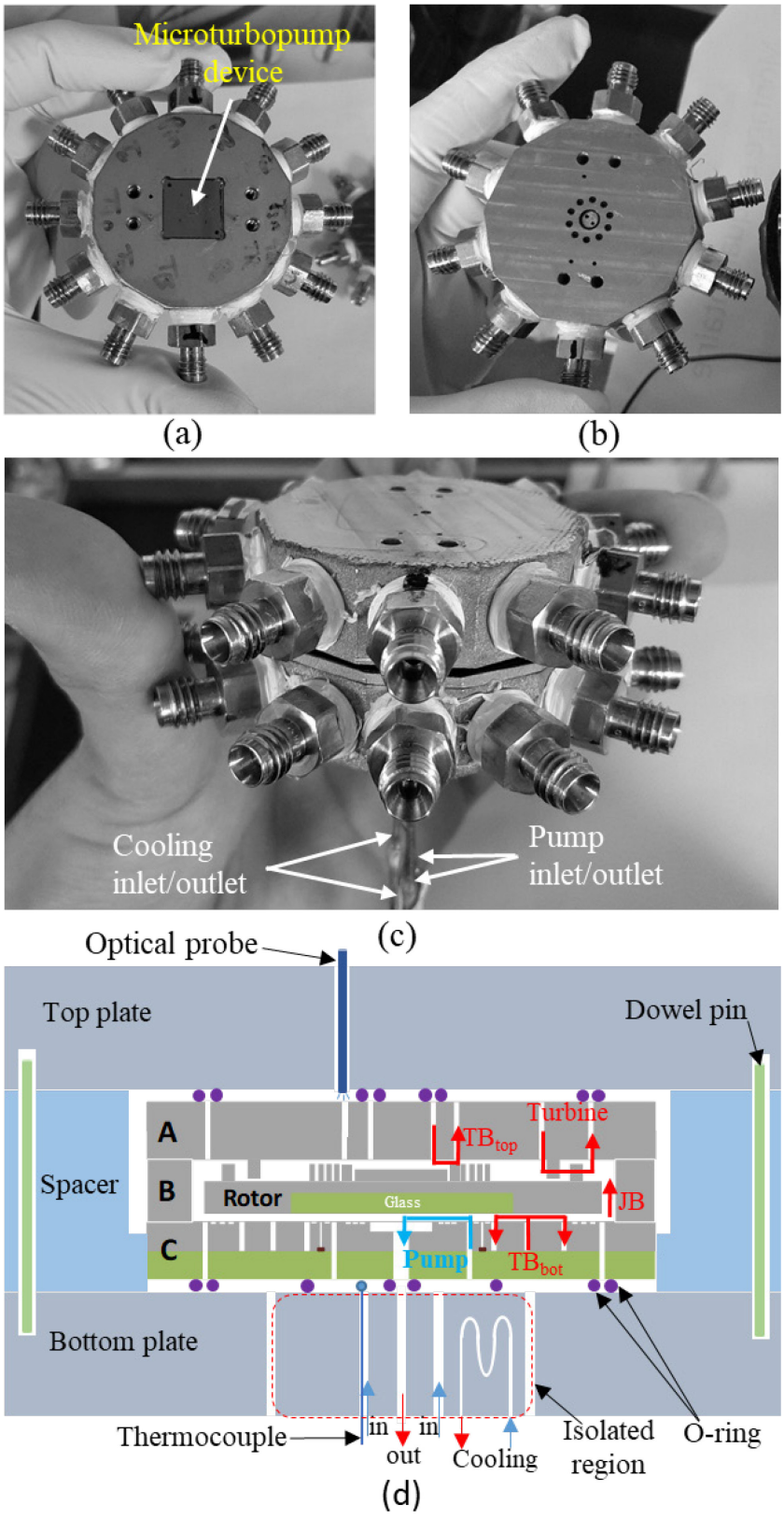

Figure 5-3 Microturbopump test packaging: (a) Bottom plate, (b) Top plate, (c) photograph of the package assembly, and (d) schematic of the package assembly.

for finer control. A multiplexed gas pressure sensor (Scanivalve Zoc17IP/8PX-APC) with eight inputs is used for pressure measurement. The liquid supply subsystem provides deionized water to the pump and to the packaging cooling system. For the pump, filtered water is simply supplied by gravity from a small water reservoir. A high-resolution liquid mass flowmeter (Sensirion ASL 1430-24, 0.3 ml/min) is used to measure the flow rate delivered by the pump. For the cooling system, the water is supplied from a pressurized water vessel. The gas subsystem and packaging are installed inside a heated enclosure to prevent convective cooling of the gas supply lines and the packaging, as shown in Fig. 5-5. A fan is installed inside the enclosure to create air recirculation for uniform temperature. Measurements are collected through a data acquisition and control system (NI CompactRIO-9074) that includes four modules (NI9213 temperature, NI9208 input current, 9205 input voltage and NI9264 output voltage). The system is implemented using Labview software and measurement data is displayed in real-time on the computer monitor.

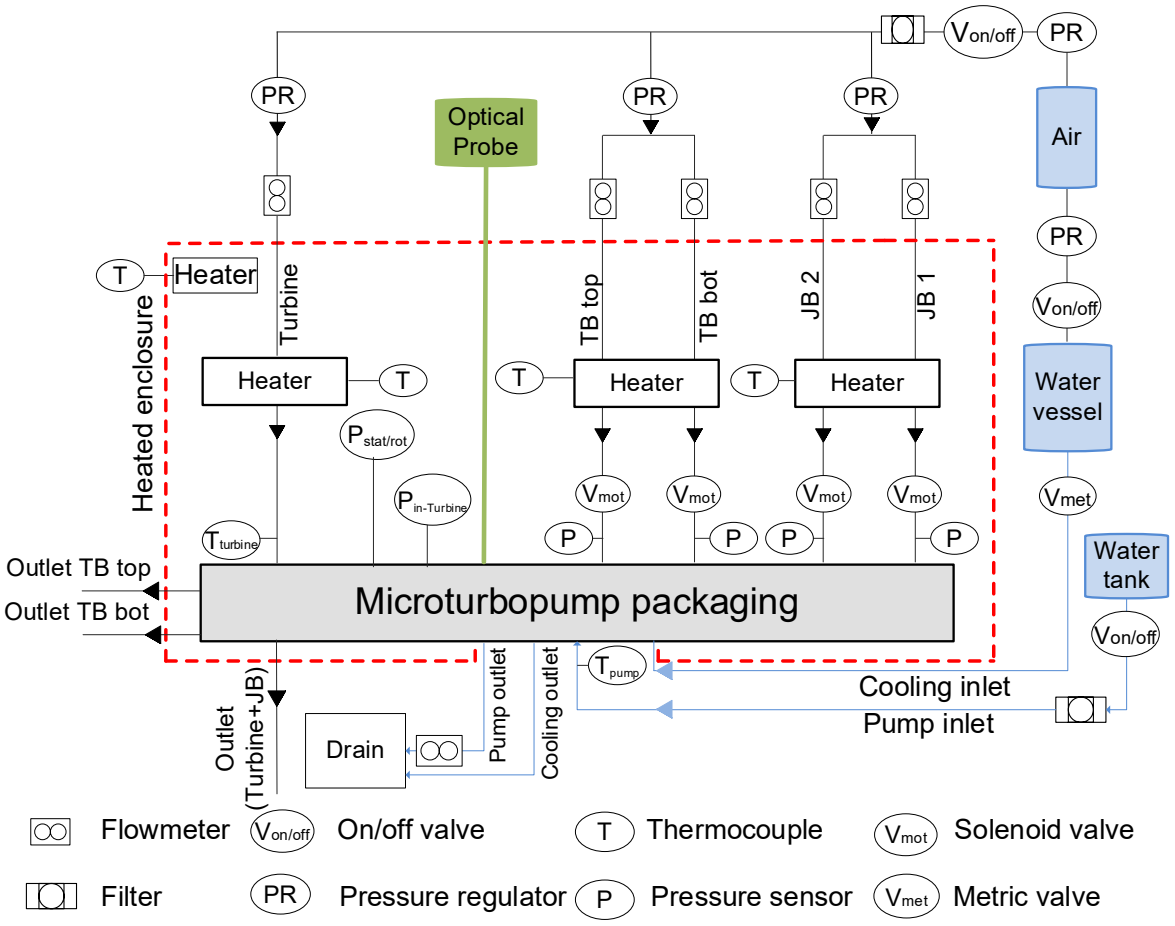

Figure 5-4 Schematic test setup used for characterization of the microturbopumps.

The rotational speed of the rotor is measured using an optical probe (Philtec RC20 DC-100 kHz). A tip diameter of 0.81 mm is inserted through the top packaging plate and leans on the top surface of the device where a through-hole was made (TB_{top} outlet) to detect the passing frequency of speed bumps on the rotor, as illustrated in Fig. 5-3d.

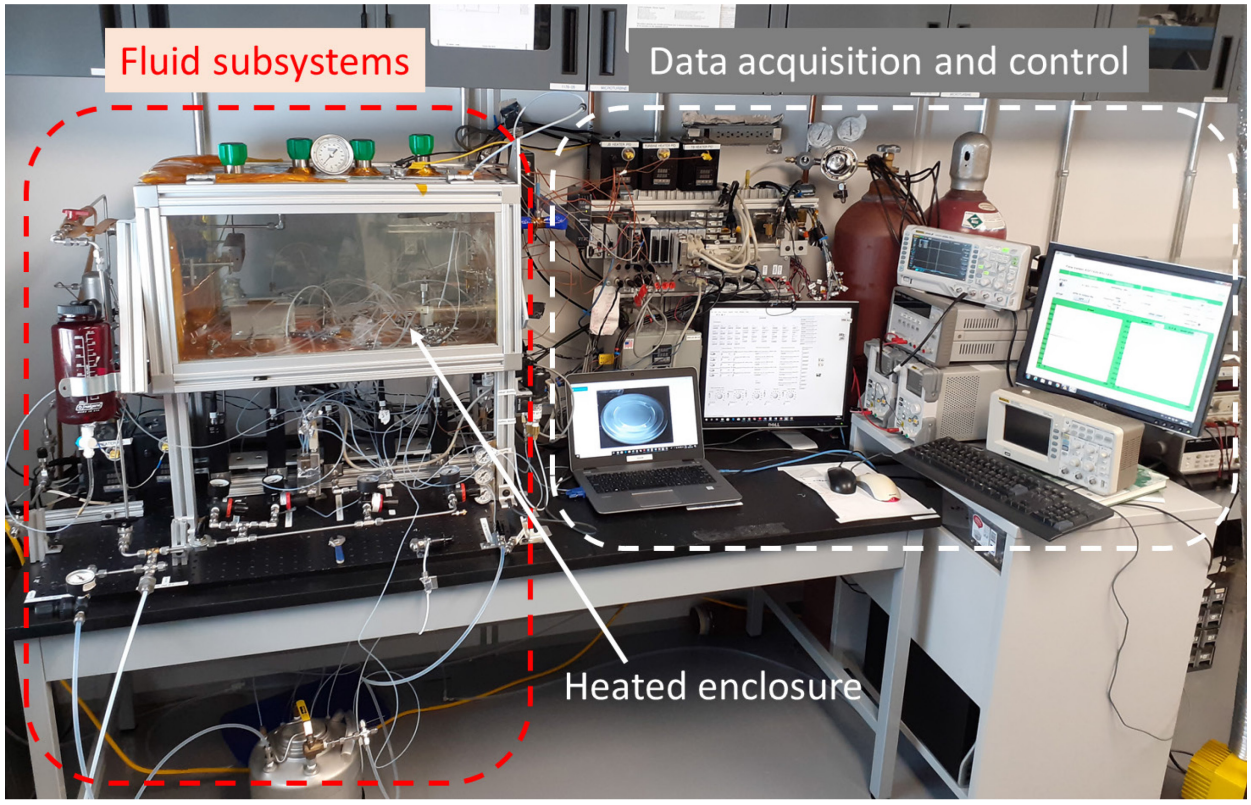

Figure 5-5 Photograph image showing the test bench for the microturbopumps characterization.

5.6 Experimental Results

All the elements are now in place to undertake the experimental characterization of the MEMS turbopump. Initially, the bearings are tested to determine the appropriate operating parameters to levitate the rotor. Once determined, the rotor is operated at high speed using pressurized air in the turbine. This allows the pump performance to be measured. Then, the tests are repeated with hot air this time in order to evaluate the capability to sustain high temperature flows in the turbine without boiling the liquid in the pump. Before testing, the pressure drop through the device and packaging feed channels is measured, so that the upstream and downstream pressure measurements can be corrected to provide the pressure at the entrance and exit of the component.

5.6.1 Cold air Component Characterization

Thrust Bearing Characterization

The thrust bearings (TB) provide axial balance of the rotor. The fabricated microturbopump has two TB's, one on the top and another on the bottom of the rotor. They consist of a circular array of micro orifices that supply pressurized gas to the clearance gap between the static part and the rotor. When operating the turbine in dynamic conditions, it is important to know the axial position of the rotor and prevent contact with the static part by adjusting the TB pressures. Since it is not practical to measure such small axial displacement of the rotor using the optical probe, we instead estimate its position by measuring the flow rate of a TB at a given applied pressure. For example, at a given TB_{bot} inlet pressure, when the rotor moves down, the clearance gap between the rotor and the static part decreases, resulting in high flow resistance. The TB_{bot} flow rate decreases as a consequence. Using this method, the flow rate behavior of the TB is considered as a rotor axial position sensor.

In this work, we used the TB_{bot} as our position sensor. Figure 5-6 shows the TB_{bot} characterization results in static conditions for both devices. They are characterized for various TB_{bot} inlet pressures. The TB_{bot} flow rate is measured by varying the TB_{top} pressure while maintaining a constant TB_{bot} pressure. At low TB_{top} pressure, the rotor is completely lifted leaning on the top static part. This represents the maximum TB_{bot} clearance gap that is geometrically known. By increasing the TB_{top} pressure, the load on the top of the rotor increases, moving the rotor down, which decreases the TB_{bot} flow rate. Note that a minimal applied pressure is necessary to start moving the rotor as clearly shown in Fig. 5-6. Similar behavior is observed for both devices. For the TB_{bot} pressures we tested it was not possible to achieve the lowest position of the rotor. Greater TB_{top} pressures are needed that are out of the capabilities of the test bench. This method allows the estimation of the rotor position and also indicates if the rotor is floating. The defined TB_{bot} gaps in Fig. 5-6 are calculated from power balance, as will be discussed next.

Journal Bearing Characterization

Before initiating the characterization of the JB, the TB's are supplied with air to float the rotor and axially balance it. The thrust bearing pressures $\{TB_{top}, TB_{bot}\}$ were {8, 6} bars for device 1 and {6, 8} bars for device 2. With these conditions, the rotor is floating as shown in Fig. 5-6. Floating the rotor is necessary before centering it in the radial direction once a pressure is supplied to the JB.

The turbine was however not supplied with air at this point. The pressure drop across the JB is measured

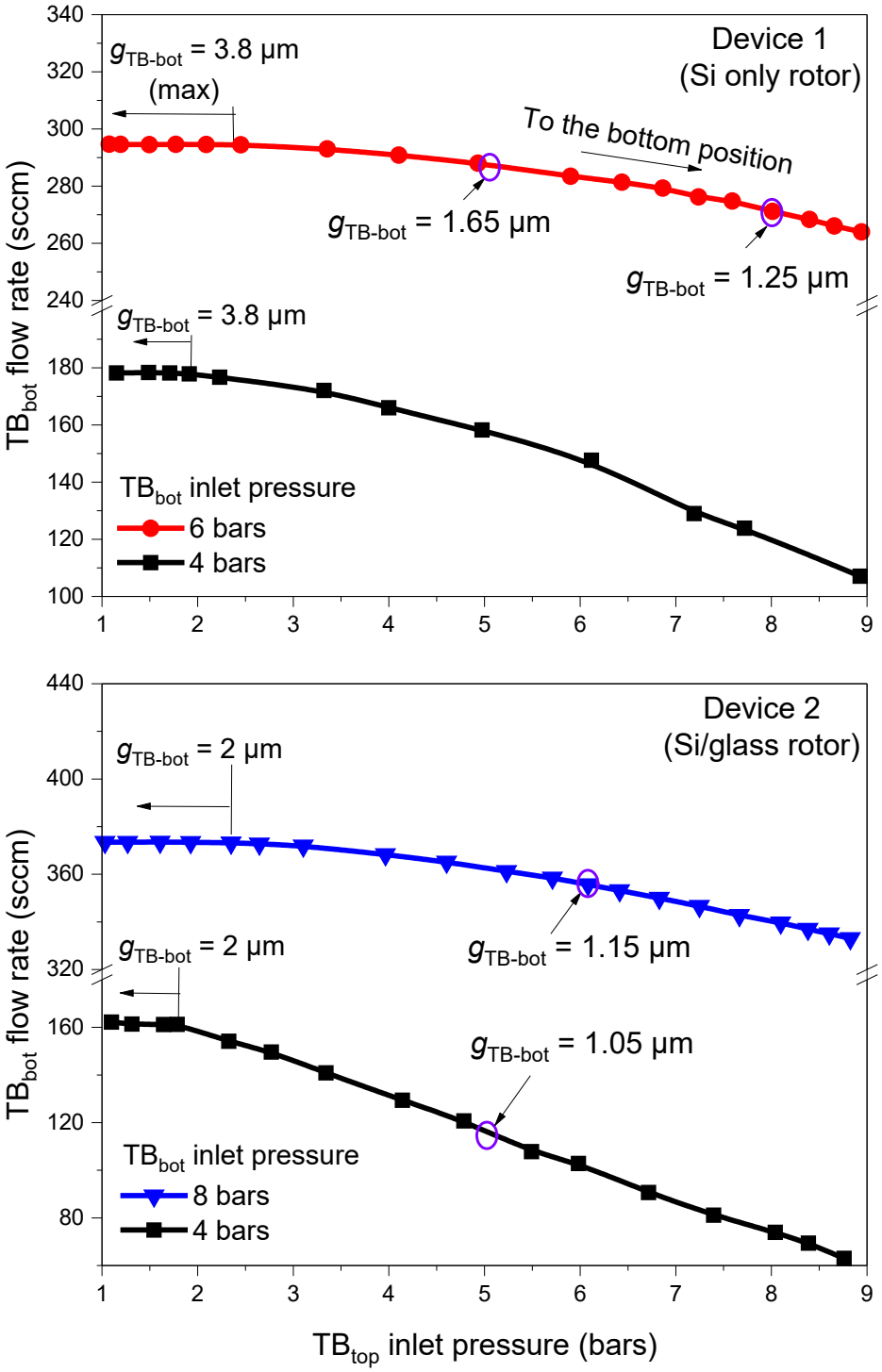

Figure 5-6 TB_{bot} flow rate plots with several inlet pressures, for device 1 (Si only rotor) and device 2 (Si/glass rotor). The measurement uncertainties are ±5 sccm and ±0.025 bar.

while varying the flow rate. Both sides of the journal bearing (JB1 and JB2) are supplied with a similar mass flow rate. When the JB is active, the rotor starts spinning within the range of 1-8 kRPM, even when the turbine is not supplied with air. The explanation is that a portion of the JB flow exits from the turbine inlet, crossing the turbine blades. Hence, the JB characterization was done in dynamic conditions. As reported by Lee *et al.* [21], the JB behavior was similar between static and dynamic conditions. Figure 5-7 shows the behavior of the measured pressure drop versus flow rate for both devices. The pressure drop increases linearly with the rise of the JB flow rate as observed. For a fixed flow rate, the pressure drop is similar for both sides of the JB (JB1 and JB2) revealing that the rotor is well centered. As shown in Fig. 5-7 both devices behave similarly, but at the same flow rate, the pressure drop for device 1 is slightly greater than in device 2. This is due to the difference in JB gap that is smaller for device 1 (see Table 5-1) causing more pressure drop.

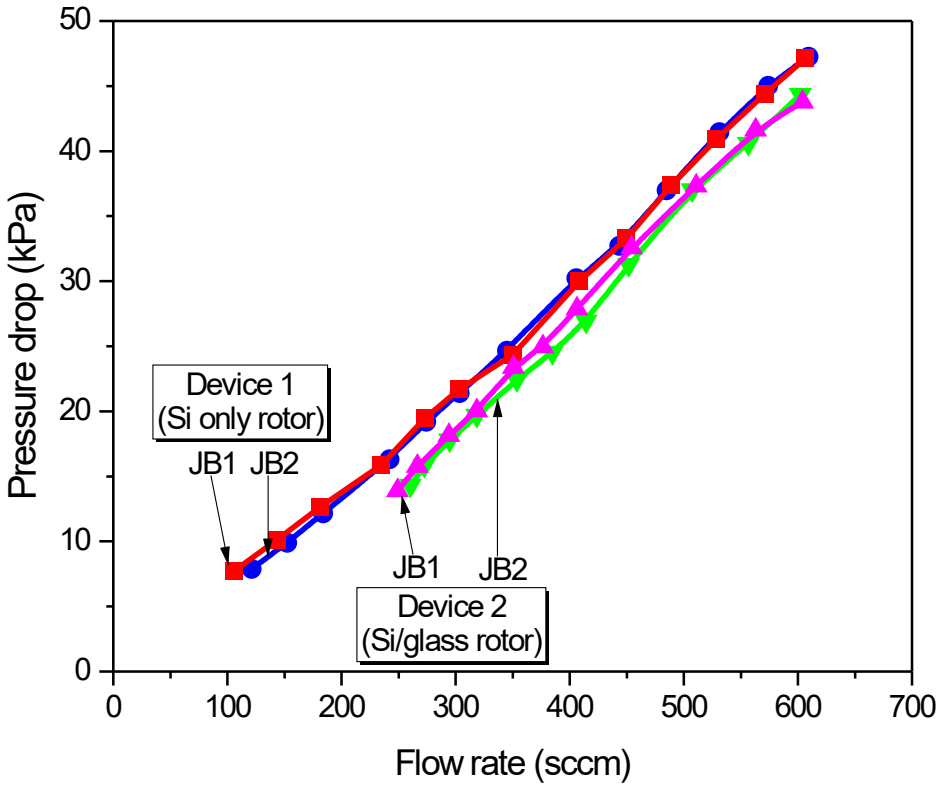

Figure 5-7 JB measured pressure drop as a function of flow rate, for devices 1 and 2. The measurement uncertainties are: ±1 kPa and ±50 sccm.

Turbine Operation Procedure and Performance

To start the rotation, we first position the rotor axially by fixing the pressures of the TB_{top} and TB_{bot} as explained in Thrust bearing characterization section. Afterwards, a constant flow rate is supplied to the JB (same flow rate for JB1 and JB2). Immediately, the rotor starts to spin. When pressure is

supplied to the turbine, the JB flow rate decreases since the turbine and JB have the same outlet, leading to a backpressure. The JB inlet pressure is then regulated to maintain a constant flow rate, while the turbine/JB outlet is maintained at atmospheric pressure.

The turbine is characterized by increasing its inlet pressure and measuring the rotational speed and pressure difference as a function of flow rate. Note that during this test no water is supplied to the pump. By increasing the turbine flow, the applied force on the turbine side increases, pushing the rotor towards the bottom position, diminishing the TB_{bot} flow rate. To lift the rotor, we decrease the TB_{top} pressure, which results reduces the total applied force on the top side and helps restore the rotor to its original axial position. The fixed operating conditions are presented in Table 5-2. The clearance gap of the components is estimated by power balance calculation as will be explained in the Cold air overall performance section.

Table 5-2 Operating conditions.

Parameter	Device 1	Device 2
TB_{bot} flow rate (sccm)	265	355
TB_{bot} pressure (bar)	6	8
JB1 flow rate (sccm)	425	460
JB2 flow rate (sccm)	420	455
TB_{top} gap (μm)	3.55	1.25
TB_{bot} gap (μm)	1.25	1.15
Pump gap (μm)	0.25	1.15
Pump seal gap (μm)	0.25	0.45
Top annular seal gap (μm)	2.55	0.85
Bottom annular seal gap (μm)	0.25	0.15

The rotational speed is plotted in Fig. 5-8 versus flow rate and in Fig. 5-9 versus pressure difference across the turbine. The rotational speed increases linearly as turbine flow rate increases. Both devices were run up to 100 kRPM. At a fixed flow rate, device 1 ran faster than device 2 as observed in Fig. 5-8. This is because device 2 ran with a smaller gap clearance in the bottom components than those for device 1 (see Table 5-1), resulting in more friction losses.

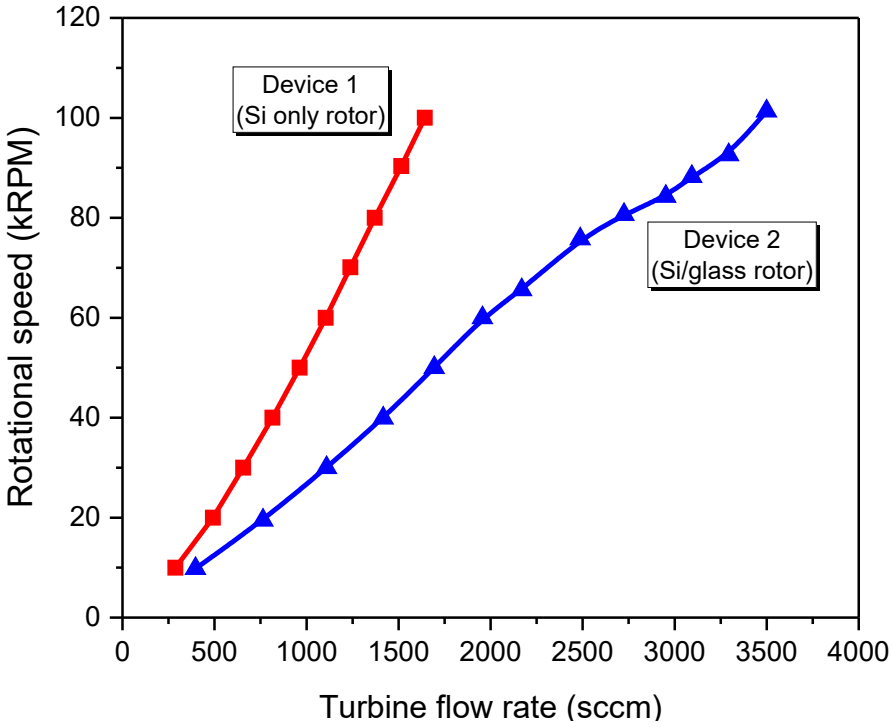

Figure 5-8 Rotational speed of the rotor as a function of the flow rate of the turbine for devices 1 (Si only rotor) and 2 (Si/glass rotor). The measurement uncertainties are: ±3 kRPM and ±200 sccm.

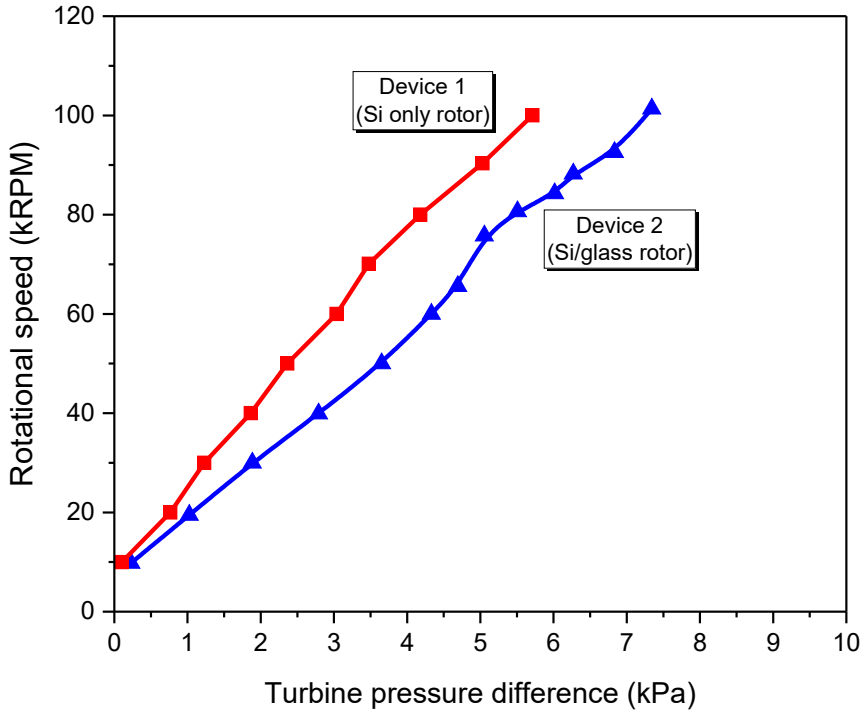

Figure 5-9 Rotational speed of the rotor as a function of pressure difference across the turbine for devices 1 (Si only rotor) and 2 (Si/glass rotor). The measurement uncertainties are: ±3 kRPM and ±1 kPa.

Pump Characterization

The viscous pump was characterized without pressurization (no pressure difference across the pump). Hence, the pump outlet was fully opened to ambient. The flowmeter installed at the outlet of the pump generates a negligible pressure drop (<200 Pa at full scale). First, the rotor is stabilized at a rotational speed of 10 kRPM with fixed operating conditions as summarized in Table 5-3. Water is introduced to the pump by gravity from a small reservoir. The water reservoir is slightly elevated above the pump level. When the rotational speed suddenly drops, it is a sign that water is entering the pump. Further, the TB_{bot} flow rate increases due to the elevation of the rotor (clearance gap increased). The additional force generated by the water flow in the pump causes this elevation. The clearance gap is then corrected to keep the initial conditions by increasing the TB_{top} pressure. Note that each time the rotational speed changes, the TB_{top} pressure is adjusted to keep the initial operation conditions. The obtained results are shown in Fig. 5-10 for both devices where the pump flow rate is measured as a function of rotational speed of the rotor. Unlike for device 1 that was ran up to 100 kRPM, we found difficulties to stabilize the rotor of device 2 at the same initial operation conditions for high rotational speed. In fact, the pump of device 2 is characterized up to a rotational speed of 50 kRPM. As detailed in Table 3, the operating conditions of device 2 show smaller seal operating gaps than for device 1 yielding in higher viscous dissipation at a given rotational speed. Increasing the rotational speed results in increasing even more the viscous dissipation, which limited the rotational speed for device 2 at 50 kRPM. As observed in Fig. 5-10, the flow rate is linearly proportional to the rotational speed. The maximum water flow rate achieved was 5.2 mg/s at 100 kRPM for device 1 and 2.55 mg/s at 50 kRPM for device 2. The obtained results agree with the prediction model developed by Lee *et al.* [20]. For device 2, the profile of the rotor bottom surface shows no effect in term of pumping performance, based on the mean gap.

Table 5-3 Operating conditions with pumping power.

Parameter	Device 1	Device 2
TB_{bot} flow rate (sccm)	280	100
TB_{bot} pressure (bar)	6	4
JB1 flow rate (sccm)	305	450
JB2 flow rate (sccm)	300	445
TB_{top} gap (µm)	3.15	1.95
TB_{bot} gap (µm)	1.65	1.05
Pump gap (µm)	0.65	1.1
Pump seal gap (µm)	0.65	0.35
Top annular seal gap (µm)	2.15	0.95
Bottom annular seal gap (µm)	0.65	0.05

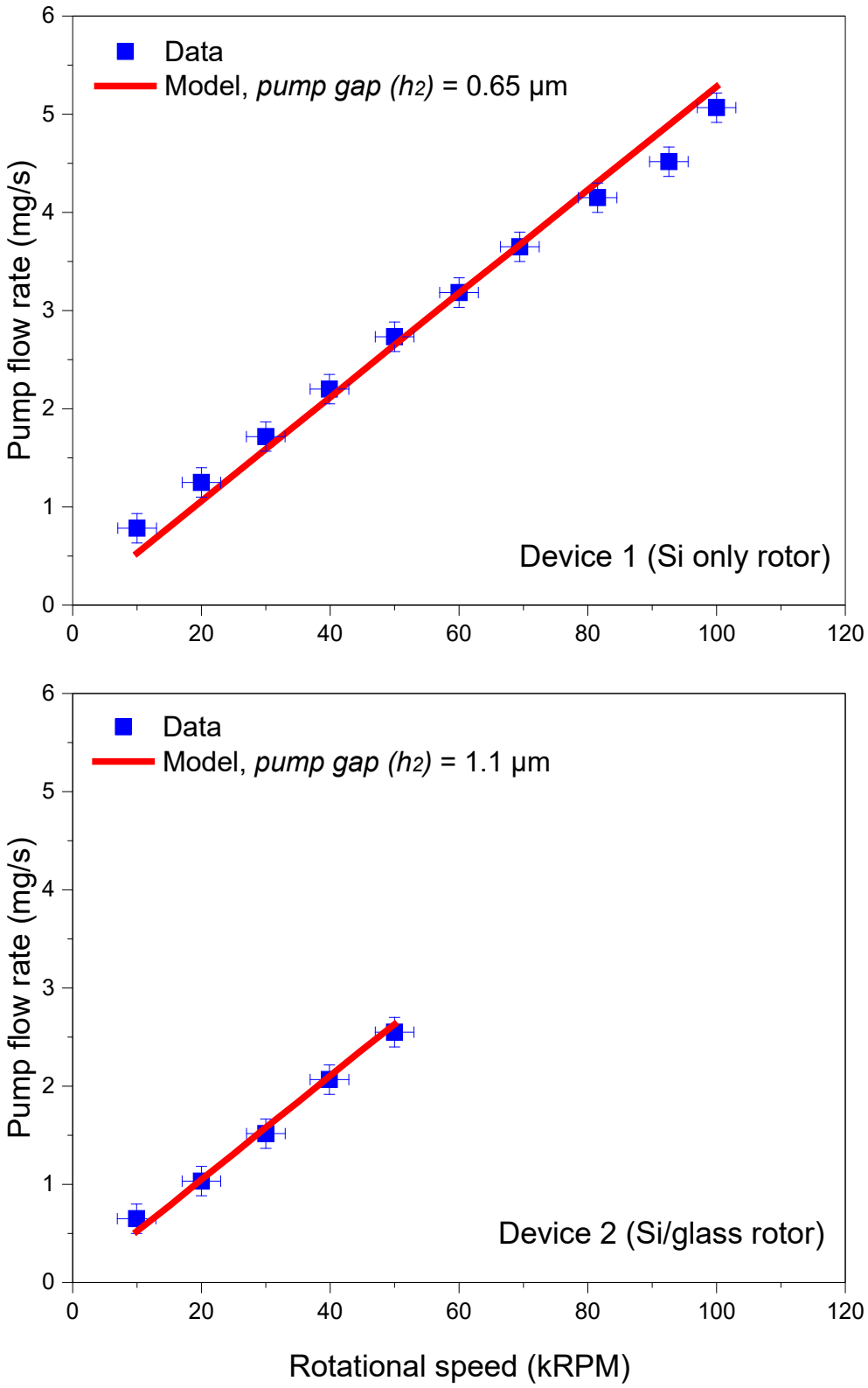

Figure 5-10 Viscous pump flow rate as a function of rotational speed.

5.6.2 Cold Air Overall Performance

In this section, we propose an approach to estimate the axial clearance gap of the TBs, seals and pump based on the power balance applied to the rotor.

Considering adiabatic evolution, the mechanical power, W_T, produced by the turbine can be estimated as:

$$W_T = \eta_{is}\, Q_T\, \Delta P_T \tag{5.1}$$

The produced mechanical power by the turbine is dissipated by viscous drag over the surfaces of the rotor disk. The power balance can be written as:

$$W_T = \left(W_{JB} + W_{TBtop} + W_{TBbot} + W_{Sealtop} + W_{Sealbot} + W_{p-Seal} + W_p \right) \tag{5.2}$$

where the TBs, JB and annular seal dissipation powers are modeled as a Couette flow in the clearance gap [20], and expressed as follows:

$$W_{TBtop} = \frac{\pi\mu\omega^2 (r_{ext}^4)}{2g_{TBtop}} \tag{5.3}$$

$$W_{TBbot} = \frac{\pi\mu\omega^2 (r_{ext}^4 - r_{int}^4)}{2g_{TBtop}} \tag{5.4}$$

$$W_{Sealtop} = \frac{\pi\mu\omega^2 \sum_i^n (r_{ext\,i}^4 - r_{int\,i}^4)}{2g_{Sealtop}} \tag{5.5}$$

$$W_{Sealbot} = \frac{\pi\mu\omega^2 \sum_i^n (r_{ext\,i}^4 - r_{int\,i}^4)}{2g_{Sealbot}} \tag{5.6}$$

$$W_{JB} = \frac{2\pi\mu\omega^2 l r_{JB}^3}{2g_{JB}} \tag{5.7}$$

The dissipated power in the pump and pump seal is calculated as:

$$W_p = T_p \times \omega \tag{5.8}$$

$$W_{p-seal} = T_{p-seal} \times \omega \tag{5.9}$$

where the torque, *T*, is calculated using the equation described in Part I of this two-part paper.

Pressure loss coefficient, *Y*, and isentropic efficiency of the turbine are defined as:

$$Y = \frac{P_{01} - P_{02}}{P_{02} - P_2} \tag{5.10}$$

$$\eta_{is} = \frac{h_{01} - h_2}{h_{01} - h_{2is}} \tag{5.11}$$

For compressible flow of an ideal gas, the isentropic efficiency can also be calculated as:

$$\eta_{is} = \frac{\frac{\frac{k-1}{2}M_2^2}{1+\frac{k-1}{2}M_2^2}}{1-\left(\frac{P_{01}}{P_2}\right)^{-\frac{k-1}{k}}} \tag{5.12}$$

Replacing Eq. 5.12 in Eq. 5.10, the relation between the isentropic efficiency and pressure loss coefficient is expressed as:

$$\eta_{is} = \frac{\frac{\frac{k-1}{2}M_2^2}{1+\frac{k-1}{2}M_2^2}}{1-\left((1+Y)\left(1+\frac{k-1}{2}M_2^2\right)^{\frac{k}{k-1}} - Y\right)^{-\frac{k-1}{k}}} \tag{5.13}$$

Omri *et al.* have performed 3D numerical simulations of the flow across the turbine blades and the pressure loss coefficient has been investigated [30]. From these CFD results, we have developed a correlation to calculate the pressure loss coefficient as a function of Reynolds number, expressed as:

$$Y = 14.9 \times Re^{-0.5} \tag{5.14}$$

The mechanical power produced by the turbine can then be plotted as a function of rotational speed for dry and wet pump conditions, as shown in Fig. 5-11. The power prediction is calculated using the right hand side of Eq. 5.2. The clearance gaps are chosen in order to satisfy the power balance of Eq. 5.2. From the plot, it is observed that the mechanical power increases quadratically as the rotational speed increases achieving 0.16 W for device 2 with a dry pump. At this point, the calculated isentropic efficiency is 52% (calculated by Eq. 5.13 where *Y* is calculated by Eq. 5.14) and *Re*=270. This is an acceptable efficiency for thermal energy harvesting, based on the Rankine power cycle analysis [19]. The efficiency could be enhanced at high-speed operation accompanied by higher Reynolds number. At a fixed rotational speed, the power produced is higher for device 2. This is because clearance gaps for the bottom and top of the annular seal, and the TB_{bot} are

smaller than for device 1 (see Tables 5-2 and 5-3). Around 45% of the total mechanical power produced by the turbine is consumed by these components.

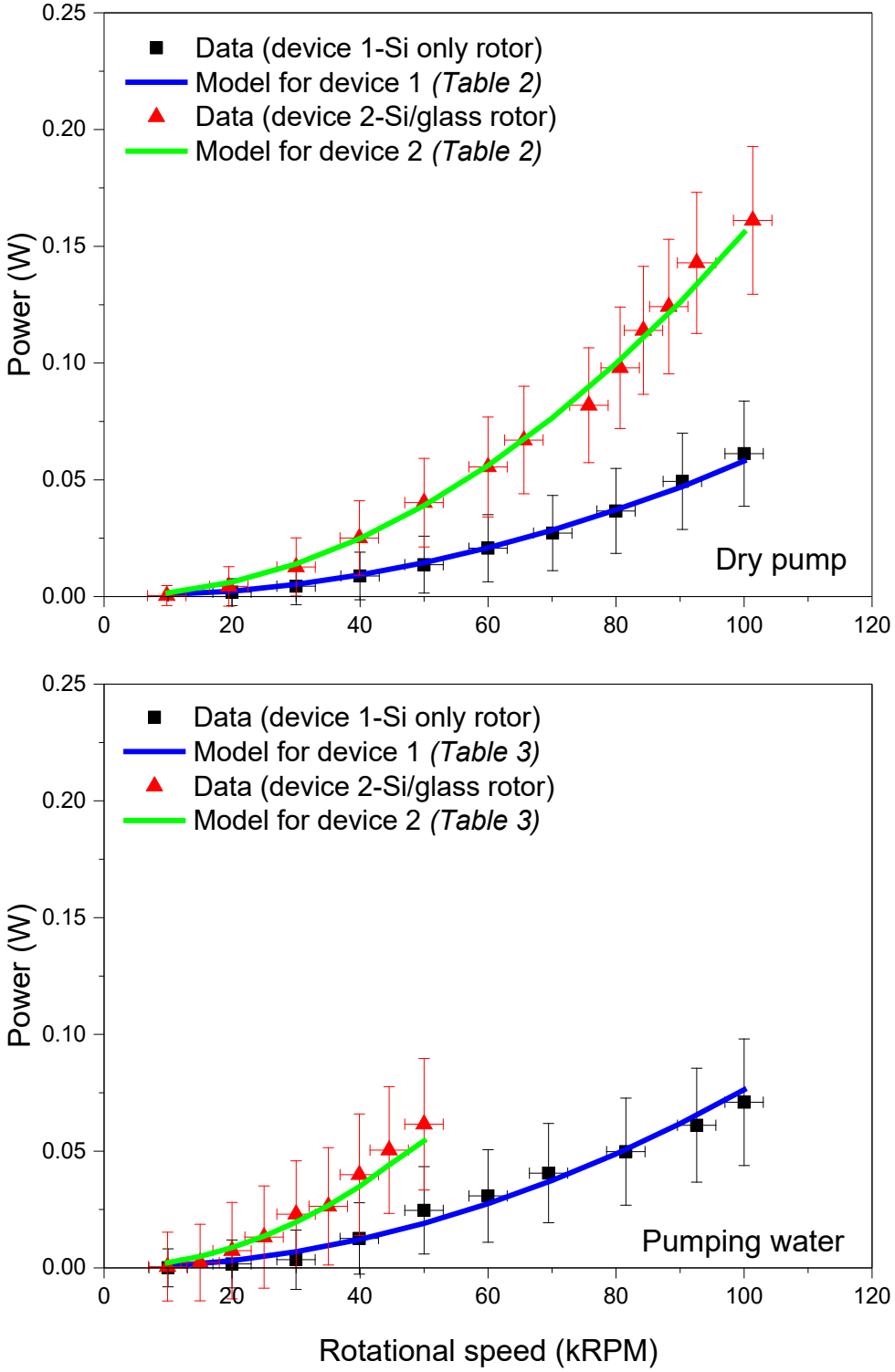

Figure 5-11 Mechanical power produced by the turbine as a function of rotational speed.

The plot in Fig. 5-11 shows good agreement between the model and experimental data. By this approach, all the clearance gaps used in the above analysis are calculated with an uncertainty of ±0.2 μm. Hence, this approach is validated by three elements. First, the pump clearance gap calculated by this approach for pump characterization shows good agreement with the prediction model (Fig. 5-10). Second, the calculated gaps are consistent if we compare them to the measured operating range (see Table 5-1). Third, the TB_{bot} clearance gaps calculated with this approach show consistent results with the thrust bearing flow-pressure relationship (section IV.A).

5.6.3 High Temperature Demonstration

All tests described above were performed at room temperature. This initial approach was adopted in order to first characterize the rotordynamic components in controlled conditions and validate the new configuration introduced in Part I. The microturbopump performance at high temperature was then explored. To evaluate the thermal insulation strategies, the pump behavior can be monitored. In fact, boiling in the pump may occur when the liquid temperature exceeds the saturation conditions. This would stop the pump operation. Furthermore, below boiling conditions, pumping performance is strongly affected by the liquid temperature in the pump, since its flow rate is inversely proportional to viscosity. As the temperature increases, water viscosity decreases, which would reduce the pump performance at fixed rotational speed and clearance gap. A change of the liquid density has a similar behavior but the variation with temperature is negligible compared to the viscosity variation. Performance of the thermal insulation can therefore be deduced by observing the pump flow rate as temperature is increased.

Devices 1 and 2 are ran at 100 and 30 kRPM respectively with same operation conditions as described in the *Pump Characterization* section. The flow rate at room temperature was 5.2 mg/s for device 1 and 1.5 mg/s for device 2. By increasing the temperature of the turbine and bearing flows, the pump flow rate was measured. The inlet temperature of water was held at approximately 20°C by controlling the cooling flow within the packaging, as illustrated in Fig. 5-3d. Note that the air flow rates of all the components changed with temperature. They were regulated in order to maintain the same operating pump clearance gap.

Figure 5-12 shows the pump normalized flow rate as a function of turbine temperature for both devices. The normalized flow rate is obtained by dividing the measured flow rate by the flow rate measured at room temperature, for ease of comparison.

For device 1, the flow rate drops as the temperature in the turbine is increased. This means that the temperature of the water in the pump increased. Using the pump model described in Part I, the pump flow rate is calculated by varying the water properties (viscosity and density) which are function of temperature (here assuming turbine temperature). The results are shown in Fig. 12 with a dark continuous line. It can be seen that the experimental behavior matches well with the model prediction assuming the water temperature being equal to the turbine flow temperature (low thermal insulation, as expected for the Si-only rotor used in device 1). Instabilities in operation started to appear as the turbine flow temperature went above 100°C. Fig. 12b shows the measured flow instabilities, compared with the stable flow measurement at low temperature shown in Fig. 12a. These instabilities come from rotor rotational speed fluctuations that were also observed during the tests, which are probably due to the water boiling in the pump. In fact, once water evaporates (dry pump situation), there is less friction in the pump, resulting in a temporary increase of the rotational speed. Once cold water enters the pump, it experiences higher rotational speed, resulting in a spike of flow rate, as can be seen in Fig. 12b. As the temperature is increased further, the pump operation suddenly fails, as seen above 135°C. The flow rate drastically decreased and became zero. As expected, heat transfer from the hot region to the pump has an impact on the operating performance. These results demonstrate that using Si-only rotor without thermal insulation has limited capabilities for high temperature operation.

Device 2 however has shown stable operation in the temperature range of 20-160°C as seen in Fig. 12. The maximum temperature was limited by the test bench capabilities, not by the device. We notice that the flow rate does not decrease as much as device 1 as the turbine flow temperature increases. When the turbine temperature reached 160°C, the water flow rate in the pump drops about 5%. Using the pump model, the temperature of the water in the pump is estimated at 60±10°C. This suggests that water in the pump with the hybrid Si-glass rotor (device 2) does not heat up as much as for the Si-only rotor (device 1), confirming the role of thermal insulation. The achieved maximum turbine temperature and the estimated temperature in the pump are in respect of the design operating point as described in Part I, which aims for a turbine inlet temperature of 175°C and a pump temperature well below its boiling point. This result shows that the thermal insulation approach adopted in this device works successfully, suggesting that the microturbopump could operate at high temperature.

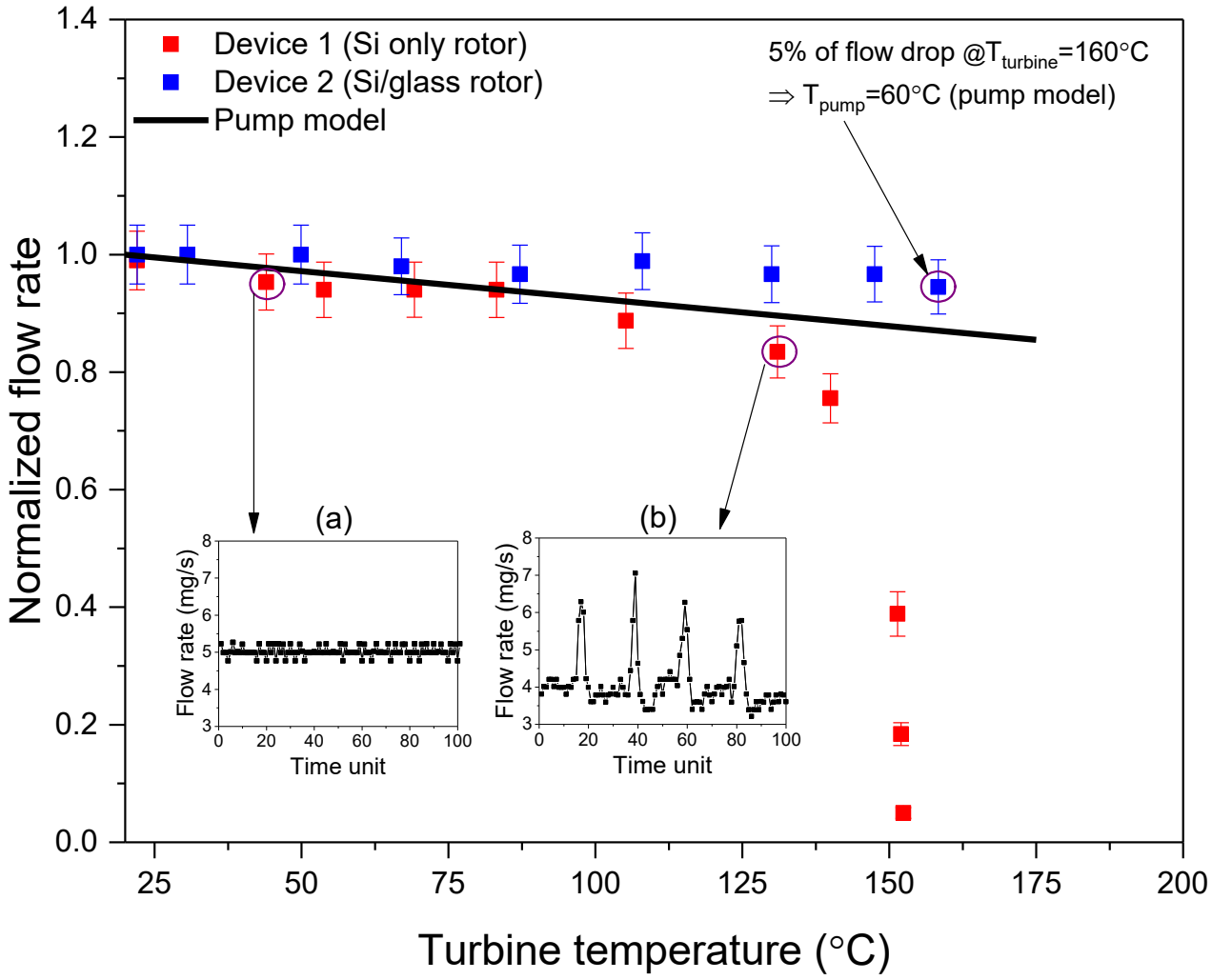

Figure 5-12 Normalized pump flow rate as a function of temperature in the turbine side. The flow rate is normalized by the flow rate at room temperature. The pump inlet temperature is kept at 20°C.

5.7 Conclusion

A second generation MEMS turbopump with thermal insulation has been successfully demonstrated and characterized with compressed air at both room and high temperature.

First, the improved device design was validated and experimentally characterised at room temperature. With a dry pump, the microturbine developed up to 0.16 W of mechanical power at an efficiency of 52% and a rotational speed of 100 kRPM. The viscous pump was characterised with atmospheric outlet pressure (no rise of pressure) up to a rotational speed up to 50 kRPM for a flow rate of 2.55 mg/s. Higher speeds could be obtained with further characterization of the axial and radial balance for optimal TB operating gaps. The analytical model of the viscous pump

developed by Lee *et al*. [20] has shown good agreement with the experimental data. Full characterization of the pump namely with back pressure will be addressed in future work. No signs of failure such as rotor crash during the tests were observed, demonstrating stable bearings operation and efficient sealing strategies.

The performance of the implemented thermal insulation approach has also been successfully evaluated by comparing a thermally insulated microturbopump with a non-insulated one. In fact, the insulated microturbopump (Si/glass rotor) has shown the ability to operate to up to 160°C in the turbine side while the non-insulated microturbopump (Si-only rotor) has shown instabilities at around 100°C and completely stopped to operate at around 135°C. These results demonstrate the success of the thermal insulation strategies developed in this work. The testing temperature was limited to 160°C by the test bench capabilities. Based on extrapolation, the microturbopump is predicted to operate until a temperature of 400°C on the turbine side before the pump flow reaches 100°C. This range meets the design requirements for a MEMS-based Rankine steam turbine for waste heat recovery for a broad range of applications.

This work succeeded in demonstrating for the first time the operation of a MEMS turbopump at elevated temperature. The thermal insulation techniques developed and demonstrated in this work could be utilized in a large range of MEMS applications.

The performance results of the microturbopump are encouraging, but additional investigations are required to further validate this concept for a viable power plant-on-a-chip. Further characterization with steam at higher temperature, representative of the Rankine cycle, are ongoing. The asymmetry of glass molding in the rotor could limit the high operating speed because of potential imbalance of the rotor. Experimental investigations to determine the maximum achievable speed will also be performed.

Acknowledgment

The authors would like to thank Étienne Léveillé, José Francisco Ambía Campos, Marie-Ève Paré, and Charles Sévigny for their contribution towards the experimental test setup and testing procedures, and Émilie Fréchette for graphic art support. Funding support from the Canada Research Chair Program, NSERC, Canadian Foundation for Innovation (CFI), KACST and GM Canada is gracefully acknowledged.

6 CONCLUSION

6.1 Synthèse

Le travail effectué dans cette thèse s'inscrit dans le projet du développement d'une microturbine à vapeur de cycle Rankine. Il s'agit de la fabrication et la démonstration expérimentale du fonctionnement d'une microturbopompe à haute température.

Le concept de la microturbopompe proposé par Liamini [23] a été modifié et optimisé dans cette thèse. Nous avons alors proposé une configuration originale en intégrant une isolation thermique localisée. La zone de la pompe a été conçue pour être complètement isolée thermiquement empêchant l'ébullition indésirable de l'eau dans la pompe et/ou la condensation de la vapeur dans le palier axial inférieur ou la turbine pendant le fonctionnement à haute température. Cette configuration est conçue en gardant les mêmes objectifs en terme de performances mécaniques (vitesse de rotation, stabilité axial et radial, pompage de l'eau) mais aussi, pour être réalisable en utilisant les méthodes de microfabrication.

Deux stratégies d'isolation thermiques ont été développées pour être intégrées dans la microturbopompe : *i*) empêcher la conduction de chaleur entre le palier axial inférieur et la pompe, un oxyde épais a été utilisé. Il est formé à partir d'une oxydation thermique d'une série de tranchées gravées dans le silicium. *ii*) empêcher la conduction de chaleur à travers le rotor entre les écoulements chauds de la turbine et la pompe, un verre borosilicaté moulé dans le rotor est utilisé. La technique de micromoulage de verre a été étudiée de façon exhaustive dans ce travail. Cette technique est aussi très utile pour fabriquer avec précision des structures en verre à haut rapport de forme comme détaillé dans le chapitre 2. Cette technique représente également une contribution importante pour le développement d'autres MEMS où l'utilisation du verre est souhaitée. C'est pour la première fois qu'un micromoulage de verre dans le silicium est démontré avec de hautes pressions environnantes lors du traitement thermique permettant ainsi la fabrication des structures à très hauts rapport de forme. Aussi, c'est pour la première fois que les limites du micromoulage sont définies permettant une utilisation optimale de cette technique.

Une turbopompe MEMS de deuxième génération fonctionnelle avec isolation thermique intégrée a été fabriquée avec succès. Le procédé de fabrication a été développé pour que la microturbopompe soit complètement fabriquée aux salles blanches (3IT.Nano) de l'Institut

Interdisciplinaire d'Innovation Technologique de l'Université de Sherbrooke. Il a fallu plus de 4000 heures de travail en salles blanches pour le développement des méthodes de microfabrication et la fabrication complète de la microturbopompe. La microturbopompe est composée d'un empilement de quatre gaufres de silicium et une gaufre de verre borosilicaté. Le procédé de microfabrication requiert sommairement :

- 19 masques lithographiques
- 14 étapes DRIE
- 11 étapes RIE
- Collage par fusion Si-Si
- Collage anodique Si-verre
- Micromoulage et polissage de verre

La microturbopompe fabriquée a été démontrée avec succès et caractérisée avec de l'air comprimé à la fois à température ambiante et à haute température. Tout d'abord, la microturbopompe avec isolation thermique intégrée a été validée et caractérisée expérimentalement à température ambiante. Avec une pompe sèche, la turbine a développé une puissance mécanique de 0.16 W avec un rendement isentropique de 52% et une vitesse de rotation de 100 kRPM. La pompe visqueuse a été caractérisée avec une pression atmosphérique à la sortie (pas de pressurisation) jusqu'à une vitesse de rotation de 50 kRPM pour un débit de 2.55 mg/s. Des vitesses plus élevées pourraient être obtenues avec une caractérisation plus poussée de l'équilibre axial et radial. Le modèle analytique de la pompe visqueuse [20] a montré une concordance avec les données expérimentales. La caractérisation complète de la pompe, notamment avec une pressurisation à la sortie, sera abordée dans les travaux futurs. Aucun signe de défaillance tel qu'un bris du rotor, lors des tests, n'a été observé, démontrant un fonctionnement stable des paliers et une efficacité des joints d'étanchéité.

L'approche d'isolation thermique mise en œuvre a également été évaluée en comparant une microturbopompe comprenant une isolation thermique avec une autre sans isolation thermique. En fait, la microturbopompe isolée (rotor : Si /verre) a montré sa capacité à fonctionner jusqu'à 160°C du côté de la turbine tandis que la microturbopompe non isolée (rotor : Si seulement) a montré des instabilités de fonctionnement à environ 100°C et complètement arrêter de fonctionner à environ 135°C. Ces résultats démontrent le succès des stratégies d'isolation thermique développées dans ce

travail. La température des essais était malheureusement limitée à 160°C par les capacités du banc d'essais. Ce qui a empêché de démontrer le fonctionnement jusqu'à 175°C qui représente la température du design de la microturbopompe. En utilisant le model de la pompe, il était possible de prédire la température de la pompe à 60 ± 10°C quand la température dans la turbine a atteint 160°C. Ce qui est très encouragent puisque la température de l'eau dans la pompe tel que la microturbopompe est conçue est de 70°C (voir Fig.2-4). Ce résultat démontre que la microturbopompe avec l'isolation fabriquée dans ce travail pourrait fonctionner à haute température pour implémenter le cycle Rankine sur puce.

6.2 Résumé des contributions

Pour la première fois, une microturbopompe pour un fonctionnement à haute température est fabriquée et caractérisée. Ce travail a apporté plusieurs contributions scientifiques, à la fois utiles pour la suite du développement du projet microturbine à vapeur et aussi pour la communauté scientifique des MEMS. Nous résumons ci-dessous ces contributions :

Microfabrication

- Une technique de micromoulage pour la fabrication des microstructures en verre à haut rapport de forme est développée et démontrée. Les conditions optimales pour l'utilisation de ce procédé ont été définies.
- Une méthode d'isolation thermique de la pompe en utilisant le verre et l'oxyde de silicium est développée.
- Un procédé de fabrication complet pour la fabrication d'une microturbopompe intégrant l'isolation thermique est défini.
- Les masques lithographiques utilisés (19) dans la fabrication sont conçus et fabriqués.
- Des recettes de gravures DRIE ont été développées et optimisées pour contrôler les paramètres de gravure.

Microturbine à vapeur et Power-MEMS

- L'efficacité de la méthode d'isolation utilisée dans ce travail est démontrée expérimentalement. Elle pourrait être utilisée dans une large gamme d'applications de *Powers-MEMS*.

- Le fonctionnement d'une pompe visqueuse à rainures en spirale est démontré pour la première fois avec une surface de verre. Les modèles de prédiction ont été validés avec les résultats expérimentaux.
- Un banc d'essai été conçu et installé spécialement pour cette caractérisation. Il est alimenté par trois sources de fluides (air, eau, vapeur). Des micro débitmètres fabriquées spécialement pour mesurer les faibles débits de vapeur à haute température sont incorporés [74,75]. Le banc de tests dispose aussi d'un système de refroidissement du *packaging* permettant de contrôler la température de l'entrée de la pompe. Il sera utilisé pour la caractérisation à la vapeur de la microturbopompe fabriquée dans ce travail et aussi pour la caractérisation future des microturbines à vapeur. Il peut être aussi très utile pour la caractérisation d'autres microsystèmes fluidiques.
- L'efficacité du joint d'étanchéité *Herringbone* utilisé pour éviter les fuites entre la pompe et le palier axial inférieure a été démontré par le bon fonctionnement de la pompe.
- Le rotor hybride (Si/verre) a été testé jusqu'à une vitesse de rotation de 100 kRPM de façon stable démontrant la précision ainsi le fonctionnement des paliers axial (*Thrust bearing*) et radial (*Journal bearing*).
- Une méthode de mesure des gaps de fonctionnement des composantes en utilisant l'équilibre des puissances est développée et vérifiée expérimentalement.
- Une méthode pour estimer la température de l'eau dans la pompe en utilisant les modèles analytiques a été présentée.

6.3 Leçons apprises

Au cours des étapes de fabrication et de caractérisation de la microturbopompe, nous avons rencontré quelques limitations qui n'étaient pas prévues. Il serait utile de les considérer dans les futurs designs et tests. Nous les citons ci-dessous :

- Effectuer une oxydation thermique d'une tranche de silicium qui présente des tranchés gravés limite le collage direct. En effet, l'oxydation thermique d'une gaufre structurée crée un rebord au niveau des coins supérieurs des tranchées qui empêchent mécaniquement le collage des gaufres.
- Le refroidissement de la zone d'entrée d'eau liquide dans le *packaging* est très important. Sans ce refroidissement, la température augmente et atteint la température de l'enceinte. Ce

qui rendrait l'évaluation des performances de l'isolation thermique impossible puisque l'eau qui entre dans la pompe sera déjà à de hautes températures.

- L'amincissement et le polissage du verre moulé pour former l'isolation thermique dans le rotor a montré un profil concave d'environ 1 µm par rapport du niveau du silicium (*Dishing*). Prendre ce résultat en considération dans la conception future. Par exemple, la région du joint d'étanchéité annulaire inférieur pourrait être gravée pour faire descendre le rotor et ainsi diminuer le gap nominal de la pompe.
- La technique de micromoulage de verre a montré des limites en termes de température de moulage et de temps de traitement comme démontré dans le chapitre 2. Des conditions optimales de micromoulage ont été définies.
- Après le nettoyage des puces, les solutions chimiques utilisées peuvent être introduites et emprisonnées dans les différentes canalisations et cavités. Il est impossible de sécher les puces seulement avec un séchage à jet d'azote. Au moment des tests, ces fluides entrent dans la cavité du rotor et empêchent le fonctionnement (forces capillaires). Sécher les puces en les mettant sous vide était une bonne solution.

6.4 Continuité des travaux

Les résultats obtenus dans cette thèse sur les performances de la microturbopompe sont encourageants, mais des recherches supplémentaires sont nécessaires pour valider davantage ce concept, notamment :

- Opérer la microturbopompe à de hautes vitesses de rotation et déterminer sa limite. Parmi les causes à étudier qui peuvent limiter la vitesse de rotation sont :
    - La dissymétrie du verre moulé dans le rotor pourrait causer un débalancement du rotor et ainsi limiter sa vitesse (décalage du centre de masse du rotor par rapport à l'axe de rotation). Les points à reconsidérer pour éviter la dissymétrie sont : une meilleure précision de l'alignement à l'étape de la photolithographie et l'uniformité de la gravure DRIE de la cavité du rotor.
    - À de hautes vitesses (hautes pressions dans la turbine), le palier axial inférieur (TB_{bot}) pourrait ne plus être en mesure de contrer les forces appliquées sur le rotor du côté de la turbine.
- Caractériser la pompe à des hautes vitesses avec pressurisation de la sortie pour déterminer

les performances et les limites de fonctionnement (élévation de pression, efficacité à haute vitesse).

- Démontrer le fonctionnement à la vapeur d'eau ainsi qu'à des température plus élevées (200°C), ce qui représente le fonctionnement réel de la microturbine à vapeur. Lors des tests dans ce travail, l'utilité de l'isolation thermique a été validée avec le critère d'absence d'évaporation dans la pompe. Avec les tests à la vapeur, il serait important de valider s'il n'y aura pas de condensation de la vapeur dans le palier axial inférieur.
- Pour un fonctionnement à la vapeur à une température de 200°C, le banc d'essais devrait être amélioré en conséquence :
    - Les tubes flexibles en PFA (*perfluoroalkoxy*) utilisés dans les tests peuvent résister à une température de 204°C et une pression de 4.2 bars, ce qui représentait une limite supérieure ce que le design prévoyait. Cependant, les tests des paliers axiaux ont démontré la nécessité d'utiliser des pressions supérieures à 4.2 bars. Il serait préférable de les remplacer avec des tubes en acier inoxydable afin d'augmenter la limite en terme de pression. Ces derniers offrent des pressions de service allant jusqu'à 500 bars pour les températures souhaitées.
    - La température maximale de l'enceinte chauffée était limitée à 160°C. Il est suggéré de remplacer l'élément chauffant par un autre plus puissant pour pouvoir chauffer l'enceinte de tests à des températures plus élevées. L'amélioration de l'isolation thermique de l'enceinte est aussi suggérée pour diminuer les déperditions de chaleur et ainsi diminuer la puissance nécessaire pour chauffer l'enceinte.
- Analyser expérimentalement les écoulements dans la turbine et valider les calculs CFD notamment, l'effet du *tip clearance* et du nombre de Reynolds sur les performances de la turbine.
- Démontrer la limite du fonctionnement des joints d'étanchéité notamment le joint d'étanchéité entre la pompe et le palier axial inférieur.

6.5 Perspectives

Le travail dans cette thèse représente une étape clé dans le projet du développement d'une microturbine à vapeur de cycle Rankine pour la génération d'électricité à partir de la récupération

de chaleur. Cependant, pour arriver au produit final, deux étapes importantes restent encore à développer comme proposées ci-dessous :

1. Concevoir et fabriquer une micro turbogénératrice pour démontrer la conversion de la chaleur en électricité. Elle comprendrait toutes les composantes de la microturbopompe sauf que la pompe est remplacée par une micro génératrice. Une micro génératrice magnétique à aimant permanant comme démontrée par Herrault *et al*. [26] représente une bonne approche pour ce projet. Leur température de fonctionnement est limitée par le point de Curie des matériaux magnétiques. L'utilisation de la technique d'isolation thermique développée dans ce travail serait à considérer.
2. Une fois le fonctionnement de la micro turbogénératrice démontré, l'objectif sera de concevoir et tester une microturbine à vapeur avec un cycle fermé. C'est une combinaison d'une microturbopompe et trois micro turbogénératrice en série comme présentée à la figure 2-4 (*Multi-spools concept*).

LISTE DES RÉFÉRENCES

[1] K.D. Wise, (2007). Integrated sensors, MEMS, and microsystems: Reflections on a fantastic voyage. Sensors and Actuators, vol. 136, no. 1, p. 39-50.

[2] Yole Development (2020). Status of the MEMS industry report. http://www.yole.fr/index.aspx (page consultée le 12 mai 2020).

[3] Y. Huang, A.S.S. Vasan, R. Doraiswami, M. Osterman et M. Pecht, (2012). MEMS Reliability Review. IEEE Transactions on device and materials reliability, vol. 12, no. 2, p. 482-493.

[4] A.H. Epstein et S.D. Senturia, (1997). Macro power from micro machinery. Science, vol. 276, no. 5316, p. 1211.

[5] A.H. Epstein et al., (1997). Micro-Heat Engines, Gas Turbines, and Rocket Engines-The MIT Microengine Project. Proc. AIAA Fluid Dynamics, Snowmass Village, CO., USA.

[6] L.G. Fréchette, S.A. Jacobson, K.S. Breuer, F.F. Ehrich, R. Ghodssi, R. Khanna, C.W. Wong, X. Zhang, M.A. Schmidt et A.H. Epstein, (2005). High-Speed Microfabricated Silicon Turbomachinery and Fluid Film Bearings. Journal of Microelectromechanical Systems, vol. 14, no. 1, p. 141–152.

[7] R. Zhou, S. Wei, Y. Liu, N. Gao, G. Wang, J. Lian et Q. Jiang, (2019). Charge storage by electrochemical reaction of water bilayers absorbed on MoS_2 monolayers. Sci. Rep. 2019, vol. 9, no. 3980.

[8] C-H. Lee, K.C. Jiang, P. Jin et P.D. Prewett, (2004). Design and fabrication of a micro Wankel engine using MEMS technology. Microelectronic Engineering, vol. 73-74, p. 529–534.

[9] K. Fu, A.J. Knobloch, F.C. Martinez et D.C. Walther, (2001). Design and Fabrication of A Silicon-Based MEMS Rotary Engine. Proc. IMECE, New York, NY., USA.

[10] Y. Suzuki, Y. Okada, J. Ogawa, S. Sugiyama et T. Toriyama, (2008). Experimental study on mechanical power generation from MEMS internal combustion engine. Sensors and Actuators A: Physical, vol. 141, no. 2, p. 654–661.

[11] S. Whalen, M. Thompson, D. Bahr, C. Richards et R. Richards, (2003). Design, Fabrication and Testing of the P3 micro heat engine. Sensors and Actuators A: Physical, vol. 104, no. 3, p. 290–298.

[12] G-E. Song, K-H. Kim et Y-P. Lee, (2007). Simulation and experiments for a phase-change actuator with bistable membrane. Sensors and Actuators A: Physical, vol. 136, no. 2, p. 665–672.

[13] T. Huesgen, J. Ruhhammer, G. Biancuzzi et P. Woias, (2010). Detailed study of a micro heat engine for thermal energy harvesting. Journal of Micromechanics and Microengineering, vol. 20, p.104004–9.

[14] T. Monin, A. Tessier-Poirier, A. Amnache, T. Skotnicki, S. Monfray, F. Formosa et L.G. Fréchette, (2018). Demonstration of a Microfabricated Self-Oscillating Fluidic Heat Engine (SOFHE). Proceedings of the Solid-State Sensors, Actuators and Microsystems Workshop, Hilton Head Island, SC, USA.

[15] T. Monin, A. Tessier-Poirier, É. Léveillé, A. Juneau-Fecteau, T. Skotnicki, F. Formosa, S. Monfray et L.G. Fréchette, (2016). First experimental demonstration of a self-oscillating fluidic heat engine (SOFHE) with piezoelectric power generation. J. of Phys.: Conf. Ser., vol. 773, no 012039, 16th Int'l Workshop on Micro and Nanotech. for Power Generat. and Energy Convers. Apps (PowerMEMS 2016), Paris, France.

[16] É. Léveillé, G. Mirshekari, S. Monfray, T. Skotnicki et L.G. Fréchette, (2012). A Microfluidic Heat Engine Based on Explosive Evaporation. Proc. 12th Int'l Workshop on Micro and Nanotech. for Power Generat. and Energy Convers. Apps (PowerMEMS 2012), Atlanta, GA, USA.

[17] T. Avertissian, É. Léveillé, M-A. Hachey, F. Formosa et L.G. Fréchette, (2018). MISTIC - Micro Stirling Heat Engines for Thermal Energy Harvesting. Proc. PowerMEMS, Daytona Beach, FL., USA.

[18] L.G. Fréchette, C. Lee, S. Arslan et Y-C. Liu, (2003). Preliminary Design of MEMS Steam Turbine Power Plant-on-a-chip. Proc. PowerMEMS, Makuhari, Japon.

[19] N. Muller et L.G. Fréchette, (2002). Performance Analysis of Brayton and Rankine Cycle Microsystems for Portable Power Generation. Proc. IMECE, New Orleans, LA., USA.

[20] C. Lee et L.G. Fréchette, (2011). A Silicon Microturbopump for a Rankine-Cycle Power Generation Microsystem—Part I: Component and System Design. Journal of Microelectromechanical Systems, vol. 20, no. 1, p. 312–325.

[21] C. Lee et L.G. Fréchette, (2011). A Silicon Microturbopump for a Rankine-Cycle Power Generation Microsystem—Part II: Fabrication and Characterization. Journal of Microelectromechanical Systems, vol. 20, no. 1, p. 326–338.

[22] A.H. Epstein, (2004). Millimeter-Scale, Micro-Electro-Mechanical Systems Gas Turbine Engines. J. Eng. Gas Turbines Power. Syst., vol. 126, no. 2, p. 205–226.

[23] M. Liamini, (2014). Conception d'une microturbine cycle Rankine microfabriquée pour le fonctionnement à haute température. Thèse de doctorat, Univ. de Sherbrooke, Sherbrooke, Canada, 184 p.

[24] C.J. Teo, (2006). MEMS Turbomachinery Rotodynamic: Modeling, Design and Testing. Thèse de doctorat, Aeronautics and Astronautics Dept., MIT, Boston, USA, 350 p.

[25] S.F. Nagle, C. Livermore, L.G. Fréchette, R. Ghodssi et J.H. Lang, (2005). An electric induction micromotor. Journal of Microelectromechanical Systems, vol. 14, no. 5, p. 1127–1143.

[26] F. Herrault, B.C. Yen, C-H. Ji, Z.S. Spakovszky, J.H. Lang et M.G. Allen, (2010). Fabrication and Performance of Silicon-Embedded Permanent-Magnet Microgenerators. Journal of Microelectromechanical Systems, vol. 19, no. 1, p. 4–13.

[27] C. Lee, (2006). Developement of a microfabricated turbopump for a Rankine vapor power cycle. Thèse de doctorat, Columbia University, New York, USA, 249 p.

[28] F. Gauthier. (2009). Étude et fabrication de micro-débitmètres à pression différentielle de type orifice plat destinés à l'installation d'une micro-turbopompe. Mémoire de maîtrise, Univ. de Sherbrooke, Sherbrooke, Canada, 129 p.

[29] P. Beauchesne-Martel, (2008). Étude numérique de l'aérothermodynamique d'écoulements laminaires subsoniques dans les microturbines et développement d'une méthodologie de conception. Mémoire de maîtrise, Univ. de Sherbrooke, Sherbrooke, Canada, 202 p.

[30] M. Omri et L. G. Fréchette, (2011). Computational investigation of the three-dimensional flow structure and losses in a low Reynolds number microturbine. Proc. ASME Turbo Expo, Vancouver, British Columbia, Canada.

[31] W.-Y. Chang et Y.-S. Hsihe, (2016). Multilayer microheater based on glass substrate using MEMS technology. Microelectronic Engineering, vol. 149, p. 25-30.

[32] S. Wang, Z. Yi, M. Qin et Q. Huang, (2019). Temperature Effects of a Ceramic MEMS Thermal Wind Sensor Based on a Temperature-Balanced Mode. IEEE Sensors Journal, vol. 19, no. 17, p. 7254-7260.

[33] S. Queste, R. Salut, S. Clatot, J-Y. Rauch, et C.G.K. Malek, (2010). Manufacture of microfluidic glass chips by deep plasma etching, femtosecond laser ablation, and anodic bonding. Microsystem Technologies, vol. 16, no. 8–9, p. 1485–1493.

[34] M. J. Ahamed, D. Senkal, A. A. Trusov, et A. M. Shkel, (2015). Study of high aspect ratio NLD plasma etching and postprocessing of fused silica and borosilicate glass. Journal of Microelectromechanical Systems, vol. 24, no. 4, p. 790–800.

[35] P. Fürjes, G. Légrádi, Cs. Dücső, A. Aszódi et I. Bársony, (2004). Thermal characterisation of a direction dependent flow sensor. Sensors and Actuators A: Physical, vol. 115, no. 2–3, p. 417-423.

[36] Gaur, S.P., Kumar, P., Rangra, K. *et al.*, (2018). Efficient thermal utilization in MEMS bulk micromachined pyroelectric infrared sensor using thermal oxide thin layer. Microsystem Technologies, vol. 24, p. 1603–1608.

[37] O. Marconot, I. Latella, A. Juneau-Fecteau, J. Sylvestre et L. G. Fréchette, (2019). Microfabricated Membranes for Radiative Near Field Measurements. 20th International Conference on Solid-State Sensors, Actuators and Microsystems & Eurosensors XXXIII (TRANSDUCERS & EUROSENSORS XXXIII), Berlin, Germany, p. 2021-2024.

[38] AR. Ghodssi, L.G. Fréchette, S.F. Nagle, X. Zhang, A.A. Ayon, S.D. Senturia et M.A. Schmidt, (1999). Thick buried oxide in silicon (TBOS): An integrated fabrication technology for multi-stack wafer-bonded MEMS processes. Proc. 10th Int. Conf. Solid-State Sens. Actuators, Transducers, Sendai, Japon, p. 1456–1459.

[39] C. Zhang et K. Najafi, (2004). Fabrication of thick silicon dioxide layers for thermal isolation. Journal Micromechanics and Microengineering, vol. 14, no. 6, p. 769–774.

[40] G. Kaltsas, A.A. Nassiopoulos et A.G. Nassiopoulou, (2002). Characterization of a silicon thermal gas-flow sensor with porous silicon thermal isolation. IEEE Sensors Journal, vol. 2, no. 5, p. 463-475.

[41] P.J. Newby, M. Aslaki, V. Aimez et L.G. Fréchette, (2014). Porous silicon carbide: A new thermal insulation material for harsh environment MEMS. Proceedings of the Solid-State Sensors, Actuators and Microsystems Workshop, Hilton Head Island, SC, USA.

[42] A. Amnache et L.G. Fréchette, (2018). Microfabrication of a Silicon Turbopump with Embedded Thermal Isolation for a Rankine MEMS Heat Engine. Proc. PowerMEMS, Daytona Beach, FL., USA.

[43] A. Amnache et L.G. Fréchette, (2019). Capabilities and Limits to Form High Aspect-Ratio Microstructures by Molding of Borosilicate Glass. Journal of Microelectromechanical Systems, vol. 28, no. 3, p. 432–440.

[44] C. Iliescu, B. Chen, et J. Miao, (2008). On the wet etching of Pyrex glass. Sensors and Actuators A: Physical, vol. 143, no. 1, p. 154–161.

[45] J. H. Park, N. E. Lee, J. Lee, J. S. Park, et H. D. Park, (2005). Deep dry etching of borosilicate glass using SF_6 and SF_6/Ar inductively coupled plasmas. Microelectronic Engineering, vol. 82, no. 2, p. 119–128.

[46] C. Zhang, G. Hatipoglu, et S. Tadigadapa, (2015). A modified inductively coupled plasma for high-speed, ultra-smooth reactive phase etching of silica glass. Proc. 18th Int. Conference Solid-State Sensors, Actuators and Microsystems. (TRANSDUCERS), Anchorage, AK, USA, p. 592–595.

[47] L. Lin, X. Jing, Q. Wang, F. Jiang, L. Cao, et D. Yu, (2016). Investigation of fused silica glass etching using C_4F_8/Ar inductively coupled plasmas for through glass via (TGV) applications. Microsystem Technology, vol. 22, no. 1, p. 119–127.

[48] K.-S. Chen, A. A. Ayon, X. Zhang, et S. M. Spearing, (2002). Effect of process parameters on the surface morphology and mechanical performance of silicon structures after deep reactive ion etching (DRIE). Journal of Microelectromechanical Systems, vol. 11, no. 3, p. 264–275.

[49] J. Albero, S. Perrin, S. Bargiel, N. Passilly, M. Baranski, L.G-M., F. Bernard, J. Lullin, L. Froehly, J. Krauter, W. Osten, et Christophe Gorecki (2015). Dense arrays of millimeter-sized glass lenses fabricated at wafer-level. Optics Express, vol. 23, no. 9, p. 11702–11712.

[50] R-U. M. Haque et K.D. Wise, (2013). A glass-in-silicon reflow process for three-dimensional microsystems. Journal of Microelectromechanical Systems, vol. 22, no. 6, p. 1470–1477.

[51] D. Senkal, M. J. Ahamad, M. H. A. Ardakani, S. Askari, et A. M. Shkel, (2015). Demonstration of 1 million Q-factor on microglassblown wineglass resonators with out-of-plane electrostatic transduction. Journal of Microelectromechanical Systems, vol. 24, no. 1, p. 29–37.

[52] P.-T. Brun, C. Inamura, D. Lizardo, G. Franchin, M. Stern, P. Houk et Neri Oxman, (2017). The molten glass sewing machine. Philosophical Transactions of the Royal Society A Mathematical Physical and Engineering Sciences, vol. 375, no. 2093, p. 20160156-1–20160156-12.

[53] K. Kawai, F. Yamaguchi, A. Nakahara, et S. Shoji, (2010). Fabrication of vertical and high-aspect-ratio glass microfluidic device by borosilicate glass molding to silicon structure. Proc. 14th Int. Conference on Miniaturized Systems for Chemistry and Life Sciences (MicroTAS), Groningen, The Netherlands, p. 1193–1195.

[54] J. Liu, J. Shang, J. Tang, et Q.-A. Huang, (2011). Micromachining of Pyrex 7740 glass by silicon molding and vacuum anodic bonding. Journal of Microelectromechanical Systems, vol. 20, no. 4, p. 909–915.

[55] P. Merz, H. J. Quenzer, H. Bernt, B. Wanger, et M. Zoberbier, (2003). A novel micromachining technology for structuring borosilicate glass substrates. Proc. 12th Int. Conf. Solid-State Sensors, Actuat. Microsyst. Dig. Tech. Papers (TRANSDUCERS), Boston, MA, USA, p. 258–261.

[56] N. Van Toan, M. Toda, et T. Ono, (2016). An investigation of processes for glass micromachining. Micromachines, vol. 7, no. 3, p. 51–62.

[57] A. Amnache et L. G. Fréchette, (2016). High-aspect ratio microstructures in borosilicate glass by molding and sacrificial silicon etching: Capabilities and limits. Hilton Head Solid-State Sensors, Actuators and Microsystems Workshop, Hilton Head, SC, USA.

[58] W. P. Maszara, G. Goetz, A. Caviglia, et J. B. McKitterick, (1988). Bonding of silicon wafers for silicon-on-insulator. Journal of Applied Physics., vol. 64, no. 10, p. 4943–4950.

[59] F. Ericson, S. Johanson, et J.-Å. Schweitz, (1988). Hardness and fracture toughness of semiconducting materials studied by indentation and erosion techniques. Materials Science and Engineering: A, vol. 105–106, p. 131–141.

[60] Borofloat 33—Thermal Properties. Available: http:// www.us.schott.com/d/borofloat/48c997e9272a461bbdf7b67a8dc9f04f/1.2/borofloat33_therm_usa_web.pdf (page consultée en 2018).

[61] Standard ASTM (2013). Standard Test Method for Softening Point of Glass, Standard ASTM C338-93.

[62] G. Vézina, H. Fortier-Topping, F. Bolduc-Teasdale, D. Rancourt, M. Picard, J-S. Plante, M. Brouillette et L.G. Fréchette, (2016). Design and Experimental Validation of a Supersonic Concentric Micro Gas Turbine. Journal of Turbomachinery, vol. 138, no. 2, p. 021007–11.

[63] J. Seo, H-S. Lim, J. Park, M.R. Park et B.S. Choi, (2017). Development and Experimental Investigation of 500-W Class Ultra-Micro Gas Turbine Power Generator. Energy, vol. 124, p. 9–18.

[64] F. Formosa et L.G. Fréchette, (2013). Scaling Laws for Free Piston Stirling Engine Design: Benefits and Challenges of Miniaturization. Energy, vol. 57, p. 796–808.

[65] D. Deng, (2015). Li-ion Batteries: Basics, Progress, and Challenges. Energy Science and Engineering, vol. 3, no. 5, p. 385–418.

[66] N. Savoulides, S.A. Jacobson, H. Li, L. Ho, R. Khanna, C-J Teo, J.M. Protz, L. Wang, D. Ward, M.A. Schmidt et A.H. Epstein, (2008). Fabrication and Testing of a High-Speed Microscale Turbocharger. Journal of Microelectromechanical Systems, vol. 17, no. 5, p. 1270–1281.

[67] A. Mehra, X. Zhang, A.A. Ayón, I.A. Waitz, M.A. Schmidt et C.M. Spadaccini, (200). A Six-Wafer Combustion System for a Silicon Micro Gas Turbine Engine. Journal of Microelectromechanical Systems, vol. 9, no. 4, p. 517–526.

[68] M. Liamini, H. Shahriar, S. Vengallatore et L. G. Fréchette, (2011). Design Methodology for a Rankine Microturbine: Thermomechanical Analysis and Materials Selection. Journal of Microelectromechanical Systems, vol. 20, no. 1, p. 339–351.

[69] C. Lee, M. Liamini et L.G. Fréchette, (2006). Design, Fabrication, and Characterization of a Microturbopump for a Rankine Cycle Micro Power Generator. Proc. Solid State Sensor, Actuator, and Microsystem Workshop, Hilton Head Island, SC., USA.

[70] Y. Tang, A. Sandoughsaz, K.J Owen et K. Najafi, (2018). Ultra Deep Reactive Ion Etching of High Aspect-Ratio and Thick Silicon Using a Ramped-Parameter Process. Journal of Microelectromechanical Systems, vol. 27, no. 4, p. 686–697.

[71] F. Fournel, H. Moriceau, C. Ventosa, L. Libralesso, Y. Le Tiec, T. Signamarcheix et F. Rieutord, (2008). Low Temperature Wafer Bonding. ECS Transactions, vol. 16, no. 8, p. 475–488.

[72] A.F. Sarioglu, M. Kupnik, S. Vaithilingman et B.T. Khuri-Yakub, (2012). Nanoscale Topography of Thermally-Grown Oxide Films at Right-Angled Convex Corners of Silicon. Journal of the Electrochemical Society, vol. 159, no. 2, p. 79–84.

[73] N. Miki et M. Spearing, (2003). Effect of Nanoscale Surface Roughness on the Bonding Energy of Direct-Bonded Silicon Wafers. Journal of Applied Physics, vol. 94, no. 10, p. 6800–6806.

[74] A. Amnache, (2012). Étude et fabrication de micro-débitmètres à pression différentielle de type orifice plat destinés à l'installation d'une micro-turbopompe. Mémoire de maîtrise, Univ. de Sherbrooke, Sherbrooke, Canada, 145 p.

[75] A. Amnache, M. Omri et L.G. Fréchette, (2018). A silicon rectangular micro-orifice for gas flow measurement at moderate Reynolds numbers: design, fabrication and flow analyses. Microfluidics and Nanofluidics, vol. 22, no.58.

[76] L.G. Fréchette, G. Lee, S. Arslan, and Y.C. Liu, (2003). Design of a Microfabricated Rankine Cycle Steam Turbine for Power Generation. Proc. of the ASME IMECE, Washington, DC, USA, p. 335-344.

[77] J.H. Horlock et J.D. Denton, (2005). A review of some early design practice using computational fluid dynamics and a current perspective. Transactions of the ASME. The Journal of Turbomachinery, vol. 127, no. 1, p. 5-13.

[78] R.E. Peacock, (1982). A review of turbomachinery tip gap effects: Part 1: Cascades. Int. Journal of Heat and Fluid Flow, vol. 3, no. 4, p. 185-193.

[79] D. Borello, K. Hanjalic, et F. Rispoli, (2007). Computation of tip-leakage flow in a linear compressor cascade with a second-moment turbulence closure. International Journal of Heat and Fluid Flow, vol. 28, no. 4, p. 587-601.

[80] A. Mehra (1997). Computational Investigation and Design of Low Reynolds Number Micro-Turbomachinery. Thèse de maîtrise, Massachusetts Institute of Technology, Cambridge, MA, p. 132.

[81] Y. Gong, B.T. Sirakov, A.H. Epstein, et C.S. Tan, (2004). Aerothermodynamics of Micro-turbomachinery. ASME IGTI Turbo Expo, Paper GT2004-53877, Vienna, Austria.

[82] S. Kang, (1993). Investigation on the Three-Dimensional Flow Within a Compressor Cascade with and without Tip Clearance. Thèse de doctorat, Dept. of Fluid Mech., Vrije Universiteit Brussels.

[83] J. Peirs, D. Reynaerts, et F. Verplaetsen, (2004). A micro turbine for electric power generation. Sensors and Actuators A: Physical, vol. A113, no. 1, p. 86-93.

[84] L. Qi, Z. Zou, P. Wang, T. Cao, et H. Liu, (2012). Control of secondary flow loss in turbine cascade by streamwise vortex. Computers & Fluids, vol. 54, no. 1, p. 45–55.

[85] C.H. Sieverding et P. Van den Bosche, (1983). Use of Colored Smoke to Visualize Secondary Flows in turbine-Blade cascade. Journal of Fluid Mechanics. vol. 134, p. 85-89.

[86] C.H. Sieverding, (1985). Recent progress in the understanding of basic aspects of secondary flows in turbine blade passages. ASME Journal of Engineering for Gas Turbines and Power, vol. 107, no 2, p. 248–257.

[87] O.P. Sharma et T.L. Butler, (1987). Predictions of Endwall Losses and Secondary Flows in Axial Flow Turbine Cascades. Journal of Turbomachinery, vol. 109, no. 2, p. 229-236.

[88] R.L. Simpson, (2001). Junction Flows. Annu. Rev. Fluid Mech, vol. 33, pp. 415-443.

[89] B. Lakshminarayana et J.H. Horlock, (1963). Review -- Secondary flows and losses in cascades and axial-flow turbomachines. International Journal of Mechanical Sciences, vol. 5, no. 3, p. 287-307.

[90] M.I. Yaras et S.A. Sjolander, (1992). Effects of simulated rotation on tip leakage in a planar cascade of turbine blades: Part I - Tip gap flow. Journal of Turbomachinery, vol. 114, no. 3, p. 652-659.

[91] L.G. Fréchette, C. Lee, et S. Arslan, (2004). Development of a MEMS-based Rankine Cycle Steam Turbine for Power Generation: Project Status. Proc. 4th Int'l Workshop on Micro and Nano Technology for Power Generation and Energy Conversion Applications (PowerMEMS '04), Kyoto, Japon, p. 92-95

[92] E.M. Greitzer, C.S. Tan, et M.B. Graf, (2004). Internal Flow: Concepts and Applications. Cambridge University Press.

[93] Y. Moon et S.R. Koh, (2001). Counter-rotating streamwise vortex formation in the turbine cascade with end fence. Journal of Computers & Fluids, vol. 30, no. 4, p. 473-490.

[94] M. Omri et L.G. Fréchette, (2010). CFD analysis of three-dimensional flows in a low Reynolds number Microturbine. PowerMEMS- The 10th International Workshop on Micro and Nanotechnology for Power Generation and Energy Conversion Applications, Leuven, Belgique.

[95] C. Lee, S. Arslan, et L.G. Fréchette, (2008). Design Principles and Measured Performance of Multistage Radial Flow Microturbomachinery at Low Re Numbers. Journal of Fluid Engineering, vol. 130, no. 11, p. 111103-1-11.

[96] P. Beauchesne-Martel et L.G. Frechette, (2008). Numerical Analysis of Sub-Millimeter-Scale Microturbomachinery Aerothermodynamics. In Proc. ASME IMECE 2008-68190, Boston, MA, USA.

[97] L.S. Langston, (2001). Secondary Flows in Axial Turbines-a Review. Heat and Mass Transfer in Gas Turbine Systems, vol. 943, no. 1, p. 11–26.

[98] M. Omri et N. Galanis, (2007). Numerical analysis of turbulent buoyant flows in enclosures: Influence of grid and boundary conditions. Int. Journal of Thermal Sciences, vol. 46, no. 8, p. 727-738.

[99] G. Haller, (2005). An objective definition of a vortex. Journal of Fluid Mechanics, vol. 525, p.1–26.

[100] H.P. Wang, S.J. Olson, R.J. Goldstein, et E.R.G. Eckert, (1997). Flow visualization in a linear turbine cascade of high performance turbine blades. ASME Journal of Turbomachinery, vol 119, no. 1, p. 1–8.

ANNEXE A : Flow Structure in a Low Reynolds Number Microturbine

A.1. Avant-propos

Auteurs et affiliation :

Mohamed Omri : King Abdulaziz University, Deanship of Scientific Research, Jeddah, Saudi Arabia
Amrid Amnache : Université de Sherbrooke, Faculté de génie, Département de génie mécanique.
Yusuf Al-turki: King Abdulaziz University, Electrical and Computer Engineering Department, Jeddah, Saudi Arabia
Ahmed A ALGhamdi : King Abdulaziz University, Deanship of Scientific Research, Jeddah, Saudi Arabia
Stéphane Moreau : professeur, Université de Sherbrooke, Faculté de génie, Département de génie mécanique.
Luc Fréchette : professeur, Université de Sherbrooke, Faculté de génie, Département de génie mécanique.

Date de soumission : article pas soumis à la date du dépôt de la thèse

Titre français : Structures de l'écoulement dans une microturbine à de faibles nombres de Reynolds

Résumé français :

Dans ce travail, basés sur des calculs numériques, des écoulements tridimensionnels dans des cascades laminaires subsoniques à des nombres de Reynolds relativement faibles (Re <2500) sont présentés. Les pales du stator et de la turbine étudié dans ce travail sont celles d'une microturbine MEMS. Des calculs 3D ont été effectués pour différents nombres de Reynolds, dégagements de pointe (de 0 à 20%) et incidences (0° à 15°) afin de déterminer l'impact des conditions aérodynamiques sur les modèles d'écoulement. Ces conditions sont appliquées à un passage d'aube avec et sans rotation, à la fois pour un carter extérieur fixe et mobile. Le passage de pale sans jeu de pointe indique la présence de deux grands tourbillons symétriques en raison de l'interaction entre les couches limites du moyeu/carenage et la pale. L'ouverture du jeu de pointe introduit le tourbillon de pointe, qui tend à devenir dominant au-dessus d'un jeu de pointe de 10%. Le mouvement relatif du mur a également un impact sur les modèles d'écoulement 3D en raison de la traînée tangentielle importante à ces faibles nombres de Reynolds. Son impact est quantifié en fonction du cisaillement de la paroi montrant la plage dans laquelle le vortex de la pointe peut être annulé par le mouvement relatif de la paroi. En plus de fournir une description et une compréhension d'écoulement 3D dans une microturbine MEMS, ces résultats suggèrent l'importance de considérer les écoulements 3D dans la conception des microturbomachines, même si la géométrie est principalement 2D.

A.2. Abstract

In this work, three-dimensional flows in laminar subsonic cascades at relatively low Reynolds numbers ($Re < 2500$) are presented, based on numerical calculations. The stator and rotor blade designs are those for a MEMS-based Rankine microturbine power-plant-on-a-chip with 109 micron chord blades. Blade passage calculations in 3D were done for different Reynolds numbers, tip clearances (from 0 to 20%) and incidences (0° to 15°) to determine the impact of aerodynamic conditions on the flow patterns. These conditions are applied to a blade passage with and without rotation, both for a stationary and moving outer casing. The 3D blade passage without tip clearance indicates the presence of two large symmetric vortices due to the interaction between hub/casing boundary layers and the blade. Opening the tip clearance introduces the tip vortex, which tends to become dominant above a tip clearance of 10%. Relative wall motion also impacts the 3D flow patterns due to the important tangential drag at these low Reynolds numbers. Its impact is quantified as a function of wall shear showing the range in which the tip vortex can be cancelled by the relative wall motion. In addition to providing a description and understanding of the 3D flow in a MEMS microturbine, these results suggest the importance of considering 3D flows in the design of microturbomachinery, even though the geometry is dominantly 2D.

Nomenclature

bw	=	*thickness of the blade*
Cp	=	*static pressure coefficient*
C	=	*chord length of the blade*
dt	=	*tip clearance size*
H	=	*distance between the hub and the casing*
M	=	*Mach number*
P	=	*static pressure*
P0	=	*total pressure*
ps	=	*pressure side*
Re	=	*Reynolds number*
Rec	=	*Reynolds number based on the chord length*
S	=	*section*
S1	=	*cascade inlet*
S2	=	*cascade mid-chord plane*
S3	=	*cascade outlet*
ss	=	*suction side*
U	=	*velocity*
Wpro	=	*profile losses*
α	=	*incidence angle*
ΔP	=	*pressure difference*
μ	=	*fluid viscosity*

ρ	=	*density*
Φ	=	*fundamental quantity*
Ω	=	*rotation speed*

Subscripts

1	=	*value at the inlet*
2	=	*value at the outlet*
in	=	*value at the inlet*
out	=	*value at the outlet*
ps-ss	=	*difference between the suction and pressure sides of the blade*
Tip	=	*value across the tip clearance zone*
Tip/ps	=	*value across the tip clearance zone on the pressure side*
Tip/ss	=	*value across the tip clearance zone on the suction side*
w	=	*value at the wall*
x	=	*x direction*
$\bar{}$	=	*average value*

A.2 Introduction

Power generation is no more limited to utility-scale power plants. Gas turbine power generation units on the 10-100 kW scale, for example, are increasingly used for energy autonomy or co-generation in some industrial installations. We could go further and imagine distributed power generation down to the 1-100 W scale. This would address the growing need for portable and distributed power to drive hand tools, mobile electronics and distributed sensors. With common manufacturing technologies however, creating miniature heat engines at such small scale is not economically viable. Instead, we currently rely on batteries that are charged through the grid, offering limited power density and autonomy.

To address the need for portable power, the concept of low-cost, batch manufactured micro heat engines has been proposed [4] and stimulated the development of multiple MEMS gas turbine and steam turbine research and development efforts worldwide [4,6,76,77,78]. Somewhat similar to their large-scale counterparts, these microengines implement thermodynamic power cycles, but within cm-scale volumes and with micron-scale features using semiconductor wafer manufacturing technologies. These techniques consist of using photolithographic patterning to imprint large arrays of micron-scale features onto a silicon wafer, in a single step. The features are then etched down into the silicon substrate to form the micro-engine structures and fluidic channels. These techniques initially developed by the microelectronics industry for integrated circuit fabrication have since been applied to create microelectromechanical systems (MEMS), such as miniature sensors,

actuators, and microfluidic systems. Photolithographic patterning, thin film deposition, and etching have allowed the fabrication of mechanical parts and microfluidic channels in silicon, as well as their integration with electrical components. Although this approach limits the structures to planar 2D extruded geometries, it allows parallel and batch fabrication with sub-micron tolerances at low unit cost. It has successfully been applied to create dime-size planar microturbines, as shown in Fig. A.1 with thousands of 100 μm chord blades formed by a single silicon etch [42].

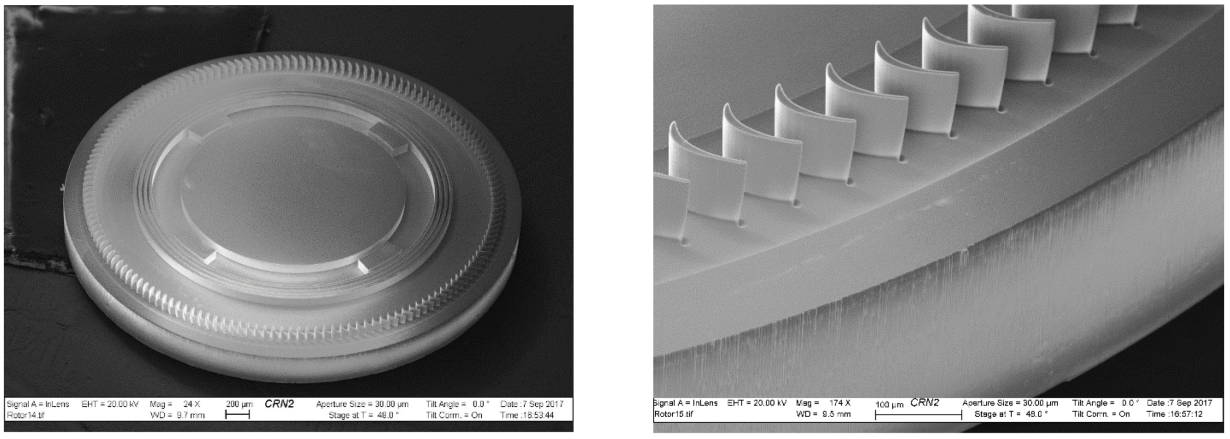

(a) Rotor (4mm dia.) (b) Blade row

Figure A -1 : Typical MEMS microturbine fabricated by lithography and etching of silicon [42].

Understanding the source of losses in these unprecedented conditions is one of the goals of the present study. Since the microfabrication techniques used here lead to straight (no twist) and uniform height blades, numerical studies of the aerothermodynamics has focused on 2D cascades, assuming a planar flow field. They have led to loss correlations as a function of Re_c, Mach number and incidence, for a limited range of blade and cascade geometries [27,79]. It has been shown that profile losses tend to increase significantly for $Re_c < 1000$, suggesting minimum blade chords on the order of 100 microns. In this range, thickness of the boundary layers developing along the blades tends to be on the order of the blade passage width, which is significantly different from the thin boundary layers typical of macroscale turbines. These studies neglect however the three-dimensional flow components that stem from hub and casing boundary layers and tip leakage flows. Initial numerical studies in a 3D blade passage (but without rotation or tip clearance) identified the presence of vortical structures that can also extend across the blade passage, making their contribution to the overall losses significant [30]. Similar studies of 3D microturbomachinery flows in the flow passage of a single stage micro gas turbine suggest that secondary flows can

increase losses by up to 50% based on the 2D profile losses, for Re_c > 10,000 [80]. A correction factor was defined to extrapolate the 3D losses from 2D CFD calculations to facilitate the design process, but without linking this factor to actual flow structures and loss mechanisms. The effect of wall shear due to relative motion of the blade passage with respect to the casing was also shown to impact the efficiency of a microturbine, but only global loss parameters were studied [81]. The three dimensional flow field remains largely unexplored and the related loss mechanisms ill-defined. To enable the development of microturbomachinery-based heat engines, an understanding of the 3D flow structures in representative configurations, including rotation and tip clearance, is therefore essential. This is a second objective of the present study.

Vortical flow structures in macroscale turbomachinery

The vortex dynamics in the case of a traditional turbine cascade, with turbulent flow and large Reynolds number (Re_c > 500,000) has been described by different authors [82-90]. In a turbine cascade with tip clearance, the leakage flow generates a vortical structure located in the upper half span of the blade, which worsens the aerodynamic characteristics in this area due to dissipation of the vortex energy and mixing losses. In addition, velocity gradients in the boundary layer developing on the hub and casing surfaces lead to horseshoe vortices that wrap around the blade with one leg of this vortex along the pressure side and the other leg along in the suction side. The pressure side leg is amplified and becomes the main passage vortex. The other leg (suction side) is drawn into the adjacent blade passage and has an opposite sense of rotation to the larger passage vortex. The tip vortex generated by the presence of a tip clearance flow, interacts with the upper passage vortex, adding to the flow complexity. In macroscale turbomachinery, these vortical structures are limited near the hub and casing walls, leaving a 2D core flow along most of the blade span.

In addition to these main vortices, which are the principal loss sources, various secondary vortices may also be present [89], such as corner vortices that appear at the junction of blade and endwall, and induced vortices, that result from the interaction between the passage vortex and the suction side wall.

Scope of this study

This work provides a comprehensive description of the 3D flow structure in subsonic laminar microturbomachinery, considering tip clearance and rotation effects on the flow structure and

losses. Computational fluid dynamics (CFD) finds its rightful place since it is difficult and even impossible to give a fine experimental description of the flow within those small devices. Unlike macro-scale turbomachinery aerodynamics, this numerical study focuses on laminar flow given the relatively low Re_c in microturbomachines. The blade configuration and operating range are representative of the multi-stage steam microturbine proposed by Frechette *et al.* [91] to implement the Rankine vapor power cycle on a chip. As in macro-scale turbines [5,92,93], a small annular tip clearance between the rotor blade tip and the casing is required. At microscale, the clearances are typically larger (relative to the blade height) however to accommodate imperfections due to the etching process and bearing tolerances. Microturbine rotors are typically supported by fluid film bearings that allow microns of tip deflection. Thus, a tip clearance of 5% of the blade height is considered as a minimum limit, while tip clearances up to 20% have been required in microturbomachines [94].

First, the structure and evolution of the vortices are detailed. A broad yet detailed investigation over the operating range and design space was required to properly identify the changes in vortex dynamics. Special importance is given to the dynamics of the tip vortex when increasing the tip gap size given its significant impact on losses. A range of tip clearances is considered from 0% (ideal geometry) to 20% of the passage height, based on the typical values achieved by microfabrication. For each geometry, incidences from 0° to 15° are considered. Moreover, rotation effects on the flow structure are included by considering the flow in a rotating reference frame at three different rotational velocities, with and without relative motion of the outer casing.

Following a description of the numerical model (Sec. A.3), we present the 3D flow structure and vortex dynamics (A.4). The effects of varying the tip clearance gap are presented in Sec. A.5 followed by the effects of rotation in Sec. A.6. Analytical criteria are also defined to determine when the dominant flow structures are to be expected, providing a basis for 3D-aware microturbomachine design.

A.3 Description and Modelling of the Problem

The blade passage modeled here is based on a steam microturbine currently under development [95]. It consists of a 4-mm diameter rotor with a single radial turbine stage. It is designed to operate at 1.2×10^6 RPM (Ω=125714 rad/s), which corresponds to a tip speed of approximately 250 m/s. The nominal blade dimensions are 109 microns chord and 100 microns height. The rotor blade is

obtained by modifying the A3K7 profile [96]. We consider a single blade passage to give an adequate description of the flow and losses within this radial turbine. Figure A.2 gives all details about the computational domain and surfaces where losses are calculated and positions where the velocity profiles will be plotted.

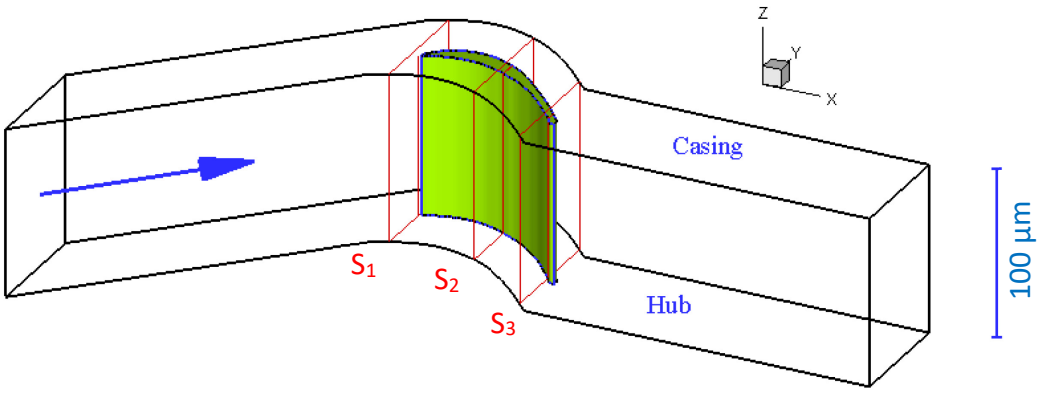

a) Sketch of the cascade computational domain, showing the relevant planes and sections.

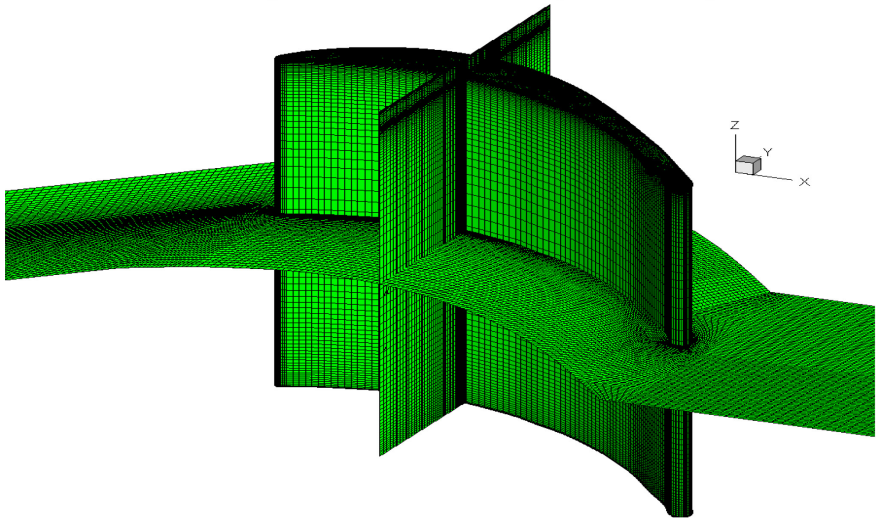

b) Computational discretization, showing grids on the blade surfaces and cross-sections to illustrate the refined grids near the tip clearance, blade surface, leading edge and trailing edge.

Figure A -2 : Computation domain and discretization for the CFD calculations of the microturbine cascade.

The fluid is water vapour entering at 600K, considered as a compressible ideal gas. Stationary adiabatic calculations are performed at different incidences (α =0°, 5°, 10° and 15°) and different tip clearances (0%, 0.5, 1.5%, 2.5%, 5%, 7.5%, 10%, 15% and 20%), varying the inlet total pressure and the scale of the cascade to vary the chord-based inlet Reynolds number from $40<Re_c<2500$, while maintaining Mach number within $0.3<M<0.5$. Losses are calculated by taking averaged

properties at the cascade's inlet (S1) and outlet (S3); plots will also be shown at the mid-chord plane (S2) (Fig. A.2).

The coupled partial differential equations describing the flow field are discretized with the finite volume method, using a commercial solver (Ansys-Fluent). Second order upwind discretization is used. The rectangular staggered grid is non-uniform in both directions: it is finer near the walls and in the tip clearances where gradients are more important. Grid size plays an important role in both convergence and accuracy of the solution. It was indicated that in the 2D case (x-y plane), 20,000 triangular nodes are sufficient to force grid independence [79,94,97] and that 15000 rectangular nodes give identical results [30]. Since the 3D geometry is simply a sweep of the 2D profile, the mesh can be described by its discretization in the three main components. Grids with increasing density were tested for blade passage without tip clearance as a reference. The study indicates that a minimum grid of 40 nodes in the Z direction is sufficient to capture losses, which is consistent with the fact that a minimum number of twelve nodes allow a representation of the boundary layer [98]. Nevertheless, further refinement of the grid was motivated by the desire to represent well the details of the vortices. Table A.1 shows the final grid density, divided into three blocs (upstream of the leading edge, the blade passage, and downstream of the trailing edge):

Table A -1 : Number of grid nodes in each direction, by block.

Direction	Upstream	Passage	Downstream
x	100	130	70
y	90	90	90
z	80	80	80

When a tip clearance is added, we maintain exactly the same mesh up to the blade height, but with an additional mesh to cover the gap. For tip clearances of 0.5%, 1.5%, 2.5%, 5%, 7.5%, 10%, 15% and 20% of blade height the added number of grid nodes along *z* are 6, 12, 16, 18, 26, 30, 30 and 30 respectively. Doubling the number of grid nodes in the tip clearance was verified not to change the results.

Convergence is declared when the cumulative residuals for all conservation equations are less than at least 10^{-10} and when the drag coefficients are mainly constant especially on the top wall of the blade.

A.4 Description of the Flow Structures

The design of recent microturbines has been generally based on 2D calculations, since classical turbines generally exhibit a core meridional flow that validates the 2D assumption. The present study is the first detailed investigation of the 3D flow structures in microturbine to support future design efforts. This section presents the vortical flow structures, consisting of the horseshoe to passage vortex, the tip vortex and the rest of secondary vortices. To distinguish the tip vortex from the passage vortex, a cascade without tip clearance (referred to as *ideal*) is considered first. Influence of Reynolds number on the passage vortex is analysed. Secondly, the more realistic configuration with tip clearance is studied, followed by a discussion of the secondary vortices also present.

To visualise the vortical structures, the Q criteria [99] is used, which is the second invariant of the velocity gradient tensor. The rotation direction is identified by coloring the vortices by the helicity and also adding some streamlines.

A.4.1 Idealized Case without Tip Clearance

Dominant Vortices

The inlet boundary layers that form along the casing and hub endwalls result in y-vorticity that can be viewed as vortex filaments in the lateral direction. As they meet the blade, they wrap around it, creating a horseshoe vortex around the obstacle (Fig. A.3a). In a blade passage, we therefore expect two branches of adjacent horseshoe vortices, along the pressure side of one blade and the suction side of the adjacent blade [87]. This is observed at the hub, but also symmetrically at the tip, for the ideal case of a cascade with no tip clearance flow. Figures A.3 b)-d) illustrate the simulated flow structures with no tip clearance, showing this symmetry. In Fig. A.3b, the value of the Q-factor chosen to draw the iso-surfaces was sufficiently high to only show the most dominant vortical structures, which are the horseshoe vortices. The pressure-side leg is amplified by the passage pressure-to-suction endwall flow and becomes the *passage vortex*, while the other leg (suction side) is weaker and has an opposite sense of rotation. Its presence is identified by streamlines and the Q-factor contours further downstream, where it gets wrapped around the pressure-side leg of the adjacent horseshoe vortex [88]. The other vortical structures in Fig. A.3b correspond to z-vorticity in the boundary layer on the suction side as well as at the blade blunt trailing-edge, from the onset of some vortex shedding.

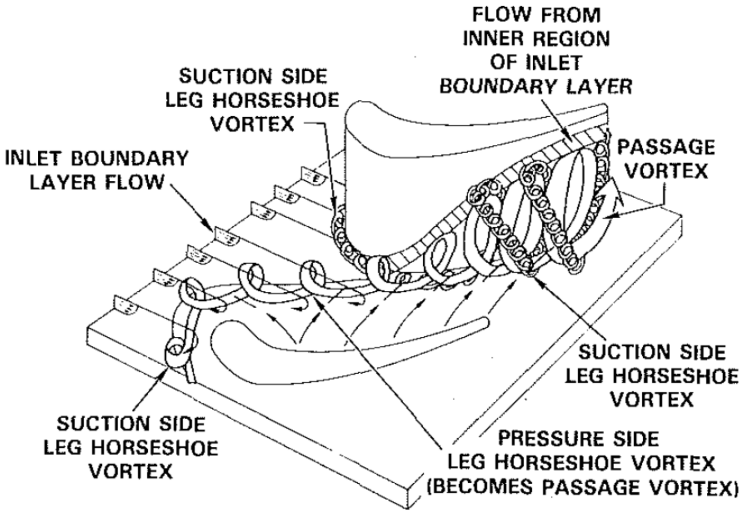

(a) Schematic of horseshoe vortex and formation of the passage vortex, according to Sharma & Butler [87].

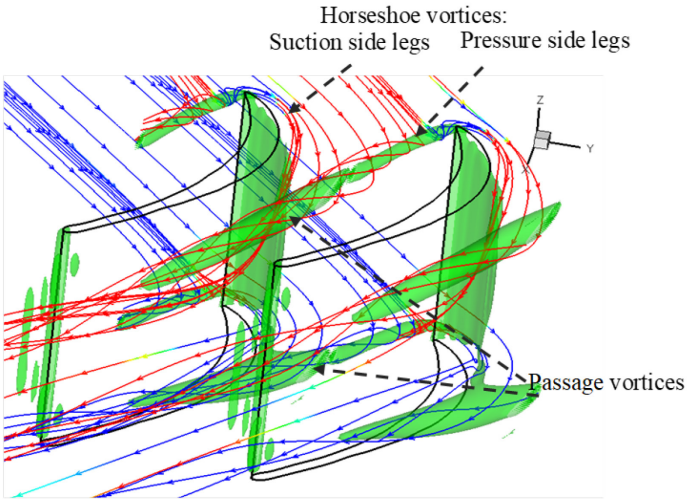

(b) Three-dimensional dominant vortical structures illustrated by Q-factor contour and streamlines, showing the pressure and suction side legs of the horseshow vortex, and the passage vortex that results (tip 0%)

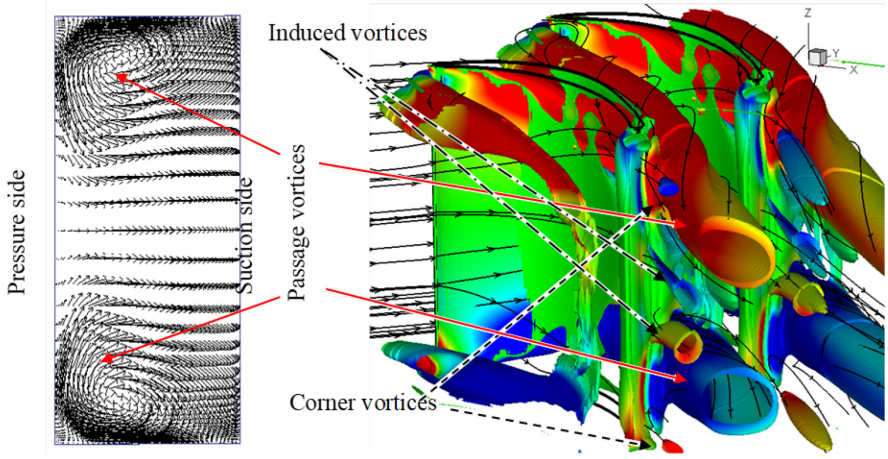

(c) Velocity vectors at mid-chord plane.

(d). Vortex structures in the turbine cascade. (Q-Factor colored by the helicity).

Figure A -3 : Vortex structures for a micro-cascade with no tip clearance at Re=1200 ±50.

Globally, the horseshoe vortex legs combine to form a pair of quasi-symmetrical, quasi-identical counter-rotating blade passage vortices (the lower is clockwise), which are positioned along the suction side near the hub and casing endwalls (Fig. A.3 (b) and (c)).

The present vortices dominate totally the flow and the secondary flow is here the primary one which is a major difference with classical turbines. Indeed, at first glance, there is no core flow by reference to the classical cases and the 2D assumption does not fit in this case. The secondary flow is no longer localised at the hub and the casing. This total large volume occupied by vortices is characteristic to the low Reynolds number; at high Reynolds numbers typically found in large-scale turbomachinery ($Re>10^5$), the secondary flows are localised near the hub and casing [97].

As mentioned in the introduction, the microturbines considered here operate in the laminar regime ($Re_c<2500$), and in this range the flow topology is affected by varying the Reynolds number. From a shape point of view, increasing the Reynolds number deforms the vortex, which is more symmetrical about its axis at the lowest Reynolds numbers (Fig. A.4 inset). Thus increasing the Re_c results in a tendency to crush the vortex on the suction side and end wall (hub or casing) leaving more space for the core flow and affecting the losses related to these secondary flows.

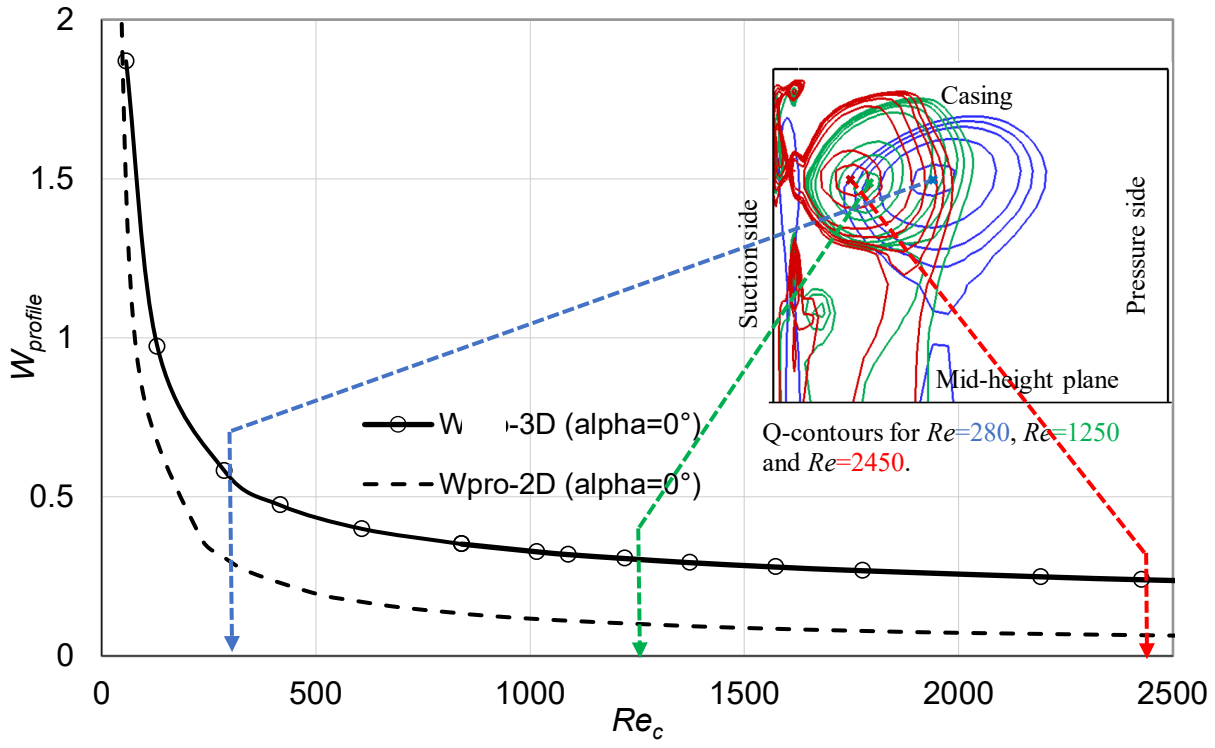

Figure A -4 : Losses versus Reynolds number for an ideal cascade (no tip clearance) with zero incidence. The inset of Q-contours shows that the top passage vortex becomes less dominant (pushed towards the blade and casing).

The low Re_c found in microfabricated turbines is also expected to increase profile losses [95], as shown here by the 2D calculations in Fig. A.4. The profile losses are considered in the ideal case (no tip clearance) for a 0° incidence as an example, defined as $W_{pro} = (\overline{P_{02}} - \overline{P_{01}})/(\overline{P_{02}} - \overline{P_1})$ where the average of each quantity Φ in a considered section is mass-averaged as: $\bar{\Phi} = \int \rho U_x \Phi \, dS / \int \rho U_x \, dS$ .We notice a gradual increase in profile loss from Re_c = 2500 to 1000, followed by a dramatic increase as Re_c is reduced below 500. The 3D losses, which include profile losses and secondary flow losses, follow the same trend, with an apparent bias increase. It can be noticed that secondary flow losses are the largest contributor, compared to the profile losses above Re_c of 1000, stressing the importance of analysing the 3D flows.

Secondary Vortices

In addition to the dominant passage vortex, we notice secondary vortices in Fig A.3d. Although the dominant vortices mostly contribute to the loss generation in the inter blades region, comprehension of the flow structure and minimization of losses are conditioned by all the vortices. Secondary vortices generally appear near the trailing edge, as sees in Fig 3d, adding more complexity in the mixing region.

A first type of secondary vortex appears resulting from the interaction between the dominant vortices and the flow in the center of passage called *induced vortices* [100]. This vortex develops near the mid-height of the blade suction side. When the passage vortex moves away from this wall appears a zone where the fluid is almost quiescent (separation region), the rotation effect of the passage vortex induced the rotation of fluid in this zone like the corner vortex in a cavity. By symmetry there are two counter rotating vortices. These are also called concentrated shed vortex (CSV), as indicated by Kang *et al*. [81].

Finally, we can also notice in Fig A.3d another pair of smaller secondary counter rotating vortices adjacent to the hub and casing, that forms along the suction side of the blade, also found at higher Re_c and called *corner vortices* [100].

A.4.2 Tip Vortex with Tip Clearance Gap

By introducing a tip clearance gap between the rotor blades and the casing, the pressure gradient between the blade pressure side and the suction side tends to force the flow through the clearance gap. This short-circuit flow is a major source of inefficiency in a turbine [92]. This leakage can

induce a tip vortex and affect the flow in the upper half span of the blade. Downstream of the trailing edge, the flow field is characterized by a strong local flow blockage in the tip region, which is important, and the dominant source of loss within the blade passage upper region. Thus, increasing tip clearance leads automatically to increase losses; then seen the importance of manufacturing turbines with the lowest possible clearance. This is not the case in micro-fabrication, where a tip clearance of less than 5% is difficult to be obtained and a tip clearance 10% is realistic or even more.

The tip vortex then appears which is shown by the vorticity layer near the suction side of the blade (Fig. A.5). This clockwise turning vortex modifies the position and the direction of the counter-clockwise top passage vortex and also reduces the shape of the upper induced vortex. The size of the tip vortex mainly depends on the tip clearance gap and the pressure difference. Presence of the passage vortex results in a deformation of the tip vortex in the mixing region. At the blade exit, we also notice that the top corner vortex is carried away by the tip vortex since they are turning in the same direction.

Given the strong impact of the tip clearance on the flow structure, the following sections will further investigate the parameters that affect it, including the tip clearance size (Sec. A.5) and the effect of a relative wall motion, as would be experienced in a rotating machine (Sec. A.6).

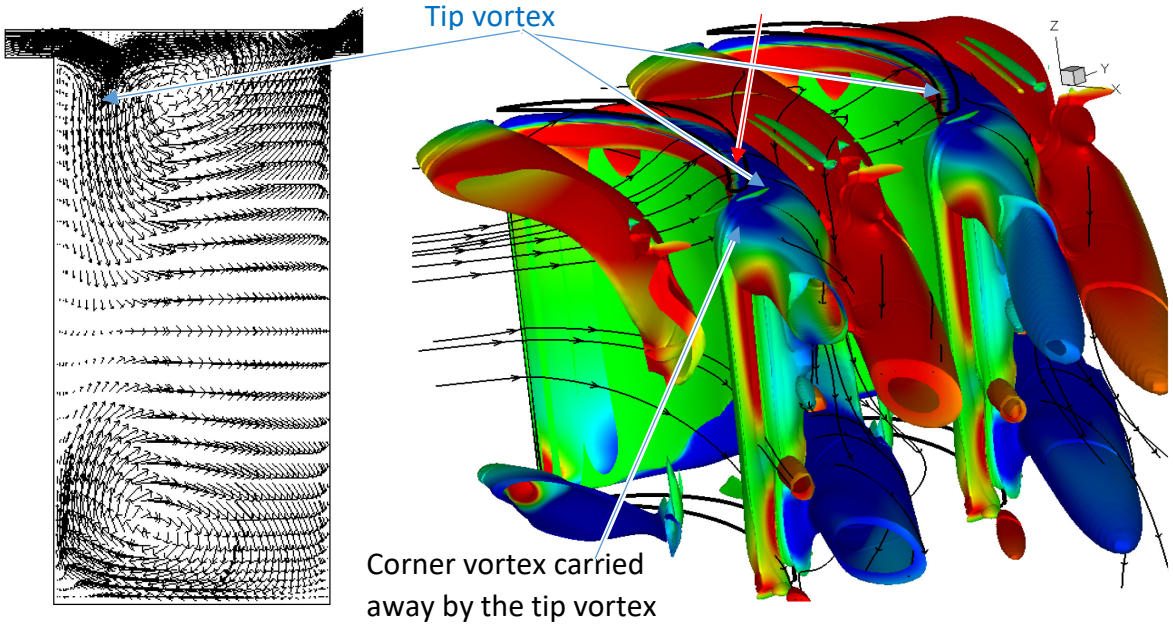

Figure A -5 : Appearance of the tip vortex with tip clearance gap and interaction with the upper passage vortex (Q-criterion with tip clearance 5%, with mid-chord cross section vector field).

A.5. Effect of the Tip Clearance Size

A.5.1 Flow Topology and Existence of the Tip Vortex

The above observations with no tip clearance remain valid when the tip clearance size remains small. As seen in Fig. A.6, which shows the vorticity magnitude contours for different small tip clearances (0%, 0.5%, 1.5% and 2.5%) in the mid-chord plane, the two passage vortices that results from the horseshow vortex remain well defined. It also indicates an absence of the tip vortex at low tip gaps but a loss of symmetry between the two passage vortices when increasing the tip gap size.

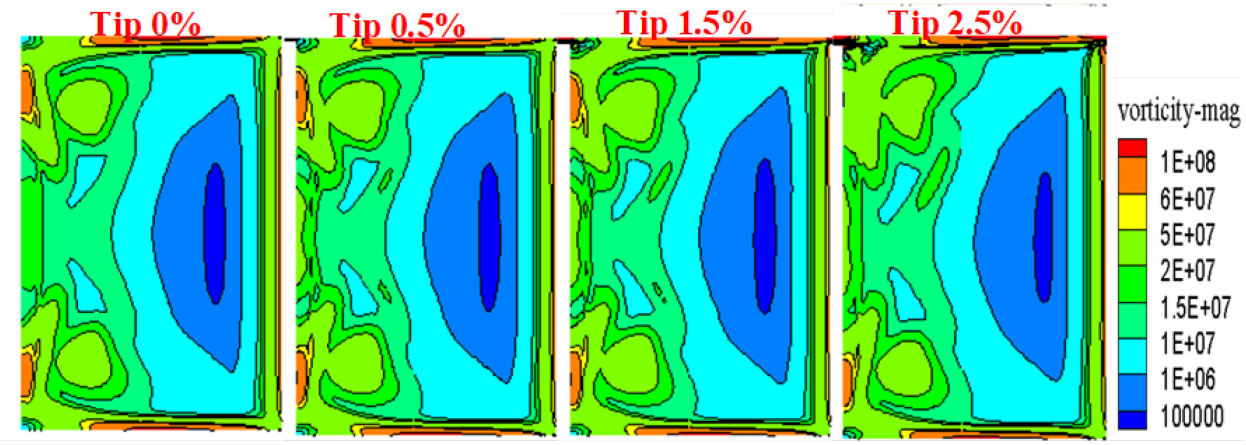

Figure A -6 : Vorticity magnitude contours at the mid-chord plane for small tip clearance, showing the absence of a tip clearance vortex below 2.5% tip clearance (Stationary blade at Re=1200±50).

For larger tip clearance gaps (10%), the presence of the tip vortex is characterized by its large size compared with the passage vortex (Fig. A.7). As seen in this figure, the tip vortex dominates the upper region making the passage vortex secondary in the cases of gaps 10% and more. This means more complexity, since the tip vortex becomes dominant and takes the place of the top passage vortex. The top passage vortex becomes distorted and disappears progressively along the flow. At the exit plane, the two principal vortices are rotating in the same direction.

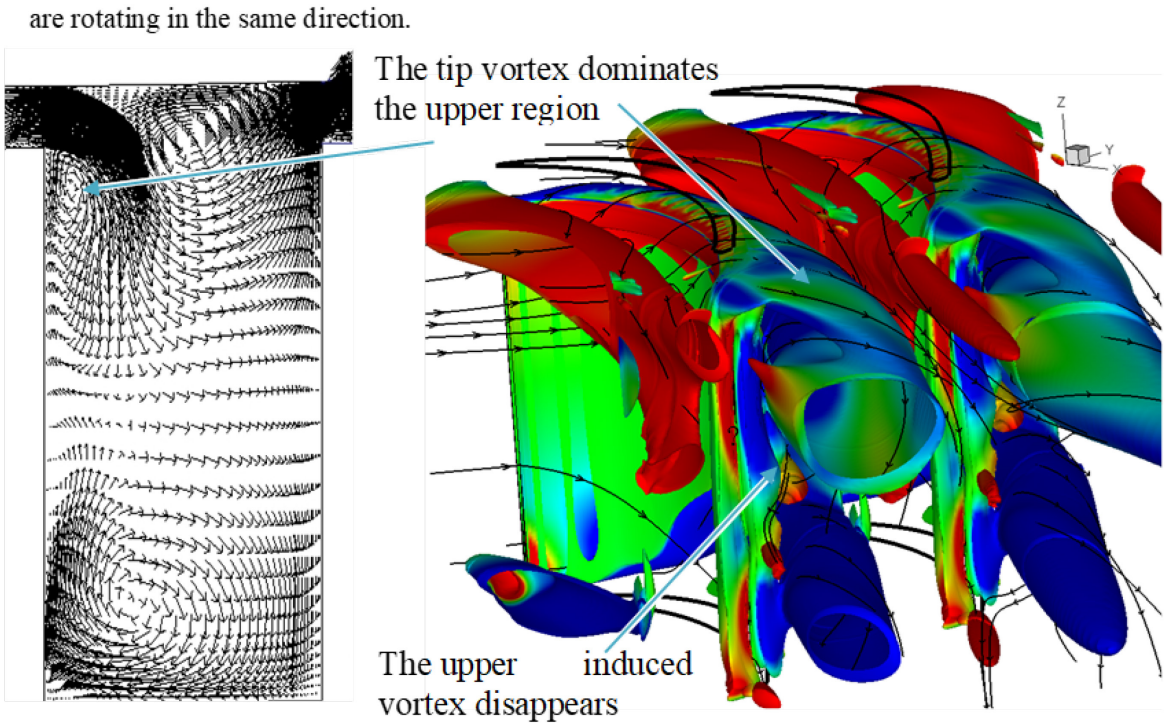

Figure A -7 : Dominant tip vortex over top passage (horseshoe) vortex (Q-criterion with tip clearance 10%, and mid-chord cross section vector field).

As summarized in Fig. 8, increasing the tip clearance size results in an increased size of the tip vortex. This figure also indicates that three different regimes occur:

- For the 2.5% tip clearance (or less), there is no tip vortex, so the structure of the flow is comparable to the ideal cascade but slightly asymmetric.

- For a 5% tip clearance, the tip vortex is present and does not exclude the top existing passage vortex (analogous to classical turbomachines). The structure of the flow is based on that of an ideal flow passage (dominant passage vortex), with the additional presence of the tip vortex.

- For the 10 % tip clearance or more, the flow configuration changes totally: the tip vortex becomes dominant over the top passage vortex.

Another important visual result from this figure is that increasing the gap size makes the tip vortex larger and leads to more mixing and then more losses are expected. To explain this regime and better determine the criteria that defines their ranges, the following sections will further analyse the tip clearance flow and the forces at play, and formulate an analytical criterion.

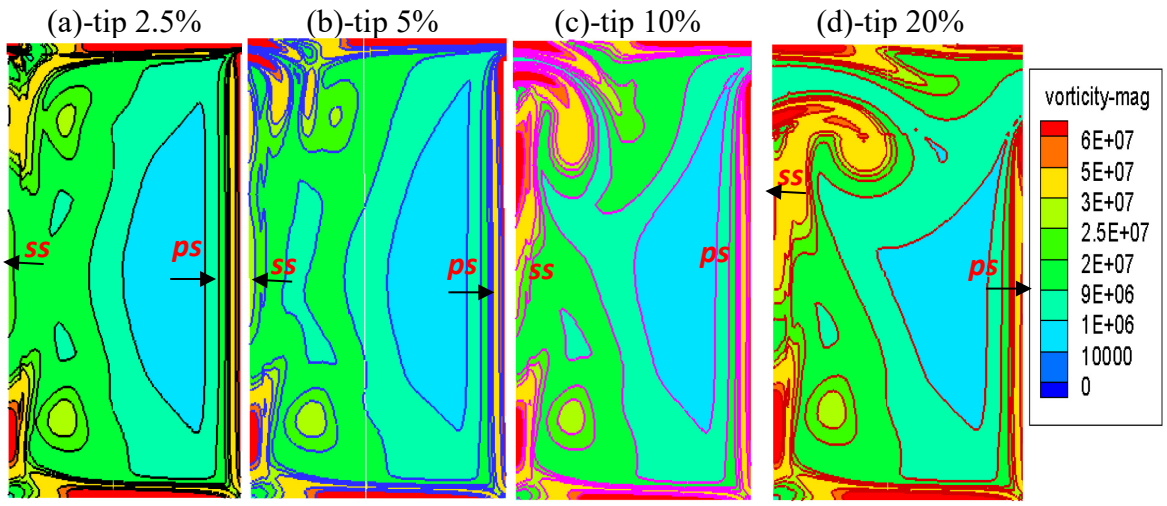

Figure A -8 : Contours of vorticity magnitude at mid-chord plane, for increasing tip clearance size (2.5% to 20%), showing the transition from no tip vortex to a dominant tip vortex.

A.5.2 Flow in the Tip Clearance Region

As indicated in the introduction, nine different tip gap sizes have been considered (0, 0.5, 1.5, 2.5%, 5%, 7.5%, 10%, 15% and 20%) in order to clarify some point such as the appearance of the tip vortex and the occupation of the top region (near the casing) by the tip vortex or by the passage vortex. From the CFD results, the flow rate and forces acting in the tip clearance region can be analysed to define the regimes for tip vortex formation. To do so, a control volume containing the tip clearance region is used, as illustrated in Fig. A.9. From mass conservation in steady-state, the mass flow rate is constant throughout the tip clearance and can be calculated at the entry or exit. The balance of wall shear and pressure force will also applied in this control volume.

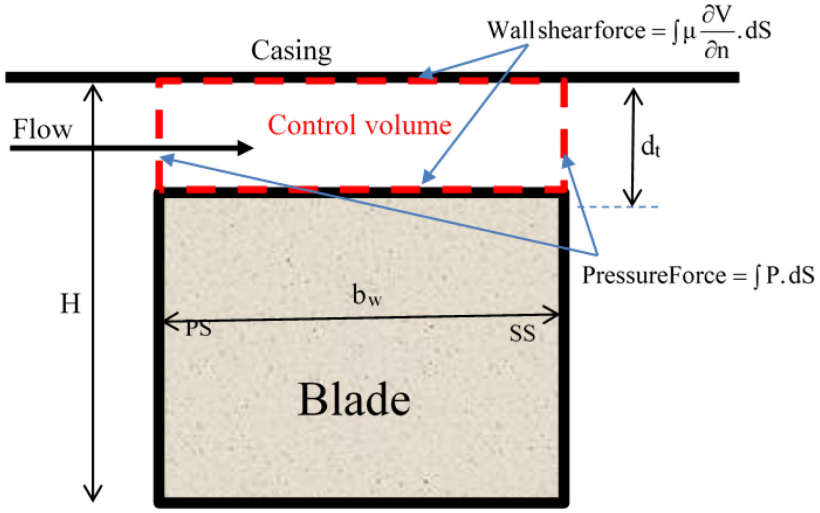

Figure A -9 : Schematic of the tip clearance control volume with the force.

Figure A.10a shows the leakage mass flow rate versus the tip clearance size. Generally, the leakage flow increases with gap size and follows a linear trend for large tip clearance (>8%). For small tip clearance (<3%), the flow rate follows a trend for Poiseuille flow, as shown by the dashed line in Fig A.10a, and appears to represent a viscous dominated regime. This is better shown by the force balance presented in Fig. A.10(b), which compares the flow leakage driving effect of the increment of blade tip pressure difference caused by the blade loading (solid line) to the viscous resistance in the gap (dashed line).

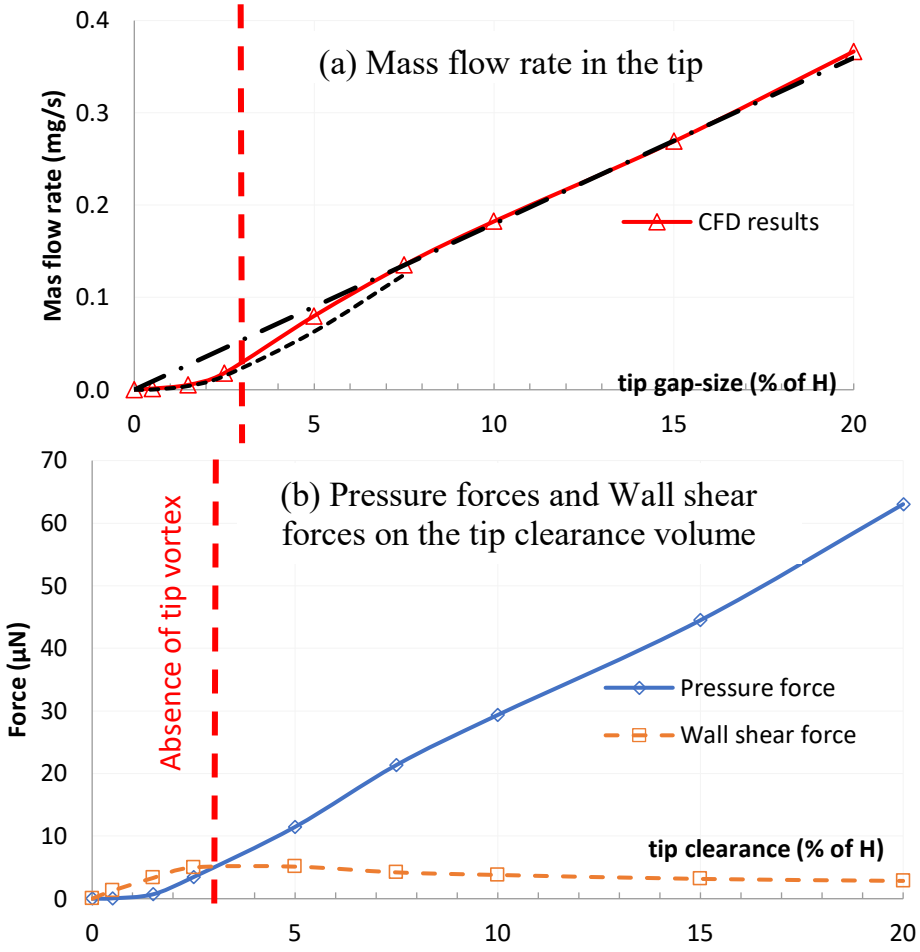

Figure A -10 : Leakage mass flow rate and force balance in the tip clearance, as a function of tip clearance size.

For a tip clearance lower than ~3%, the wall shear force is dominant and this correlates with the absence of the tip vortex observed in the previous section. The dominance of this force in the tip clearance is also coherent with the flow rate characteristic of Poiseuille flow, as indicated in Fig. A.10(a). When the driving pressure force dominates over the viscous forces, a higher momentum

tip clearance flow is created, which is coherent with the appearance and intensification of the tip vortex at larger tip clearance size see in Fig. A.8.

Moreover, the presence of a tip vortex can be verified by considering the velocity profiles in the tip clearance as indicated in the Fig. A.11. When the tip vortex is absent (tip clearances <3%), the leakage flow velocities are lower and present a fully developed profile. For larger tip clearances (5% and 10%), when the tip vortex is present, the velocities increase, and we start to observe a core flow. The asymmetry of the velocity profile is due to the effect of flow entering the gap with a spanwise velocity component from the blade side.

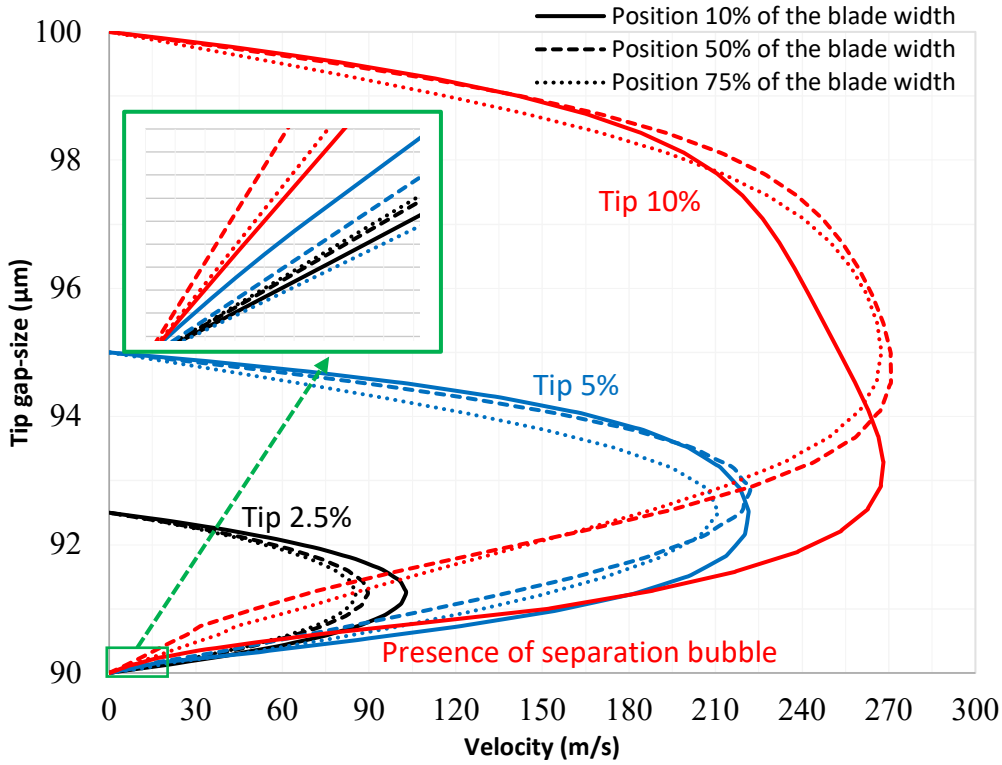

Figure A -11 : Velocity profile across the tip clearance, taken at mid- chord for three different tip gap sizes (2.5%, 5% and 10%) at three positions.

A.5.3 Dominance of the Tip Vortex

The analogy with the classical turbomachinery is quite possible when the tip vortex is present and does not dominate the upper region. For larger tip clearances however (>10%), we are dealing with new flow conditions. In the design of microturbines, we should take this regime onto account since the microfabrication and bearing technologies do not allow fabrication of small gap-sizes that would be beneficial to minimize losses. The dominance of the tip vortex is a limit that should not

be exceeded to obtain reasonable losses. This limit can be correlated with the averaged wall shear stress on the top blade, as plotted in Fig. A.12, normalised by the average wall shear stress at the hub. The wall shear stress initially increases up to a gap size ~3%, then decreases until a gap size of approximately 8%, and then appears to remain constant: Thus the viscous resistance effect is present for this gap range [0%, 8%] but for beyond (>8%), the gap is large enough to consider that the casing doesn't directly affect the top blade wall. This limit corresponds to a mass flow behaviour typically linear (Fig. A.10a), since the pressure variation from the pressure side to the suction side is mainly constant. This is effectively the gap size limit that should be respected when designing micro-turbines to prevent excessive losses. It is consistent with Fig A.11 as the wall shear for the 2.5% tip clearance is greater than for the 5% tip clearance, which in terms is larger than for the 10% tip gap.

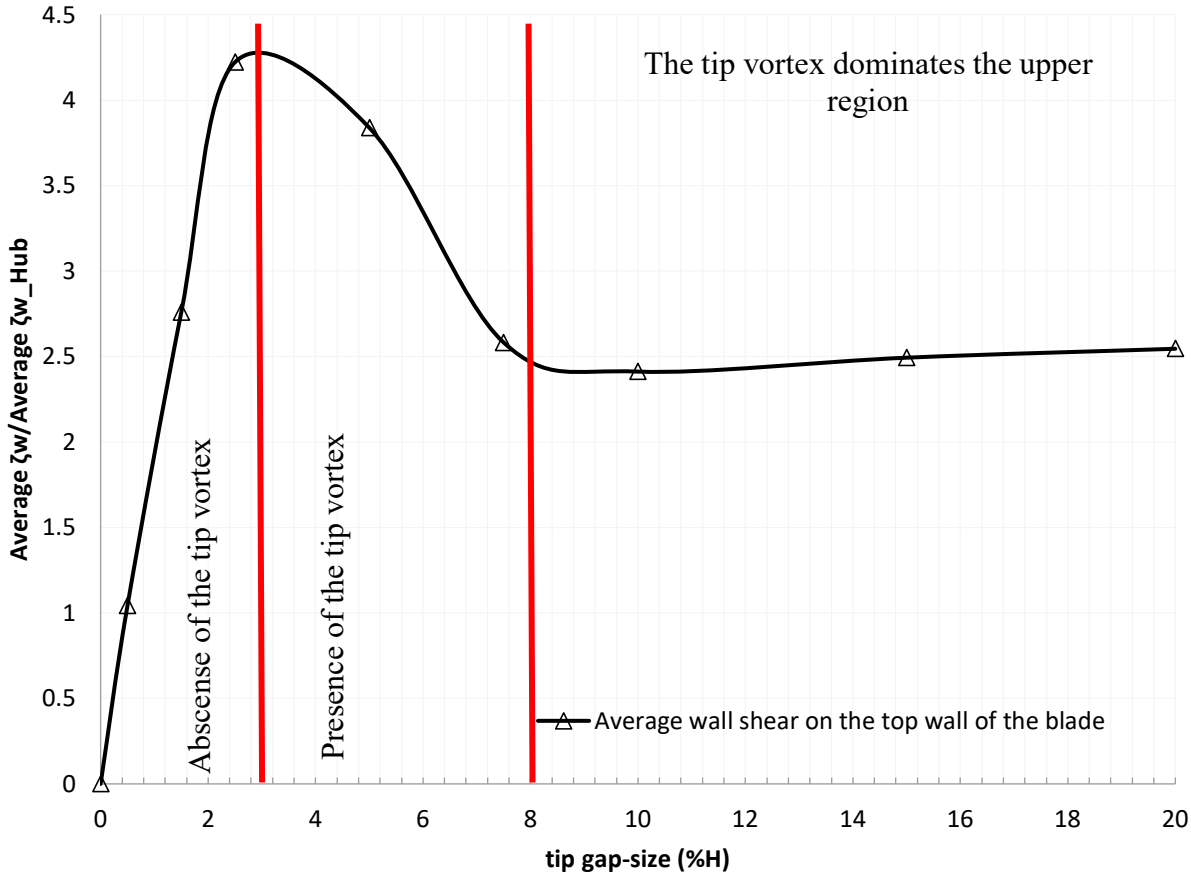

Figure A -12 : Average shear wall on the top wall of the blade (tip surface), coherent with the observed tip vortex regimes.

A.5.4 Effects on the Blade

Generally in a conventional turbine, the vortex structures are localised near the hub and casing, and their traces on the blade surface are seen only on a small fraction of the total blade surface; this is not the case when considering micro-turbines. As indicated in Fig. A.13, showing the contours of

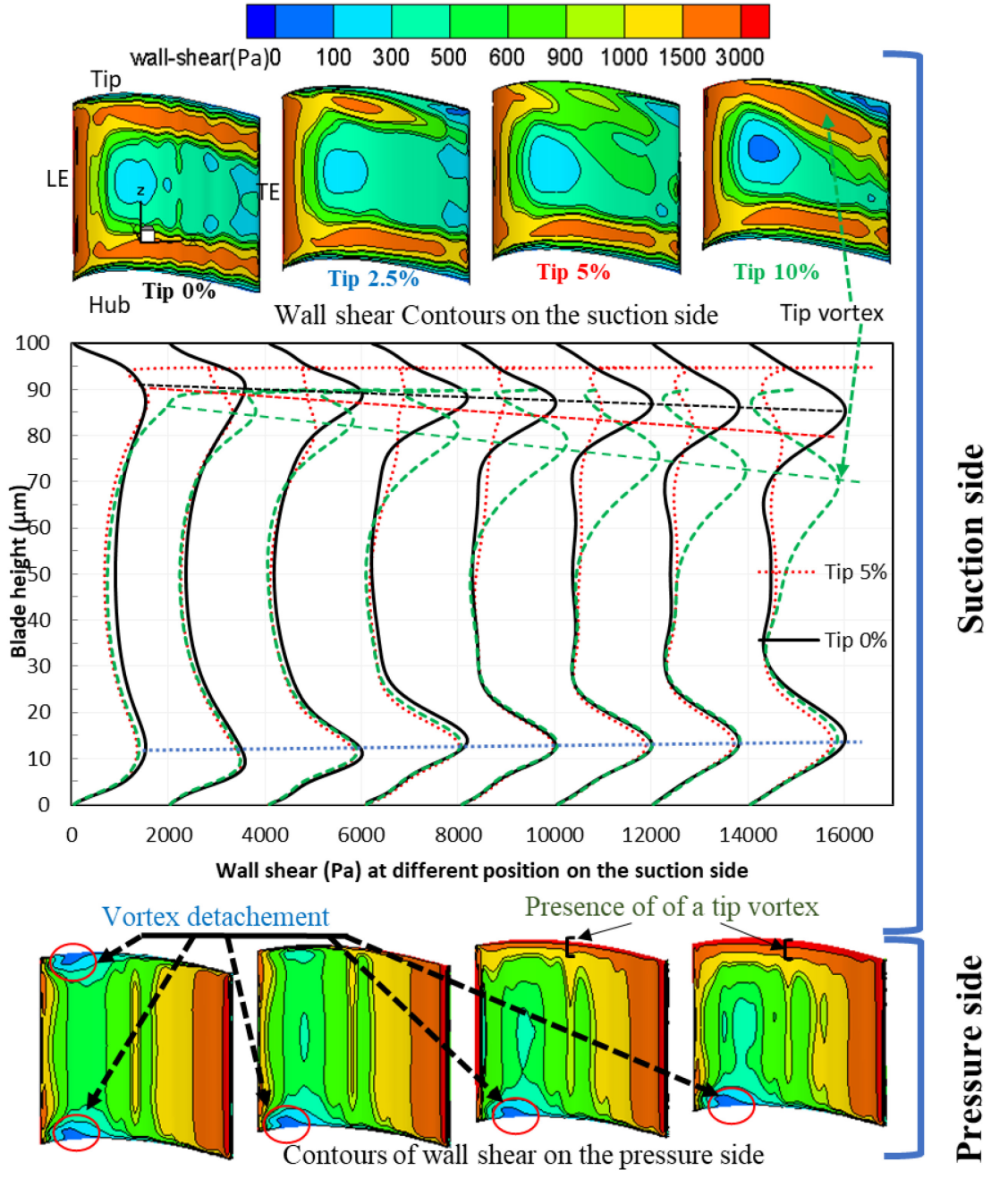

Figure A -13 : Contours of wall shear on the blade sides (ss and ps) and wall shear stress at different positions of the suction side (equipositions from the leading edge to the trailing edge).

wall shear on the suction side (ss) for different tip clearance sizes, traces of the vortices occupy a significant part of the blade span. Wall shear from the vortices show the expected symmetry for 0% tip clearance, some asymmetry due to the presence of a the small gap (2.5%), the presence of the small tip vortex at 5% gap that prevents the contact between the upper passage vortex and the suction side, and reappearance of shear near the tip, but due to the dominant tip vortex. For all these tip clearance, the lower part of the blade remains comparable.

The same observations are quantified on the suction side by plotting the wall shear stress along the span at different vertical lines from the leading to the trailing edges as indicated in the Fig. A.13. The lower region of the blade near the suction surface seems un-affected when changing the tip clearance; it indicates essentially that the lower passage vortex trace is comparable for all tip clearances (see the blue dotted line). The trajectory of the bottom passage vortex is mainly unchanged. This is not the case for top region where the presence of the tip vortex (tip 5%) pushes away the top passage vortex making its trace weak on the suction side. However, in the 10% tip clearance case, the top vortex trace is not due to the passage vortex but to the tip vortex.

Now if the pressure side (lower part of the Fig. A.13) is considered, clearly the wall shear is more important in those surfaces; it is increasingly important from the leading edge to the trailing edge. These latest cases indicates two important points: 1) the zone where the wall shear is approximately zero indicate that from those region detached the passage vortex, and 2) in the 5% and 10 % cases, the horizontal layer near the tip with maximum shear is indicative of the presence of the tip vortex.

The static pressure distributions for two tip clearances (5% and 10%) at 25%, 50% and 75% of the blade height are given in Fig. A.14 by the static pressure coefficients, $C_p=(P-P_{in})/(0.5\rho_{in}U_{in}^2)$ with P_{in}, ρ_{in} and U_{in} are respectively the static pressure, the density and the velocity at the cascade inlet. The position 50% of the blade height is supposed to be a reference since at mid-span the present vortices have little influence (see also Fig. A.11). However, on the suction side, we see a difference between the 5% and 10% tip clearances. Up to 30% of the chord (x/C=0.3), the static pressure coefficient C_p is less in the case of 10% tip clearance, but after (x/C>0.3) the trend is reversed. This is attributed to the dominant tip vortex (for 10% tip clearance) which results in more pressure on the suction side.

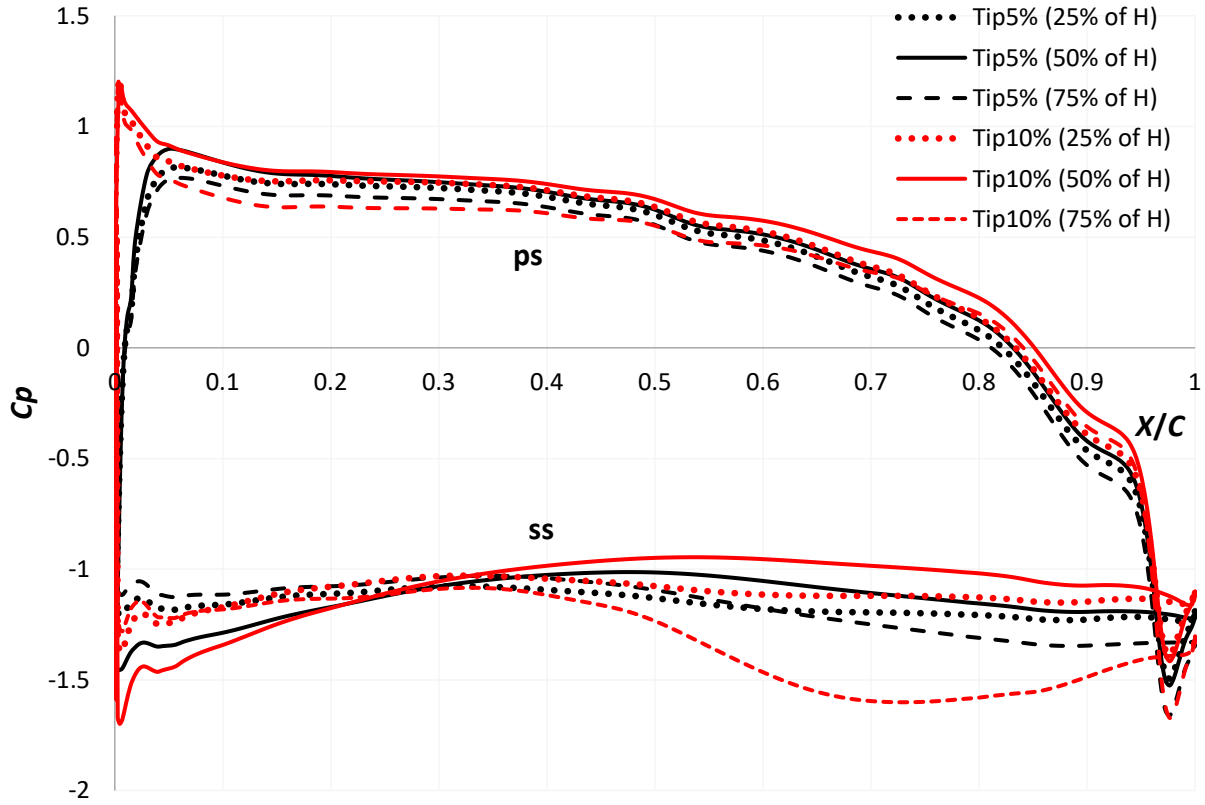

Figure A -14 : Static pressure distribution at 25% (dotted), 50% (line) and 75% (dashed) of the blade height for the tip gaps 5% (black) and 10% (red).

A.6 Effect of Rotation

Generally, the losses are estimated in a turbine by considering a static passage, or cascade, without considering the rotation effect. However, the casing relative motion transports the adjacent fluid in the opposite direction of the tip leakage flow, resulting in a reduction of the effective tip clearance section. Given the importance of viscous forces in the current range of interest, the leakage flow structure is therefore suspected to be very different from that a static condition. Furthermore, the inertial forces in a planar radial turbine may also be of importance. Rotation effects on the flow structure are illustrated by considering the following configurations: flow as a stationary reference (cascade, as the previous sections), the flow in a rotating reference frame, and a rotating reference frame with stationary top casing wall. The last case describes the real operating conditions for a microturbine.

This section will first present the vortical flow structures and the effect of rotation, then investigate further the flow through the tip clearance region to formulate an analytical criterion for determine when these effects are important.

A.6.1 Vortical Structures with Rotation

When the flow is in a rotating reference frame the presence of centrifugal and Coriolis forces are found not to change the flow structure compared to the reference non-rotating case. All the vortices in the static case are still present and evolve quasi-identically. However, with a relative motion of the outer casing wall (Fig, A.15); the latter imposes its velocity to the adjacent fluid resulting in moving the passage vortex towards the suction side. As a result, the tip clearance flow is constrained near the suction side of the blade, limiting the zone occupied by the tip vortex and reducing the leakage flow. The tip clearance flow is mostly routed parallel to the suction surface instead of forming a well-defined vortex. As a consequence of this configuration, the tip vortex is crushed or even vanished (5% tip clearance); the passage vortex on the other hand is deformed remains dominant, being less disturbed by the tip vortex.

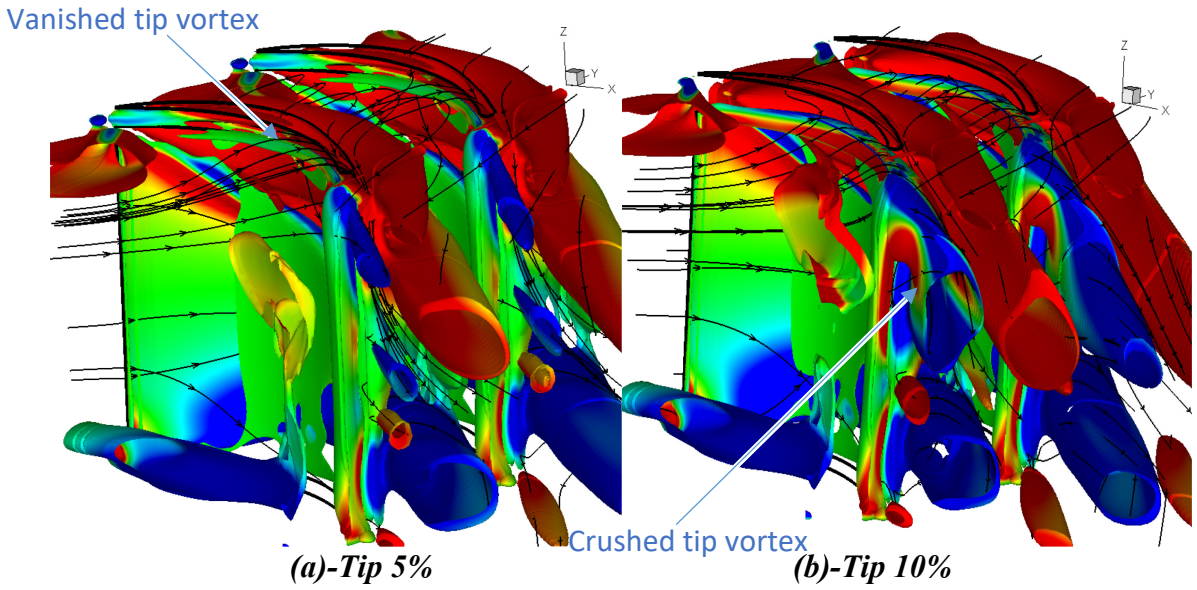

Figure A -15: Vortical structures in the case of rotating reference frame with a stationary top casing wall (Q-criterion for Re=1200 and a rotating speed=1.2x106 rpm).

A.6.2 Tip Clearance Flow with Rotation

Hence, the rotation affects the structure of the flow due to the relative motion of the outer casing wall. Evidently, we should see the impact of varying the rotation speed on the leakage flow, so three different typical speeds for microfabricated turbines are considered [6]: $1.2x10^6$(red), $0.7x10^6$(blue) and $0.12x10^6$(green) rpm. Figure A.16 indicates the position of zero tangential flow

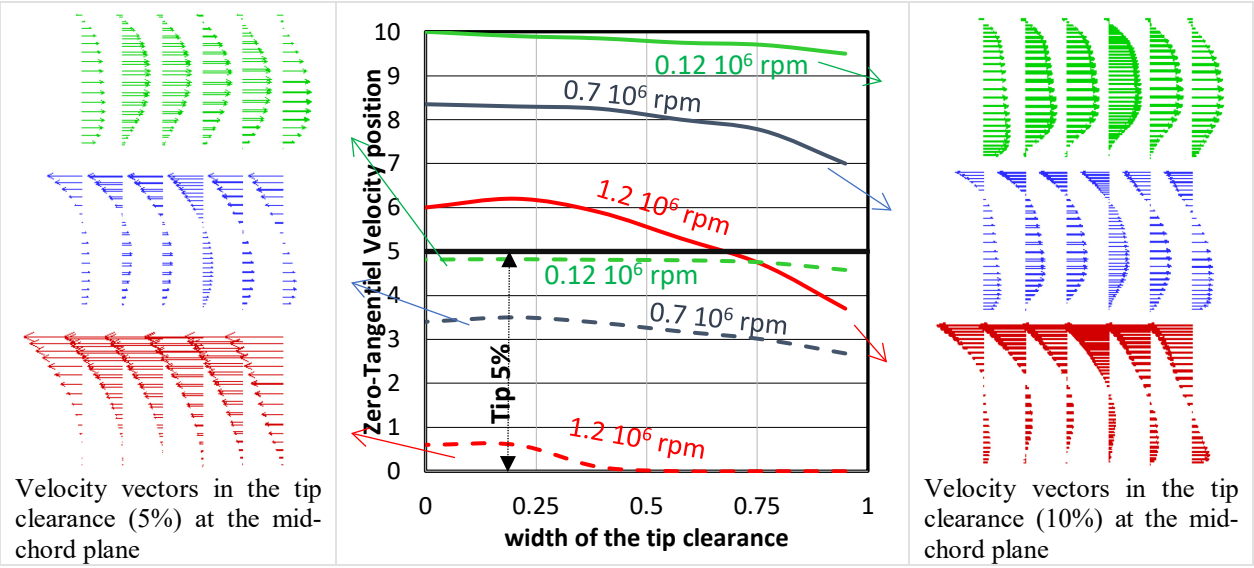

Figure A -16 : Zero tangential velocity position in the tip clearance at the mid-chord plane for Re=1200 ±50. Case with tip clearance 5% (dashed) and 10% (solid).

velocity in the tip clearance at mid-chord plane, for the tip clearances of 5% and 10%. The top figure indicates that at lower rotational velocity (0.12x106 rpm), the leakage flow is not really affected by the relative casing motion; it is comparable to the static case. When increasing the velocity, the blockage of the leakage flow begins (see 0.7x106 rpm); the blocked zone by reference to the gap size is more important for the 5% tip clearance than the 10% case. For the highest velocity (1.2x106 rpm) the leakage flow is totally blocked (even reversed) in the 5% tip clearance while partially blocked in the 10% case. It is also possible to relate this result to Fig. A.10(b), suggesting that no tip vortex is expected when the non-blocked portion of the gap is lower than 3% of blade height. More generally, these effects on the leakage flow and the dynamic vortices, allow a similarity with the static cases. The rotating case with 5% clearance (Fig. A.15a) reminds the static case without clearance (Fig. A.3d) and the rotating case with 10% clearance (Fig. A.15b) reminds the static case with 5% tip clearance (Fig. A.5).

A.6.3 Criteria for Clearance Flow Blockage due to Rotation

In Fig. A.17, we summarise the totally blocked and partially blocked tip clearance flow conditions, as a function of tip clearance and the rotational speed. This map indicates that for microturbines with a tip clearance of 10% (realistically obtained with microfabrication), the leakage flows are not totally but partially blocked.

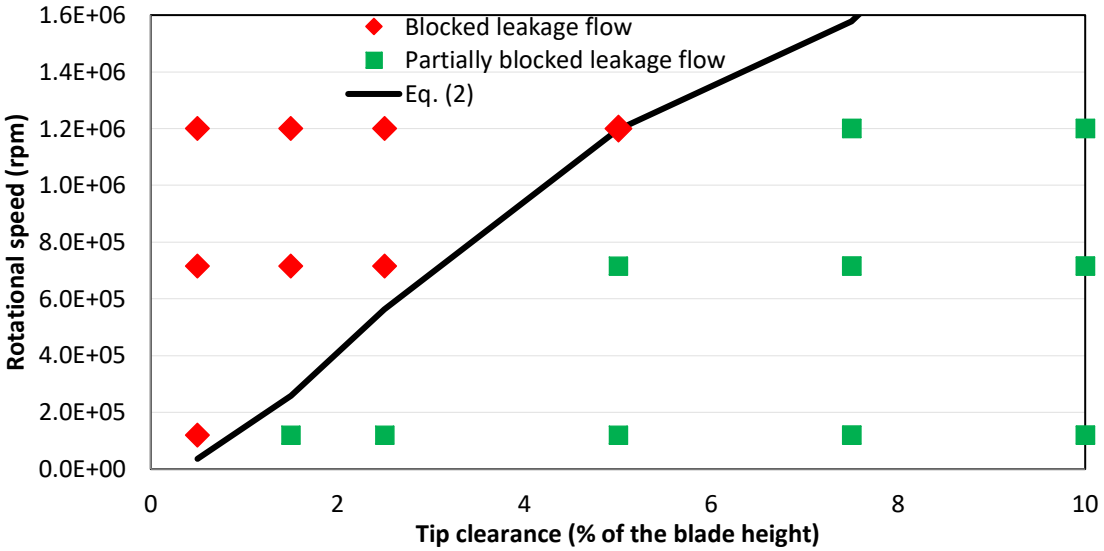

Figure A-17 : Map of blocked and partially blocked leakage flow for Re=1200 ±50

However, these calculated flows and blockage conditions do not only depend on the tip clearance, but also on the pressure difference across the ss and ps of the blade. To better define a criterion, we will compare this driving pressure difference to the net viscous wall shear forces. The velocity profiles observed in Fig. A.16 can be attributed to the superposition of a Poiseuille flow (pressure driven) and Couette flow, driven by the relative motion of the casing wall. When the rate flow induced by the relative motion balances or is greater than the Poiseuille flow, there is no flow rate to form a tip vortex. Assuming parallel plates, once can express this condition as:

$$\int_0^{d_t}\left(-\left(\frac{dP}{dy}\right).\frac{z.(d_t-z)}{2\mu}-U_w.\frac{z.}{d_t}\right).dz \le 0 \qquad (1)$$

where U_w is the wall velocity, d_t is the tip clearance size and μ is the dynamic viscosity. With the pressure gradient assumed constant,

$$-\left(\frac{dP}{dy}\right) \approx \frac{\left(P_{Tip/ps}-P_{Tip/ss}\right)}{\Delta y}=\frac{\Delta P}{\Delta y} \qquad (2)$$

where $\Delta P = \Delta P_{Tip}$ is the pressure difference across the tip clearance zone and $\Delta y = b_w$ is the thickness of the blade. The following approximate relation is then obtained:

$$\frac{{d_t}^2}{6.\mu.U_w}\frac{\Delta P}{\boldsymbol{b_w}} \le 1 \qquad (3)$$

If the pressure difference across the tip clearance zone (ΔP_{Tip}) is related to the pressure variation on the blade sides (ΔP_{ps-ss}), the estimation of this later allows us to determine if the leakage flow

is blocked or not. Looking for a relation between ΔP_{ps-ss} and ΔP_{Tip}, the numerical calculations are used in Fig. A.18, plotting their ratio versus tip clearance. Given the different regimes above and below 8% tip clearance (Fig. A.12), we can fit linear and exponential trend lines in these regimes, respectively, to define relations between the pressure difference across the tip clearance and the pressure variation on either side of the blade (Fig. A.18).

For a tip clearance lower than 8%, the blockage condition can therefore be expressed as:

$$\frac{{d_t}^2}{6.\mu.U_w}\frac{\Delta P_{ps-ss}(0.9\exp(-0.23tip(\%)))}{b_w} \leq 1 \quad (4)$$

This criterion is indicated in Fig. A.17 and seems sufficient to predict if there is a total blockage or not when the geometry of the blade, the boundary conditions and the tip gap size are known. For a tip clearance greater than 8%, there is no need for a criterion since at a maximum rotational velocity of $1.2\text{x}10^6$ the leakage flow is always partially blocked.

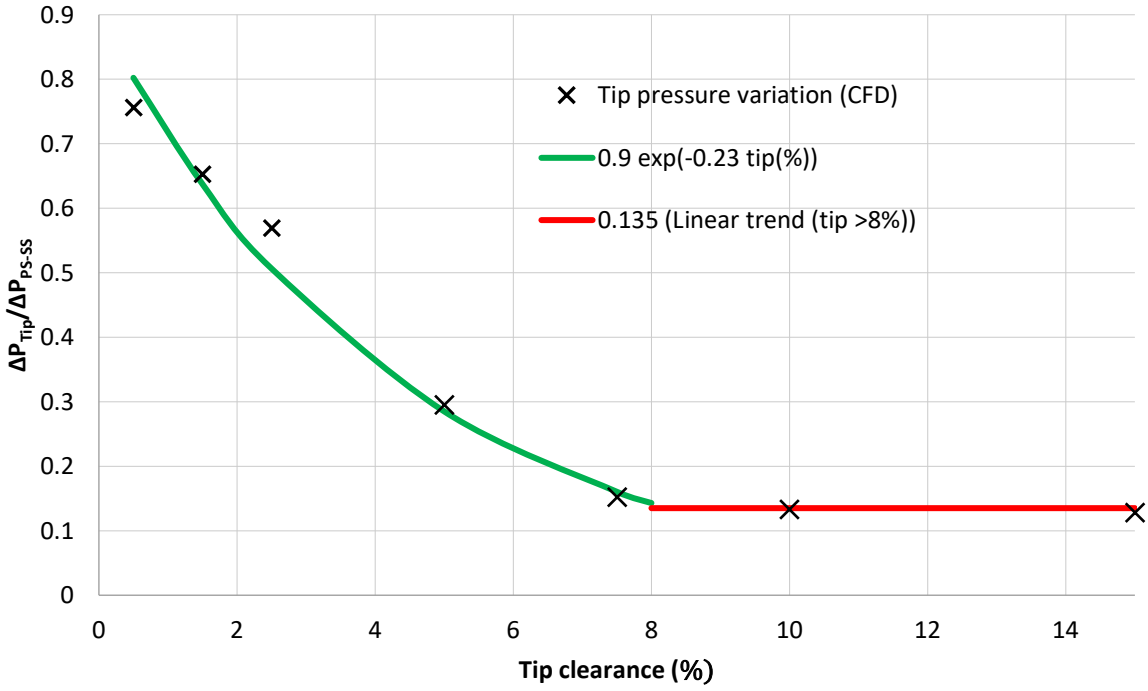

Figure A-18 : Pressure difference across the tip clearance normalised by the pressure difference between the suction and pressure sides of the blade (Re=1200 ±50).

A.7 Conclusion

This paper presented a numerical analysis of subsonic laminar flow through a cascade for microturbomachinery applications operating at low Re. Numerical calculations were done with 3D

static geometries associated to nine tip clearances (0%,0.5%,1.5% 5%, 7.5%, 10% , 15% and 20%) at for $40 \leq Re \leq 2500$ and four different incidences (0°, 5°, 10° and 15°). The same geometries were also studied with the effect of rotation.

For all the considered geometrical and physical parameters with and without rotation effect, numerical calculations indicate that the flow is essentially 3D and the whole volume is occupied by vortices. Consequently, there is no core flow and the classical 2D (meridional) design assumption would not be applicable.

When the static cascades are considered, the calculations indicate essentially three different flow configurations classified according to the tip gap size, small [0-3%], medium [3%-8%] and more than 8% of blade height. The distinction between these different flow configurations was based on a detailed study of the leakage flow. Specifically, the mass flow through the tip clearance was characterized through a comparison between the pressure and shear forces in the tip gap volume and also the wall shear applied of the top wall blade.

At relatively small tip clearance, lower than 3%, the wall shear force in the tip clearance dominates, so the leakage flow is reduced and of Poiseuille type; this correlates with the absence of the tip vortex. Also within this tip clearance range, the mean wall shear stress on the blade top-wall increases. The calculations indicate the presence of two quasi-symmetrically positioned passage vortices at the hub and casing, near the suction side. The trajectory of these vortices depends on the Reynolds number and incidence. Two secondary corner vortices were identified on the suction side at the exit blade corners near the hub and the casing. Also, induced vortex appears resulting from the interaction between the dominant vortices and the core flow.

For a tip clearance within the range [3%-8%], the tip vortex appears in view, which is justified but the driving pressure force that dominates over the shear force in the tip clearance. Increasing the tip gap within this range leads to a decrease of the blade top-wall shear. The limit 8% was determined by a leakage mass flow rate that begins to follow a linear behaviour and mean shear on the blade top-wall that tends towards a constant as tip clearance is increased. This case is more representative of the flow structure and losses in a microfabricated turbine. The tip vortex modifies the position and the direction of the upper passage vortex. This vortex carried away the top corner vortex and the upper induced vortex becomes smaller compared to the lower one.

For a tip clearance greater than 8%, the pressure difference across the tip clearance remains unchanged. Consequently, the pressure force increases by increasing the tip gap size and largely

dominates the shear force (which remains constant). The leakage mass flow rate behaves linearly since it depends on the tip gap size. The tip clearance vortex dominates totally the upper region making the top passage vortex secondary and the upper induced vortex is not seen. This situation does not exist in traditional turbomachinery, but is within the achievable range for microfabricated turbines. This tip clearance value should be considered as a limit to reduce losses when designing a microturbine.

For all the three configurations, the lower region near the hub seems to be not affected by the tip gap variation and remains qualitatively unchanged i.e. a presence of a passage vortex, corner vortex and an induced vortex.

When the flow is considered in a rotating reference frame, the effect of rotation was found to be negligible.

However, when the outer casing is stationary with respect to a rotating blade passage, the flow configuration near the tip is completely modified. The tangential shear from the wall motion reduces the tip leakage flow and negates the tip vortex, favoring the top passage vortex. The low rotational speeds lead to a partially blocked leakage flow and increasing this velocity could even lead to a totally blocked flow. Therefore increasing the rotational speed can be seen decrease the leakage flow rate which gets rid of the tip vortex and its associated losses.

At small tip clearances (lower or equal to 5%), the leakage flow can be totally blocked when increasing the rotational velocity. To define the blockage conditions, a criterion is proposed, based on the geometry of the blade, the boundary conditions and the tip gap size. When the tip gap is partially blocked there is no tip vortex if the non-blocked portion of the gap is lower than 3% of blade height, according to the calculation in the static cases.

Funding Sources

This project was funded by the National Plan for Science, Technology and Innovation (MAARIFAH) – King Abdulaziz City for Science and Technology - the Kingdom of Saudi Arabia – award number 14-ENE2142-03.

Acknowledgments

The authors acknowledge with thanks Science and Technology Unit, King Abdulaziz University for technical support.

ANNEXE B : Photomasques

Les dessins des photomasques utilisés dans la fabrication de la microturbopompe (chapitre 4) sont illustrés ci-dessous. Le numéro du photomasque représente l'étape de fabrication où il est utilisé (voir Figure 4-12). Le photomasque « *Alignment* » est utilisé pour fabriquer les marques d'alignement. Le photomasque de l'étape 2 est illustré au complet (16 puces), tandis que le reste des photomasques sont illustrés par une seule puce.

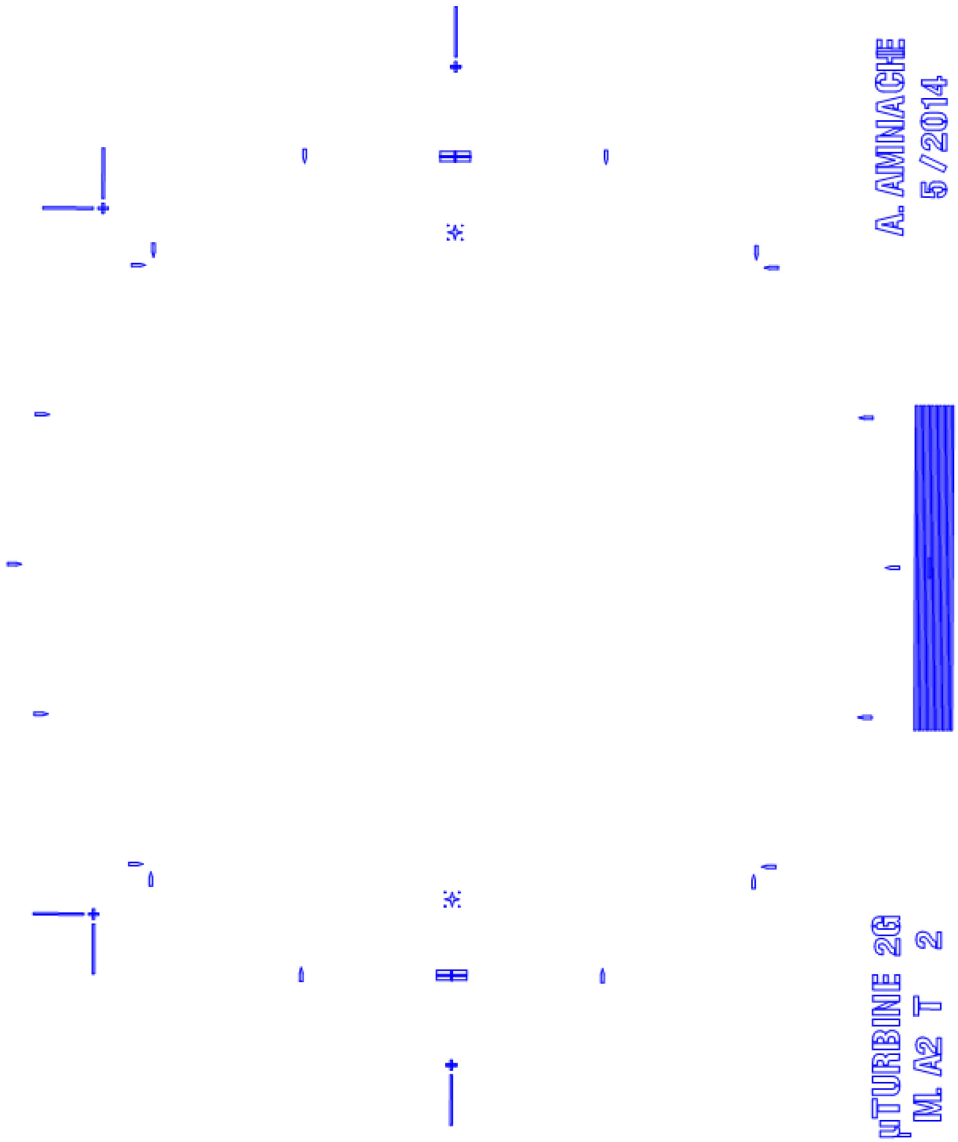

Photomasque *Alignment*

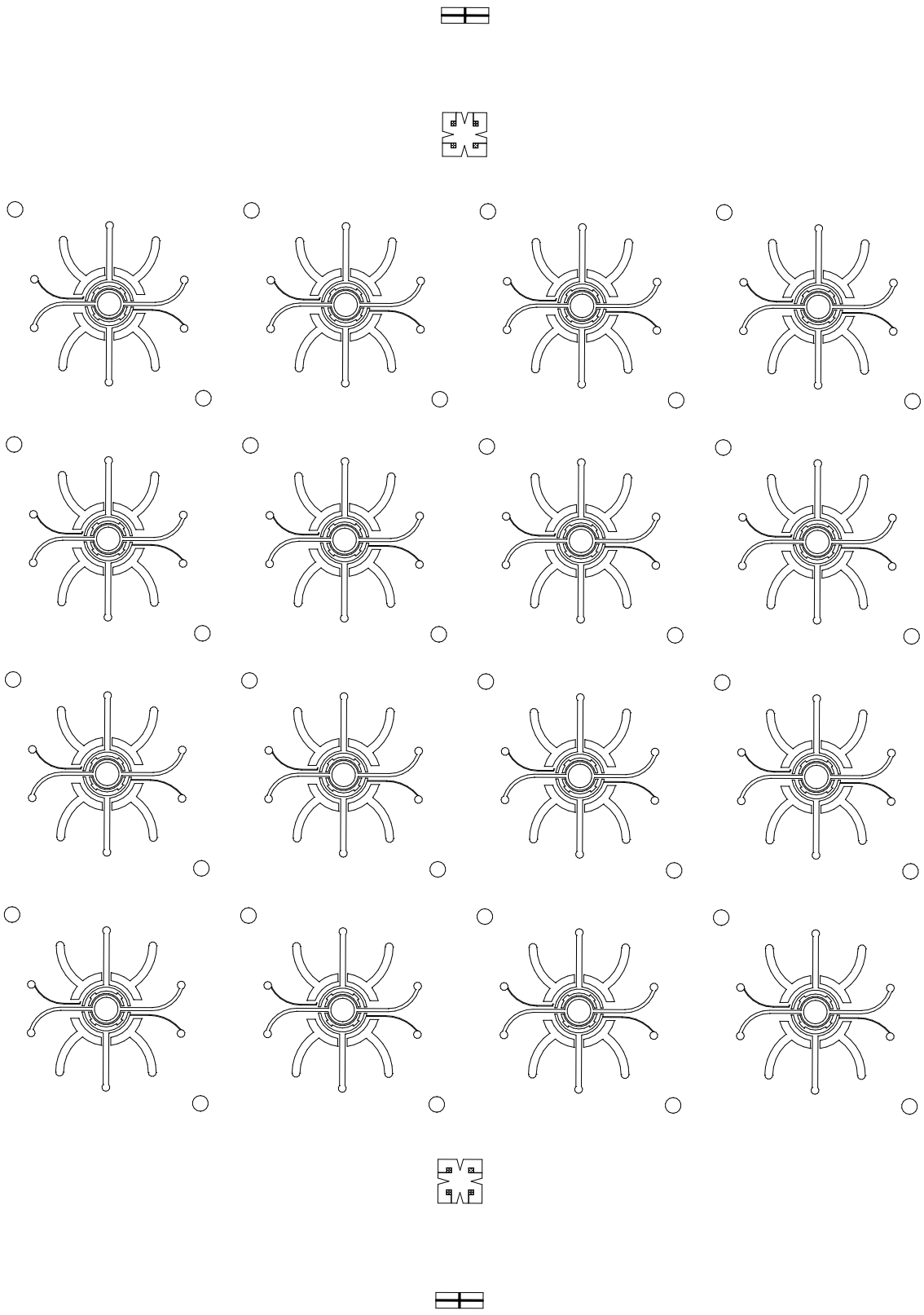

Photomasque 2

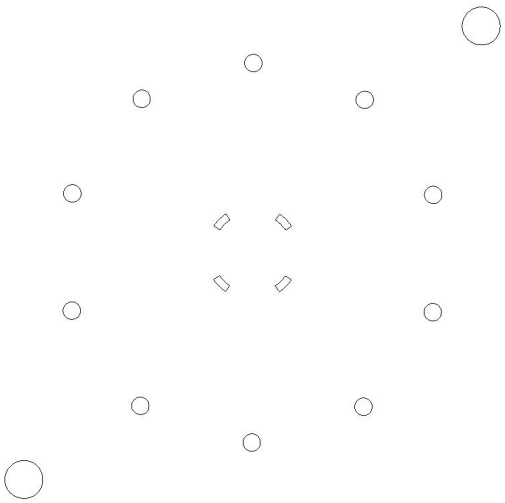

Photomasque 3

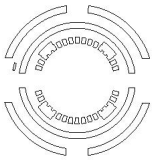

Photomasque 5

Photomasque 6

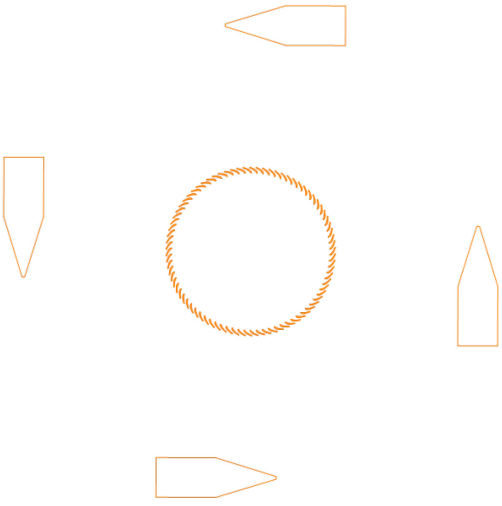

Photomasque 8

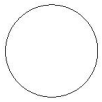

Photomasque 10

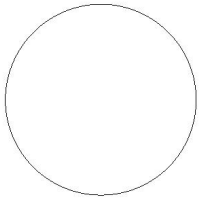

Photomasque 14

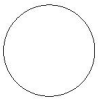

Photomasque 15

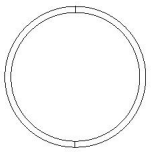

Photomasque 16

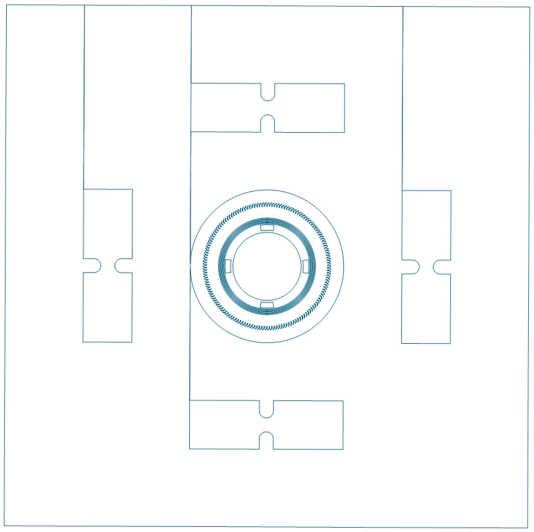

Photomasque 17

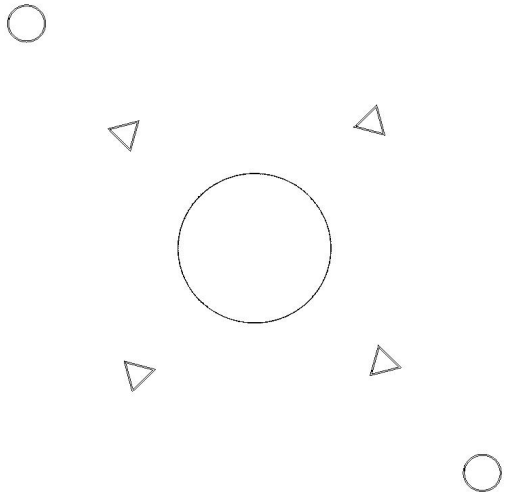

Photomasque 18

Photomasque 19

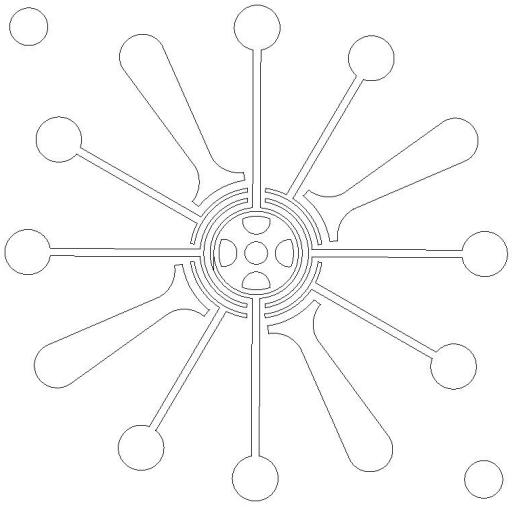

Photomasque 22

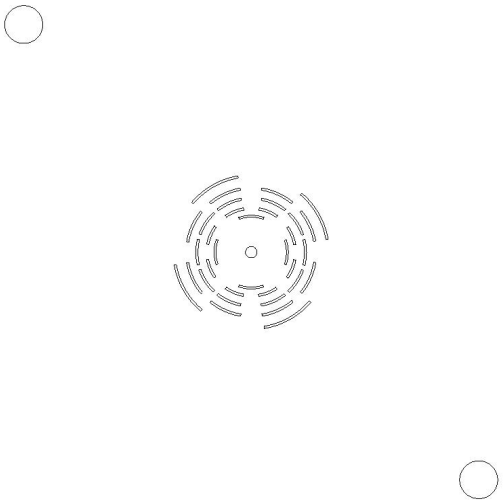

Photomasque 23

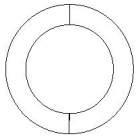

Photomasque 25

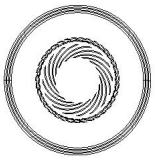

Photomasque 26

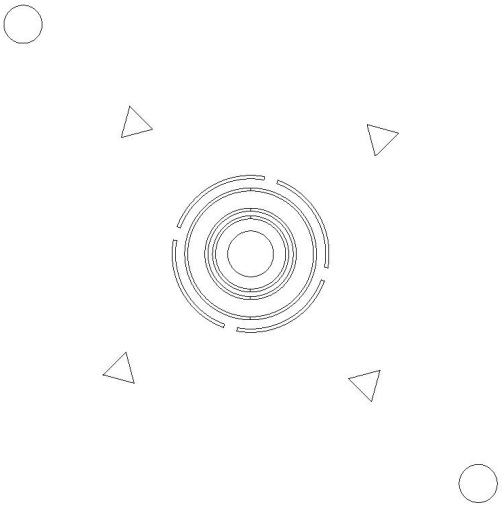

Photomasque 28

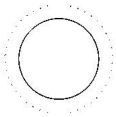

Photomasque 30

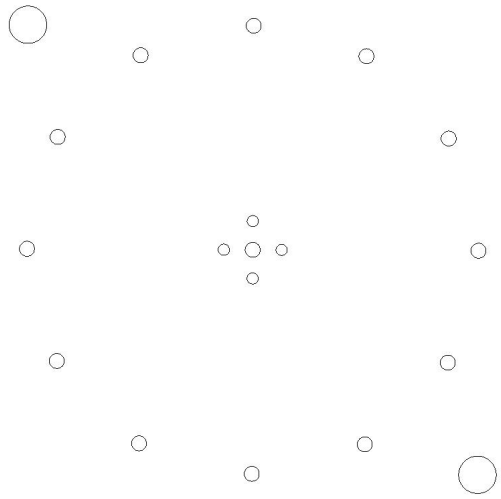

Photomasque 33